EVALUATION OF PARAMETERS INFLUENCING THE IN-VIVO RADIOACTIVITY MEASUREMENTS AND UNCERTAINTIES DUE TO INTERNAL CONTAMINATION OF ACTINIDES

By

MINAL Y. NADAR
PHYS01201304013

Bhabha Atomic Research Centre, Mumbai

A thesis submitted to the
Board of studies in Physical Sciences
In partial fulfillment of requirements
for the Degree of

DOCTOR OF PHILOSOPHY

of

HOMI BHABHA NATIONAL INSTITUTE

November 2016

Homi Bhabha National Institute

Recommendations of the Viva Voce Committee

As members of the Viva Voce Committee, we certify that we have read the dissertation prepared by **Minal Y. Nadar** entitled "**Evaluation of parameters influencing the in-vivo radioactivity measurements and uncertainties due to internal contamination of actinides**" and recommend that it may be accepted as fulfilling the thesis requirement for the award of Degree of Doctor of Philosophy.

Date:

Chairman - Dr. S.B. Degweker
Ex. Bhabha Atomic Research Centre, Trombay, Mumbai -85

Date:

Guide / Convener - Dr. M.S.Kulkarni
Bhabha Atomic Research Centre, Trombay, Mumbai -85

Date:

Examiner – Prof. S. D. Dhole
Savitiribai Phule Pune University, Pune- 411 007

Date:

Member 1- Dr. R. Baskaran
IGCAR, Kalpakkam, Tamil Nadu 603 102

Date:

Member 2- Dr. T. Palani Selvam
Bhabha Atomic Research Centre, Trombay, Mumbai -85

Date:

Member 3- Dr. D. D. Rao
Bhabha Atomic Research Centre, Trombay, Mumbai -85

Final approval and acceptance of this thesis is contingent upon the candidate's submission of the final copies of the thesis to HBNI.

I hereby certify that I have read this thesis prepared under my direction and recommend that it may be accepted as fulfilling the thesis requirement.

Date: 16/01/2017

Place: Mumbai

Signature

Guide

STATEMENT BY AUTHOR

This dissertation has been submitted in partial fulfillment of requirements for an advanced degree at Homi Bhabha National Institute (HBNI) and is deposited in the Library to be made available to borrowers under rules of the HBNI.

Brief quotations from this dissertation are allowable without special permission, provided that accurate acknowledgement of source is made. Requests for permission for extended quotation from or reproduction of this manuscript in whole or in part may be granted by the Competent Authority of HBNI when in his or her judgment the proposed use of the material is in the interests of scholarship. In all other instances, however, permission must be obtained from the author.

Minal Y. Nadar

DECLARATION

I, hereby declare that the investigation presented in the thesis has been carried out by me. The work is original and has not been submitted earlier as a whole or in part for a degree / diploma at this or any other Institution / University.

Minal Y. Nadar

List of Publications arising from the thesis

Journal

1. Methodology for the assessment of Ingested actinides from Monte Carlo simulation of voxel phantom, M. Y. Nadar, D. K. Akar, M.S. Kulkarni, D. D. Rao and K. S. Pradeepkumar, Radiat. Prot. Dosim.,2016, doi:10.1093/rpd/ncw015
2. Assessment of Uncertainties in the lung activity measurement of low energy photon emitters using Monte Carlo simulation of ICRP male thorax voxel phantom, M. Y. Nadar, D. K. Akar, M.S. Kulkarni, D. D. Rao and K. S. Pradeepkumar, Radiat. Prot. Dosim. , 2015, Vol. 167, No. 4, 461- 471.
3. Monte Carlo simulation of skull and knee voxel phantoms for the assessment of Skeletal burden of low energy photon emiters, M. Y. Nadar, D. K. Akar, H. K. Patni, I. S. Singh, L. Mishra, D. D. Rao and K. S. Pradeepkumar, Radiat. Prot. Dosim., 2014, Vol. 162, No. 4, 469 - 477.
4. Monte Carlo simulation of embedded ^{241}Am activity in injured palm, M Y Nadar, H K Patni, D K Akar, Lokpati Mishra, I. S. Singh, D. D. Rao and P. K. Sarkar, Radiat. Prot. Dosim., 2013, Vol. 154, No.2, 148-156.
5. Applying a low energy HPGe detector gamma ray spectrometric technique for the evaluation of Pu/Am ratio in biological samples, I. S. Singh, Lokpati Mishra, J.R. Yadav, M. Y. Nadar, D. D. Rao and K. S. Pradeepkumar, Appl. Radiat. Isotopes., 2015, vol. 104 , 49 – 54. doi: 10.1016/j.apradiso.2015.06.012
6. Estimation of uncertainty due to nonuniform distribution of activity in lungs using Monte Carlo simulation of thorax voxel phantom, M. Y. Nadar, D. K. Akar, M.S. Kulkarni, D. D. Rao and K. S. Pradeepkumar, Communicated to Appl. Radiat. Isotopes, 2016.
7. Uncertainties in lung measurement of actinides due to counting statistics, M. Y. Nadar, D. K. Akar, R. Sankhla, I.S. Singh, M.S. Kulkarni, D. D. Rao and K. S. Pradeepkumar (under preparation).

Conferences

1. Comparison of counting efficiencies of Phoswich detector using various realistic thorax phantoms for ^{241}Am, Minal Y. Nadar, L. Mishra, I. S. Singh and D. D. Rao, Presented in International Conference (IARPIC-2016) on "Radiological Safety in Workplace, Nuclear Facilities and Environment" during February 22-25, 2016 at DAE Township, Anupuram, Kalpakkam, Tamilnadu.
2. Estimation of ^{239}Pu activity in lungs using ^{241}Am as a tracer – solution of Human Respiratory Tract Model, Minal Y. Nadar, H. K. Patni , I. S. Singh, D. D. Rao and K. S. Pradeepkumar, Presented in IRPA-2014 Geneva, Switzerland during June 23-27, 2014. IRPA-2014 Abstract book, pp. 316-317.

3. Solution of Human Respiratory Tract Model for chronic inhalation intake, Minal Nadar, I.S.Singh, and D. D. Rao, Proc. IARPNC-2014 Mumbai, March 19-21, 2014,122.
4. Gaussian smearing of the detector spectrum obtained from Monte Carlo simulation in FLUKA, Minal Nadar, D.D.Rao and K.S.Pradeepkumar, Proc. IARPNC-2014, March 19-21, 2014 Mumbai, 164.
5. Measurement of contribution of activity in liver to lung, Lokpati Mishra, I.S.Singh, Minal Nadar, and D. D. Rao, Proc. NAC-V 2014, 20 - 24 January, 2014 Mumbai,160-161.
6. In-vivo Measurement of Pu/Am activity in liver using phoswich detector, Lokpati Mishra, I.S.Singh, Minal Nadar, and D.D.Rao, Proc. IARPNC-2014, March 19-21, 2014 Mumbai, 120.
7. Assessment and Determination of Inhomogeneous distribution of Pu/Am in Lungs, I.S.Singh, L. Mishra, M.Y.Nadar, D.D.Rao and K.S. Pradeepkumar, Proc. IARPNC-2014, March 19-21, 2014 Mumbai, 138.

Minal Y. Nadar

To

The Creator, Provider, Helper

And my daughter Angelina

ACKNOWLEDGEMENTS

CONTENTS

SYNOPSIS

Assessment of internal contamination of radionuclides in radiation workers forms an integral part of the radiation protection programme in nuclear facility [1]. Among various routes such as inhalation, ingestion and injection or wound through which activity can enter inside the body, inhalation is the most important route [2]. This makes lung monitoring of radiation workers important for the detection of radioactive materials, which are insoluble or going to be retained in the lungs for long durations (> 1 year) [1 - 2]. The insoluble and partially soluble compounds involved in the nuclear fuel cycle are oxides and nitrates of actinides respectively [2]. Actinides such as Pu, Am, U and Th are primarily alpha emitters but they also emit low energy photons (LEPs). ^{239}Pu emits 17.2 KeV U-L X-rays (2.15 %), ^{241}Am emits 60 keV gamma (35.78 %) and ^{234}Th emits 63 KeV (3.8 %) and 93 keV (5.4 %) gammas [3]. Detection of actinides in human lungs is difficult due to low yields of their LEPs and their significant attenuation in the chest wall [4]. Therefore, there is a need of specialized radiation detectors with large area, good energy resolution and very low background [1-2, 4-5].

Phoswich detector with pulse shape discrimination system and an array of HPGe detectors are used in totally shielded steel room for in vivo monitoring of actinides [5]. Both the systems are calibrated using realistic thorax physical, such as Japan Atomic Energy Research Institute (JAERI) and Lawrence Livermore National Laboratory (LLNL) phantoms as a function of muscle equivalent chest wall thickness (MEQ-CWT) [1, 5 - 6]. Different lungs sets containing uniformly distributed activity of various radionuclides such as ^{238}Pu, ^{241}Am, natural and enriched uranium are used for the

calibration. Though mainly used for lung monitoring of radiation workers, the detection systems could also be used to assess contamination of actinides in various other organs, such as liver, skeleton, GI tract or wound, provided they have been calibrated for sources in these organs or sites using suitable realistic phantoms [1]. The attenuation of LEPs (E < 100 keV) depends not only on the overlying tissue thickness and its composition but also on the shape, size and composition of the source organ as detectors are kept very close to the body to improve the detection efficiency [1, 4 - 6]. Therefore, the calibration using realistic physical or voxel phantoms is very important in case of LEP emitters.

There are various parameters that can influence the estimation of activity in lungs, gastrointestinal (GI) tract, or wound. The uncertainty in assessed activity in lungs/wound/other organs will also propagate in the intake and Committed Effective Dose (CED), therefore, to accurately assess the activity in these organs or wound sites, it is important to ascertain the parameters and quantify the uncertainty in the measurements due to them [7, 8]. In this thesis, various parameters that can influence lung activity measurements are identified and the uncertainties introduced in the lung activity due to these parameters are evaluated. The parameters studied, mainly for lung activity estimation are: MEQ-CWT, positional errors, normal background variation, variation of ^{239}Pu and ^{241}Am activity ratio in the lungs, non-uniform distribution of activity in lungs, counting statistics and contribution of source in other organs such as liver, skeleton and lymph nodes in lung measurements. Uncertainties in lung activity due to each of the identified parameters are evaluated in the form of scattering factors (SFs) so that results from this study can be compared to uncertainty values given in literature. Earlier, some experts have given uncertainty values for certain parameters based on judgment [8]. In

this thesis, importance was given to the data generation using phantoms of various weights and heights such as LLNL, JAERI and ICRP reference voxel [9] as well as resized voxel phantoms. Uncertainty values are estimated for different photon energies of actinides for Phoswich and HPGe array using various thorax physical and voxel phantoms.

To evaluate the influence of positional errors, non-uniform distribution of activity, skeletal burdens of actinides and contribution of source in other organs such as liver, skeleton and lymph node in lungs, a theoretical study is carried out using the Monte Carlo code "FLUKA" [10 -11]. The ICRP reference thorax male and resized voxel phantoms were used for this purpose. To study the variation in ^{239}Pu and ^{241}Am activity ratio, biokinetic models of Pu and ^{241}Am in combination with human respiratory tract model are solved for various types of Pu, ^{241}Am compounds (Type M and S) [12, 13]. To study the effect of MEQ-CWT, ultrasonography measurements were carried out on 70 workers of different physiques to estimate CWT and adipose content [14]. To study the effect of counting statistics and normal background variation, experimental measurements were carried out using LLNL phantom with ^{241}Am and natural uranium lung sets and uncontaminated adult male respectively in steel room whole body counter. The estimated SFs from this study are compared with the literature values. Studies are also carried out to evaluate the uncertainties due to important parameters in the estimation of activity in the GI tract/wound due to internal contamination of actinides. Parameters studied are variation of GI tract activity with respect to time of ingestion intake and depth of embedded activity and tissue equivalent material used for calibration in case of wound intakes.

Problem on the effect of diethylenetriamine pentaacetate (DTPA) administered by injection is investigated and presented, in case of intake of actinides by inhalation and wound pathway. The biokinetic models proposed by ICRP do not consider the effect of DTPA on the urine excretion, which differs from excretion in the absence of the DTPA. A methodology is given to predict enhanced urinary excretion rates by modification of the biokinetic model. Few compartments are added in the model representing DTPA biokinetics as Pu-DTPA complex formed in the blood will follow the DTPA model [15, 16]. The transfer rates to these additional compartments in the modified biokinetic model are required to vary around some assumed median values, in order to match the predicted and measured urinary excretion rates. To study the effect of DTPA administered by injection pathway, the modified Pu biokinetic model is solved. The methodology is validated for two cases from literature: inhalation of ^{241}Am, type M compound and wound of avid category of ^{239}Pu. The methodology developed in this investigation will be used to predict the enhanced urinary excretion rates, in case of intake by inhalation of type M compounds and different categories of wound contaminations, when single or multiple DTPA intakes are given by injection pathway. The methodology can also be used to predict the inhalation or wound intakes, using enhanced urine excretion data.

In summary, the thesis combines theoretical analysis, modeling and experimental methods for bridging the knowledge gaps in the estimation of the uncertainties in the lung activity assessment due to various influencing parameters and estimation of the intakes using enhanced urinary excretion data when DTPA is given intravenously. The uncertainties are also evaluated for GI tract and wound activity assessments due to few important parameters. The thesis is organized in eight chapters as given below:

Chapter 1: Introduction and Review of literature

This chapter describes the basic concepts related to internal dosimetry of actinides. The prevailing state of knowledge in direct method of assessment of actinides in vivo is briefly discussed. The shielding requirement, detection systems along with the electronics, measurement geometry, need for realistic phantoms are explained. Various metabolic and dosimetric models used in internal dose evaluation of actinides are clearly presented. The parameters influencing in vivo assessment of actinides are identified. These parameters are estimated from literature as well as from experimental procedures being followed for measurement of lung activity. A literature survey of the evaluated uncertainty values is presented in this chapter. A clear case is thus made for the need of the present work by highlighting the importance of this work, by systematically studying each parameter, taking into consideration person-to-person variability as well as effect at various energies of actinides and detection systems in assessing uncertainty in lung activity estimation.

Chapter 2: Monte Carlo method for photon transport in voxel phantom and methodology for uncertainty evaluation

This chapter describes the Monte Carlo method and various sampling techniques such as rejection and inversion. The Monte Carlo method for photon transport is briefly reviewed by describing geometry and source definition, source sampling, direction cosines, estimating path length in case of homogeneous and inhomogeneous media, sampling for the interaction point and direction parameters after a collision. The ICRP voxel phantom is described in detail as it is extensively used for photon transport in

FLUKA. The source sampling method used to sample source points in various source organs of voxel phantom is explained. Methodologies used for solution of biokinetic models and for evaluation of uncertainties are described.

Chapter 3: Uncertainties in lung measurements due to MEQ-CWT, positional errors, uncontaminated adult male background and Pu & Am activity ratio variation

This chapter describes uncertainties in lung measurement of actinides due to MEQ-CWT, positional errors, uncontaminated adult male background variation and Pu & Am activity ratio variation. Experimental and Monte Carlo simulated values are used to estimate the uncertainties in various parameters. The SFs due to positional errors are evaluated to be 1.12 and 1.05 using Phoswich and 1.14 and 1.07 using HPGe array at 18 and 60 keV respectively. These are based on ICRP male thorax and resized voxel phantoms. Combined uncertainties [8] are estimated at different energies using the uncertainties due to MEQ-CWT, positioning errors and detector background variation of an uncontaminated adult person in the form of SFs. SFs are found to decrease with increase in energy for both the detectors.

Chapter 4: Uncertainties in lung measurements due to non-uniform distribution of activity in lungs, counting statistics and contribution of activity in other organs

This chapter describes uncertainties in lung measurement of actinides due to non-uniform distribution of activity in lungs and contribution of activity in other organs evaluated using thorax voxel phantom. Estimation of skeletal activity using knee and

skull voxel phantoms and its contribution in lung measurements is explained. Experimental measurements carried out using LLNL phantom with various lung sets for evaluating uncertainty due to counting statistics. SF due to counting statistics is found to increase with decrease in lung activity. The SF due to non-uniform distribution of activity in lungs is found to be 1.24 and 1.3 at 60 keV due to phoswich and HPGe array respectively. Experimental measurements and Monte Carlo simulated values are used to estimate the uncertainties in various parameters and combined uncertainty in lung measurements as a function of energy and detector.

Chapter 5: Uncertainties in GI tract activity estimation in case of ingestion intake

This chapter describes uncertainties in abdomen measurements due to intake by ingestion pathway. Human alimentary tract model (HATM) [17] is solved to estimate the activity in various compartments of the GI tract as a function of time for type M and S compounds. Based on the activity distribution in the GI tract, Monte Carlo simulation of ICRP thorax voxel phantom is carried out to estimate counting efficiencies (CEs) and uncertainties in abdomen measurements. Higher CEs are obtained on 0.5 day when source is in small intestine and colon regions. Thereafter, CEs decrease with days post intake. It is found that to estimate ingested activity by direct measurements, CEs based on true activity distribution as per the solution of HATM should be used; otherwise an error of ~ -16 to -75 % will occur in the assessed ingested activity. The contribution of lung activity on GI tract measurements is found to increase with increase in yield and activity of the radionuclide. Contribution of GI tract activity is found to be ~ 10 % in lung measurements one day after ingestion intake and found to decrease with days post

intake. The influence of liver activity on chest and abdomen measurements is found to be ~ 30 to 50 % and ~ 75 % respectively using both the detectors.

Chapter 6: Uncertainties in wound activity estimation in case of intake by wound pathway

In case of estimation of embedded activity in wounds, it is very important to estimate the depth accurately. A methodology is given for estimation of unknown depth and activity in case of intake of Pu or mixed Pu and Am compounds by the wound pathway. Error in the wound activity due to error in depth and ratio of counts in 17.6 and 59.5 keV energy regions and ratio of counts in 26 and 59.5 keV regions is estimated. If Pu is estimated based on Am measurements, error in Pu activity estimation are evaluated using propagation of errors. Monte Carlo simulation of the palm phantom is carried out to estimate CEs for embedded wound activity at various depths, using FLUKA. In various laboratories, Polymethyl methacrylate (PMMA) material is used as a tissue equivalent material in estimating CEs for wound, but such an approximation is found to be valid only for wounds less than 10 mm deep. For wounds deeper than 10 mm, a material which is a soft tissue equivalent at lower photon energies (< 100 keV) should be used. No change is observed in estimated CEs, when source size is modified. It is observed that the relative error in the estimation of ^{239}Pu activity in the presence of ^{241}Am activity decreases with increase in ^{241}Am activity and increase in the ^{239}Pu and ^{241}Am activity ratio.

Chapter 7: Modeling to predict the effect of DTPA on wound and lung activity

This chapter describes the effect of DTPA given intravenously for intake of actinides by wound and inhalation pathway. A methodology is given to predict enhanced urinary excretion rates by modification of Pu and Am biokinetic model. Biokinetic models of Pu and Am are modified to estimate enhanced urinary excretion rates when single or multiple DTPA intakes given by injection pathway in case of inhalation of type M compounds of ^{241}Am and avid category of ^{239}Pu wound intake. The results are validated using data available for known cases of wound and inhalation intakes from literature [18].

Chapter 8: SUMMARY AND CONCLUSION

This chapter gives a summary of the work reported in the thesis and the main conclusions drawn. The brief discussion on the scope of the future work is also included. Main highlights of the work are:

- Uncertainties in lung activity measurements of actinides due to various influencing parameters (MEQ-CWT, positional errors, uncontaminated adult male background and Pu & Am activity ratio variation, non-uniform distribution of activity in lungs, counting statistics and contribution of activity in other organs) are evaluated. Estimated values are compared with the available literature values.

- Uncertainties in abdomen activity assessment due to activity variation with days post intake and in wound measurement of actinides due to depth and tissue equivalent material used for calibration are evaluated.

- Effect of DTPA on urinary excretion in case of intake by wound and inhalation of type M compounds is studied. Methodology is provided to predict the intake using enhanced urine excretion data when DTPA is administered intravenously.

The above developments constitute definite progress towards providing uncertainties in lung activity assessment of actinides. It is no longer necessary to make judgment-based assumptions in assessing uncertainty in lung monitoring. Using experimental and theoretical studies, the uncertainties in the lung activity assessment are evaluated due to all the influencing parameters. It is found that uncontaminated adult male background variation, MEQ-CWT and non-uniform distribution of activity in lungs are the most influential parameters which are sources of uncertainties in lung measurement. The uncertainties due to counting statistics are higher when activities of various radionuclides present in the lungs are around or below MDAs. Uncertainties in the GI tract and wound activity measurements are evaluated for few important parameters such as variation of GI tract activity with days post intake and depth in case of wound. Similarly, the thesis makes a serious attempt to improve our ability of assessing the internal dose when DTPA is given for chelation of actinides by bridging the existing gap between the ICRP models that do not take into consideration DTPA effect and urine analysis data for large number of internal contamination cases available in literature, through systematic theoretical analyses and modeling. The thesis combines experimental and theoretical acumen to address one of the outstanding issues in the area of internal dosimetry: the quantification of uncertainties in in-vivo measurements of actinides. The output of this work will lead to accurate and realistic estimation of lung, GI tract and wound activity.

The methodology used here for quantification of uncertainties can be used in other areas such as monitoring of fission and activation products using shadow shield whole body counter, thyroid monitoring etc. The methodology developed in the course of Ph. D. work can be applied to all categories of wound intakes and can predict the intake when DTPA is administered intravenously.

(M.S.Kulkarni)   (Minal Y. Nadar)
Research Guide   Candidate
May 10, 2016   May 10, 2016

References

[1]   International Commission on Radiation Units and Measurement. Direct determination of Body content of Radionuclides. ICRU Report 69. Journal of the ICRU. 3, No. 1. Oxford University Press (2003).

[2]   International Commission on Radiological Protection. Individual Monitoring for Internal Exposure of Workers. ICRP Publication 78. Annals of the ICRP. 27, No.3-4. Elsevier (1997).

[3]   International Commission on Radiological Protection. Radionuclide Transformations - Energy and Intensity of Emissions. ICRP Publication 38. Annals of ICRP. 11-13. Elsevier (1983).

[4]   In- vivo measurements of Low- Energy Photon Emitters. R.C.Sharma, T.Surendran, T.K. Haridasan and C. M. Sunta. Bull. Rad. Prot. , 12 (4), 41 -56 (1989).

[5]   Pendharkar K. A., Bhati S., Singh I.S., Sawant P. D., Satyabhama N., Nadar M. Y., Vijaygopal P., Patni H.K., Kalyane G.N., Prabhu S. P., Ghare V. P. and Garg S.P. Upgradation of Internal Dosimetry Facilities at BARC Trombay. BARC Newsletter. 296, 9 – 23 (2008).

[6]   International Atomic Energy Agency. Intercalibration of in vivo counting systems using an Asian phantom. IAEA-TECDOC-1334. IAEA (2003).

[7]   International organisation for Standardization. Guide to the expression of uncertainty in measurement. (1995).

[8]   Uncertainties in Internal dose Assessment. NCRP report 164. July, 2009

[9]   International Commission on Radiological Protection. Adult reference computational phantoms. ICRP Publication 110 (Oxford, UK: Pergamon Press) (2009).

[10]   Fasso`, A., Ferrari, A., Ranft, J. and Sala P. R. FLUKA: a multi-particle transport code. CERN-2005-10, INFN/TC_05/11, SLAC-R-773. INFN and CERN (2005).

[11]   Battistoni, G., Muraro, S., Sala, P. R., Cerutti, F., Ferrari, A., Roesler, S., Fasso`, A. and Ranft, J. The FLUKA code: description and benchmarking. AIP Conference Proceeding 896, 31-49 (2007).

[12]   Birchall A. and James AC. A microcomputer algorithm for solving first-order compartmental models involving recycling. Health Phys. 56, 6, 857-868 (1989).

[13]   Eckerman K.F. Dosimetric Methodology of the ICRP. ORNL CONF-9406107—7. (1994).

[14] Nadar M. Y., Singh I. S., Chaubey A., Kantharia S. and Bhati S. Ultrasonic measurements of chest wall thickness for the assessment of internal contamination due to actinides in Indian radiation workers. Recent trends in Radiation Physics Research. Proceedings of NSRP-18, 284 – 285 (2009).

[15] The retention of 14C- DTPA in Human volunteers after inhalation or intravenous injection. J.W. Stather, H. Smith, M.R. Bailey, A. Birchall, R. A. Bulman and F.E.H. Crawley. Health Physics. Vol 44 (1) 45 -52 (1983)

[16] Development of the Plutonium- DTPA biokinetic model. Kevin Konzen and Richard Brey. Health Physics. 108 (6), 565-573 (2015)

[17] International Commission on Radiological Protection. Human Alimentary tract model for Radiological Protection. ICRP Publication 100. Elsevier (2006).

[18] IDEAS database of internal contamination cases.

LIST OF FIGURES

LIST OF TABLES

LIST OF ABBREVIATIONS

AMAD Activity Median Aerodynamic Diameter

AMTD Activity Median Thermodynamic Diameter

CB Cortical Bone

CDF Cumulative Distribution Function

CED Committed Effective Dose

CEs Counting Efficiencies

GIT Gastrointestinal Tract

GSD Geometric Standard Deviation

GUM Guide to expression of uncertainty

HATM Human Alimentary Tract Model

HRTM Human Respiratory Tract Model

ICRP International Committee on Radiological Protection

JAERI Japan Atomic Energy Research Institute

LEPs Low Energy Photons

LLNL Lawrence Livermore National Laboratory

MC Monte Carlo

MDA Minimum Detectable Activity

MEQ-CWT Muscle-Equivalent Chest Wall Thickness

PDF Probability Density Function

RE Relative Error

SFs Scattering Factors

TBBM Trabecular Bone and Bone Marrow

CHAPTER 1

Introduction and review of literature

Monitoring of the radiation workers handling radioactivity in open form such as those involved in fuel fabrication and reprocessing work as well as in maintenance and decontamination jobs in reactors is a mandatory requirement of International commission of Radiation Protection (ICRP) [1] and Atomic Energy Regulatory board (AERB) [2]. Using the monitoring data, committed effective dose (CED) received by worker is estimated and investigated if it crosses the pre-defined investigation level. The monitoring of the radiation workers can be done either by direct or indirect method [1; 3]. Direct method is used if internal contaminant emits energetic photons that can be detected by external detectors. It involves use of partially or fully shielded enclosure along with shielded or open detector of large surface area and higher photon efficiency. The radiation worker needs to be monitored in pre-calibrated measurement geometry where calibration of the detection system is performed with anthropometric or anthropomorphic physical or mathematical or voxel phantoms [3]. The direct method is further divided into low energy photon (LEP) and high-energy photon (HEP) monitoring depending upon the energy of the radionuclide being monitored [4]. For example, actinides such as isotopes of Pu, Am, Th and uranium are alpha emitters but they also emit LEPs of energies < 200 keV, whereas fission and activation products are HEP emitters with energies > 200 keV. Monitoring of actinides can also be performed indirectly by analyzing the urine, nasal swab, filters of personal air samplers, in rare

circumstances blood and in confirmed accidental cases fecal samples of the radiation workers [1; 4]. The disadvantage of indirect method is that it is time consuming as time is required to process the urine or fecal samples and applicable only if intake of radionuclides results in detectable excretion [3]. Both the in vivo and in vitro procedures are termed as Bioassay [5]. In this study, parameters that influence the estimation of activity by direct method due to internal contamination of actinides are estimated. Uncertainties due to those parameters in the lung measurements and for one of important parameters in abdomen and wound measurements are evaluated.

1.1 Actinides

This series encompasses 15 elements [6] with atomic numbers from 89 to 103, actinium through lawrencium. All actinides are radioactive and release energy upon radioactive decay. Naturally occurring uranium and thorium, and synthetically produced plutonium [7] are the most abundant actinides on Earth. Uranium and transuranic radionuclides are normally encountered in operations and facilities representing various stages of the nuclear fuel cycle [8] like mining, milling, fuel fabrication, nuclear power plants, fuel reprocessing and waste disposal. In addition, they are also found in some industrial or research applications. For eg. Americium is used in the ionization chambers of most modern smoke detectors [9].

1.1.1 Nuclear properties of Pu

The atomic number of plutonium is 94. The two most important isotopes of Pu are ^{238}Pu ($T_{1/2} = 87.7$ y) and ^{239}Pu ($T_{1/2} = 24110$ y). Because of its high specific activity of alpha decay, ^{238}Pu generates significant amount of decay heat (567 watt/kg). It is

used as a constant power source for heart pacemakers and in space applications. The most significant application of ^{239}Pu is associated with its property of undergoing nuclear fission by neutron capture. Hence, ^{239}Pu is used as nuclear fuel, and as fissile material in nuclear weapons.

^{239}Pu is produced in natural uranium fuelled reactors by neutron capture in ^{238}U (which is 99.27 wt. % abundant in natural uranium), by the reaction

$$^{238}_{92}U + n \rightarrow {}^{239}_{92}U \xrightarrow[23\ min]{\beta^-} {}^{239}_{93}Np \xrightarrow[2.3\ d]{\beta^-} {}^{239}_{94}Pu$$
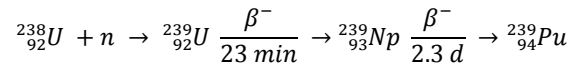
Nuclear properties of various isotopes of Pu [10] are given in the table 1.1. The subsequent absorption of a neutron by ^{239}Pu results in the formation of ^{240}Pu and the higher isotopes of Pu. Since ^{239}Pu is the first in a string of plutonium isotopes created from ^{238}U in a reactor, the longer a sample of ^{238}U is irradiated, the greater the percentage of heavier isotopes.

The isotopes of lower mass numbers (232-237) are produced by charged particle reactions (α, n) or (d, n). The remaining higher isotopes of Pu are produced by successive capture of neutrons in the reactors [11]. The isotopic composition of Pu depends mainly on the type of reactor [12] and the fuel burn up [8]. At very low burn-up used for medical isotope production, the percentage of ^{240}Pu is less than 1 %.

Table 1.1 Nuclear properties of various isotopes of Pu

	Isotope	Half-life	Emissions	Energies MeV	Mode of production
1	^{228}Pu	1.1 s	α	7.94	
2	^{229}Pu	67 s	α 50 % EC 50% SF <7 %	7.59	
3	^{230}Pu	102 s	α	6.99 (19 %) 7.057 (81 %)	
4	^{231}Pu	8.6 min	EC <99.8 % α > 0.2 %	 6.839	
5	^{232}Pu	33.8 min	EC 90 % α 10 %	 6.54 (33.6 %) 6.6 (66.3 %)	^{233}U(α, 5n)
6	^{233}Pu	20.9 min	EC 99.88 % α 0.12 %	 6.42	^{233}U(α, 4n)
7	^{234}Pu	8.8 h	EC 94 % α 6 %	 6.202 (68 %) 6.151 (32%)	^{233}U(α, 3n)
8	^{235}Pu	25.3 min	EC > 99 % α 2.8 x10^{-3} %	 5.85	^{235}U(α, 4n) ^{233}U(α, 2n)
9	^{236}Pu	2.858 y	α	5.768 (69 %) 5.721 (31 %)	^{235}U(α, 3n) ^{237}Np daughter
10	^{237}Pu	3.5 x 10^9 y 45.64 d	SF EC 100 % α 4.2 x10^{-3} %	 5.65 (7.1 %) 5.36 (42.8 %)	^{235}U(α, 2n) ^{237}Np daughter
11	^{238}Pu	87.7 y	α	5.499 (70.9 %) 5.456 (29 %)	^{242}Cm daughter ^{238}Np daughter
12	^{239}Pu	4.8 x 10^{10} y 2.411x10^4 y	SF α	 5.156 (70.8 %) 5.144 (17.1 %)	^{239}Np daughter n- capture
13	^{240}Pu	5.5x10^{15} y 6.56x10^3 y	SF α	 5.168 (72.8 %) 5.123 (27.1 %)	Multiple n-capture
14	^{241}Pu	1.34x10^{11} y 14.29 y	SF β$^-$ 99 % α 2.47 x10^{-3} %	 0.021 4.896 (82.5 %) 4.853 (12.0 %)	Multiple n-capture

15	^{242}Pu	3.75×10^5 y	α	4.902 (76.5 %)	Multiple n-
				4.858 (23.4 %)	capture
16	^{243}Pu	4.956 h	SF		Multiple n-
			β^-	0.58	capture
17	^{244}Pu	8.0×10^7 y	α 99.88%	4.589 (80.5 %)	Multiple n-
			SF 0.12%	4.546 (19.4 %)	capture
18	^{245}Pu	10.5 h	β^-	1.28	^{244}Pu(n, Γ)
19	^{246}Pu	10.84 d	β^-	0.401	^{244}Pu(n, Γ)
20	^{247}Pu	2.27 d	β^-	1.95	

Pu intended for nuclear weapons (low burn-up) has up to 6 to 7 % of ^{240}Pu. A power reactor, which has experienced higher burn up of about 30,000 MWd / t, will have over 25 % of ^{240}Pu and significant amounts of higher isotopes, ^{241}Pu and ^{242}Pu. Due to the short half-life of ^{243}Pu ($T_{1/2}$ = 5 h) the abundance of the higher isotopes in reactor produced plutonium is very small and the chain of the isotopes essentially terminates at ^{242}Pu. The beta or gamma dose from the reactor produced plutonium is mainly due to, the decay of daughters, ^{241}Am and ^{237}U. Plutonium is chemically separated from the fission products and remaining uranium in the irradiated reactor fuel. This chemical separation is called reprocessing [13].

1.1.2 Uranium

About 12 % of the world's electricity is generated from uranium in nuclear reactors [8]. In Indian pressurised heavy water reactors (PHWR), natural uranium (Nat. U) pellets are used as a fuel [14]. The used uranium fuel in the reactor, is removed after about three years, stored so that short-lived fission and activation products undergo radioactive decay and then reprocessed. Nat. U contains 48.86 % ^{238}U and ^{234}U and 2.28 % of ^{235}U activity [12]. Mass fractions for ^{238}U, ^{235}U and ^{234}U are 99.27 %, 0.72 %

and 5.36E-3 % respectively. ^{238}U is detected by 63 and 93 keV photons of its daughter product ^{234}Th ($T_{1/2}$ = 24.1 days) assuming it in secular equilibrium with its parent [4; 15]. ^{235}U is detected by its 185 keV gamma.

1.1.3   Americium

Americium [16] is produced when plutonium atoms absorb neutrons in nuclear reactors. ^{241}Pu beta decays to ^{241}Am. Americium has several different isotopes, all of which are radioactive. The most important isotope is ^{241}Am. ^{241}Am emits [17] 59.5 keV gamma of 36 % yield and it is used as a tracer for detection of Pu. The low energy X-rays of ^{241}Am and Pu isotopes are severely attenuated by overlying tissues. Therefore, Pu contamination can be identifiable by detecting 59.5 keV of ^{241}Am in lungs [18]. By detecting and comparing the intensity of low energy X-rays of 17.6 keV with 59.5 keV gammas of ^{241}Am, it is possible to predict the depth of activity in wound.

U, Pu and Am emits low energy gammas of energy less than 200 keV, compared to fission and activation products, thus detection efficiencies are lower due to attenuation by overlying tissues. Due to higher potential radiotoxicity of these heavy elements, the sensitivities of the systems required for radiation protection of workers is significantly lower [19]. Decay and radiological characteristics of uranium and selected transuranic radionuclides is given in table 1.2. Energy and yield characteristics are based on ICRP 38 [17].

Table 1.2 Decay and radiological characteristics of uranium and selected transuranic
radionuclides.

| Nuclide | Half-life year | Gamma | | Type | Inhalation dose coefficient (Sv/Bq) |
		Energy keV	Yield %		
$^{235}U^{*}$	7.038×10^{8}	143.76	10.96	F	6.0E-07
		185.72	57.0	M	1.8E-06
				S	6.1E-06
^{238}U	4.468×10^{9}	63.29	3.8	F	5.8E-07
		92.38	2.72	M	1.6E-06
		92.8	2.68	S	5.7E-06
^{238}Pu	87.7	13.6	3.57	M	3.3E-05
		17.2	4.3	S	1.1E-05
		20.2	1.04		
^{239}Pu	2.411×10^{4}	13.6	1.32	M	3.2E-05
		17.2	1.58	S	8.3E-06
		20.2	0.382		
^{241}Am	432.2	13.93	21.94	M	2.7E-05
		17.75	18.83		
		59.54	35.9		

*For natural and low enriched uranium type M and F compounds, annual intakes are limited by
considerations of chemical toxicity.

1.2   Requirements for in vivo monitoring of actinides

Direct method involves assessment of lung/liver/skeleton/wound burden of
actinides by keeping the detectors close to the body surface in the proper measurement
geometry [19; 3; 1].   As inhalation is the most likely mode of intake, thorax or lung
counting is commonly used for radionuclides with long residence times in the lung,
such as uranium oxides, plutonium and ^{241}Am oxides [1].   Lung monitoring of the
radiation workers involved in fuel fabrication, fuel reprocessing, maintenance and
decontamination jobs is carried out routinely to confirm safe working conditions in the

plants as well as to estimate lung activity in case of incidents/accidents [1; 3]. Liver and skeleton monitoring is carried out for old exposure cases [19; 1] of actinides, as actinides tend to accumulate in these organs as a function of time. Wound monitoring is required to be done in cases of accidents involving puncture or prick on the palm or fingers of hands [20]. As LEPs emitted by actinides also have low yields as well as attenuated by overlying tissues, sensitive detection systems having low background in low energy regions are needed for their estimation. Therefore, monitoring is carried out in the totally shielded steel room whole body counter lined with graded Z lining using phoswich and HPGe array detectors [21]. The detectors are also required to be kept close to the body organs to improve the efficiency; therefore, there is need to use realistic phantoms for calibration [19] as well as proper measurement geometry for harmonization of monitoring procedures [3].

1.2.1   Shielding

It is a necessary to reduce the gamma-ray background in the direct measurement [19] counting room for various reasons: to reduce the minimum detectable activity [22] (MDA), the counting duration, systematic errors caused by real variations in the background, the uncertainty [23] due to counting statistics and peaks which can cause interference during analysis of the measured spectra.

The effect of background radiation on systematic errors, uncertainties and nuclide identification depends to a great extent on the type of detector used. If a high-resolution semiconductor detector [24] is used, these errors and uncertainties can be significantly reduced since the detector can discriminate between the gamma emissions

of interest and the continuum background. However, in case of scintillator detectors, it is important to reduce the background to minimize the uncertainties in the measurement.

As actinides are LEP emitters, shielding is required [19] to reduce the Compton background in low energy regions due to cosmic rays and uranium and thorium series radionuclides present in the surroundings. This is achieved by using 20 cm thick steel room, which is internally lined with 3 mm lead, Pb, 2 mm cadmium, Cd and 0.5 mm copper, Cu. 20 cm thick mild steel reduces the 2.6 MeV photons of ^{208}Tl, daughter product of uranium series, by multiple Compton scattering to photons of ~ 150 – 250 keV. These lower energy photons are further reduced by photoelectric effect by graded Z lining. Graded Z lining [3; 4; 19] is arrangement of shielding in the descending order of atomic number. First lining of Pb (Z = 82), absorbs these scattered photons and produces characteristic x-rays of 74 to 78 keV which gets further absorbed by Cd (Z = 48). Cd produces characteristic x-rays of 22 to 25 keV which gets absorbed by Cu (Z = 29). Cu absorbs these low energy X-rays and produces its own characteristic x-ray of ~ 8 keV. Thus, using 20 cm thick steel with graded Z lining and choosing the materials of low levels of radionuclide content, background in low energy regions is reduced by a factor of 100. This is known as background reduction factor [19] for this particular shielding arrangement. The functioning of the shielding arrangement is studied by simulating the steel room and graded Z lining in FLUKA [25; 26]. The photons of 2.6 MeV are allowed to fall on the steel room from a surface of sphere. The photon flux in each layer is estimated and given in figure 1.1. FLUKA gives un-smeared output.

9

Figure 1.1 A shows the spectrum observed by 20 cm thick steel. 2.6 MeV peak is clearly visible. In figure 1.1 B, elevated background in 150 - 250 keV energy region is observed along with single and double escape peaks and annihilation peak at 2.089, 1.4 and 0.511 MeV respectively. In Figure 1.1 C, lower background is observed as 100 to 250 keV photons are attenuated by preceding Pb layer but it shows characteristic X-rays at 74 - 78 keV. Figure 1.1 D shows lower energy X-rays at 22 - 25 keV. Schematic diagram of totally shielded steel room is given in figure 1.2.

1.2.2   Detection Systems and electronics

The detection systems consist of an array of three HPGe detectors (HPGe array) and Phoswich detector. HPGe array [each of 7 cm diameter and 2.5 cm thick] with a 0.8 mm thick carbon entrance window is enclosed in a 20 cm diameter and 0.33 cm thick hollow copper cylinder [27]. Centers of the three detectors lying on the circumference of 10 cm diameter circle are positioned at 120 degrees with respect to each other. The details about the HPGe array and schematics is given in figure 1.3.

Phoswich detector is a 20 cm diameter detector which is a sandwich of 1.2 cm thick NaI (Tl) that acts as a primary detector for measuring LEPs and 5 cm thick CsI (Tl) that acts as a secondary detector and used for removing background of HEPs using pulse shape discrimination [4]. It has 0.5 mm thick Be window. Both the detection systems are additionally lined with a 0.5 mm Polymethyl Methacrylate (PMMA) window. The details of the experimental detection system consisting of both HPGe array and Phoswich are geometrically configured and simulated in FLUKA.

(A)

(B)

(C)

(D)
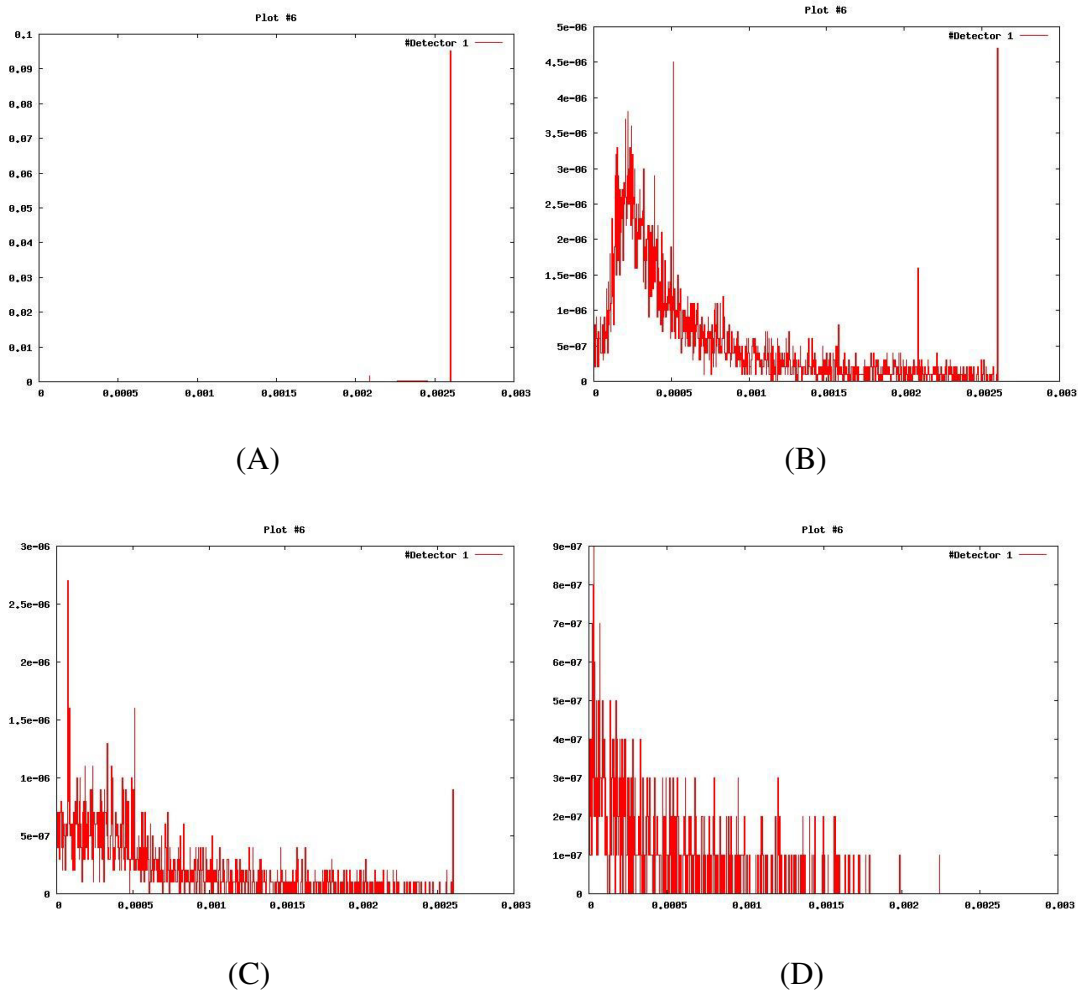
Figure 1.1 Photon flux in A) 20 cm thick steel B)3 mm Pb C) 2 mm Cd and

D) 0.5 mm Cu layer of shield obtained using FLUKA.

FLUKA is a download free, general-purpose Monte Carlo code for simulation of particle transport and interaction of radiation with matter. FLAIR, an advanced user interface [28] of the FLUKA code has been used for creation of input file and visualization of geometry.
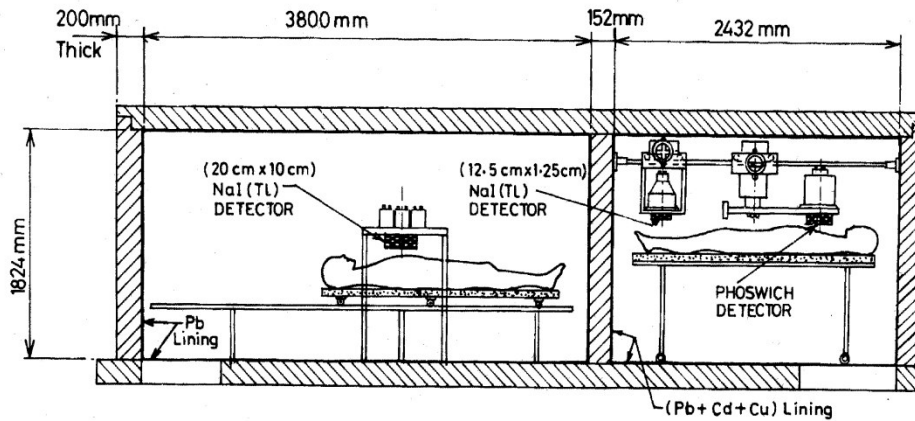
Figure 1.2 Schematic diagram of a whole body counter situated in totally shielded steel room at lung monitoring facility, BARC hospital.

(a)   (b)
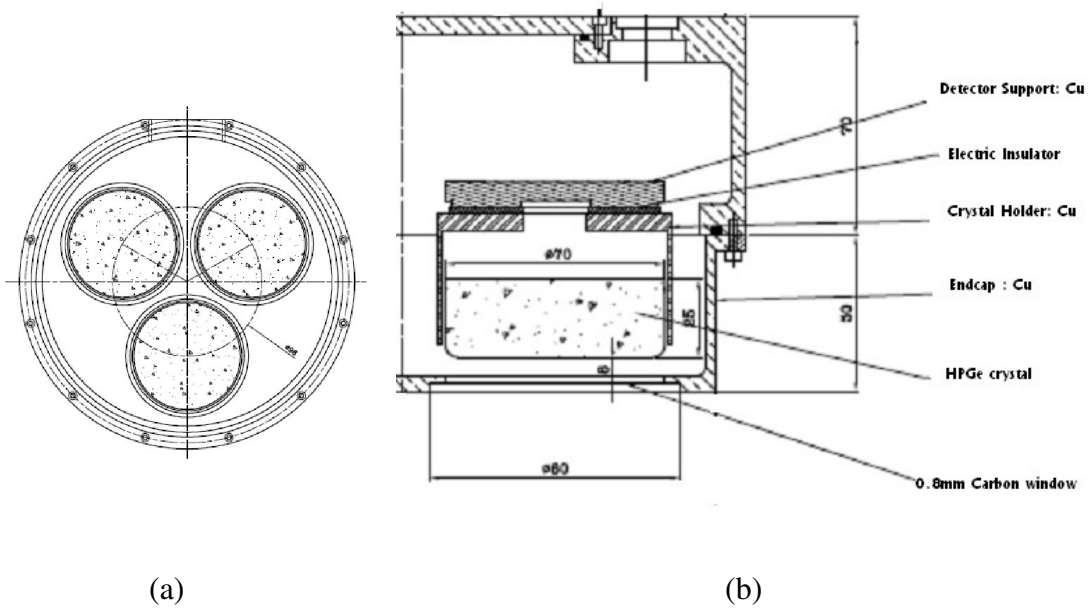
Figure 1.3 Schematic representation of (a) an array of HPGe detectors in transverse plane and (b) single crystal in vertical plane used in the simulation.

Electronics: Pulse shape discrimination (PSD) system [29] is used with the phoswich detector to reduce Compton background in low energy regions. It uses the difference in rise time properties of NaI (Tl) and CsI (Tl) detectors. For photons, NaI shows the rise time of 0.23 μsec and CsI shows two components 0.68 μsec (64 %) and 3.34 μsec (36 %) of the rise times [24]. As LEPs will get absorbed in lower thin 1.2 cm thick NaI (Tl) detector and HEPs will get absorbed in both NaI and 5 cm thick CsI (Tl) detectors, the latter is used as an anticoincidence detector for primary NaI (Tl) detector. The pulses corresponding to LEPs absorbed in NaI are allowed to pass through the logic gate using PSD system, which is optimized [4] for achieving high efficiency, low PSD loss, and low detector background. Block diagram of PSD system is given in figure 1.4.
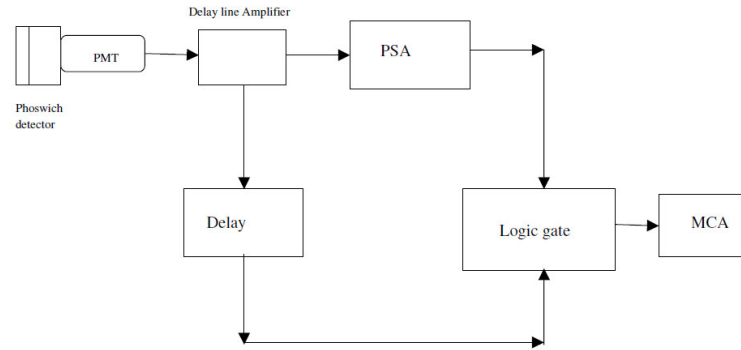
Figure 1.4 Pulse shape discrimination system used with phoswich detector.

Delay line amplifier [29] produces the single delay line shaped output pulse for each input pulse. It is obtained by adding the inverted input pulse to itself and adjusting for the pole zero cancellation. It is then given to PSD, which consists of pulse shape analyzer [29](PSA) and time to amplitude converter. PSA then measures

the time of the inverted pulse at predetermined levels of 10 % and 90 % of the peak

value and converts this time into amplitude. Time is measured by constant fraction

discriminator technique [24; 29] in which logic pulses are produced when pulse reached

10 % and 90 % of its maximum value and time between these two logic pulses is

measured and converted into amplitude. Discriminator is set such that only pulses

corresponding to NaI rise time are selected. Whenever NaI pulse is selected, a logic

pulse is passed on to the logic gate. At the other input of the logic gate, analog pulses

are allowed after providing definite delay through delay amplifier according to the time

lag observed in the PSD, so that NaI pulses and corresponding logic pulses are in

coincidence. Whenever both the pulses are in coincidence, logic gate allows analog

pulses to pass and record in the multichannel analyzer (MCA). Thus, only low energy

pulses absorbed in NaI (Tl) detector are measured using PSD system.

Electronics for HPGe array [30] consists of charge preamplifier, amplifier, and

MCA. Outputs of all the three detectors are summed to obtain final response of HPGe

array.

1.2.3   Measurement geometry

High geometrical efficiency is required to measure the low levels of activities

of LEP emitters that are of interest in occupational exposure. Anatomical references

are used to ensure accurate positioning of detectors [19]. In the standard lung

monitoring geometry [4] used for detecting inhalation intakes, detector is positioned

over the chest such that detector center is on the midline and one end of the detector is

tangential to the supra-sternal notch. Figure 1.5 shows HPGe array and Phoswich

detector positioned over the radiation worker and Asian Phantom (JAERI) in standard lung measurement geometry respectively. To measure ingested activity, detectors are positioned over the abdomen such that detector center is positioned on the midline of the phantom and one end of the detector is tangential to the lowermost rib bone. To estimate skeletal burden of actinides, it is usual to assess the activity in a region of the body that is isolated or can be shielded from interference by activity in the rest of the body [3], for example the skull or the knee. For skull measurements, detectors are positioned over the side of the skull in right or left lateral geometry such that it covers the skull aligning one side of the detector at the top of head. For knee measurements, detector center is positioned on the center of the single knee joint while person is in supine position. For wound monitoring for Pu or ^{241}Am, the palm is positioned at 10 cm distance from the HPGe array window surface, with the wound at the center of detector.

(a)   (b)

Figure 1.5 (a) HPGe array and (b) Phoswich detector positioned centrally over the radiation worker and Asian Phantom (JAERI) in standard geometry respectively.

1.2.4   Phantoms

There are two basic methods for the calibration of in-vivo counting systems: relative and absolute calibration [19]. An absolute measurement does not require a radioactive source for calibration. However, standards can be used to confirm a calibration. They require detailed knowledge of measurement configuration, the human subject, overlying tissue composition and the distribution of radioactive material in the human body. While data on counting geometry and attenuation coefficients for various tissues are available, it is difficult to approximate the distribution of source and absorbing material. Therefore, absolute method of calibration is rarely used in the calibration of in vivo monitoring systems. In contrast, relative calibrations require the use of human surrogates (phantoms) and assumed radionuclide distributions. The phantom must have the same measurement characteristics [3] as a human (anthropometric), but does not necessarily look like the human (anthropomorphic). Calibrations for HEP emitters [19] can be made with quite simple anthropometric phantoms such as BOMAB (Bottle Mannequin Absorption) phantom. However, when calibrating in-vivo measurement systems for LEP emitters, it is usually necessary to use a more realistic anthropomorphic phantom [3; 19]. The phantom contains a known quantity of the radionuclide of interest, which is distributed to represent the distribution in the human body. The type of phantom used for calibration of a direct measurement system depends on the radionuclides to be measured, their assumed distribution in the body, the geometry aspects of the in vivo measurement system and the photon energies being measured.

Anatomically realistic phantoms should be used when photons from the radionuclides of interest are severely attenuated by body tissues [19]. LEPs are easily attenuated within the first few centimeters of the body. Therefore, the detectors must be positioned close to the human body to increase the efficiency (i.e., provide a large solid angle). The response of detectors positioned close to the body are highly dependent on source distribution, thus it is usually necessary to use a realistic phantom to simulate source distributions [19; 31]. Particular care is needed in calibration for measurements of very LEP emitters, especially isotopes of plutonium where 1 mm of soft tissue attenuates 10 % of 17 keV photons [31]. The differential attenuation in muscle, adipose tissue, lung and bone must be accurately simulated and the phantom must be anatomically realistic. LLNL phantom has been designed to simulate Caucasian man (US reference worker: wt = 76 kg, Ht = 177 cm) [32] in Lawrence Livermore national laboratory (LLNL). A similar phantom has been designed at the Japan Atomic Energy Research Institute (JAERI) specifically based on the characteristics of reference Asian man (wt = 63.5 kg, Ht = 168 cm) and is known as JAERI phantom [33]. Figure 1.6 shows the LLNL and JAERI phantoms. These physical phantoms are provided with lung sets of various radionuclides having uniform source distribution.

1.2.4.1   *Physical thorax phantoms: LLNL and JAERI*

The physical thorax LLNL phantom [32] was developed under the direction of the U.S Department of Energy, primarily as a reference standard for the in-vivo counting of emissions from low-energy transuranic nuclides. The organs of interest are

the lungs, liver and lymph nodes. These organs are accommodated in a male thorax mold similar to average adult male.

Figure 1.6 Realistic physical thorax LLNL and JAERI phantoms for lung monitoring facility.

The LLNL phantom contains a synthetic bone skeleton molded within a soft-tissue-equivalent material. The organs are located in an internal cavity with a separate torso cover that closes the phantom. Anterior sections of ribs and the sternum are molded into this cover. Lungs are available with nuclides uniformly dispersed throughout the lung molding material. LLNL phantom has been validated with the inhalation of 'mock Pu' by human volunteers by various laboratories from UK and US [34]. Initially ^{103}Pd was used as Mock Pu and then validation repeated with better Pu simulant, ^{92m}Nb. Calibration factors obtained with the human subjects with varying body builds were compared with LLNL phantom containing ^{92m}Nb uniformly distributed in the lungs. Upon comparison, the calibration factor was found to be within 20 % for various laboratories.

The JAERI phantom [31; 33] is realistic to better simulate the interaction of low energy photons (< 200 keV) with bone, cartilage, muscle and adipose tissues. The torso plate is constructed of an adipose-muscle substitute mixture and contains synthetic bone, and cartilage. The phantom core contains a full rib cage, spine and scapula in the rear of the torso. The overlay plates are constructed of different adipose-muscle substitute mixtures. The torso cavities contain lungs, heart, liver and other organs. All internal organs except the lungs are constructed of muscle substitute material; the lungs are constructed of lung substitute material. The phantom was accompanied by five lung sets that were manufactured for the IAEA by the University of Cincinnati containing ^{238}Pu (low and high activity), ^{241}Am, natural and enriched uranium and ^{232}Th uniformly distributed in each lung set. JAERI phantom was validated with LLNL phantom.

1.2.4.2 *Mathematical phantoms*

There are two main types of mathematical phantoms, phantoms that approximate the sizes and shapes of organs mathematically [35] (MIRD phantom) using cylinders, planes, ellipsoids etc. and voxel phantoms [36] that use tomographic data for real individuals obtained using computed tomography or magnetic resonance imaging. Voxel phantoms have now replaced MIRD phantoms, as they are more realistic. Voxel phantom is a computational phantom [36; 37] where anatomy is represented by three-dimensional array arranged in columns, rows and slices. It is explained in detail in the next chapter.

1.2.5 Data analysis

Preselected regions of interest (ROIs) are used for peak area calculation as few radionuclides are expected in radiation workers. Background of an adult male devoid of any internal or external contamination is used to obtain the net counts in selected ROI's. From the net count rate, activity in the measured organ is estimated using calibration factors [19] for the concerned radionuclide at that geometry. Using organ activity, intake is estimated using retention fractions [1], which are available as a function of particle size, type of material inhaled, ingested or injected in the body and its biokinetic behaviour. Finally, using dose coefficient [38] of the particular radionuclide and for particular pathway, CED is estimated. The work carried out in this thesis, is restricted to the uncertainties in the organ activities due to measurements of these organs using detection systems. Uncertainties in intake and CED are not taken into consideration.

1.3 Biokinetic and dosimetric models used in internal Dosimetry

Modeling [39] refers to the mathematical descriptions of the processes involved in physical movement of radionuclides in the body following intake and the deposition of energy that constitutes exposure. Modeling includes two types of models that must be distinguished: Metabolic models and Dosimetric models.

Metabolic models [1; 39] are used to describe movement of radionuclides through the body following intake. The models depend on the intake mode (Inhalation, ingestion or wound), element, chemical form, physical form and particle size in case of inhalation intake. The models are composed of compartments, which represent the

tissues, including fluids and organs where the material is expected to spend a finite amount of time after intake; transfer routes between compartments; transfer rates associated with each transfer route; and the routes of elimination or excretion. The models have been developed by the ICRP are based on a host of experimental studies [40; 41] published in the open literature. Where data for a specific element is missing, data for elements with similar chemical characteristics is used. The metabolic models are used to calculate the total number of radioactive decays occurring within specific tissues, organs or body regions (source regions) during a given period of time (usually up to 70 y period for child and 50 years for worker).

Dosimetric models [39] are based on the radiological characteristics of the radionuclide and radiosensitivity of the organs or tissues where deposition may occur as determined from metabolic modeling. Dosimetric models represent the geometrical relationships of body structures and are used to calculate the deposition of energy in all important organs/tissues (targets) for transformations occurring in each source region, taking account of the energies and yields of all emissions. Some of the metabolic models used in internal dosimetry for CED estimation are explained below.

1.3.1   Human Respiratory Tract model (HRTM)

The HRTM published by ICRP in 1994 [42] represents a significant revision of the model used in Publication 30 [43]. The main difference is that the ICRP Publication 30 model calculates the average dose to the lungs whereas the HRTM calculates doses to specific tissues of the respiratory tract (RT) and takes account of differences in radiosensitivity. Recently, ICRP has published revised HRTM [44]. In both the

HRTMs, the RT is represented by five regions. The extrathoracic (ET) airways are divided into ET1, anterior nasal passage and ET2, which consists of the posterior nasal passage and the larynx. The thoracic (TH) regions are bronchial (BB), bronchiolar (bb) and alveolar–interstitial (AI), the gas exchange region. Lymphatic tissue is associated with the ET and TH respectively (LNET and LNTH). Reference values of dimensions and scaling factors are specified in the model.

Deposition of inhaled particulates is calculated for each region of the respiratory tract, with account taken of both inhalation and exhalation using deposition model. This is done as a function of particle size, breathing parameters, work load and is assumed independent of chemical form. Age dependent default deposition parameters are given for a range of particle sizes from 0.6 nm activity median thermodynamic diameter (AMTD) to 100 μm activity median aerodynamic diameter (AMAD). Inhalation dose coefficients are given for 5 μm AMAD, which is considered the most representative of workplace aerosols and for 1 μm AMAD, more representative of the aerosols found in public domain. For the ET regions, measured deposition efficiencies are related to characteristic parameters of particle size and airflow and are scaled by anatomical dimensions to predict deposition under other conditions (e.g., gender, ethnic group). For the thoracic airways, a theoretical model of gas transport and particle deposition is used to calculate particle deposition in each of the BB, bb and AI regions and to quantify the effects of the subject's lung size and breathing rate. The regions are treated as a series of filters, during both inhalation and exhalation. The efficiency of

each is evaluated by considering aerodynamic (gravitational settling, inertial impaction) and thermodynamic (diffusion) processes acting competitively.

Regional deposition fractions are calculated for aerosols having lognormal particle size distributions. Geometric standard deviations (σ_g) taken to be a function of the median particle diameter, increasing from a value of 1.0 at 0.6 nm to a value of 2.5 above about 1 μm. Deposition parameters are given for three reference levels of exertion for workers: sitting, light exercise, heavy exercise. For inhalation of radionuclides by workers, the reference subject is taken to be a normal nose breathing adult male at light work (2.5 hours sitting and 5.5 hours light exercise). Fractional deposition in each region of the respiratory tract of the reference worker is given in table 1.3 for 1 and 5 μm AMAD aerosols based on both the HRTMs.

Clearance model describes several routes of clearance from RT. Clearance is competitive between the movement of particles towards the gastrointestinal (GI) tract and lymph nodes (particle transport) and the absorption into blood of material from the respiratory tract. Removal rates due to particle transport and absorption to blood are taken to be independent. Particle transport is treated as a function of deposition site in the respiratory tract but is considered independent of particle size and material.

For most regions, time dependent mechanical transport is modeled by considering the region to be made up of several compartments with different clearance half-times. For example in the HRTM, the AI region is divided into three compartments, which clear to bb with biological half-lives of about 35, 700 and 7000

23

days. In the revised HRTM, AI region is divided into alveolar and interstitial compartments.

Table 1.3 Fractional deposition for normal nose breathing reference worker doing light work.

Region	% Deposition for HRTM, 1994		% deposition for revised HRTM, 2015
	1 µm AMAD	5 µm AMAD	5 µm AMAD
ET1	17	34	47.94
ET2	21	40	25.82
BB	1.24	1.8	1.78
bb	1.65	1.1	1.1
ai	11	5.3	5.32
total	51.9	82.2	81.96

It is assumed that particle transport rates are the same for all materials. A single compartment model is therefore provided to describe particle transport of all materials. Reference values of rate constants were derived, as far as possible, from human studies, since particle transport rates are known to vary greatly among mammalian species. Figure 1.7 and 1.8 describes the compartmental model for time dependent particle transport from each RT region of an insoluble material as given in HRTM and revised HRTM [44] respectively.
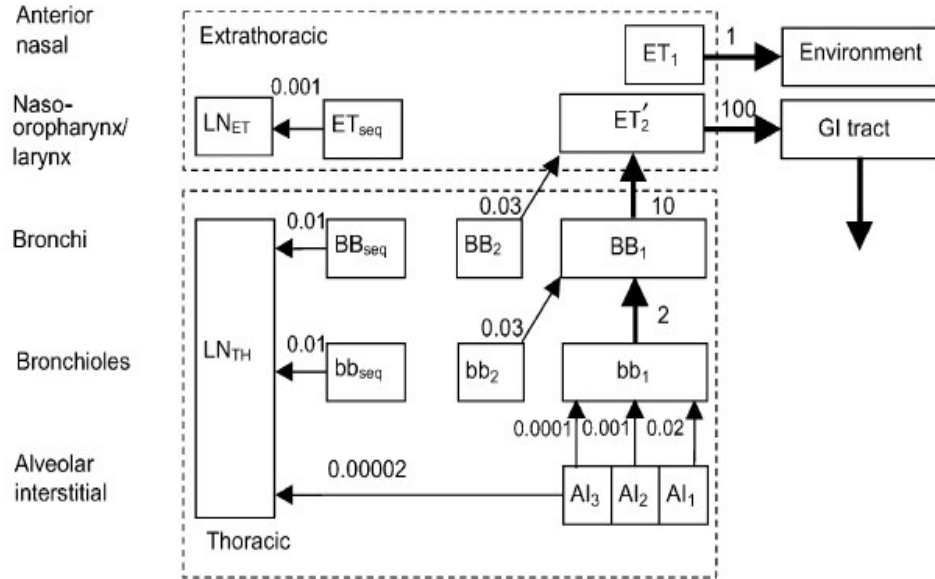
Figure 1.7 Compartmental model for particle transport from each RT region. Rates are in units of d^{-1}.
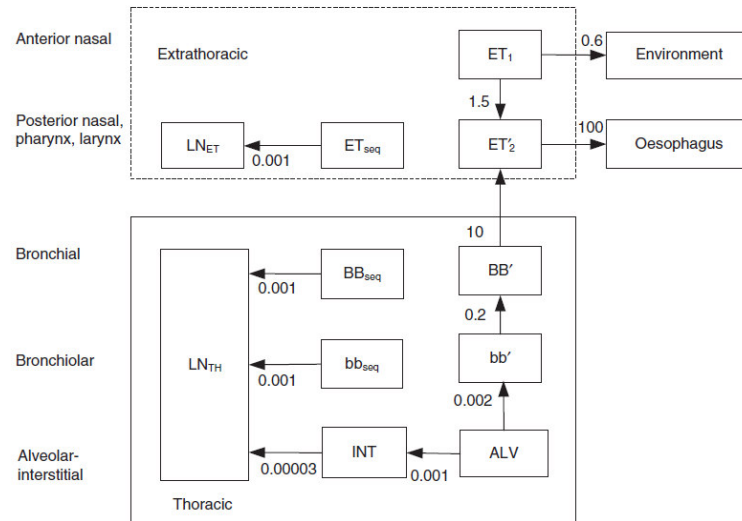
Figure 1.8 Compartmental model for time dependent particle transport from each RT region in the revised HRTM. Rates are in units of d^{-1}.

However, there is simultaneous absorption to blood, which depends on the physical and chemical form of the deposited material. It is assumed to occur at the same rate in all regions (including the lymph nodes) except ET_1, where it is assumed that none occurs. Absorption is a two-stage process: dissociation of the particles into material that can be absorbed into blood (dissolution) and absorption into blood of soluble material and of material dissociated from particles (uptake).

To account for time-dependent dissolution, it is assumed that a fraction of the deposited material dissolves relatively rapidly, and the rest dissolves more slowly. In this model, the material deposited in the respiratory tract is assigned to compartments labelled 'Particles in initial state' in which it dissolves at a constant rate s_p. Material is simultaneously transferred (at a rate s_{pt}) to a corresponding compartment labeled 'Particles in transformed state' in which it has a different dissolution rate, s_t. The ratio of s_p to s_{pt} approximates the fraction that dissolves rapidly. In different situations, the 'Particles in transformed state' may represent the residual material following dissolution of a relatively soluble component or surface layer, or material taken up by macrophages. Figure 1.9 depicts the absorption model used in the HRTM.
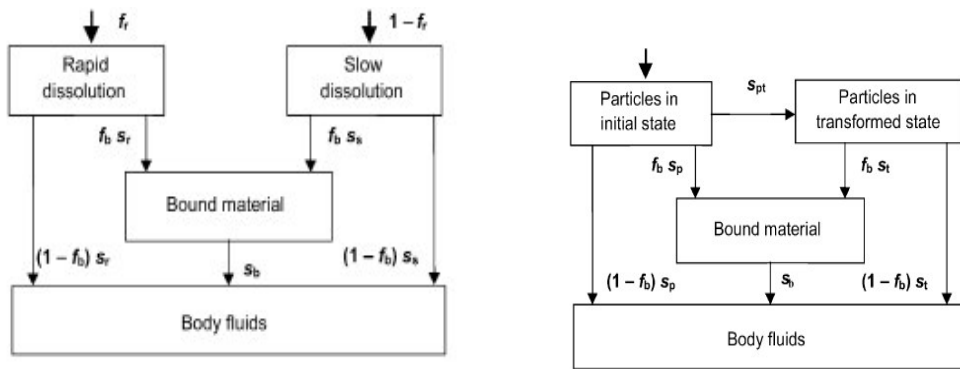
Figure 1.9 Time dependent absorption model

Absorption into the blood depends on the physicochemical form of the radionuclide deposited in the respiratory system, but is taken to be independent of deposition site, with the exception of ET1, from which no absorption is assumed. The model allows for changes in dissolution and absorption into blood with time. The use of material specific dissolution rates is recommended, but default absorption parameters are given for use when no specific information is available, namely types F (fast), M (moderate) and S (slow). The absorption rates for the different absorption types can be expressed as approximate biological half-lives and corresponding amounts of material deposited in each region that reach body fluids, as shown in the table 1.4. The 'bound' state is not invoked for the default parameters, i.e. $f_b = 0$ for all three Types.

Table 1.4 Default absorption parameters for absorption in blood from lungs.

Model parameter	F (fast)		M (moderate)		S (slow)	
	HRTM	Revised HRTM	HRTM	Revised HRTM	HRTM	Revised HRTM
Fraction dissolved rapidly, Fr	1	1	0.1	0.2	0.001	0.01
Rapid dissolution rate, d^{-1}, Sr	100	30	100	3	100	3
Slow dissolution rate, d^{-1}, Ss	-	-	0.005	0.005	0.0001	0.0001

For radionuclide inhaled by workers in particulate form, it is assumed that entry and regional deposition in the respiratory tract is governed only by the size distribution of the aerosol particles. The situation is different for gases and vapors, for which

respiratory tract deposition is material specific. Almost all inhaled gas molecules contact airway surfaces, but usually return to the air unless they dissolve in, or react with, the surface lining. The fraction of an inhaled gas or vapor that is deposited in each region thus depends on its solubility and reactivity. The HRTM assigns gases and vapors to three default solubility/reactivity (SR) classes, based on the initial pattern of respiratory tract deposition. SR0 for insoluble and non-reactive, SR1 for soluble and reactive and SR2 for highly soluble and reactive. Subsequent retention and absorption to body fluids are determined by the chemical properties of the gas or vapor. This classification is removed in the revised HRTM [44]. Default types of compounds F, M, S and V are summarized in table 1.5.

Table 1.5 Summary of default types of compounds deposited in lungs

Type	Model	Properties
F	HRTM	100 % absorbed with a half-time of 10 min. Rapid absorption of all material deposited in BB, bb and AI and 50 % of material deposited in ET2.
	Revised HRTM	100 % absorbed with a half-time of 30 min. Rapid absorption of all material deposited in bb and AI, 80 % of material deposited in BB, 25 % of material deposited in ET2 and 20 % of the material deposited in ET1.
M	HRTM	10 % absorbed with a half-time of 10 min. and 80 % with a half-time of 140 d. ~ 70 % of the deposit in AI will eventually reaches body fluids.
	Revised HRTM	20 % absorbed with a half-time of 6 h and 90 % with a half-time of 140 d. ~ 80 % of the deposit in AI will eventually reaches body fluids.
S	HRTM	0.1 % absorbed with a half-time of 10 min and 99.99 % with a half time of 7000 d. ~ 10 % deposit in AI eventually reaches body fluids.
	Revised HRTM	1 % absorbed with a half-time of 6 h and 99 % with a half time of 7000 d. ~ 30 % deposit in AI eventually reaches body fluids.
V	Both HRTM	100 % absorbed instantaneously as if they are directly injected into body fluids.

1.3.2 Human Alimentary tract model (HATM)

1.3.2.1 *ICRP 30 old GI Tract Model*

Material reaches the GI tract either directly by ingestion, indirectly by transfer from the respiratory tract. The old GI tract model [43] is represented by four compartments: stomach, small intestine, upper large intestine, and lower large intestine. Translocation from one compartment to the next is governed by first order kinetics. The old GI tract model and rate constants, λ, for transfer between compartments and new HATM [45] are given in figure 1.10. In the old model, small intestine (SI) is assumed as the only site of absorption to body fluids. The transfer coefficients for movement of intestinal contents are equal to the reciprocal of the mean residence times.

A single GI tract model is used for all ingested material, with only the fraction absorbed into the blood, f_1, differs according to the chemical composition of the ingested material.

1.3.2.2 *New Human Alimentary Tract Model (HATM)*

The ICRP has published its new HATM [45] in its Publication 100 and given in figure 1.10. HATM comprises the oral cavity, including mouth, teeth, pharynx, oesophagus, stomach, small intestine, including duodenum, jejunum, and ileum, large intestine, including ascending, transverse, and descending colon, rectum and anus.
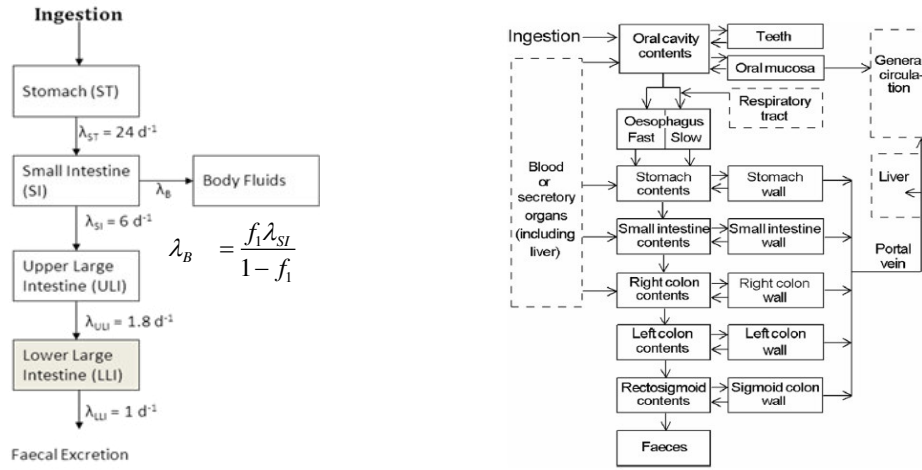
Figure 1.10 ICRP 30 GI tract model along with transfer rates including λ_B for transfer

of activity to systemic body fluids and ICRP 100 HATM.

HATM describes the entry of a radionuclide into the oral cavity by ingestion or into the oesophagus after mechanical clearance from the respiratory tract, sequential transfer through the contents of the oral cavity, oesophagus, stomach, small intestine, and segments of the colon, followed by emptying in feces. It also describes radionuclide deposition and retention on the teeth and return to the oral cavity and transfer from the oral mucosa or walls of the stomach and intestines back into the luminal contents or into blood (absorption) and transfer from various secretory organs or blood into the contents of certain segments of the alimentary tract (secretion). Absorption in the blood is assumed to take place from small intestine but provision is kept for absorption from stomach, oral cavity or any segment of colon.

Total absorption, f_A to blood is the sum of the fractions of the material entering the alimentary tract, f_i absorbed in all regions of the alimentary tract. If absorption

takes place entirely from small intestine to blood then $f_A = f_{SI}$. Uptake to blood $\lambda i_{,B}$ from compartment i of HATM is given by $\lambda_{i,B} = \frac{f_i \lambda_{i,i+1}}{1 - \sum_1^i f_k}$.

An important development in the HATM is the methodology used to calculate doses in the various regions from non-penetrating alpha and electron radiations. In the old GI tract model, it was assumed that the dose to the wall was half of that to contents of the region and an additional factor of 0.01 was included for alpha particles to allow for their short range. The HATM takes explicit account of the location of the target tissue in the mucosal layer of the wall of each region. The targets relating to cancer induction are taken in each case to be the epithelial stem cells, located in the basal layers of the stratified epithelia of the oral cavity and oesophagus and within the crypts that replenish the single cell layer epithelium of the stomach, small and large intestines.

1.3.3 NCRP 156 wound model

The NCRP Wound Model [20] was designed to predict the biokinetic behaviour of both soluble and insoluble radioactive materials. Five compartments were designated to describe certain physical or chemical states of the radionuclide within the wound site. These comprise Soluble (S), Colloidal and Intermediate State (CIS), Particles, Aggregates and Bound State (PABS), Trapped Particles and Aggregates (TPA) and Fragments. NCRP wound model is depicted in figure 1.11.
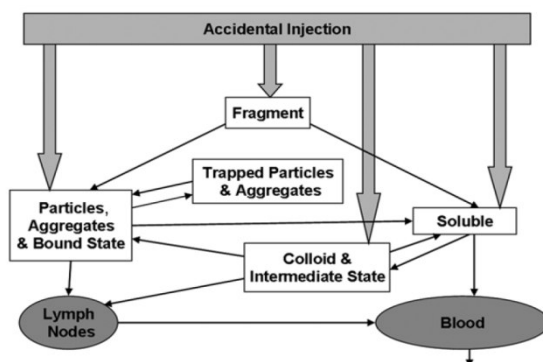
Figure 1.11 General compartmental model of the biokinetics of radionuclides or

radioactive material deposited in a wound.

In some cases, the compartments contain the radionuclide in its original physicochemical form. In others, the originally deposited material changes state and moves from one compartment to another with time. In most cases of contamination, the model simplifies to two or three compartments depending on the physical and chemical form of the radionuclide specified.

Four categories of retention were defined for radionuclides present in a wound initially in soluble form: Weak, Moderate, Strong and Avid, which refer generally to the magnitude of persistent retention in the wound. The criteria for categorization were, the amount retained 1 d after deposition and the rate of clearance of the remainder.

Release of radionuclide from the wound site occurs via blood for soluble materials and via blood and lymph nodes (LN) for particulates. Further solubilisation of particles in LN also provides radionuclide to the blood. The blood comprises the central compartment that links the wound model with the respective radioelement

specific systemic biokinetic model. Once the radionuclide reaches the blood, it behaves biokinetically as if it had been injected directly into blood and in a soluble form. The transfer rates for the wound model for various categories of material are given in table 1.6. The presence of wounds, abrasions, burns or other pathological damage to the skin may greatly increase the ability of radioactive materials to reach subcutaneous tissues and hence the blood and systemic circulation. Although much of the material deposited at a wound site may be retained at the site and can be surgically excised, soluble material can be transferred to the blood and hence to other parts of the body.

Table 1.6 Default transfer rates for the wound model for various categories of radionuclides in wounds.

Transfer	Soluble				colloids	Particles	Fragments
	weak	Moderate	strong	avid	CIS	PABS	
Soluble to blood	45	45	0.67	7	0.5	100	-
Soluble to CIS	20	30	0.6	30	2.5	-	-
CIS to soluble	2.8	0.4	2.4E-2	0.03	2.5E-2	-	-
CIS to PABS	0.25	6.5E-2	1e-2	10	5E-2	-	-
CIS to Lymph Nodes	2E-5	2E-5	2E-5	2E-5	2E-3	-	-
PABS to soluble	8E-2	2E-2	1.2E-3	0.005	1.5E-3	2E-4	0.0
PABS to Lymph nodes	2E-5	2E-5	2E-5	2E-5	4E-4	3.6E-3	0.004
PABS to TPA	-	-	-	-	-	4E-2	0.7
TPA to PABS	-	-	-	-	-	3.6E-3	5E-4
Lymph nodes to blood	-	-	-	-	3E-2	6E-4	3E-2
Fragments to soluble	-	-	-	-	-	-	0.0
Fragment to PABS	-	-	-	-	-	-	8E-3

1.3.4 Biokinetic models of Pu, Am and U

1.3.4.1 *Model for Thorium, Neptunium, Plutonium, Americium and Curium*

The model for Thorium, Neptunium, Plutonium, Americium and Curium is described in ICRP publication 67 [46] and given in figure 1.12. The skeleton is divided into cortical and trabecular components, each of which is further divided into bone surface, bone volume and bone marrow. Activity entering the skeleton is assigned initially to bone surfaces and is subsequently transferred to bone marrow by bone resorption or to bone volume by bone formation. Bone resorption [6] is a process in which osteoclasts breaks down bone and release Ca and minerals from bone to blood. Activity in bone volume is eventually transferred to bone marrow by bone resorption. Activity is removed from bone marrow to blood over a period of months and is redistributed in the same pattern as the original input to blood.

Soft tissue is represented by three compartments ST0, ST1, and ST2. ST0 is a soft tissue pool that includes the extracellular fluids and exchanges material with blood over a period of hours or days. ST1 and ST2 used to represent intermediate term retention (up to 2 years) and tenacious retention (many years) respectively in the massive soft tissues such as muscle, skin, subcutaneous fat and other tissues.

Depending upon the element, liver is viewed as a single compartment as liver 1 or two compartments, with the second compartment represented as liver 2. Liver 2 represents relatively tenacious retention, which is defined on a kinetic rather than biological basis. In case of Th and Pu, hepatic retention and faecal excretion data is

reproduced using two compartmental liver model, where liver 1 loses a portion of its activity to the GI tract over a relatively short period of ~ 1 year and the liver 2 showing greater retention of Pu for many years.
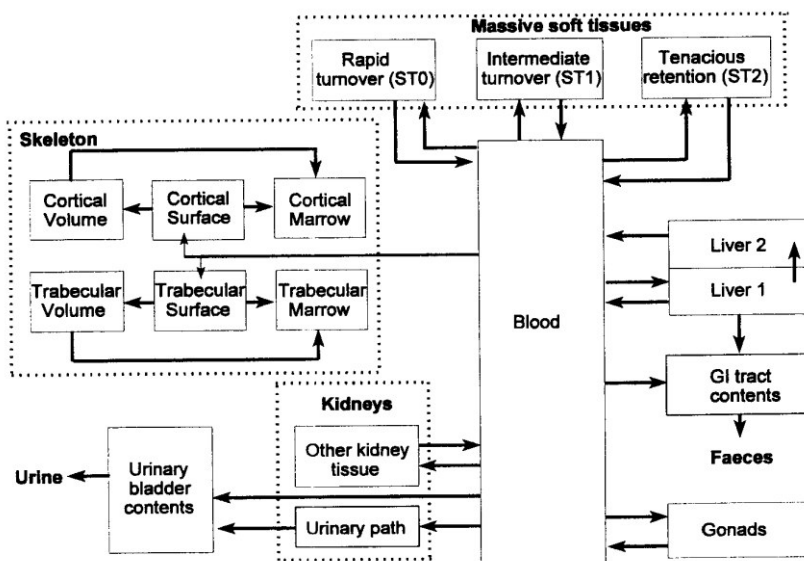
Figure 1.12 Biokinetic model for Thorium, Neptunium, Plutonium, Americium and Curium.

For Am and Cm, data is reproduced reasonably well if liver is considered as a single compartment. The kidneys are assumed to consist of two compartments, one that loses activity to urine and another that returns activity to blood. The 'urinary bladder contents' is another compartment that receives all material destined for urinary excretion.

1.3.4.2   *Model for Strontium, Radium, Uranium*

The alkaline earth elements, Strontium and Radium, follow the movement of calcium in the body but exhibit different rates of transfer from that of calcium due to

discrimination by biological membrane and bone mineral. The same general model with suitable modification is used for Uranium [47] due to its similar behaviour. The biokinetic model of Strontium, Radium and Uranium is given in figure 1.13.

Activity entering blood from the respiratory tract or GI tract is retained by bones and soft tissues or excreted in the urine and feces. All activity leaving the soft tissue compartments is assumed to return to plasma and from there it is assumed to be redistributed among tissues and excreta according to the same parameter value as for the original input to plasma.
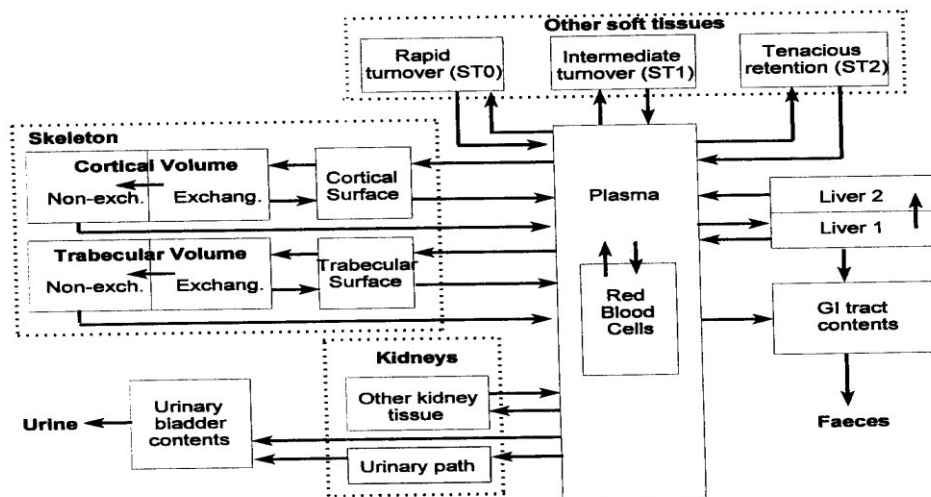
Figure 1.13 Biokinetic model for Strontium, Radium and Uranium.

Bone is divided into cortical and trabecular components, each of which is further divided into bone surface and bone volume. Bone volume is assumed to consist of two compartments EXCH and NONEXCH representing relatively exchangeable and non-exchangeable activity respectively. Activity entering the skeleton is assumed to deposit initially on bone surfaces but returns to plasma or migrates to exchangeable

bone volume within a few days. A portion of activity leaving exchangeable bone volume is assumed to return to bone surfaces and the rest is assigned to non-exchangeable bone volume from which it is gradually removed to plasma by bone resorption. Soft tissue is represented by three compartments ST0, ST1, and ST2. Liver is taken to be distinct from other soft tissues.

Excretion pathways: The number of voids per day is taken to be six. To represent the kinetics of the bladder in terms of first-order processes, the rate of elimination from the bladder is taken to be 12 d^{-1} .The activity present in the upper and lower large intestine includes material which entered the gastrointestinal tract from the systemic circulation into the upper large intestine.

1.3.5 Dosimetric model used in internal Dosimetry

The committed equivalent dose in target organ or tissue T per unit intake is referred to as a dose coefficient [43; 48] and denoted as h_T. It is computed as

$$h_T = \sum_s \sum_j U_{s,j} SEE(T \leftarrow S)_j \qquad \textbf{1.1}$$

where $U_{s,j}$ is the number of nuclear transformations of radionuclide j in source region S during the commitment period following the intake and $SEE(T \leftarrow S)$ is the specific effective energy deposited in target T per nuclear transformation of radionuclide in source region S.

1.3.5.1 _The number of nuclear transformations_

The number of transformations [43; 48] $U_{s,j}$ is obtained by

$$U_{s,j} = \int\limits_{t}^{t+\tau} q_{s,j}(t)dt \qquad\qquad \textbf{1.2}$$

where $q_{s,j}$ (t) is the activity of radionuclide j in source region *S* at time t. It is obtained from the solution of biokinetic model of a particular radionuclide when used in combination with HRTM and HATM or wound model depending upon the route of intake. τ is 50 years for an adult from the time of intake and 70 years for children.

1.3.5.2 *Specific effective energy SEE (T← S)*

The SEE [43] quantity represents the equivalent dose rate in the target tissue per unit activity in the source region. In case of an adult, SEE represents the equivalent dose in the target per nuclear transformation in the source region. The numerical values of SEE are dependent on the anatomical representation of the individual and the type, energy and intensity of the radiations emitted by the radionuclide of interest. The source regions, S, are geometric regions that might contain the radionuclide during its movement in the body. It is not necessary that source regions be tissues [48] nor is it necessary that the members correspond to volumes, e.g., the contents of the gastrointestinal tract are potential members, the surfaces of bone mineral or the airways of the respiratory tract. The target regions T, unlike source regions are the members of body tissues. The principle biological effect of concern is cancer induction, which is cellular in its origin. Specific information on the locations of cells at risk is reflected in the dosimetry of the GI tract, respiratory tract, skin and the skeleton. In all other cases, the location of the sensitive cells has not been specified. For these cases, it is assumed that the cells at risk are uniformly distributed within the volume of the target tissues

and thus the mass-averaged absorbed dose is a reasonable estimate of the dose experienced by the cells at risk. SEE is given by [43; 48]

$$SEE\ (T \leftarrow S) = \frac{\sum_R w_R E_R Y_R AF(T \leftarrow S)_R}{M_T} \qquad \textbf{1.3}$$

Where w_R is radiation weighting factor [49], E_R is energy of radiation, Y_R is a yield, M_T is mass of the target organ and AF (T ← S) is absorbed fraction i.e. Fraction of energy absorbed in target organ T due to emission of radiation in source organ S. For most of the organs, it is assumed that the energies of all α and β particles are absorbed in the source organ (The exceptions are mineral bone and content of GI tract). Thus AF (T ← S) = 0 unless T and S are same for α and β radiation. The absorbed fraction of γ-ray cannot be evaluated in simple way. Their values depend on the photon energy, size, density and relative position of the source and target organs and on the specific intervening tissues. These values are evaluated using reference anatomical models such as MIRD or voxel phantoms for the number of source and target organs.

The committed equivalent dose H_T to a target organ or tissue T includes contributions from all source organs, S, in which radionuclides are present and is given by the expression

$$H_T\ (50) = \sum_S Us\ (50)\ SEE\ (T \leftarrow S) \qquad \textbf{1.4}$$

The committed effective dose [49] (CED) is the sum of the weighted equivalent doses in all the tissues and organs of the body over a period of 50 years following an intake.

$$E(50) = \sum_T w_T H_T(50) \qquad \textbf{1.5}$$

The CED per unit intake is called dose coefficient [1] and given by ICRP for workers and member of public respectively for intake by various pathways.

1.4 Uncertainties in the measurement

Uncertainty is a parameter that characterizes dispersion of the values that could be reasonably attributed to the measurand [23]. It reflects lack of exact knowledge of the measurand. Possible sources of uncertainty are imperfect realization of measurand, non-representative sampling, inexact values of the standards or reference materials, approximations and assumptions used in the measurement method and variation in repeated observations under identical measurement conditions. According to ISO's Guide to the Expression of Uncertainty (GUM) [50], uncertainty components can be grouped into two categories: Type A and Type B standard uncertainty.

Type A standard uncertainty: this can be obtained from observed frequency distribution or repeated observations. Counting statistics gives rise to type A uncertainty, which can be described by the Poisson distribution.

Type B standard uncertainty: this can be obtained from assumed probability density function based on available knowledge. The information may include previous measurement data, experience or general knowledge of the behavior and properties, data provided in calibration, manufacturer's specification or uncertainties assigned to reference data taken from standard books.

The GUM approach is to express the result of a measurement as a best estimate of the measurand, along with an associated measurement uncertainty. The non-negative parameter characterizing the dispersion of the quantity values being attributed

to a measurand, based on the information used is known as measurement uncertainty. Knowledge about an input quantity X_i is inferred from repeated measurements (Type A evaluation of uncertainty) or scientific or other information concerning the possible values of the quantity (Type B evaluation of uncertainty). In Type A evaluations of measurement uncertainty, the assumption is often made that the distribution best describing an input quantity X, given repeated indication values of it, is a Gaussian distribution. X then has expectation equal to the average indication value and standard deviation equal to the standard deviation of the average. The Type A component of uncertainty (i.e. counting statistics) decreases with increasing activity and/or with increasing counting time whereas the Type B components can be considered independent of the activity or the counting time. Therefore, when activity levels are low and close to the limit of detection, the total uncertainty is governed by the Type A component (i.e. by counting statistics). For radionuclides that are easily detected and present in sufficient quantity, the total uncertainty is governed by the Type B components (i.e. by uncertainties other than counting statistics). The Type B components cannot be expressed in terms of Poisson statistics. Depending upon the information available, a probability distribution consistent with that information would be used.

1.5   Literature survey of the work carried out till now by other researchers

There were two international projects [51] on improving performance of internal dose monitoring programs. They were IDEAS project [52] and OMINEX project [53]. The aim of the IDEAS project was a comprehensive assessment of new techniques and

the enhancements needed to bring them into acceptance. The main aim of the OMINEX project was to ensure that resources expended on monitoring for internal dosimetry are employed with maximum effectiveness by optimizing the design and implementation of internal dose monitoring program. The parameters influencing the accuracy of in vivo monitoring were identified by OMINEX project. They are, detector to body distance, chest wall thickness, the difference between the phantom and the subject being monitored with an unknown variability and distribution of activity in an organ being monitored. In IDEAS guidelines [51], typical uncertainty values for the various parameters influencing in vivo monitoring are suggested. The suggested values are given in the table 1.7 for various components. Table 1.8 gives the total uncertainty values for direct measurements of radionuclides emitting low, intermediate and high energy photons.

Table 1.7 Typical values for the components of uncertainty for in vivo measurements of radionuclides.

Source of uncertainty (type) GSD	Typical Uncertainty		
	Low photon energy [a] $E < 20$ keV	Intermediate photon energy 20 keV $< E < 100$ keV	High photon energy $E > 100$ keV
Counting Statistics	1.4	1.3	1.07
Detector positioning	1.2	1.05	< 1.05
Background signal	1.5	1.1	< 1.05
Body dimensions	1.5	1.12	1.07
Overlying structures	1.3	1.15	1.12
Activity distribution	1.3	1.05	< 1.05

| Calibration | 1.05 | 1.05 | 1.05 |
| Spectrum evaluation | 1.05 | 1.05 | 1.03 |

a for HPGe detector spectra

Table 1.8 Total lognormal uncertainty for direct measurements of radionuclides.

Source of uncertainty (type) GSD	Typical Uncertainty		
	Low photon energy[a] E < 20 keV	Intermediate photon energy 20 keV < E < 100 keV	High photon energy E > 100 keV
Counting Statistics	1.4	1.3	1.07
Normalisation	2.06	1.25	1.15
total	2.3	1.4	1.2

a for HPGe detector spectra

In these projects, the uncertainty is given in terms of the scattering factor (SF) assuming that the distributions of the measurements follow log normal distribution. The SF is the geometric standard deviation of the distribution. For example, the SF due to counting statistics is given as SF = 1.4 for LEP counting. This means that the scattering of the measured values due to counting statistics would result in 67 % of the values to lie in between $x_{50}/1.4$ and $x_{50}*1.4$, where x_{50} is the median of all measured values.

1.6   Parameters influencing in vivo monitoring of actinides

Whole body counter situated in totally shielded steel room lined with graded Z lining is used for the quantification of lung/liver/skeleton/wound contamination of actinides [21] in the radiation workers. Phoswich and HPGe array detectors are used for

the detection of LEPs emitted from actinides and 20 cm dia. and 10 cm thick NaI (Tl)

detector is used for the detection of HEPs emitted from fission and activation products.

1.6.1 Parameters influencing lung monitoring of actinides

Phoswich or HPGe array detectors are kept over the chest at ~ 1 cm from the

body surface in standard geometry [4] so that same geometry is maintained for all the

radiation workers. After positioning, the subject is monitored for an optimized time [24]

of 50 minutes, so that relative error (RE) in the measurement at MDA [22] is ~ 30 %.

From the measured gross counts at predefined region of interest (ROIs) for various

energies, net counts are estimated using detector background measurements of an

uncontaminated adult worker. From the net counts, lung activity is estimated using the

counting efficiencies (CEs) obtained from the realistic physical thorax phantom

measurements [31; 34] as a function of muscle equivalent chest wall thickness (MEQ-

CWT) for a particular radionuclide. Uncertainties in measurements [51] are due mainly

to counting statistics, validity of counting procedures, and random fluctuations in

background. Therefore, the parameters that can influence lung activity estimation are:

1.6.1.1 *MEQ-CWT*

At low energies, the relative transmission of photons through tissue is

dependent on the photon energy and tissue thickness as well as tissue composition such

as adipose and muscle content [19]. Since adipose has a lower density than muscle [3],

the relative transmission through adipose is higher than through the same thickness of

muscle. Therefore, an important quantity in the interpretation of lung monitoring data

of radiation workers exposed to aerosols of actinides is CWT, adipose and muscle

content. CWT is defined as the exponential average of tissue thicknesses [54] from the surface of lungs at the points in the intercostal space (in between the ribs). It is defined as

$$CWT = -\frac{1}{\mu}\ln\left[\frac{1}{n}\sum_i \exp(-\mu x_i)\right]$$ **1.6**

Where μ is linear attenuation coefficient [55] for soft tissue at a particular energy, x_i are measured tissue thicknesses in cm at various points i between lung surface and the intercostal space and n is total number of points used for measurement of tissue thickness over the lungs.

According to the above equation, CWT depends upon linear attenuation coefficient μ, the value of which will vary for muscle and adipose, which are constituents of tissue overlying lungs. To remove this discrepancy, the concept of MEQ-CWT [31] has been established. MEQ-CWT is defined as the thickness of muscle-equivalent absorber that reduces the photon flux from the lungs by the same amount as the actual combination of muscle and adipose tissue in the chest. The MEQ-CWT is estimated by taking into account the average CWT, the thicknesses of adipose and muscle tissues present over the lungs at various locations over the chest and considering the attenuation of photons in those mediums at a particular energy using the following equation

$$MEQ - CWT = \frac{X[\mu_A A + \mu_M (1 - A)]}{\mu_M}$$ **1.7**

Where X is the average physical CWT, A is adipose fraction; μ_A and μ_M are the linear attenuation coefficients for adipose and muscle tissues. Using μ_A and μ_M at different energies, MEQ-CWTs can be estimated at those energies.

CEs of phoswich and HPGe array in cpm per kBq are fitted exponentially as a function of MEQ-CWT and given in table 1.9. Thus, it is very important to estimate accurate MEQ-CWT of a radiation worker.

Table 1.9 Counting efficiencies of Phoswich and HPGe array detectors as a function of CWT.

Radionuclide	Energy keV	Calibration factor as a function of CWT cpm kBq^{-1}	
		Phoswich	HPGe array
^{238}Pu	18	34.8 exp (-1.08x)	0.835 exp(-0.037 x)
^{241}Am	59.5	1976.18 exp (-0.26x)	270.93 exp(-0.145 x)
^{238}U Nat. U	63*	712.3 exp (-0.165x)	36.35 exp (-0.26x)
^{238}U Nat. U	185	2640 exp (-0.20x)	371.11 exp (-0.25x)
^{235}U.3% Enr. U	63*	1192.67 exp (-0.15x)	46.12 exp (-0.22x)
^{235}U.3% Enr. U	185	1956.43 exp (-0.25x)	508.12 exp (-0.31x)

*40-120 keV region containing 63 and 93 keV photons for phoswich detector.

MEQ-CWT of a radiation worker can be actually measured using ultra sonography and its value can be accurately estimated. But in routine monitoring, MEQ-CWT is not measured, but predicted using empirical equation based on physical parameters such as person's weight, height, chest circumference and age. Thus, it is a direct source of uncertainty in lung activity estimation.

1.6.1.2 *Positional errors*

Standard geometry based on biological marker such as supra sternal notch is maintained for lung monitoring. However, due to human error, it is possible that detector center is not at midline as well as not tangential to the supra sternal notch but few mm away from the midline in any direction along the chest. As detector is kept close to the chest, this variation in detector positioning is one of the sources of uncertainty in lung activity estimation.

1.6.1.3 *Uncontaminated adult male(normal) background variation*

^{40}K is always present in individuals being measured and large fraction of this is in muscle. In addition, spectra obtained with and without water phantom show that even without additional contamination the background continuum is increased due to the interaction of radiation mainly due to high energy cosmic ray interactions [3] with the phantom and other materials in the steel room. Background in the steel room obtained using phoswich and HPGe array varies due to the variation of the contribution of ^{40}K present in the worker's body as well as variation of cosmic background. Thus, it is one of the source of uncertainty in lung activity estimation.

1.6.1.4 *Non-uniform distribution in lungs*

In the realistic physical phantoms, uniform distribution of activity is assumed in the lungs [31; 34]. The non-uniformity in lungs of the phantoms can contribute uncertainty in the lung measurements. Thus, there is a need to quantify the uncertainty due to this parameter.

1.6.1.5   *Contribution of other organs in lungs*

Non-uniform distribution of activity in lungs is also observed if activity is present in adjacent organs such as liver or overlapping organs such as rib bones and lymph nodes and is contributing in the lungs. Therefore, contribution of source in others organs in lung measurements is required.

1.6.1.6   *Counting statistics*

Uncertainty due to counting statistics [23] are of Type A, follows Poisson distribution and decreases with increase in activity or with increasing counting time. Therefore, when activity levels are low and close to limit of detection, the total uncertainty is governed by type A component and quite significant.

1.6.2   Parameters in case of GI tract contamination

In case of internal contamination of actinides by ingestion pathway, activity will be transferred to various regions of the alimentary tract over time [45]. Therefore, it is very important to estimate the CEs as a function of days post intake as the location as well as amount of activity in GI tract varies with time. Other factors such as positional errors or normal background variation can be assumed same as that of lung contamination.

1.6.3   Parameters in case of wound contamination

In case of wound contamination [20], the depth of activity is very important as CE of low energy photons will vary with respect to depth of wound as transmission of low energy photons will vary with depth.

1.7   Scope for the present work

Assessment of lung/wound activity of actinides in the radiation workers is carried out inside the totally shielded steel room lined with graded Z lining using phoswich and HPGe array. Using the assessed organ activity, intake and CED are estimated using retention fractions and dose coefficients for respective radionuclides taking into consideration mode of intake, particle size in case of inhalation intake, type of compound etc.

In case of lung measurement, care is taken so that proper standard geometry of measurement is maintained; unwanted sources inside the steel room are avoided. Still, various parameters can influence the estimation of activity in lungs as well as in GI tract or wound. To accurately assess the activity in these organs or wound sites, it is important to ascertain these parameters and quantify the uncertainty in the measurements due to them. The uncertainty in assessed activity in lungs/wound/other organs will be propagated in the intake and CED. Therefore, it is important to assess the uncertainty in the measurement of lung, GI tract and wound activities due to various influencing parameters. In this thesis, various parameters that can influence lung activity are identified and uncertainties introduced in the lung activity due to these parameters are evaluated. The parameters studied, mainly for lung activity estimation are: MEQ-CWT, positional errors, normal background variation, variation of ^{239}Pu and ^{241}Am activity ratio in the lungs, non-uniform distribution of activity in lungs, counting statistics and contribution of source in other organs in lungs. Uncertainties in lung activity due to each of the identified parameters are evaluated in the form of SFs so that

results from this study can be compared to uncertainty values given in literature. Earlier, some experts have given uncertainty values for some parameters. In this thesis, the importance was given to the data generation using phantoms of various weights and heights such as LLNL, JAERI and ICRP reference voxel as well as resized voxel phantoms. Using these phantoms, the CEs are evaluated for source in lungs, GI tract, wound, skeleton etc. The CEs are used to generate SFs for each parameter and the SFs of all the parameters are combined to predict total SF for each radionuclide. In estimating the SFs, person-to-person variability as well as effect at different energies and detectors is taken into consideration.

1.8   Summary of chapter 1

In this chapter, basic concepts related to internal dosimetry of actinides are described. The prevailing state of knowledge in direct method of assessment of actinides in vivo is briefly discussed. Various metabolic and dosimetric models used in internal dose evaluation of actinides are clearly presented. The parameters influencing in vivo assessment of actinides are identified from literature as well as from experimental procedures being followed for measurement. A clear case is made for the need of the present work by systematically studying each parameter for assessing uncertainty in lung, GI tract and wound activity estimation.

CHAPTER 2

Monte Carlo method for photon transport in voxel phantom and methodology for uncertainty evaluation

2.1   Monte Carlo method: basic principle

Monte Carlo (MC) is a technique of numerical analysis [56], based on sequence of random numbers to obtain samples of variables of problem [57]. It allows one to estimate population mean and population variance by the sample mean and sample variance [58]. Problem variables can be a radius of a sphere or circle, the interaction of the particle or the direction along which the particle scattered or any other parameter for which the probability distribution is known. It is based on two fundamental statistical results: the law of large numbers and the central limit theorem [58]. The heart of the MC analysis is to obtain an estimate of an expected value [56; 59] such as $\langle z \rangle = \int_a^b z(x)f(x)dx$. The expectation value is obtained by

$$\bar{z} = \frac{1}{N} \sum_{i=1}^{N} z(x_i)$$ **2.1**

Where x_i are suitably sampled from probability density function f(x).

2.1.1   Probability density function [57; 60] (PDF)

PDF has the following properties:

i.   It is defined on an interval [a, b] where b > a.

ii. It is non-negative on that interval, although it can be zero for some x ε [a, b] or x belonging in the interval [a,b].

iii. It is normalized such that $\int_a^b f(x)dx = 1$

Here, a and b represent real numbers or infinite limits and the interval can be either closed or open. The quantity *f(x) dx* is the probability that a random sample x_i will assume a value within *dx* about *x*. This is stated in the form

$f(x)\ dx = \text{Prob}\ (x \le x_i \le x + dx)$

2.1.2   Cumulative distribution function [57; 60] (CDF)

It is defined as $F(x) = \int_a^x f(x')dx'$ or $F(x_i) = \text{Prob}\ (a \le x \le x_i)$

$$\text{Prob}\ (x1 \le x \le x2) = \int_{x_1}^{x_2} f(x)dx = F(x2) - F(x1) \qquad \textbf{2.2}$$

Where *f(x)* is a PDF over the interval [a,b]. CDF is a direct measure of probability [61]. The value *F (x_i)* represents the probability that a random sample of stochastic variable *x* will assume a value between *a* and x_i. CDF has following properties:

i.   *F(a) = 0*

ii.   *F(b) = 1*

iii. *F(x)* is monotonously increasing as *f(x)* is always non negative.

2.1.3   The law of large numbers

The law of large numbers [56; 58] states that as long as mean exists and variance is bounded, then normalized summation approaches the expected mean.

$$\lim_{N \to \infty} \bar{z} = \langle z \rangle \qquad \textbf{2.3}$$

That is, the MC estimate of sample mean approaches the population mean as the number of samples becomes large. Thus, MC is a numerical Quadrature [58], by which expectation value is obtained by normalized summing and it is independent of the number of variables of the function f(x) as long as x is sampled considering all the variables of the problem. This is independent of the discrete or continuous nature of function f(x).

2.1.4 The central limit theorem [56; 58] (CLT)

It states that $\bar{z}$ obtained by samples from a distribution with mean $\langle z \rangle$ and standard deviation σ (z) satisfies the equation:

$$\lim_{N \to \infty} Prob \left\{ -\lambda \le \frac{\bar{z} - \langle z \rangle}{\sigma(z)/\sqrt{N}} \le \lambda \right\} = \frac{1}{\sqrt{2\pi}} \int_{-\lambda}^{\lambda} e^{-u^2/2} du \qquad \textbf{2.4}$$

Thus, it provides the uncertainty to the estimate $\bar{z}$ obtained using MC.

It provides the following insights:

1. $\bar{z}$ is normally distributed with mean $\mu = \langle z \rangle$ and standard deviation $\sigma(z)/\sqrt{N}$

2. Irrespective of the distribution function used to generate N samples of z, provided it has finite variance, the sample mean $\bar{z}$ has normal distribution for large samples.

3. As $\lambda \to 0$, the right hand side of equation approaches 0. Thus, $\bar{z}$ approaches true mean $\langle z \rangle$ as $N \to \infty$. Thus, CLT corroborates the law of large numbers.

4. CLT provides practical way of estimating uncertainty in the MC estimate of $\langle z \rangle$ as sample standard deviation s(z) can be used to estimate population standard deviation $\sigma(z)$ and $\sigma(\bar{z}) \cong s(\bar{z}) = \frac{s(z)}{\sqrt{n}}$.

2.2 MC simulation

In many complex problems, an estimate is sought of some mean value [59; 60] $\langle z \rangle = \int_a^b z(x) f(x) dx$ in which case the underlying PDF *f(x)* is not known a priori. For example, energy deposited in the detector due to source in lungs of the phantom. Thus, *f(E)* can be constructed by simulating the movement of the source photons as they migrate through the problem geometry and by recording the energy deposited in the detector by each photon. With

enough simulated photon histories, the PDF *f(E)* can be approximated and its average value can be calculated as $\bar{E} = \langle E \rangle$.

In such simulations, one strives to mimic the actual physical process involved in the problem by taking into consideration the stochastic nature by which radiation interacts in the geometry and it is known as analog [58; 59] MC simulations. In some situations, such as detector behind shielding, one needs to introduce bias in the simulations, such simulations are known as non-analog MC [56; 58] simulations.

2.2.1 Random number generators

For the mathematical simulation of any statistical phenomenon, where only probability of occurrence of a certain process is known, random numbers [56; 59] are used. It is a number drawn from a set of possible values each of which is equally probable in [0, 1] i.e. they follow uniform distribution.

$$\text{PDF:} \quad f(\xi) = 1 \qquad \text{for } 0 \leq \xi \leq 1$$

$$\text{CDF:} \quad F(\xi) = \xi \qquad \text{for } 0 \leq \xi \leq 1$$

Each number drawn is statistically independent of the others. In computer, an algorithm is used to generate random numbers, hence they are known as pseudorandom numbers [56; 58; 59]. They are sequences constructed from mathematical algorithms that reproduce uniform distribution. They satisfy certain properties [56; 58] such as uncorrelated sequences, long period, uniformity, reproducibility and high speed.

2.2.1.1 *Linear Congruential generator* [56; 58; 59]

It is of the form: $S_{i+1} = (S_i * g + c) \bmod 2^m$

Where S_i = seed, g = multiplier= 7^5 , c = adder, 2^m = modulus that depends on number of bits used to store an integer. For 32 bits computer, period = 2^{32} or 10^{10}. Each S_{i+1} is then scaled to interval [0, 1] by dividing by 2^m. It is a multiplicative congruential generator for c =0,.

2.2.1.2   *Lagged Fibbonacci congruential generator* [58]

Fibbonacci congruential generator is of the form: $x_i = (x_{i-j} + x_{i-k}) \mod m$

Using the proper lags j, k and the modulus m, good random sequences can be obtained. Marsaglia [62] has proposed lagged Fibbonacci generator with lags of 97 and 33 that has a period of $2^{144} \sim 10^{43}$. It is used with a linear congruential generator and both are combined by a chosen operation (either multiplication, addition or subtraction). FLUKA [26], a MC photon transport code, uses lagged Fibbonacci generator [62] along with a linear congruential generator which produces pseudorandom numbers with period of $2^{202} \sim 10^{61}$.

2.2.2   Sampling techniques: Inversion, Rejection

Sampling [56; 58; 59] is a selection of an event in a sample space. A variety of techniques can be used to generate values of a random variable that has a specific distribution. All the sampling techniques are based on having a pseudorandom number generator [59] that can produce long sequences of pseudorandom numbers that are uniformly distributed in the interval [0, 1].

Given a random number ξ, the corresponding random variable associated with the CDF *F(x)* and PDF *f(x)* is given by

$$\xi = \quad F(x) = \int_{-\infty}^{x} f(x')dx'$$

Thus, a random number distributed over [0, 1] interval is used to select random event from a sample space.

2.2.2.1   *Inversion Method*

It is based on the inversion of the CDF of the random variable.

$$\xi = F(x) = \int_{-\infty}^{x} f(x')dx' \quad and \quad x = F^{-1}(\xi) \qquad \textbf{2.5}$$

It is a very efficient method of generating samples of random variables with a given distribution f(x) but it is limited to those distributions for which inverse of CDF can be evaluated [58].

2.2.2.2   *Rejection method*

The inverse of CDF presents difficulties if the PDF *f(x)* cannot be integrated to obtain *F(x)* or even if *F(x)* can be obtained, inverse of CDF is difficult to obtain analytically [58]. Then, an alternative approach of rejection method [58] can be used. Consider figure 2.1, which illustrates PDF *f(x)* defined within range [*a, b*] and known to be less than or equal to *M*. Then, selection of x_i from *f(x)* involves following two steps using rejection method:

1. Select a random value of $x \, \varepsilon \, [a, b]$ as $x_i = a + R_i(b - a)$. From this x_i calculate $f(x_i)$.

2. Select another random number R_j. If $R_j M \leq f(x_i)$, then accept x_i. Otherwise, return to step 1.
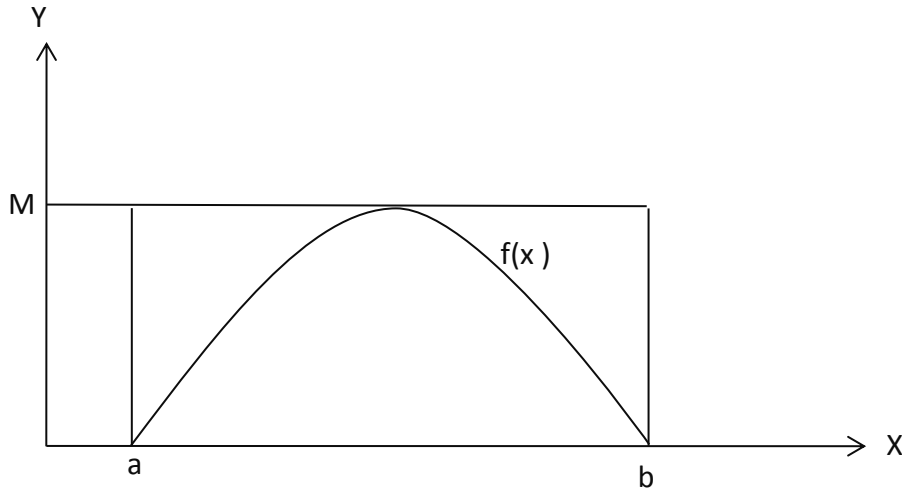
Figure 2.1 PDF *f(x)* for which sampling is needed, having M as a maximum point

The efficiency or probability of not rejecting x_i, is given by the ratio of areas $\int_a^b f(x)dx$ and *M(b-a)*, namely, 1/ *M(b-a)*.

56

2.3 Monte Carlo photon transport

In MC simulation, large numbers of pseudorandom numbers are chosen from the interval [0, 1] and using repeated sampling, the properties of some phenomenon are determined [56; 57; 59] using the PDF of those phenomenon.

It is equivalent to conducting an experiment [58] which needs to faithfully simulate the history of a single particle from birth to death, to random-walk for a single particle, to model collisions using physics equations and cross-section data, to model free-flight between collisions using computational geometry, to score the occurrences of events in each region and to save any secondary particles to analyze them later [63].

MC simulation for photon transport involves computer simulation of individual photon histories and their subsequent averaging [58] to provide the quantities of interest. A photon is followed up by selecting the values of variables and decisions made by sampling known distributions [63] using random numbers [62]. The computational model includes geometry, source sampling for position, energy and direction cosines, sampling for interactions, direction parameters after collision and scoring and analysis of errors. As the number of individual events or histories is increased, the quality of the reported average behavior of the system improves, i.e. there will be less statistical uncertainty [58; 61].

2.3.1 Geometry definition

Every point in space that a particle could possibly reach must be defined in the geometry model. 3D volumes are defined by their bounding surfaces using combinatorial geometry [58; 59], with either surfaces or primitive bodies. A region name [25; 26] is assigned to each 3D volume, which is then assigned with particular material. Composition is assumed uniform and homogeneous within cell. Scoring is defined for particular regions and reaction types [25; 26; 59].

2.3.2 Source definition: energy, sampling in a region

Source sampling is required to generate photons well defined in energy, position and direction coordinates [64]. To sample photon energy, discrete random sampling techniques are used for simulating photons of energy E_i with yield Y_i. For continuous spectrum, the total energy range is divided into number of energy bins each pre-assigned with number of photons.

To sample position coordinates of source particles, inversion or rejection techniques [58; 64] are used. For example, to sample position coordinates for a point source, it is required to assign (x, y, z) with respect to a specified Cartesian coordinate system used for defining geometry. For volume source, source particles are sampled by generating photons uniformly distributed in a volume of the source region.

2.3.3 Direction cosines

The PDF for isotropic distribution can be interpreted as choosing a point with uniform density on the surface of a sphere of unit radius [64]. The element of area ds for this sphere in spherical coordinates (θ, ϕ) is $\sin \theta \, d\theta \, d\phi$ with θ and ϕ lying in the intervals $(0, \pi)$ and $(0, 2\pi)$ respectively.
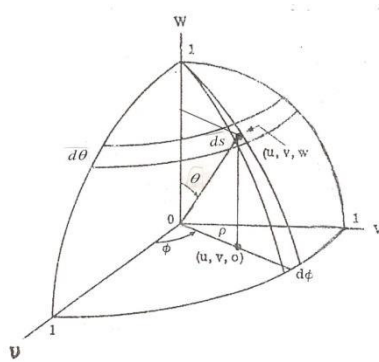
Figure 2.2 Direction cosines for isotropic distribution of source particles

The PDF is given by $f(\theta, \phi) d\theta d\phi = \frac{\sin\theta \, d\theta \, d\phi}{4\pi}$.

The PDF is a product of two marginal densities $f_1(\theta)$ and $f_2(\phi)$.

The marginal densities can be found from their joint densities as:

$$f_1(\theta) = \int_0^{2\pi} \frac{\sin\theta}{4\pi} \, d\phi = \frac{1}{2}\sin\theta \;\rightarrow\; R_1 = F_1(\theta) = \frac{1}{2}\int_0^\theta \sin\theta d\theta \;\rightarrow\; \theta = \cos^{-1}(1 - 2R_1)$$

$$f_2(\phi) = \int_0^\pi \frac{\sin\theta}{4\pi} \, d\theta = \frac{1}{2\pi} \;\rightarrow\; R_2 = F_2(\phi) = \frac{1}{2\pi}\int_0^\phi d\phi \;\rightarrow\; \phi = 2\pi R_2$$

Using θ and ϕ, the direction cosines (u, v, w) of the photon are given by

u = ρ cos ϕ , v = ρ sin ϕ and w = cos θ where ρ = sin θ and $\sin\theta = \sqrt{1 - w^2}$

2.3.4 Estimating path length in homogeneous and inhomogeneous media

2.3.4.1   _Selection of interaction point in case of homogeneous medium_ [58]

The Probability that no interaction occurs for a photon traveling a distance x is $exp(-\mu x)$.

probability an interaction occurs in the distance between x to $x + dx$ is

$p(x)dx = \mu \, exp(-\mu x)dx$

Sampling distance x from the cumulative probability P(x): $R = P(x) = \int_0^s p(x)dx$

$$R = \mu \left|\frac{e^{-\mu s}}{-\mu}\right|_0^s = 1 - e^{-\mu s} \implies s = \frac{\ln(1 - R)}{-\mu} = \frac{-\ln R}{\mu} \qquad \textbf{2.6}$$

The interaction point (x,y,z) at a distance 's' in the direction (u,v,w) from the initial point (x_i, y_i, z_i)

is determined as: $x = x_i + u.s$, $y = y_i + v.s$, $z = z_i + w.s$

2.3.4.2   _Selection of interaction point for heterogeneous Media_

Coleman technique [65] is used to assign correct probabilities of crossing any number of

boundaries. The potential site of an interaction or path length [58] is determined as

$$S = \frac{-\ln R}{\mu_{max}} \qquad \textbf{2.7}$$

where, μ_{max}, is attenuation coefficient that is greater than or equal to any of the regions.

Then, the ith medium containing the probable point of interaction (x, y, z) and its attenuation

coefficients μ_i is determined. If $R \le \frac{\mu_i}{\mu_{max}}$ then interaction site is accepted, else, the photon is

allowed another flight beginning with the point reached and continuing with the same direction and energy [64; 65].

2.3.5   Sampling for interaction at a point

The type of interaction [63] among photo-electric effect, Rayleigh or coherent scattering, Compton scattering and pair production is determined by random sampling from their individual relative probabilities (μ_i/μ_T), where μ_T is the sum of probabilities of photoelectric effect μ_{pe}, coherent scattering μ_{coh}, Compton scattering μ_c and pair production μ_{pp}.

2.3.5.1   *Photoelectric effect*

For R $\leq \mu_{pe}/ \mu_T$

The total photon energy hν is transferred to an atomic electron, which is ejected by the atom from one of its bound shells with energy [24]. $E_{e-} = h\nu - E_b$

History of the photon is terminated and polar angle θ of ejected electron is obtained from Sauter's distribution [66] .

2.3.5.2   *Coherent scattering*

For μ_{pe}/ μ_T < R $\leq (\mu_{pe} + \mu_{coh})/ \mu_T$

This results in a change in the direction of the photon since the momentum change is transferred to the whole atom [15]. There is no change in the energy of the photon. This scattering is not negligible at low energies [15]. Rejection technique is used to sample the scattering angle (θ) according to the differential cross section [66] for scattering into solid angle dΩ.

$$\frac{d\sigma}{d\Omega_{coh}} = \frac{r_0^{\ 2}}{2}\ (1+\ cos^2\theta)[F(q,Z)]^2 \qquad\qquad \textbf{2.8}$$

Where r_o is the classical electron radius and Z is the atomic number, $F(q, Z)$ is the atomic form factor that represents the probability that the recoil momentum q, is transferred to the Z electrons of an atom without any energy absorption and $q = (E_\gamma/hc)\ sin(\theta/2)$.

2.3.5.3   *Compton scattering*

For $(\mu_{pe} + \mu_{coh})/\ \mu_T\ < R\ \leq (\mu_{pe} + \mu_{coh} + \mu_c)/\ \mu_T$

The incoming gamma ray photon is deflected by a loosely bound orbital electron [24] of an absorber, which carries away a part of the photon energy. The energy E of the scattered photon and the scattering angle θ are related by,

$$E = \frac{E_0}{1 + \dfrac{E_0}{m_0 c^2}(1 - cos\theta)} \qquad \textbf{2.9}$$

2.3.5.4   *Pair production*

For $(\mu_{pe} + \mu_{coh} + \mu_c)/\ \mu_T\ < R\ \leq (\mu_{pe} + \mu_{coh} + \mu_c + \mu_{PP})/\ \mu_T$

As high energy photons of energy greater than 1.022 MeV interacts in the Coulomb field of the nucleus where it disappears and its energy is converted [24] into a pair of electron and positron (e^-, e^+) of masses $2m_0 c^2$ i.e. 1.022 MeV. The remaining energy (hv - 1.022) MeV is shared between electron and positron. The electron is absorbed and the positron annihilates with free electron after slowing down producing two annihilation photons each of energy 0.511 MeV. Annihilation photons will travel in opposite direction and each will be traced further as any other photon [63].

2.3.6   Direction parameters after collision

Once the scattering angle and energy of the scattered particle are determined, the direction cosines [58] (u', v', w') of Ω' need to be calculated. The geometry is depicted in figure 2.3.
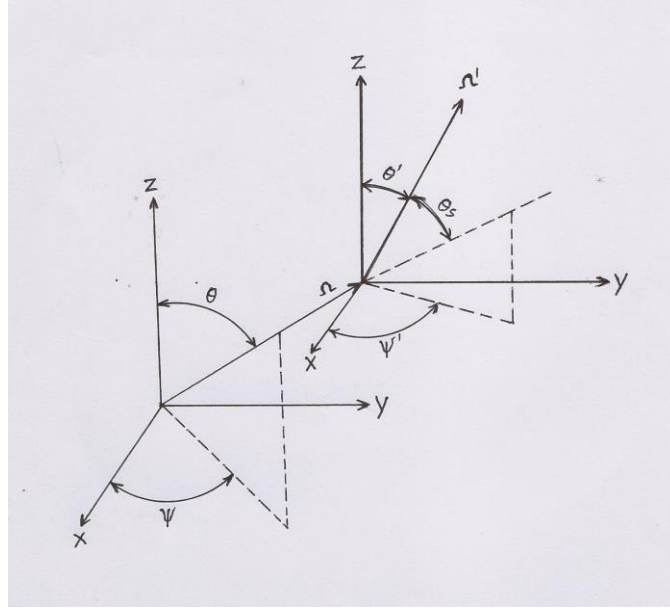
Figure 2.3 The relation between the coordinates of the particle in direction Ω before scatter and

direction Ω' after the scatter.

The angle between Ω and Ω' is the scattering angle θ_s and $\cos \theta_s = \Omega \cdot \Omega$'. The change in

azimuth $\Delta\psi_s = \psi' - \psi$ is uniformly distributed in $(0, 2\pi)$ radians. Let θ and ψ be the polar and

azimuthal angles before scatter with direction cosines $u = \sin\theta \cos\psi$, $v = \sin\theta \sin\psi$ and

$w = \cos\theta$. Consider a rotation about the z-axis through an angle ψ as shown in figure 2.4.
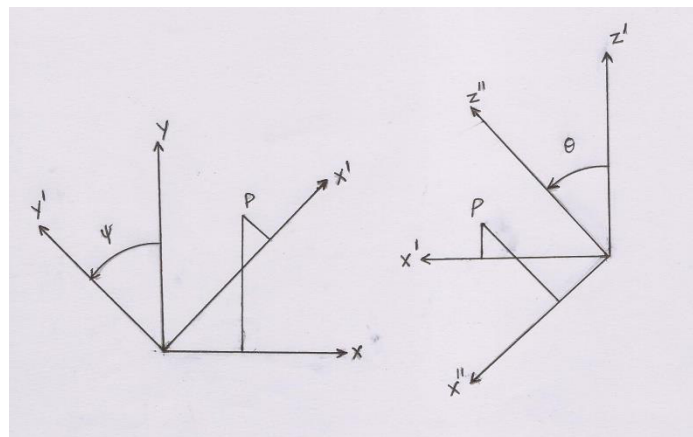
Figure 2.4 Rotation about the z-axis through an angle ψ and rotation about y-axis through an

angle θ.

62

The coordinates of the point P in the original system (x,y,z) and in the rotated systems (x',y',z') are related by

$$\begin{pmatrix} x \\ y \\ z \end{pmatrix} = \begin{pmatrix} \cos\psi & -sin\psi & 0 \\ \sin\psi & cos\psi & 0 \\ 0 & 0 & 1 \end{pmatrix} \begin{pmatrix} x' \\ y' \\ z' \end{pmatrix} = R_z(\psi) \begin{pmatrix} x' \\ y' \\ z' \end{pmatrix} \qquad \text{2.10}$$

If this rotated coordinate system is again rotated about the y'-axis by an angle θ, then the coordinates of the point P in both the systems are given by

$$\begin{pmatrix} x' \\ y' \\ z' \end{pmatrix} = \begin{pmatrix} \cos\theta & 0 & \sin\theta \\ 0 & 1 & 0 \\ -\sin\theta & 0 & \cos\theta \end{pmatrix} \begin{pmatrix} x'' \\ y'' \\ z'' \end{pmatrix} = R_y(\theta) \begin{pmatrix} x'' \\ y'' \\ z'' \end{pmatrix} \qquad \text{2.11}$$

Combining these two rotations, the point P in the (x,y,z) system is related to (x",y",z") by

$$\begin{pmatrix} x \\ y \\ z \end{pmatrix} = \begin{pmatrix} \cos\theta\cos\psi & -sin\psi & \sin\theta\cos\psi \\ \cos\theta\sin\psi & \cos\psi & \sin\theta\sin\psi \\ -\sin\theta & 0 & \cos\theta \end{pmatrix} \begin{pmatrix} x'' \\ y'' \\ z'' \end{pmatrix} \qquad \text{2.12}$$

The resulting rotation matrix is defined as

$$R_{zy}(\theta,\psi) = R_z(\psi)R_y(\theta) = \begin{pmatrix} \cos\theta\cos\psi & -sin\psi & \sin\theta\cos\psi \\ \cos\theta\sin\psi & \cos\psi & \sin\theta\sin\psi \\ -\sin\theta & 0 & \cos\theta \end{pmatrix} \qquad \text{2.13}$$

Consider a particle moving in direction Ω (u,v,w) with u =sinθ cosψ, v = sinθ sinψ and w = cos θ and is scattered through an angle θ_s, with a change is azimuth of $\Delta\psi_s$. To calculate Ω' (u',v',w') [58]:

Step 1. First rotate Ω in the laboratory system to a local coordinate system in which the vector lies along the z-axis. This is done by

$\Omega(\theta,\psi) = R_{zy}(\theta,\psi)$ (0, 0, 1) and $R_{zy}^{-1}(\theta,\psi)\Omega = (0,0,1)$

Step 2. The transformation $R_{zy}(\theta s, \Delta\psi s)$ (0, 0, 1) produces a vector in the local coordinate system, with the direction cosines given by the scattering angles namely, (sin θ_s cos $\Delta\psi_s$, sin θ_s sin$\Delta\psi_s$, cos θ_s).

63

Step 3. Finally, the transformation $R_{zy}(\theta, \psi)$ will bring the scattered vector back to the

laboratory system.

$$\Omega'(u', v', w') = R_{zy}(\theta, \psi) R_{zy}(\theta s, \Delta \psi s) R_{zy}^{-1}(\theta, \psi) \Omega (u, v, w)$$

Using the rotation matrix $R_{zy}(\theta, \psi)$ and knowing that $R_{zy}^{-1}(\theta, \psi) \Omega = (0,0,1)$, scattered direction

cosines are given by

$$u' = u \cos\theta_s + \sin\theta_s (w \cos\psi \cos\Delta\psi_s - \sin\psi \sin\Delta\psi_s) \qquad \textbf{2.14}$$

$$v' = v \cos\theta_s + \sin\theta_s (w \sin\psi \cos\Delta\psi_s - \cos\psi \sin\Delta\psi_s) \qquad \textbf{2.15}$$

$$w' = w \cos\theta_s - \sin\theta \sin\theta_s \cos\Delta\psi_s \qquad \textbf{2.16}$$

As $\sin\theta = \sqrt{1 - w^2}$, $u = \sin\theta \cos\psi$ and $v = \sin\theta \sin\psi$, these results can be written as

$$u' = u \mu_s + \sqrt{1 - \mu_s^2}(w u \cos\Delta\psi_s - v \sin\Delta\psi_s)/\sqrt{1 - w^2}$$

$$v' = v \mu_s + \sqrt{1 - \mu_s^2}(w v \cos\Delta\psi_s + u \sin\Delta\psi_s)/\sqrt{1 - w^2}$$

$$w' = w \mu_s - \sqrt{1 - \mu_s^2} \sqrt{1 - w^2} \cos\Delta\psi_s$$

Where μ_s is $\cos\theta_s$.

2.3.7 Scoring

A scoring routine [58; 59] is designed to decide whether a particle, during its transport in the

system, is inside a particular medium of the system or escaped into another medium or deflected

from the original direction. Then new direction parameters of the particle are determined. If

particle is entered in the region of interest, then particle is scored with specified parameters [64].

Variance of the result is predicted after scoring.

2.3.8 Analysis of the results

Variance of the random variable z is given by $\sigma^2(z) = \langle z^2 \rangle - \langle z \rangle^2$

When n samples are used to estimate mean of the random variable, by the central limit theorem, the variance of the resulting estimate of mean is 1/n times the variance of the population. Variance of mean [58] is given by

$$\sigma^2(\bar{Z}) = \frac{1}{n}\sigma^2(z) \qquad \textbf{2.17}$$

$$\sigma(\bar{z}) \cong s(\bar{z}) = \frac{s(z)}{\sqrt{n}} = \frac{1}{\sqrt{n}}\sqrt{\frac{n}{n-1}(\overline{z^2}-\bar{z}^2)} \cong \frac{\sqrt{(\overline{z^2}-\bar{z}^2)}}{\sqrt{n-1}} \qquad \textbf{2.18}$$

The quantity $\bar{z}$ is the sample mean, the estimate of $\langle z \rangle$. The precision of the result is a measure of deviation from the sample mean and is given by the standard deviation of sample mean $s(\bar{z})$. Accuracy is the measure of the difference between true value or population mean and the sample mean.

In MC, fractional standard deviation (RE) is used. It is obtained by dividing standard deviation with mean of the random variable [67]. It is required that for meaningful results RE should be less than 0.1 for detectors other than point detectors [68] and less than 0.05 for point or ring detectors.

2.4   Voxel phantom

Voxel phantoms [36] are anatomic models based on computed tomography, magnetic resonance or other images obtained from high-resolution scans of a single individual, and, thus, offer a more realistic replication of human anatomy [37]. As the image slice refers to a certain anatomical thickness, each pixel also defines a voxel or volume element. Voxel phantom consists of a number of slices and hence number of volume elements (voxels). Segmentation [36; 37] refers to the process by which individual pixels in an image slice are given organ identification numbers instead of their original Hounsfield numbers (image pixel intensity). The collection of all voxels with the same identification number defines a certain organ [36] or tissue.

2.4.1 ICRP reference male voxel phantom

It is based on whole body CT scan data of a 38 year old male [36] and adjusted so that it correspond to reference man [69] of weight 73 kg and height 176 cm. The data set consisted of 220 slices of 256 x 256 pixels. The voxel size was 8 mm in height with an in-plane resolution of 2.137 mm, resulting in a voxel volume [36] of 36.534 mm^3. Figure 2.5 shows the ICRP reference male voxel phantom. It is described by three dimensional (3D) voxel array [36] arranged in columns, rows and slices. In 3D array, columns correspond to X co-ordinates that increase from right to left; rows correspond to Y co-ordinates that increase from front to back and the slices to Z co-ordinates that increase from toes to vertex of the body. At each array position, the identification number [36] of the organ to which the voxel belongs is stored. In ICRP male voxel phantom, 122 individual organs are segmented.

2.4.2 Various other voxel phantoms

Various phantoms such as thorax [70], knee and skull [71] phantoms are obtained from ICRP reference male voxel phantom [36] by cutting it in X-Z planes and removing the voxels above the skin layer in X-Y plane. This modification was required to position the detectors at ~ 1 cm from the phantom surface for simulating the actual geometry of measurement [70; 71]. Figure 2.6 depicts the thorax voxel phantom obtained from ICRP reference voxel phantom.

2.4.3 Source Sampling in various regions of voxel phantom

Source is sampled in lungs, by first randomly selecting the voxel from identified lung [70] voxels and then randomly selecting a point in that voxel. The isotropic directional distribution of emitted photons is sampled using uniform distribution of the azimuthal angle and cosine of the polar angle [27; 64]. To sample the source in other regions or organs, the same methodology as of lungs is used.
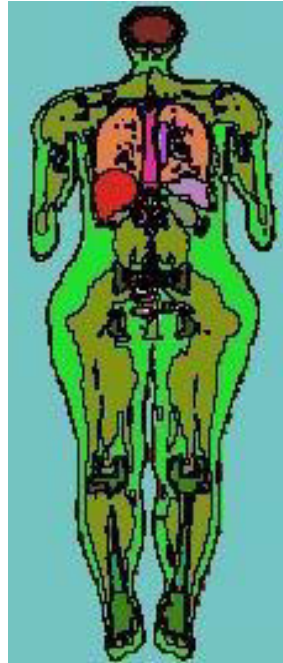
Figure 2.5 ICRP reference adult male voxel phantom
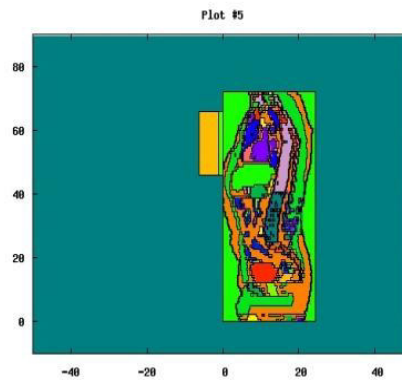
Figure 2.6 ICRP male thorax voxel phantom.

To simulate the source in GI tract, according to the solution of HATM [45], the voxels of each region are selected as per the activity distribution [72]. First, the activity distribution in various regions is normalized and cumulative distribution is calculated [60]. Using the cumulative distribution and inversion technique [58], the voxel is randomly selected from known voxels of

the contents of small intestine, right colon, left colon and recto sigmoid colon. Then, a point is randomly selected [64] in that voxel. The same method is used for source sampling for non-uniform distribution of activity in lungs as well as for sampling ^{241}Am source energy spectrum in palm phantom [27].

Seven energies of 18 keV, 60 keV, 63 keV, 74 keV, 93 keV, 185 keV and 238 keV are simulated for the photons emitted from ^{239}Pu, ^{241}Am, ^{238}U, ^{235}U and ^{212}Pb. 'Detect' card [25; 26] of FLUKA is used for scoring energy deposition in primary NaI of Phoswich detector and all the three detectors of HPGe array and for its summed output. The counting efficiencies (CEs) in the various energy regions are determined for 2 x 10^6 histories run over 5 cycles to obtain RE of less than 3 % [67]. CEs are estimated by scoring the events of energy deposition in the particular energy bin. This is done by 'detect' card in FLUKA. Preselected energy region, such as 10 keV to 250 keV is distributed in 1024 bins uniformly. Initial source photon of 60 keV will interact in the phantom and surrounding materials leading to scattered photons of various energies. These photons will reach the detector and depending upon the energy will be scored in the particular energy bin. For example, scattered photon of 43 keV after depositing its full energy in detector will be scored in the energy bin of interval 42.8 keV to 43.1 keV. Thus, event means energy deposited in detector region by one primary particle, in this case, a photon and its descendants. To estimate CE at particular energy, the scored counts are summed over the region of interest covering 3σ regions around the photo peak. σ is the standard deviation of the photon counts and related to resolution of the detector. Thus, scoring is done by detect card and CEs are evaluated in counts per photon for a particular energy region. FLUKA does not carry out the Gaussian smearing as per the detector resolution but gives output in 1024 channels for the selected energy region and step size. To estimate the detector spectrum from FLUKA output, a program was

written in MATLAB for Gaussian smearing of the output taking into consideration the detector resolution [73].

2.5　Methodology of solving the biokinetic model

Following intake [1] of a radionuclide by inhalation or ingestion or wound pathway, it will be absorbed in the systemic circulation with a subsequent distribution among the systemic organs. This is described by biokinetic models [1; 46; 47], which are given for various radionuclides depending upon their physio-chemical and biological behavior in humans or animals. Biokinetic models are mathematical representations [39; 48] of the movement of elements and their radioisotopes within the body and their uptake and retention in organs and tissues. They are described by a system of ordinary differential equations with constant coefficients [48]. The coefficients are transfer rate constants evaluated from human exposure data or from extrapolated animal data [39] and are inverse of mean half time. In these models, organ or tissue is represented by compartment.

The first step in solving a particular compartment model is to number the compartments [74] from 1 to n. The second step is to represent the model by rate matrix [74] [R]. Each element R_{ij} of the matrix contains a value r_{ij} for the transfer rate constant from compartment j to i. Each diagonal element R_{ii} contains a value for the initial amount of activity x_i (0) in compartment i.

Rate of change in any compartment i is defined as the difference between the inflow to i from other compartments and outflow from i to other compartments [48]. Activity in any compartment i can be described by following first order differential equation:

$$\frac{dx_i}{dt} = \sum_{\substack{j=1 \\ j \neq i}}^{n} r_{ij}\, x_j - x_i \sum_{\substack{j=1 \\ j \neq i}}^{n} r_{ji} \qquad\qquad \textbf{2.19}$$

69

After assigning values to the rate matrix and the radioactive decay constant λ, the rate matrix is transformed into new matrix [A]. For this, each diagonal element of [R] is replaced by negative sum of each of the row elements and then it is transposed [74]. The [R] and [A] are related by

$$a_{ij} = r_{ji} \ for \ j: 1 \ to \ n \ and \ i \neq j \qquad\qquad \textbf{2.20}$$

$$a_{ii} = -\sum_{j=1}^{n} r_{ji} - \lambda \ for \ i \neq j \qquad\qquad \textbf{2.21}$$

Using above transformation, equation 2.19 becomes

$$\frac{dx_i}{dt} = \sum_{j=1}^{n} a_{ij} x_j \qquad\qquad \textbf{2.22}$$

That is

$$\frac{d[x]}{dt} = [A][x] \qquad\qquad \textbf{2.23}$$

If the initial amounts in each compartment i are x_i (0) and contained in a column vector x (0) then, amount in compartment i, at any subsequent time is given by [74]

$$x_i(t) = e^{[A]t} x_i(0) \qquad\qquad \textbf{2.24}$$

Where e[A] is exponential of matrix [A]. It is evaluated using Pade algorithm [75] in MATLAB. For x_i (0) in atoms, equation 2.24 can be integrated with respect to time and multiplied by λ to give the total number of transformations [48; 74] u_i (t)

$$u_i(t) = \lambda [A]^{-1} \left[e^{[A]t} - [I] \right] x_i(0) \qquad\qquad \textbf{2.25}$$

Where [A]$^{-1}$ is the inverse of matrix [A] and [I] is the identity matrix.

Biokinetic models of Pu, Am, U and Th are solved using matrix algebra in MATLAB to estimate the distribution of activity for inhalation intake of 1 Bq for type S or M compounds [71]. Default transfer rates of various compartments of respiratory tract model along with the GI tract and systemic biokinetic models of respective radionuclides are used and integrated through the transfer compartment 'Blood' and the whole matrix is solved to give activity in various compartments as a function of time. Similarly, using the same methodology and default transfer rates for the movement of material for intake by ingestion [45] or wound [20] pathway, activities are predicted in various compartment as a function of time. An example of a wound model of particle category combined with biokinetic model of uranium [20] is shown in figure 2.7.

2.6   Method to evaluate uncertainty in various parameters

The GUM approach [23] is to express the result of a measurement as a best estimate of the measurand, along with an associated measurement uncertainty. The non-negative parameter characterizing the dispersion of the quantity values, being attributed to a measurand, based on the information used is known as measurement uncertainty [23; 50].
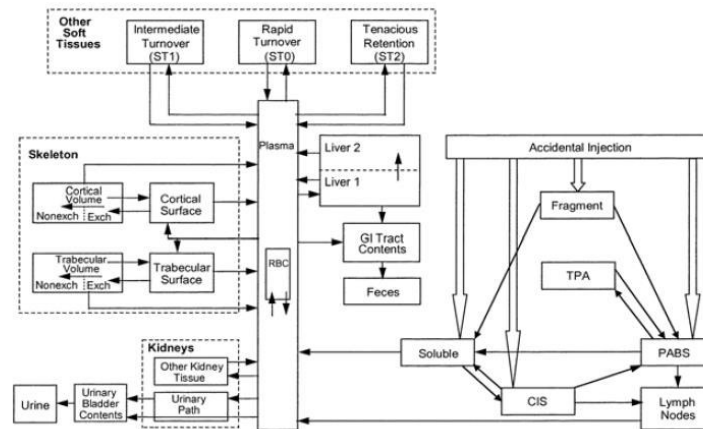
Figure 2.7 The wound model for particle category is combined with the biokinetic model of the
       Uranium

71

In Type A evaluations of measurement uncertainty [50], the Gaussian or lognormal distribution based on repeated measurements of an input quantity X are used to estimate uncertainty. X then has expectation equal to the average indication value and standard deviation equal to the standard deviation of the average [50].

For Type B evaluation of uncertainty [23], depending upon the available information, a probability distribution consistent with the information would be used. For the parameters influencing lung activity, their influence is multiplicative; hence, lognormal distribution [51; 76] is used to estimate type B uncertainty. Generally, when mean values are low, variances large and values cannot be negative, then such skewed distributions often closely fit lognormal distribution [76].

In estimating the overall uncertainty in a measurement, it is necessary to take each source of uncertainty and treat it separately [23] to obtain contribution from that source. Each of the separate components will contribute to obtain total uncertainty [50]. It is assumed that the overall uncertainty on an individual monitoring [52; 53] value can be described in terms of lognormal distribution and the scattering factor [52; 53] (SF) is defined as its geometric standard deviation [76].

Based on the IAEA/IDEAS project [52] (Work Package 3: Evaluation of incorporation cases), as well as on general considerations, the SF is obtained by using the following equation

$$SF = \exp\left(\sqrt{\frac{\sum_{i=1}^{n}[\ln(M_i) - \ln(p_i)]^2}{n - z}} \right) \qquad \textbf{2.26}$$

Where M_i and p_i are the true and predicted values respectively for i^{th} data point; z is the number of degrees of freedom and n is total number of data points. For estimating uncertainty in MEQ-CWT, positional errors, normal background variation this equation is used. The SF in case of counting statistics [51] is evaluated using the following equation

$$F = \exp\left(\frac{\sigma_A}{m}\right) \qquad\qquad \textbf{2.27}$$

The combined or total SF [51] due to various components is given by the following formula

$$\text{SF}_{\text{Total}} = \exp\left[\sqrt{\sum_i \ln^2(\text{SF}_i)}\,\right] \qquad\qquad \textbf{2.28}$$

Where SF_i is the SF of ith component.

2.7   Summary of chapter 2

In this chapter, the Monte Carlo method for photon transport and various sampling techniques such as rejection and inversion are described. The ICRP reference voxel phantom and other phantoms derived from it are described as they are extensively used for photon transport in FLUKA. The source sampling method used to sample source points in various source organs of voxel phantom is explained. Methodologies used for solution of biokinetic models and for evaluation of uncertainties are described.

CHAPTER 3

Uncertainties in lung measurements due to MEQ-CWT, positional errors, uncontaminated adult male background and Pu & Am activity ratio variation

In this chapter, the parameters influencing lung activity estimation such as MEQ-CWT, positional errors, uncontaminated adult male background variation in detection systems and Pu & Am activity ratio variation are studied. Using the methodology given in chapter 2, uncertainties are estimated for MEQ-CWT, positional errors and uncontaminated adult male background variation in the form of SFs for different energies and for Phoswich and HPGe array. Errors introduced in the Pu estimation when ^{241}Am is used as a tracer, are evaluated for different initial conditions scenarios from the solution of combined HRTM and GI tract models.

3.1   Uncertainties due to MEQ-CWT

3.1.1   MEQ-CWT of voxel phantoms

The MEQ-CWT [3] of voxel phantom is estimated by taking into account the average CWT, the thicknesses of adipose and muscle tissues present over the lungs at various locations over the chest and considering the attenuation of photons in those mediums at a particular energy using equation 1.7. The thorax voxel phantom of in-plane resolution of 2.137 mm has a MEQ-CWT of 2.25 cm at 60 keV [70]. By varying in-depth resolution of thorax voxel phantom to 1.923 and 2.35 mm, MEQ-CWT varies to 2.025 cm and 2.47 cm and lung volume varies from initial 2891 cm^3 to 2340 cm^3 and 3496 cm^3 respectively [70]. The estimated values are verified with the actual measurements at various locations over the chest.

3.1.2 Ultrasonography measurements

The measurements for CWT and adipose content were carried out on seventy radiation workers [77] of varying body parameters (Age: 23 − 59 yrs; W: 52 − 84 Kg) reported for whole body/lung monitoring. Philips iU 22 ultra sonography unit located in Medical division, BARC Hospital, which is a high-resolution system intended for general imaging, was used in B-scan mode. In B-scan mode, it is possible to differentiate between adipose and muscle boundary. First, worker's height, weight, chest circumference and age parameters were noted as a part of lung monitoring protocol and then, they were taken to ultrasonography unit for CWT and adipose content measurements. Each subject has to strip to the waist and then lie down supine on the couch. An outline is drawn on the chest of the subject, keeping a 20 cm dia. and 2 mm thick PMMA sheet tangential to sternal notch, to mark the area covered by Phoswich detector. PMMA sheet also has three 7 cm diameter hollow circles representing three HPGe detectors as they appear over worker's chest. The Radiologist determines the CWT and adipose content in each circle, which will appear in right lung, left lung and middle lung respectively and at right lower lung and left lower lung positions.

It is found that adipose content and CWT are in the range of 9 % - 40 % and 1 cm − 2.5 cm respectively. MEQ-CWT is estimated at 60 keV using the mean CWT and adipose fraction using equation 1.7. The mean value of MEQ-CWT observed is 1.77 cm with the standard deviation of 0.3 cm. MEQ-CWTs thus evaluated was correlated with respect to weight to height ratio, chest circumference and age of the subjects by the following empirical equation:

$$\text{MEQ} - \text{CWT} = A1 * (W/H) + A2 * (Ch) + A3 * (Y) + A4 \qquad \textbf{3.1}$$

where coefficients A1, A2, A3 and A4 are found to be 1.427, 0.014, 0.0025 and -0.1562 respectively at 60 keV. Correlation coefficient for this data is 0.57 and maximum absolute deviation observed is less than 32 %.

3.1.3 SFs due to MEQ-CWT as a function of energy

Considering lognormal distribution of MEQ-CWTs, the SFs are obtained using equation 2.26, from the MEQ-CWTs predicted using physical parameters from equation 3.1 and the actual MEQ-CWTs evaluated using equation 1.7. The SF is found to be 1.17 at 60 keV. Similarly, coefficients predicting MEQ-CWT as well as SFs are estimated at other energies and given in table 3.1.

Table 3.1 Coefficients of an empirical equation to estimate MEQ-CWT from physical parameters and SFs due to MEQ-CWT.

Energies	Coefficients				SF_{CWT}
keV	A1	A2	A3	A4	
18	-0.4489	0.013	0.0056	0.2288	1.25
60	1.427	0.014	0.0025	-0.1562	1.17
63	1.5343	0.0164	0.0019	-0.3225	1.17
74	0.0884	0.0159	0.0035	0.0529	1.20
93	0.0997	0.0161	0.0035	0.0335	1.22
185	0.1303	0.0164	0.0035	0.0083	1.20
238	0.1425	0.0164	0.0034	0.0028	1.20

3.1.4 Implications of variation of MEQ-CWT

Counting efficiencies (CEs) are calculated from the net counts obtained from the LLNL and JAERI phantom measurements in standard geometry in steel room WBC and known activity

in the lungs of the physical phantoms and are given in table 3.2 for ^{241}Am. The 43 to 76 keV

region is used for 60 keV of ^{241}Am in Phoswich and 58.5 to 60.5 keV region in HPGe array.

CEs are also given for thorax voxel phantom of 2.25 cm, 1.96 cm, 2.025 cm and 2.47 cm MEQ-

CWTs for source uniformly distributed in the lungs and obtained using Monte Carlo simulation

using "FLUKA" code for Phoswich and HPGe array.

Table 3.2 CEs using 20 cm dia. Phoswich detector and HPGe array for 60 keV of ^{241}Am.

Phantoms	Lung volume cm^3	Phoswich Detector		HPGe array	
		CE Equation cps.Bq^{-1}	CE cps.Bq^{-1} at 2.25 cm	CE Equation cps.Bq^{-1}	CE cps.Bq^{-1} at 2.25 cm
LLNL	3869	0.02e(-0.22*x)	1.2E-2	0.0047e(-0.34*x)	2.2E-3
JAERI	3525	0.033e(-0.26*x)	1.83E-2	0.0045e(-0.14*x)	3.28E-3
Thorax voxel (MEQ-CWT 2.25 cm)	2891	1.89E-2	1.89E-2	3.21E-3	3.21E-3
Thorax voxel # (MEQ-CWT 1.96 cm)	2040	2.51E-2	-	4.32E-3	-
Thorax voxel (MEQ-CWT 2.025 cm)	2340	2.29E-2	-	4.06E-3	-
Thorax voxel (MEQ-CWT 2.47 cm)	3496	1.55E-2	-	2.53E-3	-

x : MEQ-CWT, #: Indian ref. male

The voxel phantom with MEQ-CWT of 1.96 cm corresponds to the Indian reference male

[78] (Wt. = 51.5 kg and Ht. = 163.4 cm). The difference in CEs of various phantoms is due to

difference in lung volumes, size and shape of the lungs. Using CE equation, it is possible to

estimate the CE at a particular MEQ-CWT, but it is for same lung volumes. In case of voxel

phantom, lung volumes are also varied with MEQ-CWT when voxel in-plane resolution is

varied. From the study by Farah et. al. [79], it has been proved that lung volume is one of the important parameter, which can introduce large error in the lung activity estimation. From table 3.2, variation of ~ 11 % is observed, in case of JAERI and thorax voxel phantom for MEQ-CWT of 2.47 cm for almost same lung volume in both the phantoms. Thus, shape of the lungs is also found to be important. The SF due to variation in lung volume by keeping MEQ-CWT constant is not considered in evaluating total SF in the present study as both change with the modification of voxel size. In this study, uncertainty in MEQ-CWT is evaluated from actual measured and empirically predicted values.

3.2   Uncertainties due to positional errors

In the standard lung measurement geometry, detector is positioned over the chest such that its center is on the midline of the phantom and one end of the detector is tangential to the supra-sternal notch. To simulate the error in geometry along X-direction, detector position over the phantom is changed from a standard geometry by ± 0.5 cm, ± 1 cm and ± 1.5 cm keeping the detector end tangential to supra-sternal notch [70]. Similarly, to simulate error along Z-direction, detector position over the phantom is changed from a standard geometry by ± 0.5 cm, ± 1 cm and ± 1.5 cm, keeping the detector on the midline of the phantom. In both these geometries, detector height is kept at a constant distance of 1 cm from the phantom chest. Standard geometry used for lung measurements and positioning of the detector along X and Z direction to introduce positional errors is shown in figure 3.1.
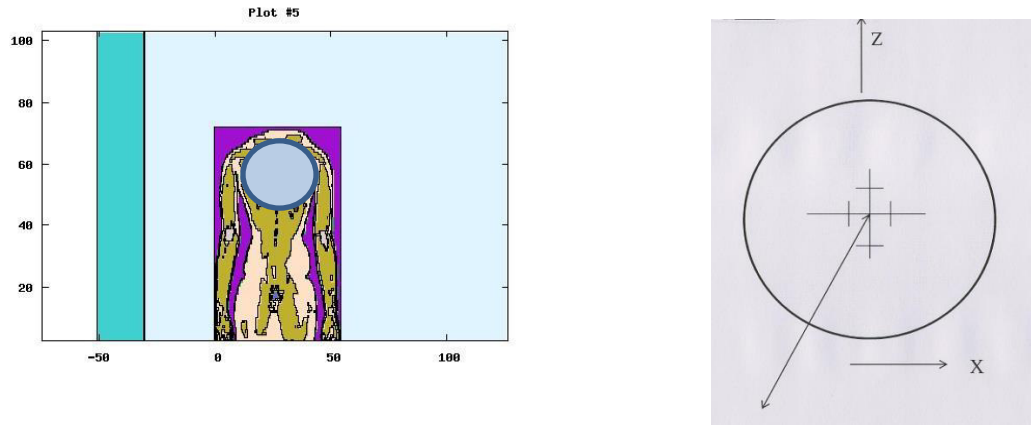
Figure 3.1 Standard geometry used for lung measurements and positioning of the detector along

X and Z direction to introduce positional errors.

Isotropic source is simulated in lungs by first randomly selecting the voxel from identified lung voxels and then randomly selecting a point in that voxel. The CEs in the various energy regions are determined for 2×10^6 histories run over 5 cycles to reduce the relative error (RE) to less than 1 %.

3.2.1   Positional errors in thorax voxel phantom of 2.25 cm MEQ-CWT

Tables 3.3 and 3.4 shows the CEs of Phoswich and HPGe array for source in the lungs of ICRP male thorax voxel phantom of 2.137 mm in-plane resolution and 2.25 cm MEQ-CWT. CEs are given in standard geometry for 18 to 238 keV photons as well as for positional errors of ± 0.5 cm to ± 1.5 cm along X and Z directions. The REs in the CEs are less than 1 % for all the energies studied. It is found that CEs are lowest at 18 keV for both the detectors as attenuation in overlying tissues is highest at this energy. Above 18 keV, as energy increases, there is an increase in the transmitted photons leading to increase in the CEs. Above 93 keV, CEs are found to decrease with energy for Phoswich as well as HPGe array as transmitted photons of high energy are not able to deposit their full energy in the active volume of detectors.

From table 3.3 and 3.4, it is observed that using Phoswich and HPGe array, the deviation in CEs at various positions with respect to the CE at standard geometry is ~ ± 1 %, ± 3 % and ± 4 % at and above 60 keV for an error of ± 0.5, ± 1 and ± 1.5 cm respectively in the vertical Z direction along chest. For a similar error, largest deviation of ± 3 %, ± 5 % and ± 9 % is observed in CEs with respect to CEs in standard geometry at 18 keV. The deviation in CEs at various positions with respect to the CE at standard geometry is found to be less than 2 % for all the energies when error in position is introduced in the horizontal X direction along the chest for both the detection systems.

3.2.2   Positional errors in resized voxel phantoms

The phantom is resized from original in-depth resolution of 2.137 mm to 1.923 and 2.35 mm so that it will correspond to the phantoms of weights 59 and 85 kg and MEQ-CWTs of 2.025 and 2.47 cm respectively. CEs of Phoswich and HPGe array are evaluated using resized phantoms and given in tables 3.5 to 3.8. For resized phantoms, the deviations in the CEs for an error of ± 0.5, ± 1 and ± 1.5 cm respectively in the vertical Z and horizontal X direction along chest with respect to the CE in standard geometry are found to be similar to the deviations observed in the phantom of original size for all the energies.

Figures 3.2 and 3.3 depicts the variation of fractional CEs with displacements in X and Z direction for Phoswich and HPGe array respectively for voxel phantom of 2.25 cm MEQ-CWT for 18, 60 and 238 keV. Fractional CEs are ratios of CEs obtained with positional errors of ± 0.5, ± 1 and ± 1.5 cm with respect to the CE obtained in standard geometry at that energy. The largest variation in CEs is observed at 18 keV and least at 238 keV for both the detectors. Fractional CEs at 60 keV are found to lie between fractional CEs obtained at 18 and 238 keV.
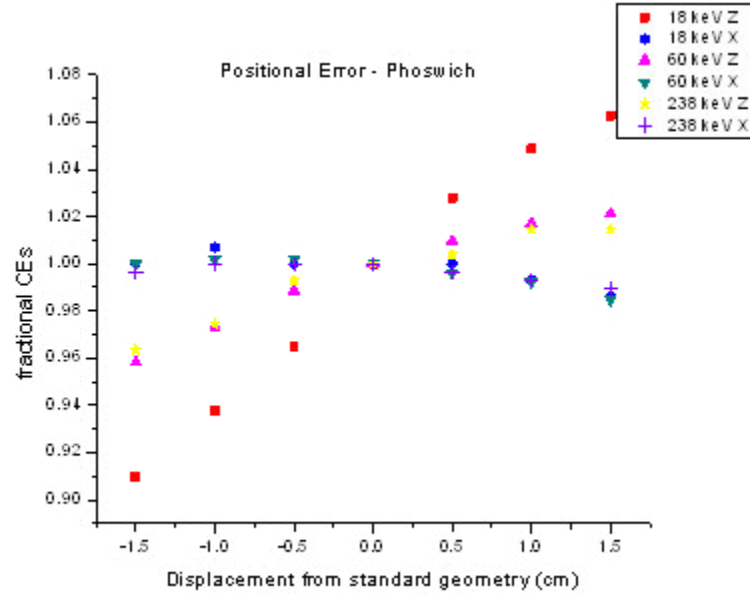
Figure 3.2 Variation of fractional CEs of Phoswich detector with displacement from standard position due to positional errors at 18, 60 and 238 keV.
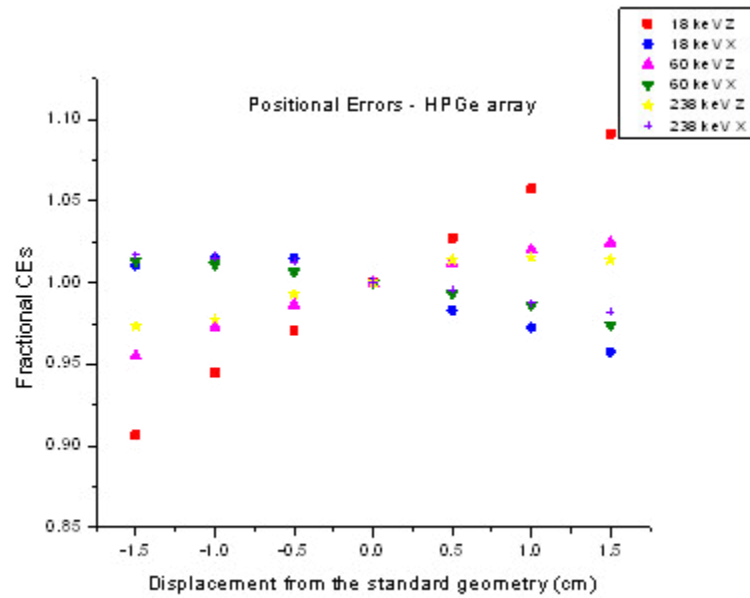
Figure 3.3 Variation of fractional CEs of HPGe array with displacement from standard geometry due to positional errors at 18, 60 and 238 keV

81

Asymmetric variation in fractional CEs is observed for displacements along both X and Z direction. The asymmetry observed along X direction is due to the presence of heart in the left lung. When the detector is positively displaced along X direction by 0.5 to 1.5 cm, it goes over left lung and due to the presence of heart, CEs decrease in comparison to the CEs when detector was over right lung. When the detector is positively displaced along Z direction by 0.5 to 1.5 cm, CEs increase due to the slight decrease in the CWT as detector goes away from the standard geometry position.

3.2.3   SFs due to positional error

SF due to positional error is the GSD observed in the counts that are obtained using CEs at different positions for 50 minutes of counting time, at minimum detectable activities [22] (MDA) of the detector, considering the yield of the photons at those energies and assuming that the measurements follow lognormal distribution [76]. 50 minutes of an optimized time [24] is used for lung monitoring of radiation workers. At this optimized time, the RE is 30 % at MDA level. The values of the SF will not be different if other activities are assumed in lungs for estimating positional errors. The SFs are also estimated for resized voxel phantoms for positional errors of ± 0.5 cm to ± 1.5 cm in X and Z direction. Using the SFs of all the three phantoms for positional error in X and Z direction, combined SFs [51] are estimated for Phoswich and HPGe array using equation 2.28.

Table 3.9 gives SFs due to positional errors in X and Z direction using voxel phantoms of three in-depth resolutions as well as combined SFs obtained from these three SFs for Phoswich and HPGe array. As observed from table 3.9, the SFs are 1.07 and 1.03 at 18 keV and 60 keV respectively using HPGe array for positional error along Z direction for male thorax voxel phantom   of   2.25   cm   MEQ-CWT.

Table 3.3 Counting Efficiencies (counts photon-1) of Phoswich detector at various positions along Z and X direction on chest of thorax voxel phantom of 2.25 cm MEQ-CWT

Energy (keV)	Detector in standard geometry	Counting Efficiencies (counts/Photon) of detector at various positions along Z						Counting Efficiencies (counts/Photon) of detector at various positions along X					
		0.5 cm Z-	1cm Z-	1.5cm Z-	0.5 cm Z+	1cm Z +	1.5cm Z +	0.5 cm X-	1cm X-	1.5cm X-	0.5 cm X+	1cm X+	1.5 cm X+
18	1.44E-03	1.39E-03	1.35E-03	1.31E-03	1.48E-03	1.51E-03	1.53E-03	1.44E-03	1.45E-03	1.44E-03	1.44E-03	1.43E-02	1.42E-03
60	5.26E-02	5.20E-02	5.12E-02	5.04E-02	5.31E-02	5.35E-02	5.37E-02	5.27E-02	5.27E-02	5.26E-02	5.24E-02	5.22E-02	5.18E-02
63	5.99E-02	5.92E-02	5.85E-02	5.75E-02	6.05E-02	6.09E-02	6.10E-02	6.01E-02	6.01E-02	6.00E-02	5.97E-02	5.94E-02	5.91E-02
74	4.75E-02	4.69E-02	4.62E-02	4.56E-02	4.79E-02	4.83E-02	4.85E-02	4.76E-02	4.75E-02	4.76E-02	4.73E-02	4.70E-02	4.67E-02
93	4.22E-02	4.18E-02	4.12E-02	4.05E-02	4.26E-02	4.29E-02	4.31E-02	4.23E-02	4.24E-02	4.23E-02	4.20E-02	4.19E-02	4.16E-02
185	3.34E-02	3.29E-02	3.24E-02	3.20E-02	3.37E-02	3.39E-02	3.40E-02	3.34E-02	3.35E-02	3.34E-02	3.33E-02	3.32E-02	3.29E-02
238	2.74E-02	2.72E-02	2.67E-02	2.64E-02	2.75E-02	2.78E-02	2.78E-02	2.74E-02	2.74E-02	2.73E-02	2.73E-02	2.72E-02	2.71E-02

Table 3.4 Counting Efficiencies (counts photon-1) of HPGe array at various positions along Z and X direction on chest of thorax voxel phantom of 2.25 cm MEQ-CWT

Energy keV	Detector in TSG	Counting Efficiencies (counts/Photon) of detector at various positions along Z						Counting Efficiencies (counts/Photon) of detector at various positions along X					
		0.5 cm Z-	1cm Z-	1.5cm Z-	0.5 cm Z+	1cm Z +	1.5cm Z +	0.5 cm X-	1cm X-	1.5cm X-	0.5 cm X+	1cm X+	1.5cm X +
18	4.72E-04	4.58E-04	4.46E-04	4.28E-04	4.85E-04	4.99E-04	5.15E-04	4.79E-04	4.79E-04	4.77E-04	4.64E-04	4.59E-04	4.52E-04
60	8.91E-03	8.79E-03	8.67E-03	8.51E-03	9.02E-03	9.09E-03	9.13E-03	8.97E-03	9.01E-03	9.03E-03	8.85E-03	8.79E-03	8.68E-03
63	9.63E-03	9.50E-03	9.35E-03	9.20E-03	9.74E-03	9.83E-03	9.86E-03	9.69E-03	9.74E-03	9.74E-03	9.57E-03	9.45E-03	9.36E-03
74	9.74E-03	9.63E-03	9.46E-03	9.27E-03	9.82E-03	9.87E-03	9.93E-03	9.82E-03	9.87E-03	9.90E-03	9.62E-03	9.49E-03	9.38E-03
93	1.01E-02	9.96E-03	9.83E-03	9.69E-03	1.02E-02	1.02E-02	1.03E-02	1.01E-02	1.02E-02	1.02E-02	1.00E-02	9.93E-03	9.86E-03
185	8.66E-03	8.62E-03	8.44E-03	8.32E-03	8.72E-03	8.74E-03	8.75E-03	8.69E-03	8.78E-03	8.79E-03	8.61E-03	8.51E-03	8.43E-03
238	7.13E-03	7.08E-03	6.97E-03	6.94E-03	7.23E-03	7.24E-03	7.23E-03	7.22E-03	7.24E-03	7.25E-03	7.10E-03	7.04E-03	7.00E-03

Table 3.5 Counting Efficiencies (counts. photon-1) of Phoswich detector at various positions along Z and X direction on chest of thorax voxel phantom of 2.025 cm MEQ-CWT

Energy keV	Detector in TSG	Counting Efficiencies (counts/Photon) of detector at various positions along Z						Counting Efficiencies (counts/Photon) of detector at various positions along X					
		0.5 cm Z-	1cm Z-	1.5cm Z-	0.5 cm Z+	1cm Z +	1.5cm Z +	0.5 cm X-	1cm X-	1.5cm X-	0.5 cm X+	1cm X+	1.5cm X +
18	2.15E-03	2.09E-03	2.04E-03	1.98E-03	2.19E-03	2.23E-03	2.26E-03	2.20E-03	2.16E-03	2.19E-03	2.16E-03	2.14E-03	2.11E-03
60	6.38E-02	6.31E-02	6.23E-02	6.13E-02	6.44E-02	6.49E-02	6.51E-02	6.41E-02	6.43E-02	6.43E-02	6.34E-02	6.29E-02	6.23E-02
63	7.21E-02	7.13E-02	7.04E-02	6.95E-02	7.28E-02	7.32E-02	7.34E-02	7.24E-02	7.25E-02	7.26E-02	7.18E-02	7.12E-02	7.04E-02
74	5.77E-02	5.71E-02	5.65E-02	5.56E-02	5.83E-02	5.87E-02	5.89E-02	5.81E-02	5.84E-02	5.84E-02	5.75E-02	5.69E-02	5.63E-02
93	5.13E-02	5.07E-02	5.01E-02	4.94E-02	5.17E-02	5.21E-02	5.23E-02	5.16E-02	5.18E-02	5.18E-02	5.11E-02	5.07E-02	5.01E-02
185	4.06E-02	4.02E-02	3.97E-02	3.90E-02	4.10E-02	4.13E-02	4.14E-02	4.10E-02	4.11E-02	4.10E-02	4.02E-02	4.00E-02	3.95E-02
238	3.29E-02	3.26E-02	3.20E-02	3.16E-02	3.31E-02	3.33E-02	3.36E-02	3.29E-02	3.31E-02	3.32E-02	3.26E-02	3.24E-02	3.21E-02

Table 3.6 Counting Efficiencies (counts. photon-1) of HPGe array at various positions along Z and X direction on chest of thorax voxel phantom of 2.025 cm MEQ-CWT

Energy keV	Detector in TSG	Counting Efficiencies (counts/Photon) of detector at various positions along Z						Counting Efficiencies (counts/Photon) of detector at various positions along X					
		0.5 cm Z-	1cm Z-	1.5cm Z-	0.5 cm Z+	1cm Z +	1.5cm Z +	0.5 cm X-	1cm X-	1.5cm X-	0.5 cm X+	1cm X+	1.5cm X +
18	7.15E-04	6.95E-04	6.75E-04	6.50E-04	7.31E-04	7.48E-04	7.63E-04	7.18E-04	7.29E-04	7.32E-04	7.07E-04	6.96E-04	6.78E-04
60	1.13E-02	1.11E-02	1.09E-02	1.07E-02	1.14E-02	1.14E-02	1.15E-02	1.14E-02	1.14E-02	1.15E-02	1.11E-02	1.10E-02	1.09E-02
63	1.21E-02	1.19E-02	1.17E-02	1.15E-02	1.22E-02	1.22E-02	1.23E-02	1.22E-02	1.23E-02	1.23E-02	1.19E-02	1.18E-02	1.16E-02
74	1.21E-02	1.20E-02	1.18E-02	1.16E-02	1.22E-02	1.23E-02	1.24E-02	1.22E-02	1.23E-02	1.24E-02	1.20E-02	1.18E-02	1.17E-02
93	1.25E-02	1.24E-02	1.22E-02	1.21E-02	1.27E-02	1.27E-02	1.28E-02	1.26E-02	1.27E-02	1.28E-02	1.24E-02	1.23E-02	1.22E-02
185	1.06E-02	1.05E-02	1.04E-02	1.03E-02	1.07E-02	1.07E-02	1.07E-02	1.07E-02	1.08E-02	1.08E-02	1.06E-02	1.05E-02	1.04E-02
238	8.78E-03	8.70E-03	8.62E-03	8.53E-03	8.81E-03	8.82E-03	8.83E-03	8.79E-03	8.85E-02	8.90E-03	8.70E-03	8.61E-03	8.54E-03

Table 3.7 Counting Efficiencies (counts. photon-1) of Phoswich detector at various positions along Z and X direction on chest of thorax voxel phantom of 2.47 cm MEQ-CWT

Energy keV	Detector in TSG	Counting Efficiencies (counts/Photon) of detector at various positions along Z						Counting Efficiencies (counts/Photon) of detector at various positions along X					
		0.5 cm Z-	1cm Z-	1.5cm Z-	0.5 cm Z+	1cm Z +	1.5cm Z +	0.5 cm X-	1cm X-	1.5cm X-	0.5 cm X+	1cm X+	1.5cm X +
18	9.82E-04	9.48E-04	9.18E-04	8.87E-04	1.00E-03	1.03E-03	1.06E-03	9.75E-04	9.78E-04	9.86E-04	9.69E-04	9.62E-04	9.46E-04
60	4.30E-02	4.24E-02	4.17E-02	4.10E-02	4.34E-02	4.39E-02	4.42E-02	4.32E-02	4.34E-02	4.35E-02	4.27E-02	4.24E-02	4.20E-02
63	4.89E-02	4.83E-02	4.76E-02	4.68E-02	4.94E-02	4.98E-02	5.01E-02	4.91E-02	4.93E-02	4.94E-02	4.86E-02	4.82E-02	4.77E-02
74	3.86E-02	3.80E-02	3.75E-02	3.68E-02	3.90E-02	3.94E-02	3.97E-02	3.88E-02	3.90E-02	3.91E-02	3.83E-02	3.80E-02	3.77E-02
93	3.43E-02	3.39E-02	3.34E-02	3.28E-02	3.46E-02	3.49E-02	3.52E-02	3.45E-02	3.47E-02	3.49E-02	3.41E-02	3.38E-02	3.35E-02
185	2.72E-02	2.69E-02	2.67E-02	2.62E-02	2.75E-02	2.77E-02	2.77E-02	2.73E-02	2.75E-02	2.76E-02	2.70E-02	2.68E-02	2.65E-02
238	2.23E-02	2.23E-02	2.20E-02	2.17E-02	2.25E-02	2.28E-02	2.29E-02	2.25E-02	2.25E-02	2.26E-02	2.23E-02	2.23E-02	2.21E-02

Table 3.8 Counting Efficiencies (counts. photon-1) of HPGe array at various positions along Z and X direction on chest of thorax voxel phantom of 2.47 cm MEQ-CWT

Energy keV	Detector in TSG	Counting Efficiencies (counts/Photon) of detector at various positions along Z						Counting Efficiencies (counts/Photon) of detector at various positions along X					
		0.5 cm Z-	1cm Z-	1.5cm Z-	0.5 cm Z+	1cm Z +	1.5cm Z +	0.5 cm X-	1cm X-	1.5cm X-	0.5 cm X+	1cm X+	1.5cm X +
18	3.08E-04	2.98E-04	2.89E-04	2.76E-04	3.21E-04	3.32E-04	3.40E-04	3.12E-04	3.17E-04	3.22E-04	3.08E-04	3.00E-04	2.94E-04
60	7.02E-03	6.88E-03	6.78E-03	6.65E-03	7.13E-03	7.19E-03	7.23E-03	7.06E-03	7.13E-03	7.19E-03	6.93E-03	6.85E-03	6.75E-03
63	7.57E-03	7.47E-03	7.35E-03	7.21E-03	7.67E-03	7.75E-03	7.83E-03	7.64E-03	7.71E-03	7.77E-03	7.50E-03	7.42E-03	7.31E-03
74	7.65E-03	7.55E-03	7.43E-03	7.31E-03	7.74E-03	7.80E-03	7.86E-03	7.74E-03	7.81E-03	7.87E-03	7.58E-03	7.47E-03	7.37E-03
93	8.05E-03	7.95E-03	7.84E-03	7.70E-03	8.13E-03	8.20E-03	8.26E-03	8.11E-03	8.18E-03	8.24E-03	7.98E-03	7.93E-03	7.78E-03
185	6.98E-03	6.86E-03	6.77E-03	6.65E-03	7.00E-03	7.06E-03	7.11E-03	6.97E-03	7.04E-03	7.07E-03	6.91E-03	6.82E-03	6.75E-03
238	5.75E-03	5.76E-03	5.69E-03	5.56E-03	5.88E-03	5.87E-03	5.90E-03	5.84E-03	5.87E-03	5.89E-03	5.74E-03	5.74E-03	5.65E-03

Table 3.9 Scattering factors (SFs) due to positional errors in Z and X direction along the chest of voxel phantoms of various MEQ-CWTs and combined SFs for phoswich and HPGe array

Energy	SFs using Phoswich detector due to positional error							SFs using HPGe array due to positional error						
	± 1.5 cm error along Z			± 1.5 cm error along X			combined Z and X	± 1.5 cm error along Z			± 1.5 cm error along X			combined Z and X
(keV)	2.25	2.025	2.47	2.25	2.025	2.47		2.25	2.025	2.47	2.25	2.025	2.47	
18	1.067	1.055	1.073	1.008	1.016	1.020	1.119	1.073	1.065	1.086	1.027	1.030	1.035	1.146
60	1.026	1.025	1.031	1.008	1.014	1.014	1.053	1.029	1.032	1.035	1.016	1.024	1.025	1.069
63	1.025	1.023	1.028	1.008	1.013	1.015	1.050	1.029	1.030	1.033	1.017	1.026	1.024	1.067
74	1.026	1.024	1.031	1.009	1.015	1.015	1.053	1.028	1.026	1.026	1.024	1.024	1.026	1.064
93	1.025	1.024	1.028	1.008	1.014	1.016	1.051	1.025	1.024	1.028	1.015	1.019	1.022	1.056
185	1.027	1.025	1.023	1.008	1.017	1.016	1.050	1.022	1.018	1.029	1.017	1.016	1.020	1.052
238	1.022	1.025	1.021	1.006	1.014	1.009	1.044	1.019	1.016	1.024	1.015	1.017	1.018	1.046

The combined SF of 1.05 of Phoswich and 1.07 of HPGe array at 60 keV as observed in table 3.9 is found to be similar to the SF given in the literature [51] of 1.05 above 20 keV for detector positioning. SFs are found to decrease with increase in energy. The combined SF of 1.12 of Phoswich and 1.15 of HPGe array at 18 keV is smaller than the value of 1.2 given in the literature [51] for energies less than 20 keV by 6.7 % and 4.2 % respectively. The predicted SFs represent uncertainties due to detector positioning only, as source is sampled in whole lungs with 2×10^6 particles. Also, there is an absence of detector background variation as internal sources [3] such as potassium ^{40}K as well as external sources such as cosmic rays are not simulated in Monte Carlo code 'FLUKA'.

3.3   Uncertainties due to variation of uncontaminated adult male background

The SFs due to normal background variation are obtained by monitoring an uncontaminated adult male under Phoswich and HPGe array for 50 minutes [70]. Background of an adult male devoid of any internal or external contamination when measured under detector in standard measurement geometry in steel room will be known as normal detector background. He is monitored 15 times in standard geometry under both the detectors in totally shielded steel room WBC. SFs are evaluated from the measured counts and average counts using equation 2.26.

As given in table 3.10, the SFs are found to be 1.12 and 1.46 at 18 keV and 1.04 and 1.22 at 60 keV using Phoswich and HPGe array respectively due to normal background variation. For 63 and 93 keV, 40 to 120 keV energy region is used. This is due to the variation of the contribution of ^{40}K as well as cosmic background in the measurements. SFs

for Phoswich detector are smaller than the HPGe array due to its large size and higher background of ~ 65 cpm compared to ~ 2 cpm of HPGe array.

Table 3.10 SFs due to normal background variation for Phoswich and HPGe array

Energy	Phoswich			HPGe array		
(keV)	mean counts	Std. Dev.	SF	mean counts	Std. Dev.	SF
18	816.67	97.7	1.12	105.53	32.8	1.46
60	2651.28	112.4	1.04	114.5	17.5	1.22
63*	6220.89	208.5	1.03	110.35	23.8	1.24
74	2651.28	112.4	1.03	110	25	1.24
93	6220.89	208.5	1.03	120	23.3	1.23
185	2197.95	82.7	1.04	116.78	23.7	1.26
238	2197.95	82.7	1.04	110	25	1.26

3.4   Pu and Am activity ratio variation when Am is used as a tracer

In case of ^{239}Pu, detection becomes difficult, as U-L X-rays of 17.2 keV having 2.13 % yield [17; 19] are attenuated by the overlying MEQ-CWT. It has been observed that internal exposures of Pu is invariably associated with either ^{241}Pu or ^{241}Am or both along with the other isotopes of Pu [4; 18]. ^{241}Am emits Np-L X rays of 17.8 keV having ~ 19 % yield which are indistinguishable from U-L X rays of ^{239}Pu and 59.5 keV gamma ray with ~ 36 % yield which are easily detectable. Therefore, ^{241}Am is used as a tracer [18] to estimate Pu from lung measurements.

The variation in ratio of Pu to Am activities is studied by solution of combined HRTM and old GI tract model of Pu and Am using matrix algebra. Transfer rates of various compartments of respiratory tract model along with the GI tract models of ^{241}Am, ^{239}Pu and ^{241}Pu are used and integrated through a transfer compartment 'Blood' and the whole matrix is solved to give activity in various compartments as a function of time [48; 74]. In the program, growth of ^{241}Am from ^{241}Pu is taken into consideration. It is observed from figure 3.4 and 3.5 that for Pu and Am, both following type S or type M categories, ratio of ^{239}Pu and ^{241}Am activities in the lungs varies by less than 5 % at the end of one year. For ^{241}Am behaving as type M and Pu as type S, the ^{239}Pu to ^{241}Am activities ratio changes from 1.1 to 5.8 at the end of one year, changing by a factor of ~5 as observed from figure 3.6. In case of initial absence of Am, and buildup of Am from ^{241}Pu, the ratio changes rapidly depending upon the type of ^{241}Pu involved as depicted in figures 3.7 and 3.8.

As for type S or type M categories of Pu and Am, ratio of ^{239}Pu and ^{241}Am activities in the lungs varies by less than 5 % at the end of one year, the uncertainty due to variation of Pu and Am activity ratio is given by SF of 1.05. For other initial conditions, the change in the Pu and Am activity ratio is found to be ~ 5 or more. In those cases, it will not be described as the uncertainty, but the error which can be removed from follow up measurements of the person and studying the variation of the Pu and Am activity ratio.
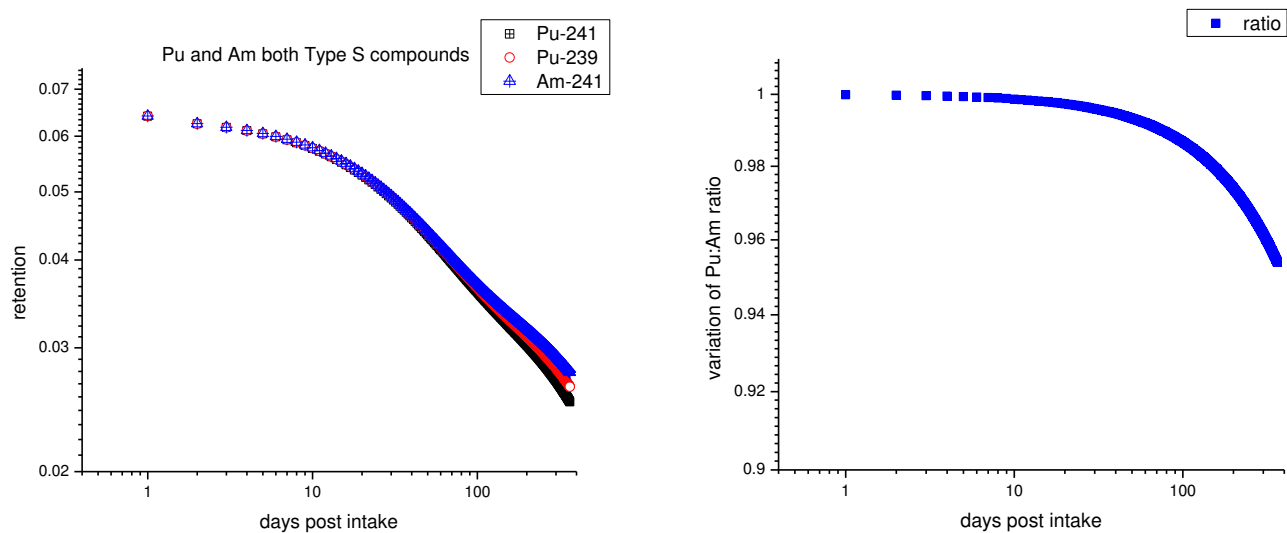
Figure 3.4 Variation of ^{239}Pu, ^{241}Pu and ^{241}Am activities from initial 1 Bq each and for Pu and ^{241}Am are behaving as type S compounds.
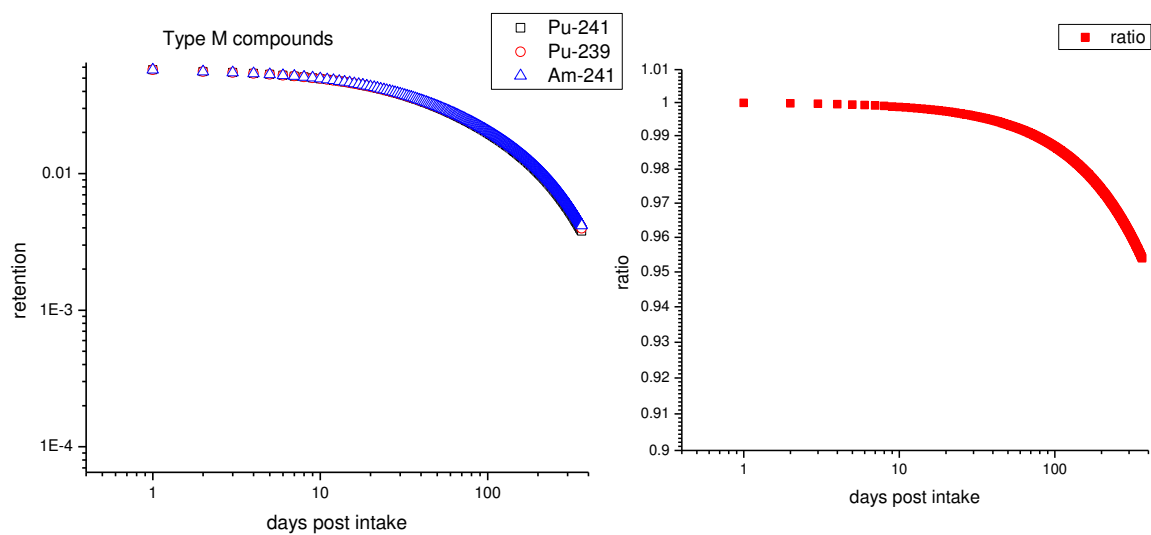
Figure 3.5 Variation of ^{239}Pu, ^{241}Pu and ^{241}Am activities from initial 1 Bq each for Pu and ^{241}Am are behaving as type M compounds.
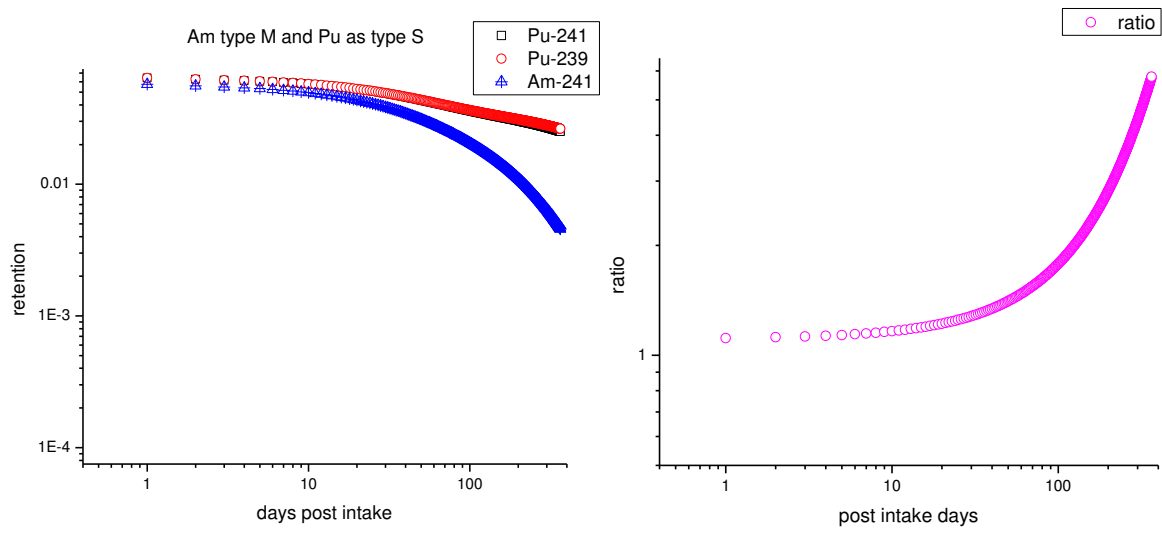
Figure 3.6 Variation of ^{239}Pu, ^{241}Pu and ^{241}Am activities from initial 1 Bq each for Pu behaving as type S and ^{241}Am behaving as type M compound.
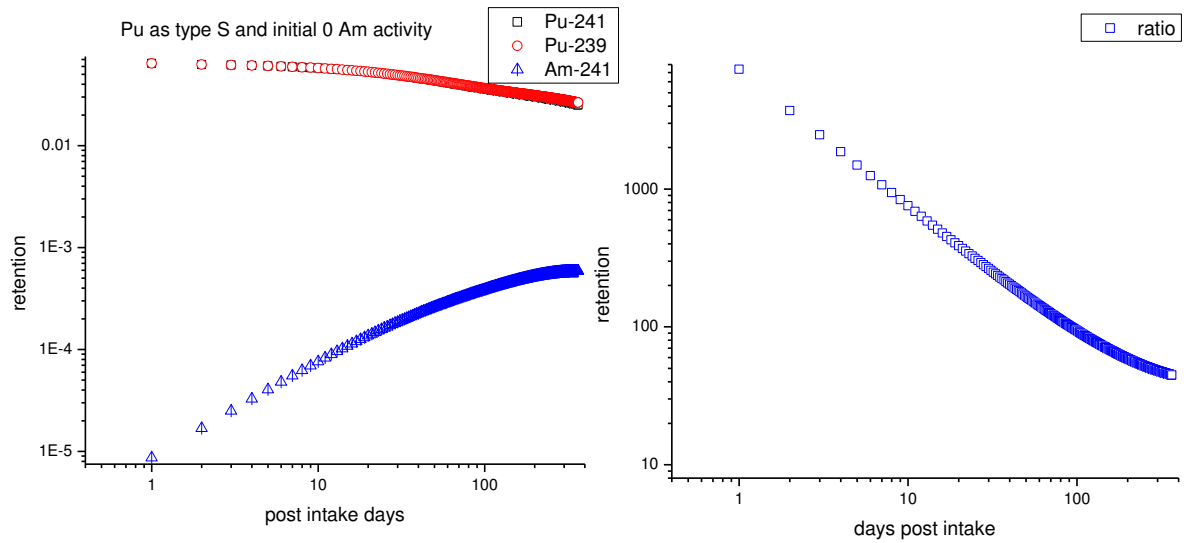
Figure 3.7 Variation of ^{239}Pu, ^{241}Pu activities from initial 1 Bq each in the absence of ^{241}Am activity for Pu and ^{241}Am as type S compounds.
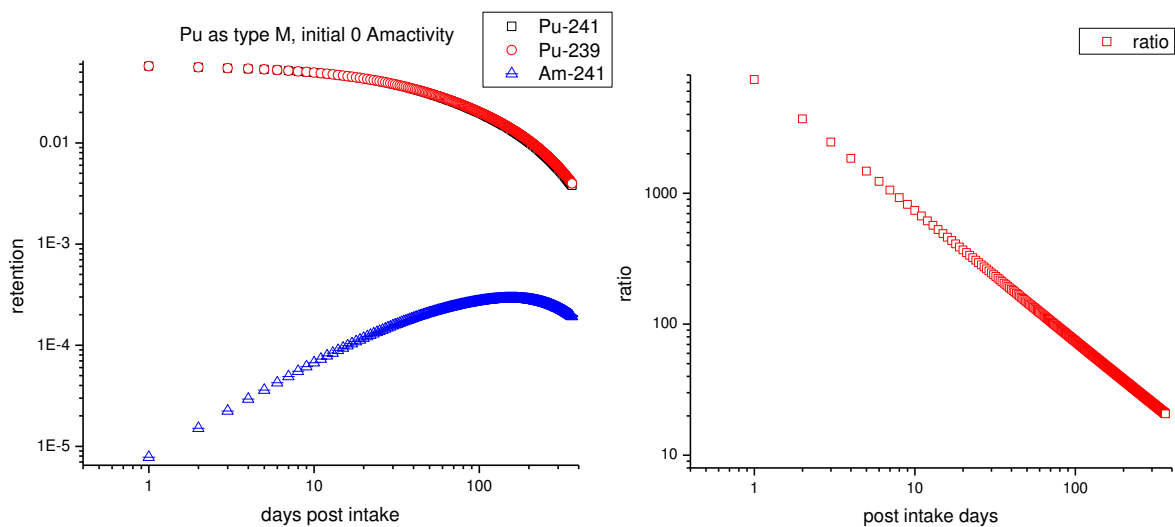
Figure 3.8 Variation of ^{239}Pu, ^{241}Pu activities from initial 1 Bq each in the absence of ^{241}Am activity for Pu and ^{241}Am as type M compounds.

The results of the study will be useful in estimating the Pu activity in the lungs from follow up measurements of ^{241}Am in the occupational worker as initial assumptions or observations can be verified using the computed ratios and the dose can be re-evaluated if needed.

For type S or type M categories of Pu and Am, ratio of ^{239}Pu and ^{241}Am activities in the lungs varies by less than 5 % at the end of one year, thus, the uncertainty due to variation of Pu and Am activity ratio is given by SF of 1.05. The SFs are not evaluated for Pu and Am activity ratio variation in case of mixed type M and S compounds of Pu and Am as it will result in an error which could be rectified by using the follow up measurements and the data provided from the solution of models.

3.5   Summary of chapter 3

In this chapter, uncertainties in lung measurement of actinides due to MEQ-CWT, positional errors, uncontaminated adult male background variation and activity ratio variation of Pu and Am are evaluated. Experimental and Monte Carlo simulated values are used to estimate the uncertainties in various parameters. The SFs due to positional errors are evaluated to be 1.12 and 1.05 using Phoswich and 1.14 and 1.07 using HPGe array at 18 and 60 keV respectively. These are based on ICRP male thorax and resized voxel phantoms. SFs are found to decrease with increase in energy for both the detectors.

CHAPTER 4

Uncertainties in lung measurements due to non-uniform distribution of activity in lungs, counting statistics and contribution of activity in other organs

Evaluation of uncertainties in lung measurements due to important parameters such as non-uniform distribution of activity in lungs and counting statistics is carried out in this chapter. Contribution in lung measurements due to source in liver, rib bones and lymph nodes is evaluated.

4.1   Uncertainty due to non-uniform distribution of activity in the lungs

Lung monitoring systems used for quantification of actinides are calibrated as function of MEQ-CWT using realistic physical thorax phantoms [19; 31] with lung sets of various radionuclides having uniform activity distribution. The non-uniformity in the distribution of activity in the lungs [51] of the physical phantom is one of the parameters that can introduce the uncertainty, in the lung activity assessment. There is a need to estimate detector and energy specific SFs for non-uniform distribution of activity in the lungs of the phantoms of different physiques so that all the factors that can contribute uncertainty due to non-uniform distribution can be taken into account. ICRP reference male thorax voxel phantom [36] and resized phantoms are used to simulate source uniformly as well as non-uniformly in the lungs. Variation in the counting efficiencies (CEs) due to non-uniform distribution in ICRP reference voxel phantom and resized phantoms is studied for phoswich

and HPGe array. CEs are used to estimate SFs due to non-uniform distribution for each of the three phantoms and combined SFs at different energies.

4.1.1 Source sampling along lateral direction in the lungs

For uniform distribution, source is simulated by first randomly selecting the voxel from known voxels of the lungs and then randomly selecting a point in that voxel. For assigning weights to a particular region of the lung in lateral direction, upper right, upper left, lower right and lower left voxels of the lungs are identified and arranged in sequence. Then voxels are selected from each region by assigning weights of 0.4, 0.5, 0.6 and 1 respectively and then randomly selecting a point in that voxel. For example, when weight of 0.4 is required for upper right lung, upper right lung voxels are chosen randomly in 40 % of the times and the remaining lung voxels are chosen randomly in 60 % of times. Figure 4.1 shows source points in upper right lung with weightage of 0.6.

4.1.2 Source sampling along Anterior-posterior direction in the lungs

From middle Y-plane of the phantom, lungs are divided into approximately equal anterior and posterior parts and voxels in these regions are identified. They are arranged in sequence. The voxels in anterior region are selected by assigning weights of 0.4, 0.5, 0.6 and 1. The lung voxels in posterior region are selected for remaining weights and for weight of 1. After randomly selecting point in the voxel, the isotropic directional distribution of emitted photons is sampled from a uniform distribution of the azimuthal angle and the cosine of the polar angle. Six photon energies from 18 to 238 keV are simulated for the photons emitted from ^{239}Pu, ^{241}Am, ^{238}U, ^{235}U and ^{212}Pb.

95
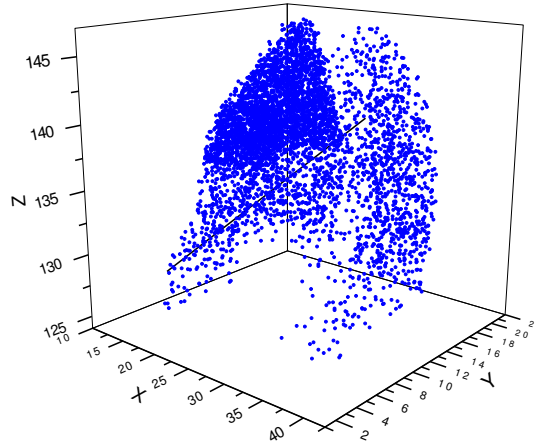
Figure 4.1 Sampling of source points in upper right lung with weightage of 0.6.

4.1.3 CEs due to non-uniform distribution of activity along lateral direction in lungs

CEs are obtained by sampling source points non uniformly along the lateral direction in the lungs of the voxel phantom of in-plane resolutions 2.137, 1.923 and 2.35 mm. The lungs are divided equally using sagittal and coronal planes into upper right and left, lower right and left lung regions respectively. These are given in table 4.1 to 4.6 for phoswich and HPGe array respectively for 18 - 238 keV photons. The three in-plane resolutions correspond to the phantoms of weights 73, 59 and 88 kg and MEQ-CWTs of 2.25, 2.025 and 2.47 cm respectively. It can be seen from the tables 4.1 and 4.2, that higher weights of 0.4 to 0.6 given to upper and lower right lung regions leads to overestimation in CEs by ~ 3 to 10 % compared to uniform source distribution in whole lungs. The overestimation increases to 15 to 30 % when highest weight of 1 is given to these regions for both the detectors. When weights of 0.4 to 1 are given to upper and lower left lung regions, underestimation in CEs of ~ 10 to 30 % is observed with respect to uniform source distribution in lungs. This is due to

smaller lung volume by ~ 12 % of left lung, compared to right lung. The heart in the left side of lung cavity also reduces the photon flux from upper left lung. For source in lower left lung region, highest underestimation of 60 to 95 % is observed at and above 60 keV and by a factor of ~ 2.5 at 18 keV.

Using CEs given in tables 4.1 and 4.2, fractional CEs are estimated by taking the ratio of CEs due to non-uniform distribution and CEs using uniform source distribution in lungs and depicted in figure 4.2 for 18, 60, 185 and 238 keV photons for phoswich and HPGe array respectively. The first four-abscissa points are due to weights of 0.4, 0.5, 0.6 and 1 given to upper right lung. Subsequent quadruplets correspond to lower right, upper left and lower left lung respectively with weights of 0.4, 0.5, 0.6 and 1 given to each region. It can be seen from the figures that almost all the fractional CEs are within 0.6 to 1.3 for all the energies and for both the detectors. At 18 keV, fractional CEs show fluctuations within 0.4 to 1.4 for a weight of 1 given to upper right and lower left lung. Similar trend in deviations is observed in tables 4.3 to 4.6 when phantom in-plane resolution is varied from 2.137 to 1.923 and 2.35 mm respectively.

4.1.4   CEs due to non-uniform distribution of activity along anterior-posterior direction in lungs

CEs are obtained by sampling source points non-uniformly along the anterior-posterior direction in the lungs of the voxel phantom of in-plane resolutions 2.137, 1.923 and 2.35 mm by dividing the lungs equally using coronal plane. They are given in table 4.7 to 4.8 for phoswich and HPGe array respectively for 18 to 238 keV photons. When source is sampled in anterior regions of the lungs, it is found that overestimation increases from 5 % to

65 % as weight is increased from 0.5 to 1 for both the detectors at and above 60 keV. At 18 keV, the overestimation increases by a factor of 2 when highest weightage of 1 is applied to anterior lungs. For weightage of 0.4 to anterior lungs, the deviation in the CEs with respect to CEs obtained with uniform source distribution in the lungs is found to be less than 10 %. This is because actual partitioning of the lung voxels in the anterior and posterior lungs regions is around 0.46 and 0.54 respectively. For source in posterior lungs, underestimation of ~ 50 to 60 % is observed in CEs for both the detectors.
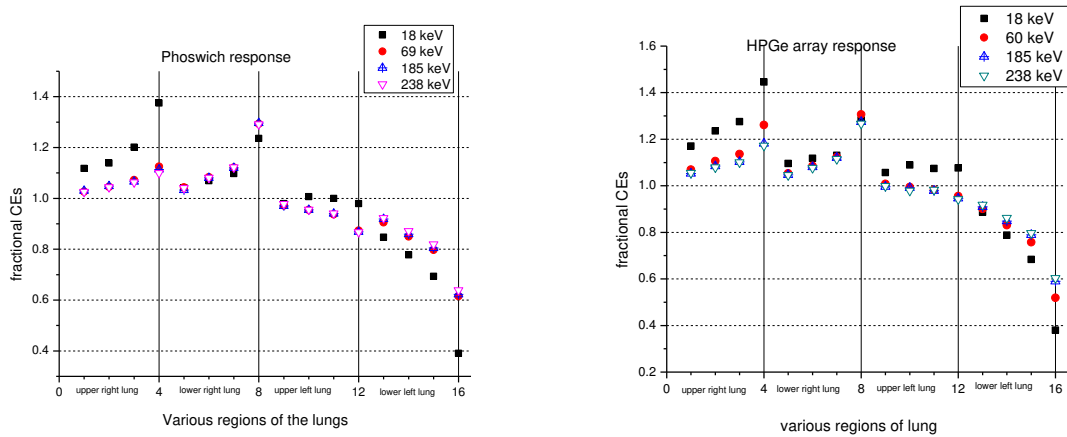
Figure 4.2 Variation of fractional CEs due to non-uniform distribution in the various regions of lungs using Phoswich and HPGe array detector. The first four-abscissa points are due to weights of 0.4, 0.5, 0.6 and 1 given to upper right lung. Subsequent quadruplets correspond to lower right, upper left and lower left lung respectively with weights of 0.4, 0.5, 0.6 and 1 given to each region.

4.1.5   SFs due to non-uniform distribution of activity in lungs

Uncertainty due to non-uniform distribution in lungs is estimated using CEs predicted from reference thorax phantom as well as resized phantoms. The CEs due to weight of 1 for

source in right lung, left lung, anterior and posterior lung are excluded as the aim is to estimate uncertainty due to non-uniform distribution of activity in lungs. The weightage of 1 to these regions will be an error in the lung activity distribution. Table 4.9 gives SFs of voxel phantoms of three in-plane resolutions, combining SFs obtained for weights of 0.4 to 0.6 given to different regions of lungs and combined SFs for Phoswich and HPGe array. SF is the GSD observed in the counts evaluated using equation 2.26. Counts are obtained using CEs at various non-uniform distributions for 50 minutes of counting time, at 5 Bq of activity in the lungs considering the yield [17] of the photons at those energies and assuming that the measurements follow lognormal distribution [76]. Using the SFs of all the three phantoms for non-uniform distribution in lungs, combined SFs are estimated for Phoswich and HPGe array using equation 2.28. They specify the uncertainty in the lung activity estimation at different energies due to non-uniform distribution of activity in lungs. As observed from table 4.9, the SFs are 1.56 and 1.30 at 18 keV and 60 keV respectively using HPGe array. For HPGe array, total SF is highest at 18 keV and as energy increases the total SF decreases to 1.25 at 238 keV. The deviations in combined SFs obtained using HPGe array with respect to combined SFs obtained using Phoswich detector, are found to be highest -12 % at 18 keV, ~ 5 % at 60 keV which reduces to 1.6 % at 238 keV photons. The influence of variation in lung volume due to resizing of voxel phantoms is not studied at present.

The combined SF of 1.24 of Phoswich and 1.3 of HPGe array at 60 keV as observed in table 4.9 is different from the SF given in the literature [51] of 1.05 above 20 keV for variation of activity distribution. SFs are found to decrease with increase in energy and converge at 1.25 at 238 keV. The combined SF, 1.78 of Phoswich and 1.56 of HPGe array at

18 keV is greater than the value of 1.3 given in the literature [51] for energies less than 20 keV by 37 % and 20 % respectively. The SFs for non-uniform distribution of activity in lungs of resized voxel phantoms are obtained by assuming 0.4 to 0.6 weight distribution in different parts of the lungs. For assumption of different weights such as only 0.4, different SFs are possible. The literature values are based on judgment and experimental values with physical phantom for variation of activity distribution in the phantom. The voxel data gives more realistic representation of variability of activity distribution in lungs and the values are obtained for discrete energies while literature values are typical values given for range of energies.

Table 4.1 Counting efficiencies using Phoswich detector for source in various regions of the lungs of voxel phantom of in-plane resolution of 2.137 mm with varying weights.

Energy keV	uniform distribution in lungs	Weights given to Upper right lung				Weights given to Upper left lung				Weights given to lower right lung				Weights given to lower left lung			
		0.4	0.5	0.6	1	0.4	0.5	0.6	1	0.4	0.5	0.6	1	0.4	0.5	0.6	1
18	1.44E-03	1.61E-03	1.64E-03	1.73E-03	1.98E-03	1.41E-03	1.45E-03	1.44E-03	1.41E-03	1.50E-03	1.54E-03	1.58E-03	1.78E-03	1.22E-03	1.12E-03	9.99E-04	5.63E-04
60	5.26E-02	5.42E-02	5.52E-02	5.66E-02	5.94E-02	5.13E-02	5.04E-02	4.95E-02	4.61E-02	5.51E-02	5.72E-02	5.92E-02	6.83E-02	4.78E-02	4.49E-02	4.21E-02	3.25E-02
63	5.99E-02	6.14E-02	6.26E-02	6.38E-02	6.71E-02	5.82E-02	5.70E-02	5.59E-02	5.21E-02	6.23E-02	6.46E-02	6.71E-02	7.72E-02	5.47E-02	5.14E-02	4.82E-02	3.77E-02
93	4.22E-02	4.34E-02	4.43E-02	4.50E-02	4.77E-02	4.11E-02	4.05E-02	3.97E-02	3.72E-02	4.39E-02	4.56E-02	4.75E-02	5.46E-02	3.82E-02	3.60E-02	3.37E-02	2.58E-02
185	3.34E-02	3.44E-02	3.50E-02	3.56E-02	3.72E-02	3.24E-02	3.19E-02	3.14E-02	2.90E-02	3.45E-02	3.61E-02	3.74E-02	4.33E-02	3.07E-02	2.87E-02	2.69E-02	2.08E-02
238	2.74E-02	2.78E-02	2.83E-02	2.88E-02	2.98E-02	2.65E-02	2.59E-02	2.55E-02	2.35E-02	2.82E-02	2.93E-02	3.04E-02	3.50E-02	2.50E-02	2.36E-02	2.22E-02	1.73E-02

Table 4.2 Counting efficiencies using HPGe array for source in various regions of the lungs of voxel phantom of in-plane resolution of 2.137 mm with varying weights.

Energy keV	uniform distribution in lungs	Weights given to Upper right lung				Weights given to Upper left lung				Weights given to lower right lung				Weights given to lower left lung			
		0.4	0.5	0.6	1	0.4	0.5	0.6	1	0.4	0.5	0.6	1	0.4	0.5	0.6	1
18	4.72E-04	5.36E-04	5.66E-04	5.84E-04	6.62E-04	4.84E-04	4.99E-04	4.92E-04	4.93E-04	5.02E-04	5.12E-04	5.18E-04	5.87E-04	4.06E-04	3.61E-04	3.13E-04	1.74E-04
60	8.91E-03	9.41E-03	9.73E-03	1.00E-02	1.11E-02	8.87E-03	8.75E-03	8.65E-03	8.41E-03	9.27E-03	9.55E-03	9.89E-03	1.15E-02	7.93E-03	7.31E-03	6.67E-03	4.57E-03
63	9.63E-03	1.01E-02	1.04E-02	1.08E-02	1.17E-02	9.59E-03	9.46E-03	9.34E-03	9.07E-03	9.96E-03	1.03E-02	1.07E-02	1.23E-02	8.57E-03	7.91E-03	7.26E-03	5.03E-03
93	1.01E-02	1.07E-02	1.10E-02	1.12E-02	1.22E-02	1.01E-02	9.95E-03	9.85E-03	9.48E-03	1.05E-02	1.09E-02	1.12E-02	1.29E-02	9.04E-03	8.41E-03	7.73E-03	5.45E-03
185	8.66E-03	9.00E-03	9.27E-03	9.43E-03	1.01E-02	8.52E-03	8.48E-03	8.37E-03	8.09E-03	8.95E-03	9.24E-03	9.58E-03	1.09E-02	7.78E-03	7.25E-03	6.75E-03	5.04E-03
238	7.13E-03	7.47E-03	7.64E-03	7.79E-03	8.30E-03	7.07E-03	6.93E-03	6.96E-03	6.67E-03	7.40E-03	7.62E-03	7.89E-03	8.97E-03	6.50E-03	6.10E-03	5.64E-03	4.27E-03

Table 4.3 Counting efficiencies using Phoswich detector for source in various regions of the lungs of voxel phantom of in-plane resolution of 2.025 mm with varying weights.

Energy keV	uniform distribution in lungs	Weights given to Upper right lung				Weights given to Upper left lung				Weights given to lower right lung				Weights given to lower left lung			
		0.4	0.5	0.6	1	0.4	0.5	0.6	1	0.4	0.5	0.6	1	0.4	0.5	0.6	1
18	2.15E-03	2.30E-03	2.36E-03	2.46E-03	2.81E-03	2.22E-03	2.27E-03	2.29E-03	2.43E-03	2.27E-03	2.28E-03	2.31E-03	2.43E-03	1.88E-03	1.74E-03	1.59E-03	9.97E-04
60	6.38E-02	6.50E-02	6.57E-02	6.63E-02	6.90E-02	6.36E-02	6.31E-02	6.30E-02	6.17E-02	6.55E-02	6.70E-02	6.88E-02	7.56E-02	6.02E-02	5.79E-02	5.53E-02	4.58E-02
63	7.21E-02	7.32E-02	7.38E-02	7.45E-02	7.73E-02	7.15E-02	7.11E-02	7.06E-02	6.94E-02	7.38E-02	7.57E-02	7.76E-02	4.37E-02	6.81E-02	6.53E-02	6.27E-02	5.25E-02
93	5.13E-02	5.21E-02	5.27E-02	5.33E-02	5.54E-02	5.09E-02	5.08E-02	5.06E-02	4.97E-02	5.25E-02	5.40E-02	5.55E-02	6.05E-02	4.81E-02	4.61E-02	4.42E-02	3.63E-02
185	4.06E-02	4.12E-02	4.15E-02	4.18E-02	4.34E-02	4.02E-02	4.00E-02	3.97E-02	3.92E-02	4.12E-02	4.27E-02	4.38E-02	4.81E-02	3.80E-02	3.68E-02	3.51E-02	2.92E-02
238	3.29E-02	3.35E-02	3.34E-02	3.38E-02	3.48E-02	3.25E-02	3.24E-02	3.22E-02	3.15E-02	3.39E-02	3.46E-02	3.55E-02	3.91E-02	3.12E-02	2.98E-02	2.88E-02	2.42E-02

Table 4.4 Counting efficiencies using HPGe array for source in various regions of the lungs of voxel phantom of in-plane resolution of 2.025 mm with varying weights.

Energy keV	uniform distribution in lungs	Weights given to Upper right lung				Weights given to Upper left lung				Weights given to lower right lung				Weights given to lower left lung			
		0.4	0.5	0.6	1	0.4	0.5	0.6	1	0.4	0.5	0.6	1	0.4	0.5	0.6	1
18	7.15E-04	7.89E-04	8.30E-04	8.74E-04	1.01E-03	7.41E-04	7.60E-04	7.71E-04	8.16E-04	7.34E-04	7.38E-04	7.52E-04	7.85E-04	6.27E-04	5.66E-04	5.01E-04	2.70E-04
60	1.13E-02	1.18E-02	1.21E-02	1.24E-02	1.37E-02	1.14E-02	1.14E-02	1.14E-02	1.14E-02	1.16E-02	1.18E-02	1.21E-02	1.32E-02	1.02E-02	9.55E-03	8.89E-03	6.22E-03
63	1.21E-02	1.26E-02	1.30E-02	1.32E-02	1.45E-02	1.22E-02	1.22E-02	1.22E-02	1.23E-02	1.24E-02	1.27E-02	1.30E-02	1.41E-02	1.09E-02	1.03E-02	9.58E-03	6.82E-03
93	1.25E-02	1.31E-02	1.34E-02	1.38E-02	1.50E-02	1.27E-02	1.26E-02	1.26E-02	1.26E-02	1.29E-02	1.32E-02	1.35E-02	1.47E-02	1.14E-02	1.08E-02	1.01E-02	7.28E-03
185	1.06E-02	1.10E-02	1.12E-02	1.15E-02	1.24E-02	1.07E-02	1.07E-02	1.06E-02	1.05E-02	1.09E-02	1.12E-02	1.15E-02	1.24E-02	9.75E-03	9.23E-03	8.73E-03	6.64E-03
238	8.78E-03	9.08E-03	9.25E-03	9.42E-03	1.00E-02	8.85E-03	8.79E-03	8.73E-03	8.70E-03	9.05E-03	9.20E-03	9.43E-03	1.02E-02	8.11E-03	7.70E-03	7.28E-03	5.59E-03

Table 4.5 Counting efficiencies using Phoswich detector for source in various regions of the lungs of voxel phantom of in-plane resolution of 2.35 mm with varying weights.

Energy keV	uniform distribution in lungs	Weights given to Upper right lung				Weights given to Upper left lung				Weights given to lower right lung				Weights given to lower left lung			
		0.4	0.5	0.6	1	0.4	0.5	0.6	1	0.4	0.5	0.6	1	0.4	0.5	0.6	1
18	9.82E-04	1.04E-03	1.08E-03	1.14E-03	1.35E-02	9.81E-04	1.00E-03	9.98E-04	1.05E-03	1.00E-03	1.03E-03	1.05E-03	3.57E-04	8.26E-04	7.42E-04	6.58E-04	3.57E-04
60	4.30E-02	4.42E-02	4.50E-02	4.57E-02	4.88E-02	4.25E-02	4.20E-02	4.14E-02	3.96E-02	4.45E-02	4.60E-02	4.75E-02	2.64E-02	3.94E-02	3.72E-02	3.49E-02	2.64E-02
63	4.89E-02	5.06E-02	5.12E-02	5.19E-02	5.52E-02	4.84E-02	4.81E-02	4.77E-02	4.55E-02	5.11E-02	5.25E-02	5.42E-02	3.08E-02	4.50E-02	4.27E-02	4.05E-02	3.08E-02
93	3.43E-02	3.54E-02	3.62E-02	3.66E-02	3.92E-02	3.41E-02	3.36E-02	3.34E-02	3.21E-02	3.56E-02	3.69E-02	3.83E-02	2.06E-02	3.14E-02	2.96E-02	2.78E-02	2.06E-02
185	2.72E-02	2.80E-02	2.83E-02	2.86E-02	3.05E-02	2.67E-02	2.65E-02	2.63E-02	2.53E-02	2.83E-02	2.92E-02	3.01E-02	1.67E-02	2.51E-02	2.34E-02	2.24E-02	1.67E-02
238	2.23E-02	2.30E-02	2.32E-02	2.33E-02	2.47E-02	2.21E-02	2.17E-02	2.16E-02	2.06E-02	2.30E-02	2.39E-02	2.46E-02	1.43E-02	2.06E-02	1.96E-02	1.86E-02	1.43E-02

Table 4.6 Counting efficiencies using HPGe array for source in various regions of the lungs of voxel phantom of in-plane resolution of 2.35 mm with varying weights.

Energy keV	uniform distribution in lungs	Weights given to Upper right lung				Weights given to Upper left lung				Weights given to lower right lung				Weights given to lower left lung			
		0.4	0.5	0.6	1	0.4	0.5	0.6	1	0.4	0.5	0.6	1	0.4	0.5	0.6	1
18	3.08E-04	3.48E-04	3.68E-04	3.86E-04	4.61E-04	3.36E-04	3.36E-04	3.40E-04	3.61E-04	3.27E-04	3.35E-04	3.30E-04	3.55E-04	2.56E-04	2.27E-04	2.00E-04	1.06E-04
60	7.02E-03	7.35E-03	7.58E-03	7.83E-03	8.74E-03	7.06E-03	7.06E-03	7.07E-03	7.07E-03	7.21E-03	7.41E-03	7.59E-03	8.43E-03	6.42E-03	5.95E-03	5.46E-03	3.54E-03
63	7.57E-03	7.98E-03	8.24E-03	8.46E-03	9.37E-03	7.63E-03	7.65E-03	7.66E-03	7.60E-03	7.81E-03	7.99E-03	8.22E-03	9.09E-03	6.95E-03	6.42E-03	5.89E-03	3.85E-03
93	8.05E-03	8.43E-03	8.62E-03	8.81E-03	9.78E-03	8.05E-03	8.05E-03	8.02E-03	8.04E-03	8.21E-03	8.41E-03	8.65E-03	9.59E-03	7.40E-03	6.92E-03	6.34E-03	4.25E-03
185	6.98E-03	7.19E-03	7.43E-03	7.54E-03	8.18E-03	6.98E-03	6.99E-03	6.92E-03	6.84E-03	7.17E-03	7.33E-03	7.51E-03	8.37E-03	6.57E-03	6.14E-03	5.71E-03	3.93E-03
238	5.75E-03	6.02E-03	6.12E-03	6.25E-03	6.79E-03	5.81E-03	5.76E-03	5.77E-03	5.71E-03	5.96E-03	6.10E-03	6.24E-03	6.92E-03	5.55E-03	5.20E-03	4.83E-03	3.41E-03

Table 4.7 Counting efficiencies using Phoswich detector for source in various regions of the lungs in the Anterior- posterior direction of voxel phantom with varying weights.

Energy keV	Phantom of in-plane resolution 2.137 mm					Phantom of in-plane resolution 1.923 mm					Phantom of in-plane resolution 2.35 mm				
	0.4	0.5	0.5	Anterior	Posterior	0.4	0.5	0.5	Anterior	Posterior	0.4	0.5	0.5	Anterior	Posterior
18	1.31E-03	1.58E-03	1.84E-03	3.17E-03	5.35E-05	1.91E-03	2.33E-03	1.25E-03	4.63E-03	1.11E-04	8.74E-04	1.06E-03	1.84E-03	2.13E-03	2.75E-05
60	4.91E-02	5.50E-02	6.11E-02	8.40E-02	2.58E-02	6.01E-02	6.69E-02	7.33E-02	9.92E-02	3.34E-02	4.01E-02	4.50E-02	5.01E-02	6.99E-02	1.97E-02
63	5.56E-02	6.20E-02	6.84E-02	9.36E-02	3.06E-02	6.79E-02	7.51E-02	8.20E-02	1.10E-01	3.92E-02	4.58E-02	5.12E-02	5.68E-02	7.85E-02	2.38E-02
93	3.91E-02	4.37E-02	4.82E-02	6.71E-02	2.11E-02	4.79E-02	5.30E-02	5.81E-02	7.92E-02	2.73E-02	3.20E-02	3.58E-02	3.96E-02	5.55E-02	1.64E-02
185	3.44E-02	3.46E-02	3.83E-02	5.29E-02	1.66E-02	3.80E-02	4.19E-02	4.61E-02	6.27E-02	2.14E-02	2.53E-02	2.84E-02	3.15E-02	4.37E-02	1.31E-02
238	2.54E-02	2.82E-02	3.10E-02	4.28E-02	1.38E-02	3.09E-02	3.42E-02	3.74E-02	5.05E-02	1.77E-02	2.09E-02	2.33E-02	2.58E-02	3.57E-02	1.09E-02

Table 4.8 Counting efficiencies using HPGe array for source in various regions of the lungs in the Anterior- posterior direction of voxel phantom with varying weights

Energy keV	Phantom of in-plane resolution 2.137 mm					Phantom of in-plane resolution 1.923 mm					Phantom of in-plane resolution 2.35 mm				
	0.4	0.5	0.5	Anterior	Posterior	0.4	0.5	0.5	Anterior	Posterior	0.4	0.5	0.5	Anterior	Posterior
18	4.46E-04	5.42E-04	6.33E-04	1.04E-03	2.03E-05	6.51E-04	7.93E-04	9.45E-04	1.55E-03	3.94E-05	2.83E-04	3.49E-04	4.15E-04	6.83E-04	9.50E-06
60	8.24E-03	9.34E-03	1.05E-02	1.52E-02	3.58E-03	1.04E-02	1.17E-02	1.31E-02	1.86E-02	4.87E-03	6.42E-03	7.38E-03	8.31E-03	1.21E-02	2.63E-03
63	8.91E-03	1.01E-02	1.12E-02	1.62E-02	4.00E-03	1.12E-02	1.26E-02	1.40E-02	1.98E-02	5.41E-03	6.98E-03	7.96E-03	8.94E-03	1.30E-02	3.01E-03
93	9.39E-03	1.06E-02	1.18E-02	1.68E-02	4.38E-03	1.17E-02	1.32E-02	1.46E-02	2.04E-02	5.85E-03	7.41E-03	8.45E-03	9.47E-03	1.35E-02	3.28E-03
185	7.98E-03	9.00E-03	9.98E-03	1.41E-02	4.00E-03	9.86E-03	1.10E-02	1.22E-02	1.68E-02	5.25E-03	6.42E-03	7.25E-03	8.04E-03	1.15E-02	3.08E-03
238	6.62E-03	7.41E-03	8.22E-03	1.14E-02	3.43E-03	8.18E-03	9.12E-03	1.00E-02	1.38E-02	4.42E-03	5.35E-03	6.03E-03	6.71E-03	9.41E-03	2.63E-03

Table 4.9 Scattering factors due to non-uniform distribution in lungs for voxel phantom of in-plane resolutions of 2.137 (73 kg), 1.923 (59 kg) and 2.35 mm (88 kg) using Phoswich and HPGe array detectors

Radio nuclide	Energy keV	yield %	Scattering factors due to Phoswich detector for phantom of in-plane resolution							Scattering factors due to HPGe array for phantom of in-plane resolution						
			2.137 mm		1.923 mm		2.35 mm		total	2.137 mm		1.923 mm		2.35 mm		total
			lat	AP	lat	AP	lat	AP	SF	lat	AP	lat	AP	lat	AP	SF
Pu-239	18	2.15	1.17	1.17	1.14	1.38	1.17	1.45	1.78	1.19	1.21	1.17	1.2	1.21	1.21	1.56
Am-241	60	35.78	1.1	1.1	1.06	1.09	1.09	1.1	1.24	1.13	1.11	1.1	1.1	1.11	1.12	1.3
Th-234[*]	63	3.8	1.1	1.09	1.06	1.09	1.16	1.21	1.34	1.13	1.1	1.1	1.1	1.11	1.12	1.29
Th-234[*]	93	5.41	1.1	1.09	1.06	1.09	1.1	1.1	1.24	1.12	1.1	1.1	1.11	1.1	1.11	1.28
U-235	185	54	1.1	1.09	1.06	1.09	1.09	1.1	1.23	1.11	1.1	1.09	1.1	1.08	1.1	1.25
Pb-212	238	44.63	1.1	1.09	1.05	1.09	1.08	1.1	1.23	1.1	1.1	1.08	1.09	1.08	1.11	1.25

4.2 Uncertainty due to counting statistics

Counting statistics [23] gives rise to Type A uncertainty, as it could be obtained from a probability density function derived from an observed frequency distribution, which is a Gaussian distribution. This is because photons emitted from the radioactive source follows Poisson distribution [24], which interact in the detector and deposit energy. The number of carriers (electrons collected from photocathode in case of scintillator or number of electron- hole pairs in semiconductor detector) generated in the detector are discrete [24] and subject to random fluctuation from event to event in the detector due variety of different processes by which they interact. For large N, the Poisson distribution becomes Gaussian.

The best available estimate of the expectation value μ of the quantity q, is the average of the n observations, q_k.

$$\bar{q} = \frac{1}{n} \sum_{k=1}^{n} q_k \qquad \textbf{4.1}$$

The experimental variance of the observations, which is variance of the probability distribution of q, is given by

$$s^2(q_k) = \frac{1}{n-1} \sum_{j=1}^{n} (q_j - \bar{q})^2 \qquad \textbf{4.2}$$

The variance of the mean is given by assuming that all the observations are taken from the same distribution,

$$s^2(\bar{q}) = \frac{s^2(q_k)}{n} \qquad \textbf{4.3}$$

The experimental standard deviation of $s(\bar{q})$ which is square root of $s^2(\bar{q})$ is the measure of uncertainty of $\bar{q}$ when given for 95 % confidence interval. It is smaller by square root of n [58]

compared to s (q_k). The uncertainty due to counting statistics is expected to decrease with increase in activity or with increasing counting time. Therefore, when activity levels are low and close to limit of detection, the total uncertainty is governed by type A component and can be quite significant.

4.2.1 Measurements for uncertainty in counting statistics

To estimate the uncertainty due to counting statistics, it is required to have subjects, with various levels of lung activities. After monitoring those subjects for large number of time, it is possible to predict the uncertainties at various energies and activities. However, due to unavailability of such persons and practical problem in actually measuring such persons for large number of times, an alternate method is used. LLNL phantom with ^{241}Am and natural uranium lung set is monitored 30 times for 120 s, 100 s, 60 s, 30 s and 15 s respectively. Using this data, mean and standard deviation is evaluated for each monitoring period. The phantom data is then combined with the uncontaminated adult male measurement data. Uncontaminated adult male will be assumed as normal subject in the discussion. Using the mean and standard deviation of phantom and subject measurement data, error in the net counts is estimated using propagation of error [24]. Figure 4.3 shows the frequency distribution of LLNL phantom measurement data for 120 s of monitoring period. The data fits equally well with normal and lognormal distributions. SFs of counting statistics are evaluated as exponential of RE, using equation 2.27.

4.2.2 MDAs of Phoswich and HPGe array for ^{241}Am and natural uranium

MDAs of phoswich and HPGe array are evaluated using normal subject measurement data for 50 minutes of counting time and counting efficiencies (CEs) obtained with LLNL phantom for ^{241}Am and natural uranium using the methodology given by Curie [22]. Detector background of an uncontaminated adult person in lung measurement geometry in a totally

shielded steel room whole body counter is used for this purpose. The CEs, normal background

and MDAs obtained are given in table 4.10. The equation used for estimating MDA is

$$MDA = \frac{4.65 \sqrt{B} + 2.7}{k\,T}$$ **4.4**

Where B is background counts of an uncontaminated adult male, T is counting time in seconds

and k is counting efficiency in cps Bq^{-1}.

Table 4.10 MDAs of Phoswich and HPGe array for counting time of 3000 seconds using
Counting efficiencies with LLNL phantom of CWT 1.76 cm.

Radio-nuclide	Energy keV	Phoswich			HPGe array		
		CE cps/Bq	Normal Background counts	MDA Bq	CE cps/Bq	Normal Background counts	MDA Bq
^{241}Am	60	1.5E-2	2651.3	5.3	2.67E-3	114.5	6.5
Nat. U.	63	7.675E-3	6222	16*	3.33E-4	110.36	51.5
U-238	93	-	-	-	4.27E-4	120	42
Nat. U.	185	2.467E-2	2198	3	3.78E-3	116.8	4.7
U-235							

*MDA for phoswich is due to combined peak of 63 and 93 keV photons due to its poor resolution.

For HPGe array, MDA is ~ 51.5 Bq, 42 Bq and 5 Bq for 63, 93 and 185 keV of natural

uranium corresponding to ^{238}U and ^{235}U. MDAs of Phoswich for ^{238}U and ^{235}U are 16 Bq and 3

Bq respectively. The lower MDAs for U-238 with phoswich is due to its higher efficiency for

combined peak of 63 keV and 93 keV photons. These peaks are distinguishable in HPGe due to

its higher resolution of 0.6 keV at 60 keV compared to Phoswich detector, which is ~ 12 keV at

60 keV.

4.2.3   Variation of SFs due to counting statistics with lung activity for ^{241}Am

LLNL phantom with ^{241}Am lung set is monitored 30 times for 120, 100, 60, 30 and 15 seconds respectively.   Mean and standard deviations are obtained for each set.   Normal uncontaminated adult male also monitored ~ 15 times in standard lung measurement geometry under Phoswich and HPGe array.   From mean and standard deviation of LLNL phantom and normal subject data, a superimposed data is obtained which corresponds to the data of subjects with various levels of activities in lungs.   The lung activity corresponding to monitoring period of 120, 100, 60, 30 and 15 seconds is obtained by assuming that these net counts are due to monitoring a subject for 50 minutes.   Thus, net counts at 120 s with LLNL phantom having ^{241}Am lung set if superimposed on a normal subject data will correspond to lung activity of 37 Bq of ^{241}Am for 50 minutes of monitoring period.
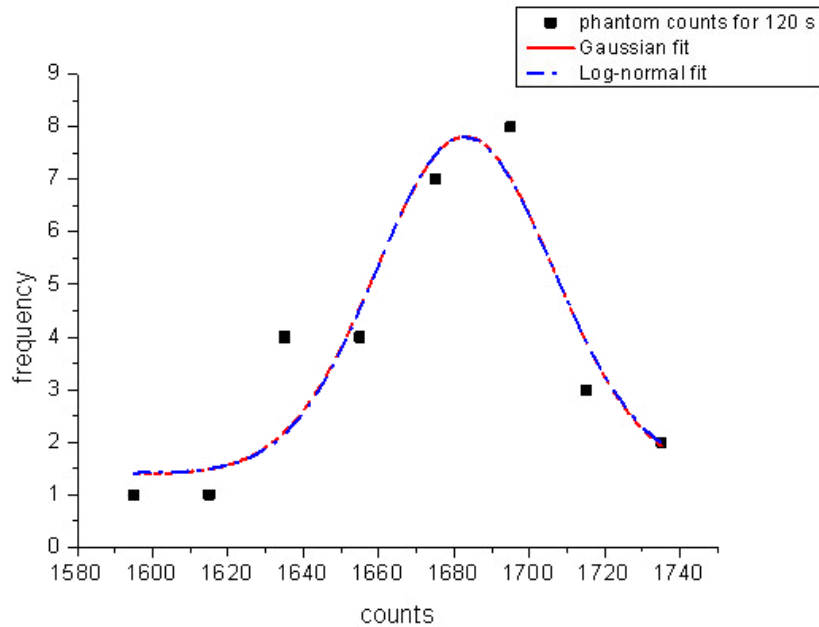
Figure 4.3 Normal and log-normal fitting to phantom measurement data.

The SFs at different lung activities are obtained by first evaluating net counts from phantom measurement data at various periods.   The net counts are combined with the mean

109

counts of normal subject data to obtain subject counts with various levels of activities. From propagation of error, standard deviation of the combined mean counts is obtained from standard deviation of subject and phantom data. Mean counts and standard deviation of superimposed data are used to calculate RE and SF as exponential of RE and given in table 4.11 for 60 keV of ^{241}Am for various lung activities.

Table 4.11 SFs due to counting statistics as a function of lung activity of ^{241}Am.

Sr.	Avg. Lung	SFs of Phoswich detector at 60 keV				SFs of HPGe array at 60 keV			
No.	activity# Bq	Mean counts net$^{@}$	Std. Dev. of counts*	Rel. Error %	SF	Mean counts net$^{@}$	Std. Dev. of counts*	Rel. Error %	SF
1	--	2651.3	112.4	4.2	1.04	114.5	17.5	15.3	1.22
2	37	1581.1	32.2	7.4	1.07	293.7	16.7	8.2	1.08
3	31	1309.8	44.1	9.2	1.09	249.4	15.8	9.4	1.1
4	18	782.9	35.3	15.0	1.16	144.0	9.6	13.8	1.14
5	9	395.5	23.4	29.0	1.33	70.7	7.7	27.0	1.31
6	4.6	200.0	10.2	56.4	1.75	36.1	4.4	49.9	1.64

*standard deviation of mean is given for normal subject data, $^{@}$ mean of 30 measurements.
Lung activity values observed with Phoswich and HPGe array are within ±2.5 % of given values

For estimating SF due to counting statistics in normal subject measurement data, mean counts and standard deviation is used from the subject measurement data. To calculate RE at various lung activities, total standard deviation is obtained from standard deviation of LLNL phantom and uncontaminated adult male data, at the mean counts obtained at that lung activity. It is found from table 4.11 that as lung activity decreases from 37 Bq to 4.6 Bq, the SF increases from 1.07 to 1.75 for Phoswich and 1.08 to 1.64 for HPGe array. The RE increases from 7 % to 56 % using Phoswich and 8 % to 50 % for HPGe array for the same. The SF for lung activity, which would result in a RE of 10 %, is found to be ~ 1.1 for both the detectors at 60 keV.

4.2.4 Variation of SFs with lung activity for natural uranium

The SF values are also predicted for 63, 93 and 185 keV as a function of lung activity of natural uranium using phoswich and HPGe array and given in tables 4.12 and 4.13 respectively. More data is required due to lower yields of 63, 93 keV photons compared to ^{241}Am and lower quantity of ^{235}U (0.72 %) in Nat. U. [12] emitting 185 keV. LLNL phantom with natural uranium lung set is additionally acquired for 180, 360, 600 seconds in addition to 120, 100, 60, 30 and 15 seconds, 30 times.

From table 4.12, it is observed that SF of ~1.15 is observed with Phoswich for RE of 15 % which corresponds to lung activity of 54.7 Bq of ^{238}U and 9 Bq of ^{235}U respectively. MDA of Phoswich for ^{238}U and ^{235}U are 16 Bq and 3 Bq respectively. For lung activities less than MDA, SF increases to 1.93 for 13.8 Bq of lung activity for ^{238}U and 1.7 for 2.2 Bq of lung activity for ^{235}U. 5 Bq and 9 Bq of lung activities of ^{235}U are possible by counting the LLNL phantom with natural uranium lung set 30 times for 360 s and 600 s respectively.

Table 4.12 The SFs due to counting statistics using Phoswich detector for natural uranium.

Sr. No.	combined peak of 63 and 93 keV of ^{238}U in 40 -120 keV region					185 keV of ^{235}U in 165 -215 keV region				
	Avg. Lung activity Bq	mean counts net@	Std. dev. of counts*	RE %	SF	Lung activity Bq	mean counts net@	Std. Dev. of counts*	RE %	SF
1	-	6222	208.5	3.3	1.03	-	2198	82.7	3.76	1.04
2	297.4	6847.7	84.1	3.3	1.03	9.0	669.7	40.3	13.7	1.14
3	177.7	4092.3	77.3	5.4	1.05	5.1	376.7	32.8	23.6	1.27
4	54.7	1259.3	49.7	17.0	1.18	2.2	162.4	24.0	53.0	1.7
5	45.0	1037.2	22.8	20.2	1.22	2.1	157.1	15.5	86.5	2.37
6	27.2	626.6	24.8	33.5	1.39					
7	13.8	317.5	17.1	65.8	1.93					

*standard deviation of mean is given for normal subject data, @ mean of 30 measurements.

For HPGe array, MDA is ~ 51 Bq, 42 Bq and 5 Bq for 63, 93 and 185 keV of natural uranium corresponding to ^{238}U and ^{235}U. It is observed from table 4.13 that for lung activity corresponding to net counts obtained at 120 s is 58 Bq. At this lung activity, REs observed at 63 and 93 keV are 1.53 and 1.4 respectively. Lower value at 93 keV, is due to comparatively higher counts because of its higher yield of ~ 5.4 % compared to 3.8 % of 63 keV. For higher lung activities of ~ 8 and 12 Bq of ^{235}U, RE reduces considerably leading to lower SF as observed from table 4.13.

Table 4.13 The SFs due to counting statistics predicted for 63, 93 and 185 keV using HPGe array as a function of lung activity of natural uranium.

Sr. no.	lung activity avg. (Bq)	63 keV				93 keV				185 keV				
		mean net counts @	Std. dev. of counts*	RE %	SF	mean net counts	Std. dev. of counts	RE %	SF	lung activity avg. (Bq)	mean net counts @	Std. dev. of counts*	RE %	SF
1	--	110.4	23.8	21.5	1.24	120	23.3	19.4	1.23	--	116.8	23.6	20.2	1.26
2	261.5	262.3	15.5	10.8	1.11	333.5	17.7	8.8	1.09	12.3	139.6	13.2	19.4	1.21
3	156.4	157.2	13.5	13.5	1.19	198.9	11.9	13.2	1.14	7.8	88.7	10.1	29.0	1.33
4	78.1	76.4	7.5	32.7	1.38	102.0	11.8	25.6	1.29	3.8	44.2	7.7	56.3	1.75
5	58.7	59.5	8.7	42.5	1.53	74.1	9.8	34.1	1.4	2.6	29.6	5.8	97.5	2.65
6	50.3	50.8	8.6	49.8	1.64	63.8	7.8	38.5	1.47					
7	31.5	31.7	6.0	77.3	2.16	40.0	6.6	60.5	1.83					

*standard deviation of mean is given for normal subject data, @ mean of 30 measurements.

4.2.5   SFs due to counting statistics as a function of energy

The SFs at various energies are predicted at MDA level of lung activities for ^{241}Am and various energies of natural uranium and given in table 4.14. From table 4.14, the SF of 1.39 is observed with Phoswich detector for natural uranium lung set for 40 -120 keV energy region. It is for combined peak of 63 and 93 keV. The SFs are higher at 1.53, 1.47 and 1.33 at 63, 93 and

185 keV due to lower efficiency of HPGe detector at these energies compared to Phoswich detector. The SFs evaluated at MDA using HPGe array are found to decrease with increase in energy as given in table 4.14. The low value at 60 keV, is due to its higher yield of 36 % compared to 3.8 % of 63 keV. For higher lung activities, the SFs would be less than 1.1 as predicted from ^{241}Am and natural uranium measurements from tables 4.11 to 4.13. The evaluated SF is found to be similar, at MDAs of ^{241}Am and natural uranium to the literature value of 1.3.

Table 4.14 SFs due to counting statistics as a function of energy using basic LLNL phantom.

Sr. No.	Energy keV		Phoswich Detector				HPGe array			
			lung activity Bq	mean	Std. Dev.	SF	lung activity Bq	mean	Std. Dev.	SF
1	60	Normal	-	2651	112.4	1.33	-	114.5	17.5	1.31
		phantom	9.0	395.5	23.4		9.0	70.7	7.7	
2	63 *	Normal	-	6221	208.5	1.39	-	110.3	23.8	1.53
		phantom	27.2	626.5	24.8		58.7	59.5	8.7	
3	93	Normal	-	-	-	-	-	120	23.3	1.47
		phantom	-	-	-		50.3	63.8	7.8	
4	185	Normal	-	2198	82.7	1.27	-	116.8	23.6	1.33
		phantom	5.0	376.7	32.8		7.8	88.7	10.1	

*Combined peak of 63 and 93 keV

4.3   Estimation of skeletal activity of actinides

In case of internal contamination of long-lived actinides such as Pu, Am, U and Th by inhalation or injection pathway, major portion of activity will be deposited in the skeleton and liver over a period [1]. The accumulated activity in the whole skeleton due to actinides, which are

LEP emitters, is estimated by measuring activity in the skull or knee by keeping the detectors close to these body parts [19]. There are studies in which CEs are estimated for various types or builds of skull and knee phantoms, both physical and voxel, using various detection systems [80; 81; 82; 83; 84; 85]. In this study, skull and knee phantoms derived from ICRP reference male voxel phantom [36] are used and source is sampled in the bones of these phantoms according to the retention of activity in different parts of the skeleton. Biokinetic models of Pu, Am, U and Th given by ICRP [1] are solved [74] to estimate the activity in different parts of the skeleton as a function of time. Monte Carlo code FLUKA [25] is used to estimate CEs of Phoswich and HPGe array using these phantoms for 18 to 238 keV photons describing sources of ^{239}Pu, ^{241}Am, ^{238}U, ^{235}U and ^{232}Th. Default parameters are used in solving biokinetic models to estimate the distribution of activity between the trabecular bone and bone marrow (TBBM) and cortical bone (CB) regions, so that it will be representative of the distribution of actinides in the skeleton. The variation in the CEs of both the detection systems for source distributed in TBBM, CB and in both TBBM and CB regions of both the phantoms is studied. The methodology is provided for estimation of skeletal activity from skull and knee measurements.

4.3.1 Skull and knee voxel phantoms and measurement geometry

Skull and single knee phantoms were derived from ICRP reference male voxel phantom by cutting it in x-z planes and removing the voxels above the skin layer in x-y plane [71]. This modification was required to position the detectors close to the surface of the skull and knee phantoms for simulating the actual geometry of measurement. Detectors are positioned over the side of the skull in right lateral geometry such that it covers the skull aligning one side of the detector at the top of head. For estimating CE using knee phantom, detector center is positioned

on the center of the knee joint in supine position. Figures 4.4 depict the phoswich detector positioned over the skull and knee voxel phantoms as viewed by FLAIR.
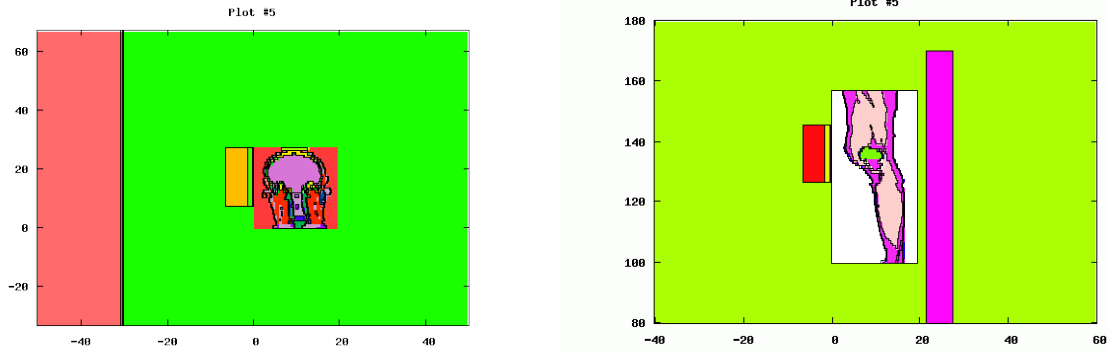
Figure 4.4 Phoswich detector positioned over the skull in right lateral geometry and knee phantom as viewed by FLAIR.

4.3.2   Solution of Biokinetic models

Biokinetic models of Pu, Am, U and Th are solved [74] to see the distribution of activity for inhalation intake of 1 Bq for type S or M compounds [42]. Default transfer rates of various compartments of respiratory tract model [42] along with the GI tract [45] and systemic biokinetic models of respective radionuclides [1; 46; 47] are used and integrated through the transfer compartment 'Blood' and the whole matrix is solved to give activity in various compartments as a function of time [48; 74]. Figure 4.5 (a) shows the retention in various compartments of bone as a function of time for Pu behaving as a type S compound after inhalation intake of 1 Bq.
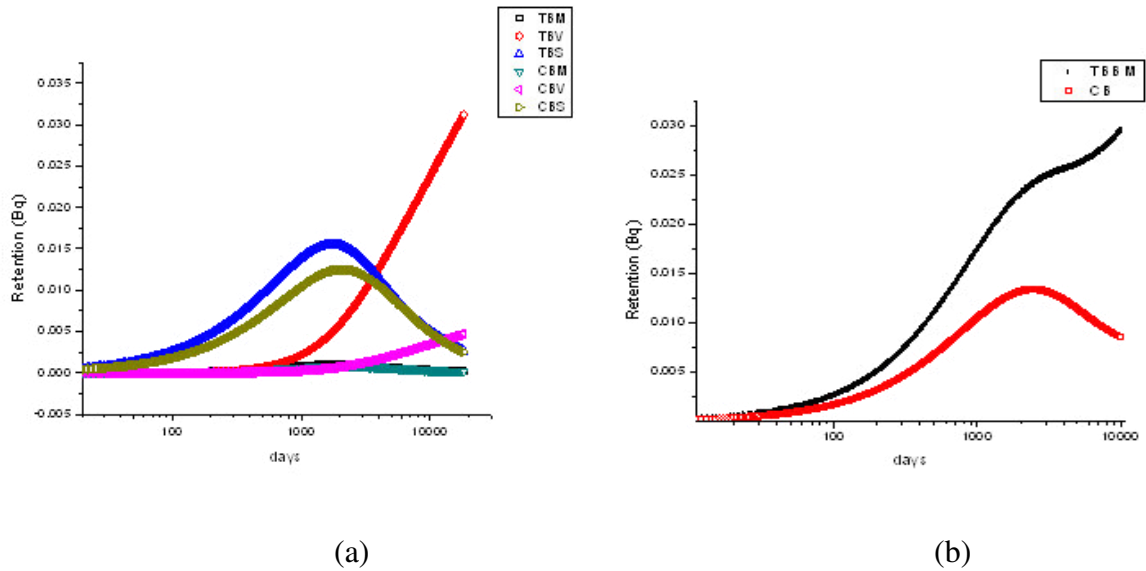
Figure 4.5 (a)Retention factors as a function of time for trabecular bone marrow (TBM), volume (TBV) and surface (TBS) and cortical bone volume (CBV), marrow (CBM) and surface (CBS) for Pu behaving as a type S compound after inhalation intake of 1 Bq. (b) retention factors for trabecular bone and bone marrow (TBBM) and cortical bone (CB) as a function of time.

It can be seen from figure 4.5 (a) that, activity will be transferred to the cortical and trabecular bone, with the maximum activity in the trabecular and cortical bone surfaces at ~ 5.5 years, which gets adsorbed in trabecular bone volume showing the maximum activity at ~ 25 years. Trabecular bone and bone marrow (TBBM) activity is sum of activity in trabecular bone volume (TBV), trabecular bone marrow (TBM), trabecular bone surface (TBS) and cortical bone marrow (CBM). Cortical bone (CB) activity is sum of activities of cortical bone surface (CBS) and cortical bone volume (CBV). Figure 4.5 (b) shows the retention in TBBM and CB as a function of time for type S compounds of Pu.

Similarly, from the solution of biokinetic models of Pu, for type M compounds, activities retained in TBBM and CB regions and their ratio 'R' is estimated. 'R' is defined as the ratio of

the activity in TBBM region and CB region. The variation of R as a function of time for Pu behaving as type S and M compound is shown in Figure 4.6 (a) and for Am behaving as type M and for U, Th as type M and S is shown in figure 4.6 (b).

(a)   (b)
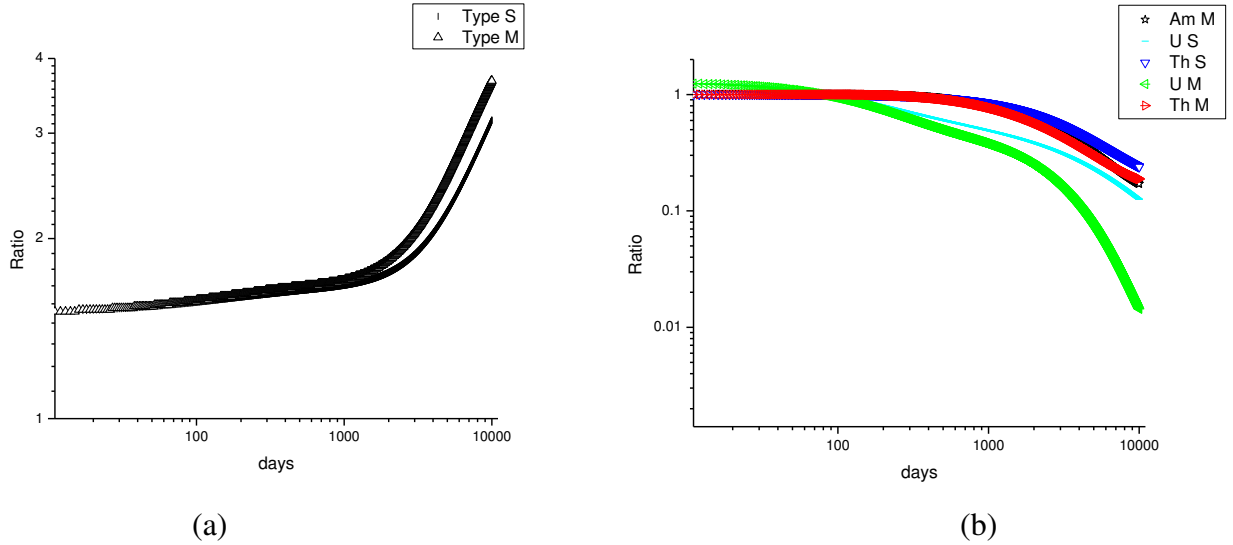
Figure 4.6 Variation of ratio of activities in TBBM and CB region as a function of time for (a) Pu type S and M compounds and (b) Am type M, U type M and S, Th type M and S compounds.

It can be seen from figure 4.6 (a) that R is ~ 1.5 till 1000 days after intake which thereafter increases rapidly to 3 at ~ 5000 days after intake for both the types of Pu compounds. It is found from figure 4.6 (b) that R is ~ 1 for about 1000 days, thereafter it decreases to ~ 0.2 for Am as type M, Th as type M and S and U as type S at ~ 10000 days after intake. For U behaving as type M, it decreases to 0.02. Thus, for Am, U and Th, the deposition in bones is quite different from Pu. In case of Pu, more activity is deposited in the TBBM compared to CB whereas in case of Am, U and Th more activity is deposited in the CB region. Using this biokinetic behaviour, CEs are estimated for the following four major cases:

Case 1. When activity is uniformly distributed in TBBM region.

Case 2. When activity is uniformly distributed in CB region.

Case 3. When activity is uniformly distributed in both TBBM and CB regions.

Case 4. When activity is distributed in TBBM and CB region according to the R of 1.5 or 3 for Pu and R of 0.2 for Am (type M), U (type S), Th (type M & S) and 0.02 for U (type M).

4.3.3   Source sampling in the Monte Carlo code FLUKA

Trabecular bone, bone marrow (both active and inactive) and bone surfaces are not identified separately in ICRP voxel phantom and they are part of spongiosa region, which is identified for different bones [36; 86]. Cortical bone (volume and surface) and cortical marrow are identified separately in ICRP male voxel phantom as cortical bone and medullary cavities. In cranium and mandible bone voxels of skull as well as femur, tibia and fibula bone voxels of knee, TBBM and CB voxels are located so that source can be simulated according to the solution of biokinetic models. Source is simulated in different parts of the bones by first randomly selecting the voxel from known bone voxels and then randomly selecting a point in that voxel. The isotropic directional distribution of emitted photons is sampled from a uniform distribution of the cosine of the polar angle and a uniform distribution of the azimuthal angle. Seven photon energies in the range of 18 to 238 keV are simulated for the photons emitted from ^{239}Pu, ^{241}Am, ^{238}U, ^{235}U and ^{232}Th and for source in TBBM, CB and in both the regions respectively. CEs are also evaluated for non-uniform source distribution with R-values of 1.5, 3.0 for Pu and 0.2, 0.02 for Am, U and Th by sampling the photons in that proportion respectively in TBBM and CB regions. 'Detect' card of FLUKA is used for scoring energy deposition in the HPGe array and in primary NaI of Phoswich detector. The counts per photon in the various energy regions are determined for 2 x 10^6 histories run over 5 cycles to reduce the RE to less than 3 %.

4.3.4   Validation of the CEs of Phoswich detector using knee and skull voxel phantom

The CE of Phoswich detector obtained from knee voxel phantom are validated experimentally using the physical knee phantom, which is measured inside totally shielded steel room WBC as a part of IAEA inter-comparison exercise [87] at 60 keV of ^{241}Am. The deviation in the ^{241}Am activity estimated in the physical knee phantom using the CE obtained using knee voxel phantom with source uniformly distributed in cortical and TBBM region is found to be 8.3 % with respect to the actual activity present in the phantom [87].

The deviation in the CE of Phoswich detector using skull voxel phantom for source uniformly distributed in the CB region of the skull with respect to the CE estimated using Cristy's mathematical phantom [83] is found to be -35 % at 60 keV of ^{241}Am. The large deviation is due to the realistic nature of the voxel phantom and the uniform source sampling carried out in CB of skull voxel phantom, which consists of CBV and CBS of cranium and mandible but on the surface of the cranium and facial bones in the Cristy's mathematical model [83].

4.3.5   CEs from skull or knee measurement

4.3.5.1   *CEs using skull voxel phantom*

CEs of phoswich and HPGe array obtained in right lateral geometry using skull phantom are given in table 4.15 for 18 keV for R of 1.5 and 3 and in table 4.16 for all the other energies for R of 0.2 and 0.02 as well as for source in various bone regions.

Table 4.15 CEs (counts photon^{-1}) of Phoswich and HPGe array at 18 keV for source in various bone regions of the skull and knee voxel phantoms.

		CB	TBBM	CB and TBBM	R=3	R=1.5
Skull	Phoswich	2.26E-03	5.47E-04	1.53E-03	1.08E-03	1.34E-03
	HPGe array	7.36E-04	1.20E-04	4.72E-04	3.08E-04	4.02E-04
knee	Phoswich	2.36E-03	8.47E-04	1.97E-03	1.57E-03	1.82E-03
	HPGe array	7.95E-04	2.58E-04	6.44E-04	5.13E-04	5.93E-04

Table 4.16 CEs (counts photon^{-1}) of Phoswich and an array of HPGe detectors for source in various bone regions of the skull voxel phantom.

Energy keV	Phoswich detector					HPGe array				
	CB	TBBM	CB and TBBM	R=0.2	R=0.02	CB	TBBM	CB and TBBM	R=0.2	R=0.02
60	6.50E-02	5.07E-02	5.89E-02	6.31E-02	6.48E-02	1.24E-02	8.79E-03	1.09E-02	1.20E-02	1.24E-02
63	7.23E-02	5.73E-02	6.60E-02	7.05E-02	7.22E-02	1.33E-02	9.55E-03	1.17E-02	1.28E-02	1.32E-02
74	6.54E-02	5.20E-02	5.98E-02	6.37E-02	6.53E-02	1.38E-02	1.01E-02	1.22E-02	1.33E-02	1.37E-02
93	6.20E-02	4.95E-02	5.67E-02	6.03E-02	6.17E-02	1.45E-02	1.08E-02	1.29E-02	1.40E-02	1.44E-02
185	5.10E-02	4.11E-02	4.68E-02	4.97E-02	5.09E-02	1.20E-02	9.38E-03	1.09E-02	1.17E-02	1.20E-02
238	4.13E-02	3.36E-02	3.80E-02	4.03E-02	4.12E-02	9.86E-03	7.77E-03	8.96E-03	9.57E-03	9.80E-03

From table 4.16, higher CEs are obtained using both the detectors when activity is in the CB region compared to activity in TBBM or in both the regions. At 18 keV, the deviation in the CE of both the systems obtained with source in CB region with respect to source in both CB and TBBM regions is found to be ~ 48 % as seen from table 4.15. From table 4.16, the deviation in the CEs obtained using source in CBs with respect to source in TBBM is ~ 30 % with the Phoswich detector and the deviation is ~ 40 % at 60 keV using HPGe array, and reduces with increase in energy to ~ 25 % at 238 keV for both the detectors. The CEs evaluated for source in

both CB and TBBM region are found to be in between the CEs obtained using source in CB region and TBBM region respectively by ~ 10 to -20 % using both the detection systems.

For non-uniform source distribution, the deviation in the CEs for R =1.5 using both the detection systems is found to be ~ 30 % when compared with the CEs obtained with R = 3. CEs obtained with R of 0.2 and 0.02 are closer to CEs with source in CB using both the detection systems by -3 % and -1 % respectively as these corresponds to more source particles from CB region; but varies from uniform source distribution in CB and TBBM region by ~ 10 %.

Table 4.17 CEs (counts photon^{-1}) of Phoswich and HPGe array for source in the various bone regions of the knee voxel phantom.

Energy	Phoswich detector					HPGe array				
keV	CB	TBBM	CB and TBBM	R=0.2	R=0.02	CB	TBBM	CB and TBBM	R=0.2	R=0.02
60	5.46E-02	7.90E-02	6.12E-02	5.64E-02	5.49E-02	1.14E-02	1.54E-02	1.25E-02	1.17E-02	1.15E-02
63	6.05E-02	8.80E-02	6.78E-02	6.23E-02	6.06E-02	1.22E-02	1.66E-02	1.34E-02	1.25E-02	1.23E-02
74	5.37E-02	7.71E-02	5.98E-02	5.50E-02	5.36E-02	1.26E-02	1.74E-02	1.40E-02	1.31E-02	1.28E-02
93	5.03E-02	7.21E-02	5.61E-02	5.18E-02	5.05E-02	1.32E-02	1.84E-02	1.46E-02	1.36E-02	1.33E-02
185	4.16E-02	5.84E-02	4.63E-02	4.27E-02	4.16E-02	1.13E-02	1.55E-02	1.24E-02	1.16E-02	1.14E-02
238	3.39E-02	4.72E-02	3.74E-02	3.49E-02	3.40E-02	9.29E-03	1.27E-02	1.02E-02	9.56E-03	9.35E-03

4.3.5.2   *CEs using knee voxel phantom*

CEs for Phoswich and HPGe array are given in tables 4.15 for 18 keV for R of 1.5 and 3 and in table 4.17 for all the other energies for R of 0.2 and 0.02 as well as for source in various

knee bone regions. From table 4.17, higher CEs are obtained using Phoswich and HPGe array, for source in the TBBM region of the knee voxel phantom as this region is positioned directly below the detector in the simulated geometry. The CEs with source in TBBM region are found to be ~ 40 % and ~ 23 % higher with respect to the source in CB and in both the regions of the phantom respectively using Phoswich and HPGe array. At 18 keV, CE is higher when source is in CB region due to the attenuation of these LEPs by overlying CB layer in case of source in TBBM region. On comparing CEs at 18 keV, given in table 4.15 with the CEs at higher energies given in tables 4.16 to 4.17, it is found that CEs are lowest at 18 keV for both the detectors and both the phantoms as attenuation is highest at this energy. Above 18 keV, as energy increases, there is an increase in the transmitted photons leading to increase in the CEs. In the energy range of 60 to 93 keV, CEs are showing a variation of ~ 12 %. Above 93 keV, CEs are found to decrease with energy for phoswich as well as HPGe array as transmitted photons of high energy are not able to deposit their full energy in the active volume of detectors due to the limiting thickness of the detectors.

4.3.6   Estimation of skeletal activity using knee and skull measurements

CEs estimated for phoswich and HPGe array in counts per photon at a particular energy are converted into cps per Bq using its emission probability to estimate the activity due to radionuclide present in the skull or knee region. Table 4.18 gives the energies and intensities of the photons of various radionuclides considered in this study [17] along with MDAs for HPGe array for skull and knee measurements.

The combined CB and TBBM masses of the skull and a single knee phantom are found to be ~ 10 % and 9.3 % of the total skeletal mass of 10450 gm. In evaluating the bone masses, the number of voxels of CB and TBBM regions is taken into consideration along with their

respective densities. The volume of a single voxel is 2.137 mm x 2.137 mm x 8 mm ie. 36.534 mm³ [16]. Knowing fractional skeletal mass from table 4.19, total skeletal activity can be estimated from measured skull or knee activity.

Table 4.18 MDAs (Bq) of an array of HPGe detector system for various radionuclides.

Radionuclide	Energy	Yield	HPGe array	
	keV	%	Skull Phantom	Knee phantom
Pu-239	17.6	2.15	2348.6	2583.4
Am-241	59.5	35.78	5.5	4.7
Th-234	63.3	3.8	46.6	44.7
Pb-212	74.8	10.65	5.3	4.5
Th-234	93.2	5.41	33.2	28.2
U-235	185.7	54.0	3.6	3.4

Table 4.19 Fraction of the skeletal mass of skull and knee voxel phantom.

Bone material	Number of voxels		Density	Mass (gm)	
	Skull phantom	Knee phantom	gm/cm³	Skull phantom	Knee phantom
Cortical bone	8023	5407	1.92	562.78	379.28
Spongiosa	10665	14566	1.117^k, 1.245^s	485.10	594.35
Total mass				1047.88	972.63
Fraction of total skeletal mass				0.10	0.09

k : density of spongiosa in knee bones, s: density of spongiosa in cranium

4.3.7 Minimum Detectable Activity (MDA)

Due to lower background of HPGe array and better resolution with full width at half maximum of 0.6 keV compared to 12 keV of Phoswich detector at 60 keV, the identification and quantification of LEP emitters is possible even in the presence of other radionuclides with HPGe

array. Therefore, MDA [22] values are estimated for HPGe array system for source uniformly distributed in both CB and TBBM region of the skull or knee phantoms for all the radionuclides for 30 minutes of counting time and given in table 4.18. Normal subject background (Detector background of an uncontaminated adult person in measurement geometry such as detector over skull or knee in a totally shielded steel room WBC) is used for this purpose. MDA of ~ 5 Bq is obtained at 60, 74 and 185 keV where photons are having considerable yield; at 63 and 93 keV, MDAs are found to be ~ 45 and 30 Bq respectively. Highest MDA of ~ 2500 Bq is found at 18 keV of ^{239}Pu due to low yield and higher attenuation of these LEPs. As the CEs of phoswich detector are ~ 5 times higher than the HPGe array for uniform source distribution in CB and TBBM region and their background is ~ 30 times higher than HPGe array for both the phantoms, MDAs would be similar to HPGe array at all the energies.

Dose at the MDA can be obtained by first estimating the skeletal activity using fraction of skeletal mass in the skull or knee regions given in table 4.19 and then intake from the retention values in skeleton for 1 Bq of inhalation intake and finally using dose coefficient for a particular radionuclide. Higher MDA of ~ 2500 Bq limits the use of the CEs estimated using skull and knee phantoms for ^{239}Pu, but CEs are estimated, as physical phantoms are not available for ^{239}Pu skeletal burden estimation.   Other techniques such as urine bioassay and lung monitoring will be useful for pure ^{239}Pu intake estimation.

4.3.8   Errors in the estimated knee or skull activity

Ratio 'R' corresponds to the ratio of activity in TBBM and cortical bone regions as obtained from the solution of biokinetic models of Pu, Am, U and Th etc. The biokinetic models are based on the data obtained from in vivo measurements, excretion and autopsy measurements on workers exposed to actinides [88], studies on the distribution and excretion observed in

laboratory animals and injection data in humans and laboratory animals [89]. Thus, it implies that ratio 'R' is the representative ratios of activities in TBBM and CB in adult workers. There are inherent uncertainties in the rates of removal from bone surfaces and burial in bone volume, but to estimate uncertainties in those rates is beyond the scope of this study. The uncertainties due to distribution of activity in TBBM and CB regions are discussed.

R is estimated to be 1 till 1000 days after inhalation intake for all the compounds of Am, U and Th. Therefore, assuming uniform source distribution in TBBM and CB region, CEs should be estimated and used for these radionuclides until 1000 days after intake. R is found to be 1.5 for type M and S types of Pu, therefore CE assuming R of 1.5 should be used for Pu until 1000 days after intake. After that, CEs according to the observed R should be used which corresponds to CEs assuming R of 3 for Pu and CEs assuming R of 0.2 for Am (type M), U (Type S) and Th (type M and S) and CEs assuming R = 0.02 for type M compounds of U. If R is not known, then error in the estimated skeletal activity will be due to the use of CE, which is not representative of the actual distribution of activity in the skeleton.

For Pu, largest deviation of ~ 30 % and ~ 16 % is observed in CEs obtained with R of 1.5 using skull and knee phantoms respectively with respect to the CEs obtained assuming R of 3. The deviation in CEs obtained with R= 1.5 and R=3 with CEs with source in both CB and TBBM regions is found to be -15 % and -30 % in case of skull phantom and -8 % and -20 % in case of knee phantom. Thus, overestimation and underestimation of ~ 30 % could occur due to unknown distribution of skeletal activity in case of Pu. For other radionuclides, deviation of ~ ±10 % is observed in CEs obtained using skull and knee phantoms for uniform distribution of activity in TBBM and CB region with respect to the CEs obtained assuming R of 0.2 and R of

0.02. As there is a single biokinetic model for adult population, the same CEs will be useful for young as well as elderly male subjects for various radionuclides considered in this study.

4.3.9 Variation of overlying tissue thickness in skull and knee phantoms

To see the effect of variation of overlying tissue thickness, the voxel size is varied from 2.137 mm to 1.923 and 2.351 mm, so that there will be variation of ± 1 mm in 10 mm thick overlying tissue. Voxel in-plane resolution of 1.923 mm corresponds to phantom weight of 59.1 kg while voxel in-plane resolution of 2.351 mm corresponds to phantom weight of 88.3 kg, for slice thickness of 8 mm. CEs are evaluated using both the detector systems and both the phantoms. In figure 4.7, CEs of HPGe array using knee and skull phantoms of voxel sizes 2.137, 1.923 and 2.351 mm for uniform source distribution in TBBM and CB region are depicted.
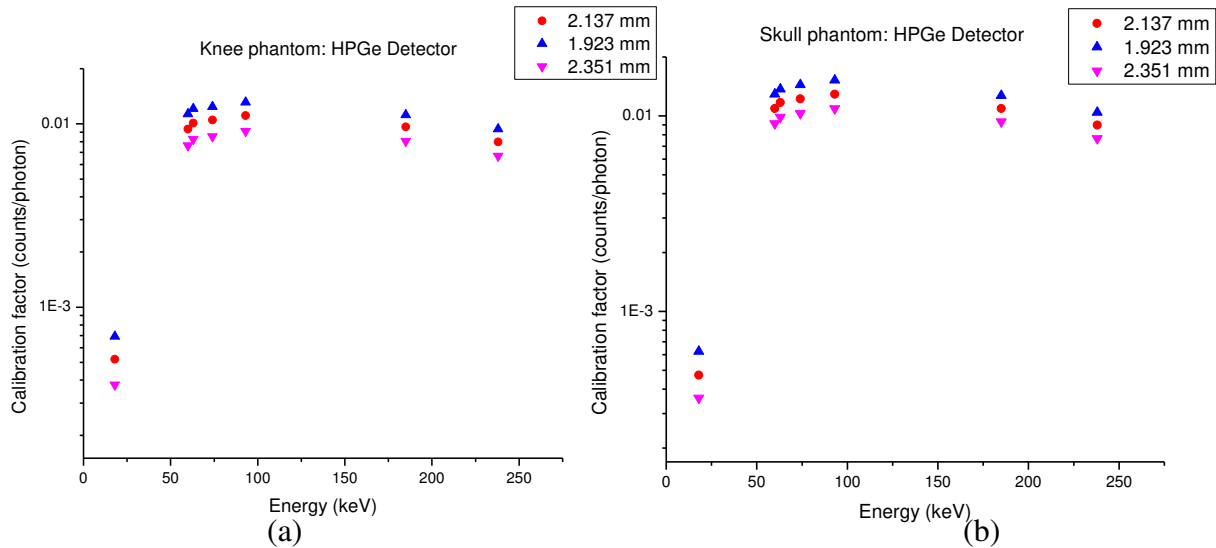
Figure 4.7 The CEs of HPGe array for (a) knee and (b) skull phantoms for uniform source distribution in TBBM and CB region for voxel sizes 2.137, 1.923 and 2.351 mm.

It is found that for reduced phantom, CEs are higher due to lesser attenuation of photons compared to the earlier CEs for source in CB and TBBM regions. By increasing the absorber thickness to 2.351 mm, CEs are lower than the CEs with voxel size 2.137 mm due to higher

attenuation and scattering of photons in overlying tissues. The deviation in the CEs obtained with voxel size of 1.923 or 2.351 mm with respect to the CEs obtained with voxel size of 2.137 mm is found to be ~ ± 30 % at 18 keV, which reduces to ~ ± 15 % at 238 keV. The uncertainties that will be introduced by measuring somebody who is different from reference man can be found from figure 4.7 and table 4.20 as these contains the CEs for radiation workers having weight in the range of ~ 73 ± 15 kg. The deviation in the CEs obtained with voxel size of 1.923 mm with respect to 2.351 mm is found to be ~ 67 % at 18 keV, which reduces to ~ 30 % at 238 keV, for knee voxel phantom for both the detection systems. Using skull voxel phantom, the deviation in the CEs obtained with voxel size of 1.923 mm with respect to 2.351 mm is found to 73 % with HPGe array and 97 % with phoswich detector at 18 keV, which reduces to 36 % at 238 keV for both the detection systems. These deviations in the CEs are due to extreme weight variation of ~ 30 kg in the ICRP reference adult male voxel phantom. The deviations of ~ 15 % are observed for energies above 18 keV, when compared with CEs using reference man.

Table 4.20 CEs using Phoswich detector for skull and knee voxel phantom for 1.923 mm and 2.351 mm voxel sizes for uniform source distribution in TBBM and CB regions.

Energy	Skull Phantom		Knee phantom	
keV	1.923 mm	2.351 mm	1.923 mm	2.351 mm
18	2.25E-03	1.14E-03	2.13E-03	1.19E-03
60	6.89E-02	5.03E-02	5.76E-02	4.18E-02
63	7.68E-02	5.65E-02	6.40E-02	4.73E-02
74	6.96E-02	5.11E-02	5.52E-02	4.04E-02
93	6.60E-02	4.86E-02	5.09E-02	3.71E-02
185	5.47E-02	4.02E-02	4.19E-02	3.07E-02
238	4.43E-02	3.27E-02	3.45E-02	2.54E-02

It is important to estimate skeletal activity because in case of old exposures, activity will be in skeleton and 8.47 % of skeletal activity will be in rib bones [36] which will contribute in the lung measurements. It is required that skeletal activity is evaluated from previous measurements, so that net counts due to fresh intake can be estimated accurately.

4.4 Uncertainty due to activity in other organs

To estimate the contribution of source in liver, ribbons, GI tract and lymph nodes in lung measurements, source is sampled in those organs of male thorax voxel phantom and photon energy spectrum observed in the detector positioned over the chest in standard lung measurement geometry in 'FLUKA'. Contributions are estimated for both the detectors for 18 to 238 keV photons. Contributions in lung measurement due to source in GI tract is studied and described in detail in chapter 5.

4.4.1 Contribution of liver in lung measurements

The contributions in Phoswich and HPGe array for various lung measurement geometries and for source in liver are given in table 4.21. For source in liver, the contributions are found to be ~ 48 % for all the energies at and above 60 keV and ~ 18 % at 18 keV in standard lung measurement geometry using Phoswich detector. Using HPGe array, the contribution in lung measurement is found to increase with energy. It is found to increase from 32 to 40 % for 60 to 238 keV energies and ~ 11 % at 18 keV in standard lung measurement geometry. The different contributions are observed in right and left lung geometries as observed from table 4.21. Right and left lung geometries corresponds to detector positioning over right and left lung respectively, with one end of the detector tangential to suprasternal notch and other perpendicular end tangential to midline of the phantom. For right lung geometry, higher contribution of ~ 50 % is observed compared to 15 % with left lung geometry using Phoswich detector. In case of HPGe

detector, contribution in right lung geometry, is found to increase from 36 % to 44 % as energy

increases from 60 to 238 keV and in left lung geometry, it is found to increase from 6 % to 11 %.

At 18 keV, contributions are least in left lung compared to right lung geometry. They are found

to be 20 % and 12 % for right lung and 2.4 and 0.6 % for left lung geometry using Phoswich and

HPGe array. The lower contribution in the left lung is due to lesser contribution of scattered

photons from liver.

Table 4.21   Contribution in counts photon^{-1} in various lung measurement geometries for source

in liver.

	Geometries used for measurements using							
	Phoswich detector				HPGe array			
	source in lungs	source in liver			source in lungs	source in liver		
Energy keV	Standard lung	Standard lung	Right lung	left lung	Standard lung	Standard lung	Right lung	left lung
18	1.44E-03	2.44E-04	2.70E-04	3.25E-05	4.58E-04	6.09E-05	6.51E-05	3.70E-06
60	5.28E-02	3.37E-02	3.63E-02	9.78E-03	8.80E-03	3.99E-03	4.53E-03	7.56E-04
63	5.99E-02	4.01E-02	4.26E-02	1.20E-02	9.50E-03	4.49E-03	5.02E-03	8.74E-04
74	4.73E-02	2.94E-02	3.19E-02	8.60E-03	9.62E-03	4.55E-03	5.13E-03	8.96E-04
93	4.24E-02	2.53E-02	2.76E-02	7.25E-03	9.97E-03	4.95E-03	5.58E-03	1.04E-03
185	3.34E-02	2.11E-02	2.25E-02	6.34E-03	8.55E-03	4.81E-03	5.34E-03	1.29E-03
238	2.71E-02	1.82E-02	1.96E-02	5.99E-03	7.08E-03	4.24E-03	4.60E-03	1.21E-03

4.4.2   Contribution of activity in rib bones to lungs

The contributions in Phoswich and HPGe array for various lung measurement geometries

and for source in rib bones are given in table 4.22. For source in rib bones, the contribution in

lung measurement is found to be ~ 45 % for all the energies at and above 60 keV and ~ 31 % at

18 keV in standard measurement geometry using Phoswich detector. Using HPGe array, the

contribution in lung measurement is found to increase with energy. It is found to increase from 23 to 40 % for 18 to 238 keV energies in standard lung measurement geometry. Slightly higher contributions are observed in right lung geometry compared to left lung geometries for all the energies using both the detectors. For Phoswich detector, contributions of ~ 45 % are observed in right lung geometry and 36 % in left lung geometry. In case of HPGe detector, contribution in right lung geometry, is found to increase from 41 % to 47 % as energy increases from 60 to 238 keV and in left lung geometry, it is found to increase from 35 % to 41 %. Contributions are found to be 51 % and 38 % for right lung and 46 and 36 % for left lung geometry using Phoswich and HPGe array at 18 keV.

Table 4.22 Contribution in counts photon^{-1} in various lung measurement geometries for source in rib-bones.

	Geometries used for measurements using							
	Phoswich detector				HPGe array			
	source in lungs	source in rib bones			source in lungs	source in rib bones		
Energy keV	Standard lung	Standard lung	Right lung	left lung	Standard lung	Standard lung	Right lung	left lung
18	1.44E-03	4.47E-04	7.39E-04	5.55E-04	4.58E-04	1.06E-04	2.10E-04	1.67E-04
60	5.28E-02	2.18E-02	2.39E-02	2.10E-02	8.80E-03	2.82E-03	3.63E-03	3.11E-03
63	5.99E-02	2.58E-02	2.78E-02	2.44E-02	9.50E-03	3.16E-03	3.94E-03	3.39E-03
74	4.73E-02	2.14E-02	2.24E-02	1.94E-02	9.62E-03	3.26E-03	4.06E-03	3.52E-03
93	4.24E-02	1.81E-02	2.01E-02	1.72E-02	9.97E-03	3.52E-03	4.33E-03	3.76E-03
185	3.34E-02	1.50E-02	1.62E-02	1.41E-02	8.55E-03	3.41E-03	3.90E-03	3.42E-03
238	2.71E-02	1.27E-02	1.36E-02	1.18E-02	7.08E-03	2.97E-03	3.34E-03	2.90E-03

4.4.3 Contribution of lymph node activity in lungs

Contributions of lymph nodes situated in arms and trunk, in lung measurements is studied for 18 to 238 keV of photons. The contributions in Phoswich and HPGe array for various lung measurement geometries and for source in lymph nodes situated in arms and trunk are given in tables 4.23 and 4.24 respectively. For source in lymph nodes situated in arms, the contribution in lung measurement is found to increase with energy. It is found to increase from ~ 6 to 9 % and 3 to 7 % for 60 to 238 keV for Phoswich and HPGe array. At 18 keV, contributions are observed to be ~ 0.2 % and 3 % in standard measurement geometry for Phoswich and HPGe array. The different contributions are observed in right and left lung geometries. They are found to be 15 % and 10 % for right lung geometry using Phoswich and HPGe array. In left lung geometry, contribution of ~ 20 % is observed using both the detectors.

For source in lymph nodes situated in trunk, the contribution in lung measurement is found to be ~ 42 % using both the detectors for 60 to 238 keV. At 18 keV, contributions are observed to be ~ 52 % and 56 % in standard measurement geometry for Phoswich and HPGe array. The different contributions are observed in right and left lung geometries. It is found to increase from ~ 20 to 26 % for both the detectors for 18 to 238 keV in right lung geometry. For Phoswich and HPGe array, contribution is found to increase from ~ 32 to 35 % and 26 to 31 % respectively for 18 to 238 keV photons in left lung geometry.

Table 4.23 Contribution in counts photon^{-1} in various lung measurement geometries for source in lymph nodes (arms).

	Geometries used for measurements using							
	Phoswich detector				HPGe array			
	source in lungs	source in lymph nodes (arms)			source in lungs	source in lymph nodes (arms)		
Energy keV	Standard lung	Standard lung	Right lung	left lung	Standard lung	Standard lung	Right lung	left lung
18	1.44E-03	3.00E-06	8.59E-04	1.54E-03	4.58E-04	1.00E-04	1.24E-04	4.43E-04
60	5.28E-02	3.14E-03	7.79E-03	1.05E-02	8.80E-03	2.42E-04	7.34E-04	1.68E-03
63	5.99E-02	4.01E-03	9.05E-03	1.20E-02	9.50E-03	3.01E-04	8.10E-04	1.82E-03
74	4.73E-02	2.97E-03	7.33E-03	9.62E-03	9.62E-03	3.40E-04	8.48E-04	1.85E-03
93	4.24E-02	2.77E-03	6.53E-03	8.77E-03	9.97E-03	3.89E-04	9.14E-04	1.91E-03
185	3.34E-02	2.55E-03	5.21E-03	6.88E-03	8.55E-03	4.97E-04	9.39E-04	1.74E-03
238	2.71E-02	2.50E-03	4.52E-03	5.82E-03	7.08E-03	4.73E-04	8.41E-04	1.49E-03

Table 4.24 Contribution in counts photon^{-1} in Phoswich and HPGe array for various lung measurement geometries for source in lymph nodes (trunk).

	Geometries used for measurements using							
	Phoswich detector				HPGe array			
	source in lungs	source in lymph nodes (trunk)			source in lungs	source in lymph nodes (trunk)		
Energy keV	Standard lung	Standard lung	Right lung	left lung	Standard lung	Standard lung	Right lung	left lung
18	1.44E-03	7.59E-04	3.31E-04	4.72E-04	4.58E-04	2.56E-04	9.22E-05	1.22E-04
60	5.28E-02	2.23E-02	1.28E-02	1.72E-02	8.80E-03	3.56E-03	1.82E-03	2.25E-03
63	5.99E-02	2.59E-02	1.52E-02	2.01E-02	9.50E-03	3.82E-03	2.00E-03	2.48E-03
74	4.73E-02	1.99E-02	1.14E-02	1.53E-02	9.62E-03	3.84E-03	2.03E-03	2.52E-03
93	4.24E-02	1.74E-02	9.98E-03	1.34E-02	9.97E-03	4.06E-03	2.21E-03	2.68E-03
185	3.34E-02	1.41E-02	8.15E-03	1.10E-02	8.55E-03	3.58E-03	2.09E-03	2.54E-03
238	2.71E-02	1.18E-02	7.15E-03	9.42E-03	7.08E-03	3.02E-03	1.83E-03	2.20E-03

4.5   Summary

In this chapter, uncertainties in lung measurement of actinides due to non-uniform distribution of activity in lungs and contribution of activity in other organs are evaluated using thorax voxel phantom. The SF due to non-uniform distribution of activity in lungs is found to be 1.24 and 1.3 at 60 keV due to phoswich and HPGe array respectively. Estimation of skeletal activity using knee and skull voxel phantoms and its contribution in lung measurements is explained. Experimental measurements were carried out using LLNL phantom with ^{241}Am and Nat. U. lung sets for evaluating uncertainty due to counting statistics. SF due to counting statistics is found to increase with decrease in lung activity.

CHAPTER 5

Uncertainties in GI tract activity estimation in case of Ingestion intake

In case of internal contamination due to actinides by ingestion or inhalation pathway, activity will be transferred to various regions of the alimentary [1; 42; 43; 45] or gastrointestinal tract (GIT) over a period. The retained or excreted activity of actinides, which are LEP emitters, can be estimated either by detecting the photons coming from the abdomen region using closely spaced external detectors [19] or by measuring the excreted activity in the feces over a few days after the ingestion intake [1]. Using appropriate retention factors or excretion rates, intake can be estimated. Processing and quantifying the excreted activity is a time consuming process, and hence direct monitoring of the abdomen region by external detectors is often performed to quantify the retained ingested activity ensuring that no external contamination is left over the hands or face of the worker.

Lung monitoring systems are calibrated as a function of chest wall thickness using realistic physical thorax [31] phantoms with activity uniformly distributed in lungs and using lung set for various radionuclides or by using voxel phantoms [36]. Realistic physical phantom to estimate ingested activity is not available at present. In this study, ICRP reference male voxel phantom [36] is used to simulate source in various regions of GIT. HATM [45] given by ICRP is solved to estimate the retained activity in different parts of the GIT as a function of time [48; 74]. Using the solution of HATM, CEs of Phoswich and an array of HPGe detectors are estimated for 0.5 day to 5 days post intake for various photon energies in 18 to 238 keV range describing sources of actinides. The variation in the CEs of both the detection systems is studied and the

methodology is provided for estimation of ingested activity from abdomen measurements. The contribution of source in lungs to the GIT measurements and vice a versa is also studied in case of intake by both inhalation and ingestion pathways. The transfer of activity to GIT in case of inhalation intake and its effect on CEs of detection systems is studied by sampling source in both lungs and GIT. The contribution of source in liver to chest and abdomen measurements is also studied.

5.1   ICRP male voxel phantom and abdomen measurement geometry

The thorax voxel phantom consisting of thorax and abdomen region used in this study is derived from ICRP reference male voxel phantom [36] of in-plane resolution 2.137 mm and slice thickness of 8 mm. It is obtained by cutting the original phantom in X-Z planes and removing the voxels above the skin layer in X-Y plane. This modification was required to position the detectors at ~ 1 cm from the phantom abdomen for simulating the actual geometry of measurement. The same co-ordinate system as of voxel phantom was used for defining detector geometry in FLUKA [25; 26].

In the standard geometry used for lung monitoring of radiation workers to detect inhalation intakes, detector is positioned over the chest such that detector center is on the midline of the phantom and one end of the detector is tangential to the suprasternal notch. To measure ingested activity, the detector center is positioned on the midline of the phantom and one end of the detector is kept tangential to the lowermost rib bone, so that the detector will be over abdomen. From this abdomen geometry, the detector is shifted to extreme right side of the body to measure activity in liver. Figure 5.1 shows HPGe array positioned over the abdomen of voxel phantom as viewed by Flair [28].
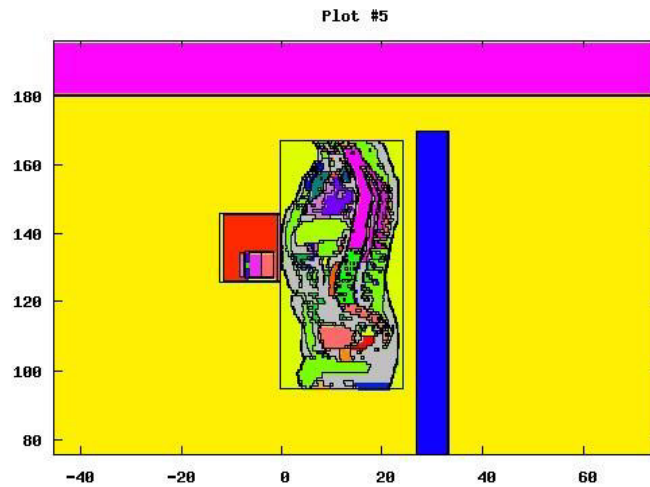
Figure 5.1 HPGe array positioned in abdomen measurement geometry over ICRP male voxel
phantom as viewed by Flair.

5.2   Source sampling according to solution of biokinetic models

5.2.1   Solution of HATM

HATM [45] of ICRP given in figure 1.10 is solved to see the distribution of activity in various

regions of GIT as a function of time after ingestion intake of 1 Bq of type M and S compounds

[1]. Default transfer rates of various compartments of the HATM and systemic biokinetic model

of Plutonium [1] are used and integrated through the transfer compartment 'Blood'. The whole

matrix is solved to give activity in various compartments as a function of time [48; 74]. Figure 5.2

shows the retention in contents of small intestine, right colon, left colon, rectosigmoid colon and

colon as a function of time for type S compounds after ingestion intake of 1 Bq.

136
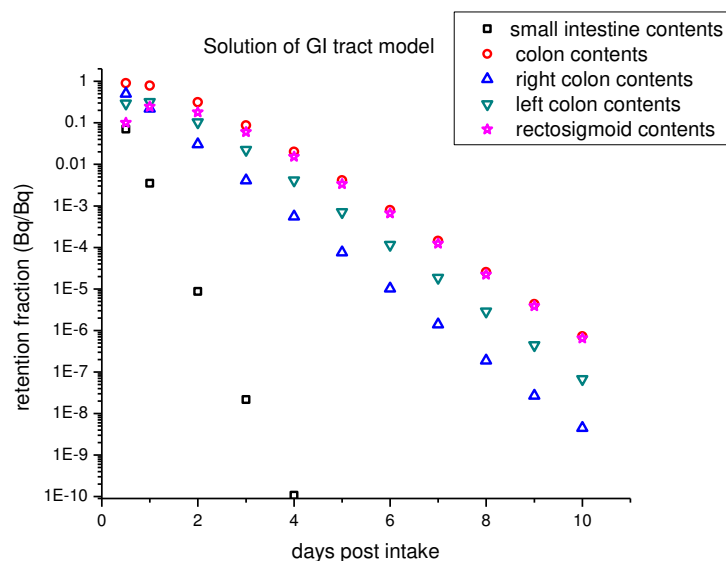
Figure 5.2 Retention in various compartments of alimentary tract as a function of time for type S compounds after ingestion intake of 1 Bq.

Colon activity is the sum of activities in right, left and rectosigmoid colon. It can be seen from figure 5.2 that activity is cleared very fast from small intestine to various regions of colon. From rectosigmoid colon, it is excreted via fecal excretion. After 1 day, all the retained activity in GIT is in various regions of the colon. The retention in various compartments of GIT is found to be similar for type S and M compounds as the rate of absorption from the small intestine to blood is changed from 6E-5 d^{-1} to 3E-4 d^{-1}. As these rates of absorption in small intestine are very small compared to 6 d^{-1}, the rate of removal from small intestine to right colon contents, which is same for both type M and S compounds. Table 5.1 gives activity in various regions of GIT for 0.5 to 5 days post ingestion intake of 1 Bq. There is a reduction by a factor of ~ 256 in GIT retained activity from 1 to 5 days post ingestion intake as the mean residence time in each compartment of colon is 12 hours. For type F compounds, total absorption will occur in small intestine, so these retention values are not applicable.

137

Table 5.1 Distribution of activity (Bq) in various regions of alimentary tract for 1 Bq of ingestion
intake.

Days post intake	Small Intestine	Right colon	Left colon	Recto sigmoid colon	Retained fraction in Alimentary tract Bq Bq^{-1}
0.5	7.04E-02	5.06E-01	2.92E-01	1.01E-01	9.69E-01
1	3.51E-03	2.20E-01	3.16E-01	2.46E-01	7.85E-01
2	8.69E-06	3.04E-02	1.03E-01	1.79E-01	3.13E-01
3	2.16E-08	4.12E-03	2.22E-02	6.04E-02	8.68E-02
4	1.07E-10	5.58E-04	4.12E-03	1.53E-02	2.00E-02
5	5.74E-11	7.55E-05	7.09E-04	3.34E-03	4.12E-03

5.2.2   Solution of HRTM

HRTM in combination with HATM is solved for type M compounds of ^{241}Am and type S compounds of ^{239}Pu. The activities in lungs and various regions of GIT are predicted as a function of time and given in table 5.2. It is observed from table 5.2 that significant fraction of activity goes to GIT till two days after inhalation intake. The fractions present in the various regions of GIT are highest on 0.5 day after intake and decreases with increase in time. The fractions present in lungs and various regions of GIT are slightly different for type M and S compounds. The deviations in the fractions present in the lungs for type M with respect to type S compounds are ~ -10 to -12 % in the span of 0.5 to 5 days. The source particles are sampled in both lungs and GIT using the fractions given in table 5.2 for type M compounds and CEs are estimated. The method is given to predict the CE of both the detectors in case of inhalation of type S compounds.

Table 5.2 Distribution of activity (Bq) in lungs and various regions of alimentary tract for 1 Bq of acute inhalation intake.

Days post intake	Type M compound of ^{241}Am					Type S compound of ^{239}Pu				
	lung	small intestine	right colon	left colon	rectosigmoid	lung	small intestine	right colon	left colon	rectosigmoid
0.5	5.96E-02	3.10E-02	2.01E-01	1.12E-01	3.76E-02	6.63E-02	3.28E-02	2.12E-01	1.18E-01	3.95E-02
1	5.75E-02	2.12E-03	8.99E-02	1.25E-01	9.59E-02	6.41E-02	2.28E-03	9.50E-02	1.32E-01	1.01E-01
2	5.58E-02	1.72E-04	1.32E-02	4.24E-02	7.20E-02	6.25E-02	1.92E-04	1.39E-02	4.48E-02	7.61E-02
3	5.48E-02	1.02E-04	2.08E-03	9.52E-03	2.49E-02	6.18E-02	1.15E-04	2.22E-03	1.01E-02	2.63E-02
4	5.40E-02	9.08E-05	5.24E-04	2.02E-03	6.61E-03	6.11E-02	1.03E-04	5.74E-04	2.16E-03	7.00E-03
5	5.32E-02	8.71E-05	3.00E-04	5.74E-04	1.67E-03	6.05E-02	9.89E-05	3.37E-04	6.27E-04	1.79E-03

5.2.3   Source sampling in the Monte Carlo code FLUKA

To simulate the source in GIT according to the solution of HATM, the voxels of each region are selected as per the activity distribution given in table 5.1. First, the activity distribution is normalized and cumulative distribution is calculated. Using the cumulative distribution and inversion technique [58], the voxel is randomly selected from known voxels of the contents of small intestine, right colon, left colon and recto sigmoid colon. Then a point is randomly selected in that voxel. The isotropic directional distribution of emitted photons is sampled from a uniform distribution of the azimuthal angle and the cosine of the polar angle. Seven photon energies of 18, 60, 63, 74, 93, 185 and 238 keV are simulated for the photons emitted from ^{239}Pu, ^{241}Am, ^{238}U, ^{235}U and ^{212}Pb. Similar scheme is used for sampling source in liver, lungs and in both lungs and various regions of GIT using activity distribution given in table

139

5.2. The counts photon^{-1} in the various energy regions are determined for 2 x 10^6 histories run over 5 cycles so that REs in the CEs are less than 3 %.

5.3   CEs of Phoswich and HPGe array over abdomen geometry for source in GIT of voxel phantom

Tables 5.3 and 5.4 show the CEs of Phoswich and HPGe array evaluated for source in various regions of GIT of voxel phantom for 18 to 238 keV photons for 0.5 to 5 days post ingestion intake and for detector over the abdomen region. From tables 5.3 and 5.4, it is found that CEs are lowest at 18 keV for both the detectors due to maximum attenuation of photons within the phantom. Above 18 keV, as energy increases, there is an increase in the transmitted photons leading to an increase in the CEs. Above 63 and 93 keV, CEs are found to decrease with energy for Phoswich and HPGe array respectively as transmitted photons of high energy are not able to deposit their full energy in the active volume of detectors due to the limiting thickness of the detectors. CEs of Phoswich detector are higher than CEs using HPGe array by a factor of ~ seven. This is due to the higher active area of phoswich detector (314 cm^2 compared to 115.4 cm^2 of HPGe array) viewing the abdomen region.   Higher CEs are obtained using both the detectors on half day after ingestion intake. Afterwards, CEs are found to decrease with increase in post intake days. For Phoswich detector, the CEs obtained on 1 to 5 days post ingestion intake are found to be reduced by ~ 16 %, 43 %, 57 %, 65 % and 70 % respectively with respect to CEs obtained on 0.5 day for all the energies. For HPGe array, the CEs obtained on 1 to 5 days post ingestion intake are found to be reduced by ~ 20 %, 50 %, 60 %, 70 % and 75 % respectively with respect to CEs obtained on 0.5 day for all the energies. Thus, there is need to use the CE according to the days post intake, otherwise an error in the range of -16 to -75 % will be introduced in the evaluated ingested activity.

140

Table 5.3 Counting efficiencies in counts photon^{-1} of Phoswich detector in abdomen measurement geometry for source in alimentary tract.

Energy keV	Days post intake					
	0.5	1	2	3	4	5
18	1.60E-03	1.38E-03	9.15E-04	6.71E-04	5.19E-04	4.35E-04
60	8.14E-02	6.79E-02	4.61E-02	3.50E-02	2.88E-02	2.50E-02
63	9.38E-02	7.83E-02	5.29E-02	4.03E-02	3.33E-02	2.90E-02
74	7.01E-02	5.85E-02	3.98E-02	3.03E-02	2.49E-02	2.16E-02
93	6.13E-02	5.11E-02	3.45E-02	2.65E-02	2.18E-02	1.87E-02
185	4.92E-02	4.13E-02	2.80E-02	2.15E-02	1.79E-02	1.55E-02

Table 5.4 Counting efficiencies (counts photon^{-1}) of HPGe array in abdomen measurement geometry for source in alimentary tract.

Energy keV	Days post intake					
	0.5	1	2	3	4	5
18	5.43E-04	4.61E-04	3.01E-04	2.11E-04	1.66E-04	1.35E-04
60	1.14E-02	9.21E-03	5.83E-03	4.26E-03	3.37E-03	2.78E-03
63	1.24E-02	1.00E-02	6.39E-03	4.63E-03	3.63E-03	3.00E-03
74	1.25E-02	1.01E-02	6.41E-03	4.64E-03	3.65E-03	3.04E-03
93	1.31E-02	1.05E-02	6.70E-03	4.87E-03	3.85E-03	3.21E-03
185	1.16E-02	9.39E-03	5.99E-03	4.45E-03	3.59E-03	3.02E-03

5.4   Mixed exposure scenario: Inhalation and Ingestion intake

In case of mixed exposure by both inhalation and ingestion pathway, it is required to estimate inhaled and ingested activity separately to estimate the committed effective dose. As both can influence each other, estimation of inhaled and ingested activity is difficult. The follow up monitoring of a worker is required. Apart from follow up of a worker by direct abdomen and chest measurements, there is a need to estimate fecal activity as ~ 40 % and 98 % of activity is excreted in feces for inhalation and ingestion intakes respectively. In this study, the aim is to

estimate ingested activity by direct measurement. Thus, importance is given to the evaluation of CEs in case of ingestion intake and to reduce the uncertainties in its assessment. Therefore, contributions of source in lungs and liver in abdomen measurements are studied. The contribution of source in GIT to lung measurements is also studied to estimate its effect on lung measurements.

5.4.1 Contribution of lung activity on GIT measurements in case of absence of activity in GIT

The contribution of lung activity in GIT measurements in absence of activity in later is evaluated for uniform source distribution in lungs and given in table 5.5 for Phoswich and HPGe array over abdomen. Contribution is found to be least for 18 keV and increases with energy till 63 keV for Phoswich and 185 keV for HPGe array and thereafter decreases with increase in energy. The contribution factors given in counts photon^{-1} will have to be converted into counts second^{-1} Bq^{-1} (cps Bq^{-1}) for estimating the contribution of lung activity in GIT measurements for each radionuclide using yield given in table 5.5.

5.4.2 Contribution of lung activity on GIT measurements considering transfer of activity from respiratory tract to GIT in case of inhalation intake

Considering the fractions given in table 5.2 for inhalation intake, source is sampled in both lungs and various regions of GIT. CEs of Phoswich and HPGe array detectors are then estimated by positioning them over chest and abdomen region and given in Table 5.6 and 5.7 respectively.

From table 5.6, for Phoswich detector over abdomen, CEs obtained on 1 to 5 days post intake are found to be reduced by ~ 20 %, 55 %, 75 %, 83 % and 85 % respectively with respect to CEs obtained on 0.5 day for all the energies. When these CEs are compared to the CEs due to

ingestion intake given in table 5.3 with Phoswich detector positioned over abdomen, they are lower by 10 %, 15 %, 30 %, 47 % and 60 % respectively on 0.5 to 5 days post intake.

Table 5.5 Contribution of lung activity in abdomen measurements using Phoswich and HPGe array detectors in counts photon^{-1}.

Energy	Radionuclide	Yield	counts photon^{-1}	
keV		%	Phoswich	HPGe array
18	Pu-239	2.15	3.35E-05	1.82E-05
60	Am-241	35.78	7.34E-03	1.11E-03
63	Th-234	3.8	9.07E-03	1.24E-03
74	Pb-212	10.65	6.81E-03	1.32E-03
93	Th-234	5.41	5.98E-03	1.47E-03
185	U-235	54.0	5.27E-03	1.66E-03
238	Pb-212	44.63	4.81E-03	1.50E-03

Table 5.6 Counting efficiencies (counts photon-1) of Phoswich detector for source sampled in both lungs and various compartments of alimentary tract for 1 Bq of inhalation intake.

Energy keV/ day	Phoswich detector over chest (counts photon^{-1})						Phoswich detector over abdomen (counts photon^{-1})					
	0.5	1	2	3	4	5	0.5	1	2	3	4	5
18	2.07E-04	2.42E-04	4.32E-04	8.61E-04	1.26E-03	1.41E-03	1.42E-03	1.15E-03	6.42E-04	2.74E-04	1.37E-04	1.01E-04
60	1.26E-02	1.27E-02	1.86E-02	3.27E-02	4.53E-02	5.03E-02	7.25E-02	5.76E-02	3.27E-02	1.83E-02	1.16E-02	9.66E-03
63	1.50E-02	1.50E-02	2.14E-02	3.72E-02	5.12E-02	5.68E-02	8.35E-02	6.62E-02	3.79E-02	2.14E-02	1.40E-02	1.18E-02
74	1.12E-02	1.12E-02	1.66E-02	2.93E-02	4.07E-02	4.52E-02	6.29E-02	4.99E-02	2.86E-02	1.61E-02	1.05E-02	8.88E-03
93	9.82E-03	9.84E-03	1.46E-02	2.61E-02	3.63E-02	4.03E-02	5.48E-02	4.32E-02	2.46E-02	1.40E-02	9.17E-03	7.86E-03
185	8.01E-03	8.15E-03	1.19E-02	2.05E-02	2.87E-02	3.15E-02	4.43E-02	3.47E-02	2.01E-02	1.17E-02	7.87E-03	6.87E-03
238	7.14E-03	7.16E-03	9.94E-03	1.69E-02	2.33E-02	2.60E-02	3.68E-02	2.95E-02	1.72E-02	1.02E-02	6.97E-03	6.23E-03

Similar trend is also observed with HPGe array. For both the detectors over chest and for source in both lungs and GIT, CEs increases with days post inhalation intake. This is because initially, higher activity is transferred to GIT, which reduces with time. It is mainly lung activity contributing to chest measurement on the 5th day onwards after inhalation intake.

Table 5.7 Counting efficiencies (counts photon-1) of HPGe array for source sampled in both lungs and various compartments of alimentary tract for 1 Bq of inhalation intake.

Energy keV/ day	HPGe array over chest (counts photon^{-1})						HPGe array over abdomen (counts photon^{-1})					
	0.5	1	2	3	4	5	0.5	1	2	3	4	5
18	6.41E-05	7.62E-05	1.47E-04	2.85E-04	4.14E-04	4.65E-04	4.76E-04	3.98E-04	2.16E-04	9.40E-05	4.48E-05	2.63E-05
60	1.53E-03	1.66E-03	2.85E-03	5.42E-03	7.64E-03	8.53E-03	1.00E-02	8.06E-03	4.50E-03	2.42E-03	1.55E-03	1.29E-03
63	1.68E-03	1.83E-03	3.14E-03	5.87E-03	8.26E-03	9.21E-03	1.09E-02	8.72E-03	4.92E-03	2.69E-03	1.74E-03	1.48E-03
74	1.73E-03	1.84E-03	3.15E-03	5.84E-03	8.34E-03	9.30E-03	1.10E-02	8.80E-03	4.99E-03	2.73E-03	1.80E-03	1.54E-03
93	1.85E-03	1.97E-03	3.31E-03	6.15E-03	8.63E-03	9.62E-03	1.15E-02	9.21E-03	5.20E-03	2.97E-03	1.95E-03	1.71E-03
185	1.88E-03	1.94E-03	2.95E-03	5.33E-03	7.42E-03	8.20E-03	1.02E-02	8.21E-03	4.79E-03	2.88E-03	2.05E-03	1.84E-03
238	1.65E-03	1.70E-03	2.50E-03	4.44E-03	6.13E-03	6.86E-03	8.66E-03	6.99E-03	4.08E-03	2.50E-03	1.85E-03	1.65E-03

The CEs for source distributed in both lungs and GIT can be obtained using the fractions given in table 5.2 and CEs for source in GIT given in tables 5.3, 5.4 and contribution of lung activity in GIT measurements given in table 5.5 for detector over abdomen. For example, to estimate the CE of Phoswich detector on day 1 due to inhalation intake and for detector over abdomen, the CE due to activity only in GIT is 6.79E-2 counts photon^{-1} from table 5.3, contribution of lung activity in GIT measurements is 7.34E-3 counts photon^{-1} from table 5.5. From table 5.2, the fraction present in the lungs is 5.75E-2 that is 0.1548 after normalizing with

total activity in lungs and GIT. The remaining fraction in GIT will be 0.8452. Using these weighting fractions, the CE on day 1 will be 5.85E-2 counts photon^{-1}, which is ~ 1.5 % deviated from the simulated value of 5.76E-2 counts photon^{-1} given in table 5.6. The slight deviation is the result of applying weighting fraction to whole GIT instead of individual components of GIT. Using this method, the CE is 5.8E-2 counts photon^{-1} for type S compounds for Phoswich detector over abdomen. It is found to be similar to type M compounds, as the activity present in the lungs was higher by 10 to 12 % for type S compounds compared to type M compounds.

5.4.3 Contribution of liver activity in chest and abdomen measurements

The activity in the liver could make significant contribution to detector placed both over chest and abdomen. Simulations were carried out to estimate the CE of both the detectors positioned over liver, chest and abdomen, by sampling source uniformly in liver and given in table 5.8. At 18 keV, least contribution of 18 % and 11 % is observed in lungs with Phoswich and HPGe array. At and above 60 keV, contribution in the lung is ~ 50 % and 30 % of the CE observed by keeping detector over liver using Phoswich and HPGe array respectively. The contribution in abdomen measurements is found to be ~ 75 % using both the detectors as they are kept on the center and at extreme right for measuring GIT and liver activity respectively. As liver contamination is possible only in old exposure cases, it is required that the liver activity be known from the previous measurements, so its influence in both chest and abdomen measurements can be evaluated using the CEs given in table 5.8.

5.4.4 Contribution of GIT activity in lung measurements in the absence of activity in lungs

The contribution of GIT activity in lung measurements is given in tables 5.9 and 5.10 for Phoswich and HPGe array positioned over chest of the voxel phantom in standard lung

measurement geometry, for no activity in lungs and for uniform source distribution in lungs respectively. On comparing these CEs with the CEs obtained by simulating source in GIT, it is found that highest contribution in lung measurements is observed on 0.5 day after ingestion intake and thereafter it reduces with time. CEs are not given for 18 keV, as RE is more than 5 %. Using Phoswich detector, contribution of ~ 10 % is observed in lung measurements 1 day post intake, which reduces to ~ 4 % on fifth day post intake for all the energies. Using HPGe array, on 0.5 day post ingestion intake, contribution in lung measurements is less than 5 % below 100 keV and ~ 10 % above 100 keV. On the third day post intake, contribution reduces to ~ 2 % below 100 keV and ~ 5 % above 100 keV.

Table 5.8 CEs (counts photon^{-1}) of Phoswich and HPGe array for source sampled in liver and detectors over liver, chest and abdomen.

Energy keV	Phoswich detector			HPGe array		
	liver	chest	abdomen	liver	chest	abdomen
18	1.36E-03	2.44E-04	1.08E-03	5.43E-04	6.09E-05	4.72E-04
60	7.13E-02	3.37E-02	5.45E-02	1.24E-02	3.99E-03	9.29E-03
63	8.27E-02	4.01E-02	6.36E-02	1.34E-02	4.49E-03	1.01E-02
74	6.33E-02	2.94E-02	4.81E-02	1.36E-02	4.55E-03	1.03E-02
93	5.56E-02	2.53E-02	4.20E-02	1.42E-02	4.95E-03	1.08E-02
185	4.53E-02	2.11E-02	3.41E-02	1.23E-02	4.81E-03	9.46E-03
238	3.78E-02	1.82E-02	2.90E-02	1.04E-02	4.24E-03	7.99E-03

5.5   MDA of Phoswich and HPGe array for estimation of abdominal activity

Due to lower background of HPGe array and better resolution with full width at half maximum of 0.6 keV compared to 12 keV of Phoswich detector at 60 keV, the identification and quantification of LEP emitters is possible even in the presence of other radionuclides. The MDA [22] values are estimated for Phoswich and HPGe array for 30 minutes of counting time using CE at 0.5 day and given in table 5.11. Detector background of an uncontaminated adult

person in abdomen measurement geometry in a whole body counter situated in totally shielded steel room is used for this purpose. As CEs decrease, MDAs will increase with post ingestion intake days.

Table 5.9 CEs in counts photon^{-1} of Phoswich detector in lung measurement geometry.

Energy keV/ Day post intake	Contribution of source in alimentary tract in lung measurements (counts photon^{-1})						CE (counts photon^{-1}) for source in lungs and detector over chest
	0.5	1	2	3	4	5	
18*	--	--	--	--	--	--	1.44E-03
60	6.25E-03	5.23E-03	3.58E-03	2.61E-03	2.03E-03	1.72E-03	5.26E-02
63	8.01E-03	6.85E-03	4.56E-03	3.36E-03	2.71E-03	2.20E-03	5.99E-02
74	5.59E-03	4.63E-03	3.16E-03	2.32E-03	1.81E-03	1.49E-03	4.75E-02
93	4.60E-03	3.92E-03	2.60E-03	1.91E-03	1.49E-03	1.25E-03	4.22E-02
185	4.08E-03	3.53E-03	2.33E-03	1.72E-03	1.40E-03	1.20E-03	3.34E-02
238	4.04E-03	3.38E-03	2.34E-03	1.73E-03	1.42E-03	1.17E-03	2.74E-02

Table 5.10 CEs in counts photon^{-1} of HPGe array in lung measurement geometry for source in alimentary tract.

Energy keV/ Day post intake	Contribution of source in alimentary tract in lung measurements (counts photon^{-1})						CE (counts photon^{-1}) for source in lungs and detector over chest
	0.5	1	2	3	4	5	
18*	--	--	--	--	--	--	4.72E-04
60	3.57E-04	3.14E-04	2.14E-04	1.59E-04	1.24E-04	1.03E-04	8.91E-03
63	4.39E-04	3.82E-04	2.51E-04	1.89E-04	1.46E-04	1.21E-04	9.63E-03
74	4.57E-04	3.95E-04	2.73E-04	1.96E-04	1.58E-04	1.32E-04	9.74E-03
93	5.65E-04	4.80E-04	3.21E-04	2.37E-04	1.90E-04	1.61E-04	1.01E-02
185	8.21E-04	7.10E-04	4.76E-04	3.54E-04	2.82E-04	2.37E-04	8.66E-03
238	7.99E-04	6.87E-04	4.71E-04	3.65E-04	2.88E-04	2.43E-04	7.13E-03

*Values are not given for 18 keV as relative error is more than 5 %.

Using HPGe array, MDA of ~ 4 Bq is obtained at 60 keV of ^{241}Am, 185 keV of ^{235}U, 74 and 238 keV of ^{212}Pb where photons are having considerable yield. At 63 and 93 keV of ^{234}Th, MDAs are found to be ~ 39 and 23 Bq, respectively. Highest MDA of ~ 1685 Bq is found at

17.2 keV of ^{239}Pu due to low yield and higher attenuation of these LEPs. Dose at the MDA can be obtained by first estimating the intake from the retention fractions in GIT given in table 5.1 and finally using dose coefficients for a particular radionuclide [1].

Table 5.11 MDAs of Phoswich and HPGe array at 0.5 day post ingestion intake along with the energies and yields of various radionuclides and region of interests.

Radionuclide	Energy keV	Phoswich		HPGe array	
		Region of interest	MDA (Bq)	Region of interest	MDA (Bq)
Pu-239	17.2	12 - 25	1800.0	16.5 - 18	1685.0
Am-241	59.5	43 - 76	4.3	59.2 - 60.8	3.7
Th-234*	63.3	40 - 120	12.9	62.2 - 63.8	38.9
Pb-212	74.8	60 - 88	5.2	73.2 - 75.6	3.7
Th-234*	93.2	40 - 120	12.9	92.2 - 93.8	23.1
U-235	185.7	165 - 215	4.0	184.0- 186.7	2.6

*63 keV and 93 keV energies are not distinguishable in Phoswich detector and leads to MDA of 12.9 Bq due to uncontaminated subject background counts in 40 -120 keV region.

5.6 Exemplification: Estimation of ingested activity of ^{241}Am from abdomen measurement

CEs estimated for Phoswich and HPGe array in counts photon^{-1} at a particular energy have to be converted into cps Bq^{-1} using its emission probability to estimate the activity due to radionuclide present in the GIT. Table 5.5 gives the energies and intensities of the photons of various radionuclides [17] considered in this paper. A worker with contamination due to ingestion pathway needs to be monitored in abdomen measurement geometry. From the measured net count rate and using the CE corresponding to post intake days in cps Bq^{-1}, activity present in GIT can be estimated.

In case of mixed inhalation and ingestion intake, follow up monitoring of the worker is required to estimate both lung and GIT activity accurately. After five days of ingestion intake,

lung activity could be estimated as all the GIT activity will be excreted (Some fraction will be absorbed in blood [1] depending upon the type of inhaled or ingested material). From the measured lung activity, its contribution in abdomen measurements and thus net GIT activity due to ingestion intake can be evaluated.

In this study, default particle size of 5 µm AMAD as well as default transfer rates given in the HRTM and HATM are used for solving the models. The fraction of inhaled activity transferred to GIT increases with the size of the inhaled particles [90]. The CEs evaluated from the present study could be used to estimate the activity in GIT irrespective of the size of inhaled particles and will be helpful in estimating the particle size from the GIT and lung activity measurements. It is possible that in reality, there may be inter and intra-individual variation [3] in the transfer rates, mainly in the various compartments of the HATM.

5.7 Summary

In this chapter, based on the activity distribution in the GI tract, CEs of Phoswich and HPGe array detectors are estimated for photon energies from 18 to 238 keV. Higher CEs are obtained on 0.5 day when source is in small intestine and colon regions. Thereafter, CEs decrease with days post intake. It is found that to estimate ingested activity by direct measurements, CEs based on true activity distribution as per the solution of HATM should be used; otherwise an error of ~ -16 to -75 % will occur in the assessed ingested activity. Contribution of GI tract activity is found to be ~ 10 % in lung measurements one day after ingestion intake and found to decrease with days post intake. The influence of liver activity on chest and abdomen measurements is found to be ~ 30 to 50 % and ~ 75 % respectively using both the detectors.

CHAPTER 6

Uncertainties in wound activity estimation in case of intake by wound pathway

Although, inhalation is a major route of intake at workplaces where actinides are handled [1], there is a potential hazard of injury while working with sharp tools inside the glove boxes. If the sharp tool edges are contaminated with radionuclides, this could lead to the activity being injected in the wound. National Council on Radiation Protection and Measurements (NCRP) in its publication 156 [20] observed that more than 90 % of the wounds have occurred on arms and hands, mainly on fingers of radiation workers with puncture wounds being the majority. The wound site is characterized by five compartments [20] viz. (a) fragments, (b) soluble, (c) colloid and intermediate state, (d) particles, aggregates and bound state (PABS) and (e) trapped particles and aggregates depending upon the physical and chemical properties of the material and two additional compartments of blood and lymph nodes for transfer of material from wound site. Soluble category is further divided into weak, moderate, strong and avid depending upon the rate of absorption of activity from wound to blood. Insoluble Uranium and transuranium (e.g. Am, Pu) compounds mainly follow either PABS or fragment categories and if of soluble type, these compounds can mainly follow the characteristics of strong or avid categories [20]. In majority of the cases of internal contamination by wound, activity is removed by surgical excision of the tissue. The activity, which could not be removed after excision from the wound site, is retained tenaciously for insoluble compounds of PABS and fragment categories and is encapsulated in tissue with time [20; 91; 92]. Such activity remaining at the wound site before or after excision is known as localised or embedded activity [20; 93].

150

The embedded and injected activity can be detected, quantified and mapped by using special wound monitors viz. PIN diode [94], miniature NaI (Tl) [95] or HPGe detectors [96; 97]. There are reported studies of using photon detectors incorporated in lung monitoring system as well as miniature photon detectors for estimation of embedded activity in the fingers [96; 98; 99]. These detectors are usually calibrated for point source embedded in tissue equivalent materials such as Polymethyl methacrylate (PMMA), Polyurethane etc [20; 96; 98; 99] of variable thicknesses. Most of these studies involved experimental [96; 98; 99], analytical [100] and Monte Carlo [101; 102] methods to estimate ^{241}Am activity in finger or slab phantom by assuming a point source in tissue equivalent medium for different detection systems. There are no reported studies on evaluation of CEs of lung monitoring system for wound occurred on palm due to mixture of Pu and ^{241}Am activity and the effect of using PMMA as palm tissue simulant. Therefore, a study was planned to derive CEs for lung monitoring system incorporating HPGe array (each of 7 cm diameter and 2.5 cm thick) due to wound contamination of ^{241}Am.

In this study, a methodology to estimate an embedded ^{241}Am activity in soft tissue and its depth is evaluated by simulating ^{241}Am source at different depths in a palm phantom using the Monte Carlo code FLUKA [25; 26] for HPGe array. CEs at various depths of soft tissue for ^{241}Am are estimated for this purpose. The effect of source size at a particular depth on CEs has been studied. Study is also carried out to estimate the errors due to use of PMMA as a tissue equivalent material for calibration of wound monitoring system. Finally, possible use of different relative intensities of low energy photons of ^{241}Am escaping from the wound for estimation of depth and activity, in case of pure ^{241}Am and mixture of Pu and ^{241}Am is demonstrated. REs in the estimation of ^{239}Pu from ^{241}Am measurements are evaluated. Experimental measurements using phoswich detector and palm phantom was carried out and CEs

are provided as a function of depth. Due to poor resolution of phoswich detector, lower energies of ^{241}Am will appear as a single peak in 12- 25 keV region. Therefore, it could not be used to estimate depth of activity. Therefore, methodology to estimate an embedded ^{241}Am activity in soft tissue and its depth, is provided for HPGe array.

6.1   Detection Systems and phantom setup

HPGe array used for estimating CEs for wound is described in section 1.2.2. The schematic diagrams of HPGe array with all the three detectors in transverse plane and a single detector in vertical plane are given in figure 1.3 in section 1.2.2. These details of the experimental detection system are geometrically configured and simulated in FLUKA code. A phantom of dimension 10 cm x 10 cm x 4 cm is designed to approximate the palm of a hand for theoretical evaluation of CEs due to embedded activity. Source is simulated at the center of this slab at 2 mm depth and the phantom is kept at 10 cm distance from the PMMA window of HPGe array such that the phantom center matches with the HPGe array enclosure center.

This geometry is chosen to minimize the errors due to positioning a palm below a 20 cm diameter HPGe array. Tissue layers of thicknesses varying from 1 mm to 30 mm are simulated to consider different depths of embedded activity from the outermost soft tissue layer. Figure 6.1 shows the palm phantom below HPGe array as configured in FLAIR [28].

6.2   Source sampling in the Monte Carlo code FLUKA

There is a possibility of embedded activity being distributed over an area, and hence simulations are carried out for a source uniformly distributed in circles of 5, 10, 15 mm diameters and also for a point source. For these circular areas, source is simulated by random selection of points at a particular depth and of a particular radius by the inversion technique. The isotropic directional distribution of emitted photons is sampled from a uniform distribution of the

cosine of the polar angle and a uniform distribution of the azimuthal angle. Photons of different

energies (13.9, 17.8, 20.82, 26.3 and 59.5 keV) are sampled randomly as per their relative yields.

Table 6.1 gives the energies and yields of the photons of ^{241}Am [103].
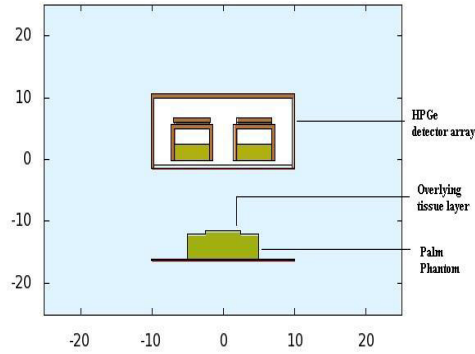
Figure 6.1 Geometrical representation of palm phantom below HPGe detectors array, taken with

FLAIR.

Simulations are carried out using the ICRP soft tissue [69] and PMMA material for the

phantom and overlay slabs. 'Detect' card of FLUKA is used for scoring energy deposition in the

HPGe array. Outputs from all the three detectors are summed to obtain the final response of

HPGe array. The counts per photon in the various energy regions are determined for 2 x 10^7

histories run over 10 cycles to reduce the RE in the CEs to less than 1% for various energies,

depths and source diameters.

6.3 Variation in CEs, Ratio1 and Ratio2 values with depth

The data generated in the simulations are used to obtain CEs of HPGe array for the

estimation of embedded ^{241}Am activity. The ratio of counts in 59.5 keV to 17.8 keV energy

regions is defined as Ratio1 and the ratio of counts in 59.5 keV to 26.3 keV energy regions as

Ratio2. Figure 6.2 shows CEs of HPGe array for 59.5, 26.3 and 17.8 keV photon energies of ^{241}Am point source due to different overlying soft tissue thicknesses.

Table 6.1 Energies of photon emissions and yields considered for simulation of ^{241}Am source, taken from IAEA publication.

Energy keV	Yield
13.9	0.1303
17.81	0.1886
20.82	0.0481
26.3	0.024
59.5	0.3578
13.9	0.1303
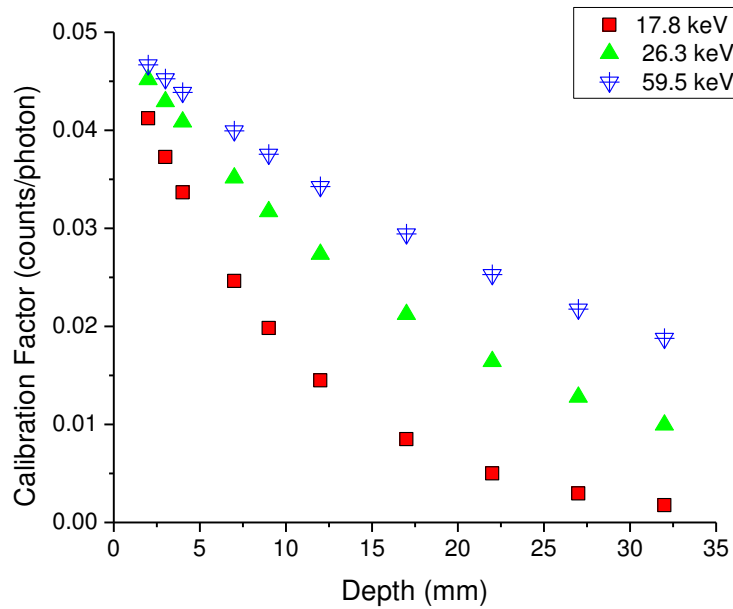
Figure 6.2 CEs of HPGe detectors array for 17.8, 26.3 and 59.5 keV photons from 241Am at different depths of soft tissue.

It is observed from figure 6.2 that CEs are decreasing with increase in the depth of embedded activity and decrease in the initial photon energy. Figure 6.3 shows the variation in

154

Ratio1 and Ratio2 for different thicknesses of soft tissue overlying [241]Am point source. As can be observed from Figure 6.3, Ratio1 and Ratio2 values increase with increase in depth. The decrease in interaction cross section with increase in energy leads to higher CEs at 59.5 keV compared to 26.3 and 17.8 keV. Due to lowest yield of 26.3 keV photons, higher values of Ratio2 are observed compared to Ratio1 at a particular depth. The decrease in the transmitted photons with increase in the depth leads to decrease in CEs with increase in depth at a particular energy. The combined effect of variation of interaction cross section with energy and decrease in transmitted photons with depth leads to the lowest values of CEs at 17.8 keV at all the depths and increase in Ratio1 and Ratio2 with increase in depth.
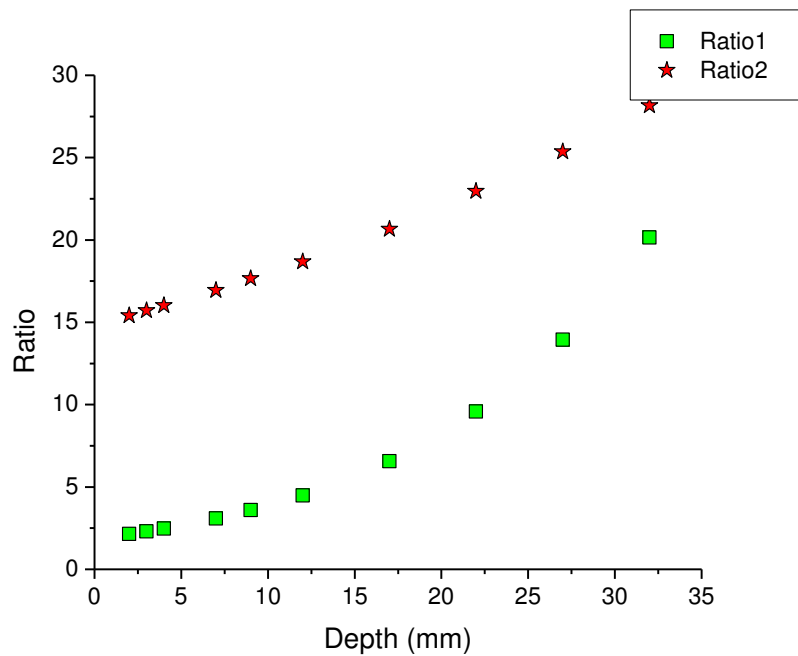
Figure 6.3 Ratio of counts in 59.5 keV and 17.8 keV energy regions as Ratio1 and Ratio of counts in 59.5 keV and 26.3 keV energy regions as Ratio2, of 241Am as a function of depth for HPGe array.

The CEs at 59.5, 26.3 and 17.8 keV photon energies shown in Figure 6.2 and Ratio1, Ratio2 values shown in Figure 6.3 are fitted with an exponential function with respect to depth. The equations obtained are of the form a * exp (b * x), where 'x' is a depth in mm. The parameters 'a' and 'b' of all the fitted equations along with their relative errors are given in Table 6.2. The correlation coefficients are found to be greater than 0.9998 for all the fitted equations. Using the equation parameters given in Table 6.2, CEs as well as Ratio1 and Ratio2 can be calculated for any intermediate depth.

Table 6.2 Equation parameters for CEs (counts photon^{-1}) and ratios fitted with respect to depth 'x' (mm) for ^{241}Am in the form of y = a* exp (b * x) along with the RE.

Equation para-meters	Equation parameters for CEs						Equation parameters for ratios			
	59.5 keV		26.3 keV		17.6 keV		Ratio1		Ratio2	
	Values	RE %	Values	RE %	Values	RE %	Values	RE %	Values	RE %
a	4.95 E-2	0.09	5.00E-02	0.06	5.09E-02	0.21	1.84E+00	0.44	1.47E+01	0.17
b	-3.05E-2	0.27	-5.04E-02	0.13	-1.05E-01	0.35	7.48E-02	0.21	2.01E-02	0.42

6.4 Effect of error in Ratio1 and Ratio2 on depth

To estimate the effect of errors in the Ratio1 and Ratio2 on depth, ± 5 % to ± 20 % error is introduced in the Ratio1 and Ratio2. The depths are calculated for the modified ratios and given in Table 6.3. It is observed from Table 6.3 that ±10 % error in the Ratio1 results in the deviation of ±15 % in depth when activity is at 10 mm depth. It reduces to about ±5 % at 20 mm depth due to increase in depth and increases to ±50 % as depth reduces to 5 mm. In the case of ±10 % error in the Ratio2, deviation about ±50 % is observed when the actual depth is 10 mm. The estimated deviations in depth evaluations are always higher for Ratio2 than the

corresponding Ratio1 results because of relatively lower yield of 26.3 keV photons of ^{241}Am. Thus, Ratio1 should be used to evaluate depth of embedded activity in case of contamination due to pure ^{241}Am. For an error of ±1mm in depth, deviation in the estimation of activity is about ±3 % which increases to about ±10 % for an error of ±3 mm in depth, at all depths.

Table 6.3 Variation in depth estimation of ^{241}Am due to error in Ratio1 and Ratio2.

Error	Predicted depths due to error in Ratio1 and Ratio2							
%	Actual depth = 5mm		Actual depth = 10 mm		Actual depth = 15 mm		Actual depth = 20 mm	
	Ratio1	Ratio2	Ratio1	Ratio2	Ratio1	Ratio2	Ratio1	Ratio2
5	4.28	2.44	9.32	7.50	14.31	12.44	19.32	17.44
10	3.56	--	8.59	4.81	13.58	9.75	18.60	14.75
15	2.80	--	7.83	1.96	12.82	6.90	17.83	11.90
20	1.98	--	7.02	--	12.01	3.89	17.02	8.89
-5	5.62	7.42	10.65	12.48	15.65	17.42	20.66	22.42
-10	6.24	9.73	11.28	14.79	16.27	19.74	21.28	24.74
-15	6.84	11.95	11.87	17.01	16.86	21.95	21.88	26.95

However, in the case of mixed contamination due to Pu isotopes and ^{241}Am, Ratio2 values should be used for depth estimation, as counts in 17.8 keV region, are due to both Uranium L X-rays from Pu isotopes (17.5 keV) and Neptunium L X-rays (17.8 keV) of ^{241}Am.

6.5   Variation in CEs, Ratio1 and Ratio2 values with variable diameter source

Source size is modified from a point source to planar circular source of diameters 5, 10 and 15 mm to see its influence on CEs and ratios. No change is observed in the evaluated CEs for 59.5 keV when source size is modified as shown in Table 6.4. Similar results are obtained for CEs at 26.3 keV and 17.8 keV of ^{241}Am as well as for Ratio1 and Ratio2. This is due to the large size of the HPGe array that makes the distribution of source up to 15 mm diameter appear to be a point source at 10 cm distance from the HPGe array.

Table 6.4 CEs (counts. photon^{-1}) of HPGe array at 59.5 keV for different diameter sources of ^{241}Am.

Depth mm	point source	5 mm diameter	10 mm diameter	15 mm diameter
2	4.667E-02	4.665E-02	4.664E-02	4.664E-02
3	4.526E-02	4.521E-02	4.519E-02	4.518E-02
4	4.387E-02	4.381E-02	4.380E-02	4.378E-02
7	3.994E-02	3.993E-02	3.991E-02	3.988E-02
9	3.756E-02	3.755E-02	3.753E-02	3.751E-02
12	3.425E-02	3.423E-02	3.422E-02	3.420E-02
17	2.942E-02	2.941E-02	2.942E-02	2.939E-02
22	2.530E-02	2.528E-02	2.527E-02	2.524E-02
27	2.177E-02	2.176E-02	2.176E-02	2.173E-02
32	1.877E-02	1.876E-02	1.875E-02	1.873E-02

6.6 Variation in CEs, Ratio1 and Ratio2 values estimated using soft tissue and PMMA material

Table 6.5 gives CEs at 17.8, 26.3 and 59.5 keV when the phantom and overlay materials are chosen as PMMA and as soft tissue and deviations in CEs estimated using PMMA with respect to soft tissue material. The deviations in CEs at 59.5 keV are less than 3 % up to a depth of about 1.2 cm, which increases to about 8 % at 3 cm depth. The CEs show deviations of about -2 % to -12 % and -7 % to -70 % for 26.3 keV and 17.8 keV respectively for depths in the range of 0.2 – 3 cm.

Table 6.5 CEs of HPGe array at 17.8, 26.3 and 59.5 keV of ^{241}Am using PMMA and soft tissue

material in the phantom setup and deviations in the CEs.

Depth mm	CE at 17.8 keV Count photon^{-1}		Dev. %	CE at 26.3 keV Count photon^{-1}		Dev. %	CE at 59.5 keV Count photon^{-1}		Dev %
	PMMA	Soft tissue		PMMA	Soft tissue		PMMA	Soft tissue	
2	4.41E-02	4.14E-02	-6.6	4.45E-02	4.36E-02	-2.2	4.66E-02	4.67E-02	0.1
3	4.06E-02	3.73E-02	-8.8	4.24E-02	4.17E-02	-1.7	4.51E-02	4.53E-02	0.4
4	3.73E-02	3.37E-02	-10.6	3.99E-02	3.91E-02	-2.1	4.36E-02	4.38E-02	0.5
7	2.86E-02	2.47E-02	-15.6	3.41E-02	3.38E-02	-0.7	3.94E-02	4.01E-02	1.7
9	2.39E-02	1.98E-02	-20.5	3.08E-02	3.00E-02	-2.8	3.69E-02	3.76E-02	2.0
12	1.82E-02	1.44E-02	-26.7	2.63E-02	2.51E-02	-4.9	3.34E-02	3.42E-02	2.3
17	1.15E-02	8.51E-03	-35.1	2.03E-02	1.91E-02	-6.1	2.83E-02	2.93E-02	3.4
22	7.34E-03	5.01E-03	-46.5	1.58E-02	1.45E-02	-9.2	2.40E-02	2.53E-02	4.9
27	4.68E-03	2.96E-03	-58.1	1.21E-02	1.11E-02	-9.3	2.04E-02	2.17E-02	6.3
32	2.98E-03	1.78E-03	-67.4	9.53E-03	8.53E-03	-11.7	1.73E-02	1.88E-02	7.8

Table 6.6 gives Ratio1 and Ratio2 values when phantom set up and overlay materials are chosen as PMMA and soft tissue. Deviations in Ratio1 and Ratio2 values estimated using PMMA with respect to soft tissue material are less than 23 % and 7 % respectively till a source depth of about 1.2 cm. As the depth of the source increases to 3 cm, deviation increases to about 45 % for Ratio1 and 17 % for Ratio2.

Table 6.6 Ratio1 and Ratio2 using PMMA and soft tissue material in the phantom setup and deviations in the Ratios using PMMA with respect to soft tissue material.

Depth	Ratio1		Deviation	Ratio2		Deviation
mm	PMMA	Soft tissue	%	PMMA	Soft tissue	%
2	2.00E+00	2.14E+00	6.3	1.56E+01	1.60E+01	2.3
3	2.11E+00	2.30E+00	8.5	1.59E+01	1.62E+01	2.0
4	2.22E+00	2.47E+00	10.0	1.63E+01	1.67E+01	2.5
7	2.62E+00	3.08E+00	15.1	1.72E+01	1.77E+01	2.5
9	2.93E+00	3.60E+00	18.6	1.79E+01	1.87E+01	4.7
12	3.48E+00	4.51E+00	22.8	1.89E+01	2.03E+01	6.9
17	4.67E+00	6.54E+00	28.5	2.08E+01	2.29E+01	8.9
22	6.21E+00	9.57E+00	35.1	2.26E+01	2.60E+01	12.9
27	8.26E+00	1.39E+01	40.7	2.50E+01	2.92E+01	14.2
32	1.10E+01	2.01E+01	45.1	2.71E+01	3.28E+01	17.4

The difference in CEs, Ratio1 and Ratio2 values evaluated using PMMA and soft tissue below 100 keV, is due to differences in electron density which leads to difference in linear attenuation coefficients of these materials [55]. This difference increases with decrease in energy. Thus, PMMA could be used for experimental estimation of CEs due to embedded activity of [241]Am at 59.5 keV when activity is less than 1 cm deep, as it does not show much difference with respect to soft tissue material. In all other cases, when activity is at higher depths, a material which simulates soft tissue in the lower energy regions (< 100 keV) should be used. A possible source of error in the estimation of embedded activity is due to incorrect depth evaluation, originating most probably from the CEs based on PMMA instead of soft tissue material.

6.7   Estimation of wound activity and depth in actual case

6.7.1   Estimation of depth and embedded activity due to pure ^{241}Am

To use the present data, monitoring is required to be carried out by maintaining a distance of 10 cm between the palm surface and the HPGe array window surface in the case of intake of ^{241}Am through wound on palm. Mapping can be carried out using a Pb collimator to determine the spread of contamination and to locate the point from which highest counts are observed. This point should be positioned at the center of the detector enclosure at 10 cm distance. The depth of the source can be determined by comparing the ratio of net counts in 59.5 keV and 17.8 keV regions with the Ratio1 given in Figure 6.4. The CEs for 59.5 keV shown in figure 6.3 can then be used to estimate the embedded ^{241}Am activity in the wound for the evaluated depth. For estimation of MDA [22] of HPGe array, background counts are obtained by positioning the palm of an uncontaminated adult person at 10 cm distance from the HPGe array in the totally shielded steel room whole body counter [21]. MDA is predicted using CEs at 59.5 keV from table 4.1 and background counts of an adult male in standard geometry for measurement period of 600 seconds using equation 4.4. At 7 mm depth, 1.7 Bq is the MDA of HPGe array for ^{241}Am, in palm using the evaluated CEs at 59.5 keV in 600 seconds of counting time. MDA increases with increase in the depth, as it is inversely proportional to CE.

REs in different ^{241}Am activities (1 Bq, 10 Bq and 100Bq) at 7 mm depth, using counts in 59.5, 26.3 and 17.8 keV energy regions based on the estimated CEs and REs in ratios (Ratio1 and Ratio2) for monitoring period of 600 seconds are given in Table 6.7. Here, RE is the fractional standard deviation $(1/(\text{counts})^{1/2})$ which is inherent in counting statistics following Poisson distribution.

Table 6.7 RE (%) in the estimation of ^{241}Am activity at 7 mm depth using CEs at 59.5, 26.3 and 17.8 keV and Ratios (Ratio1 and Ratio2) for monitoring period of 600 seconds for embedded activity.

Energies and ratios	^{241}Am activity		
	1 Bq	10 Bq	100 Bq
59.5 keV	34.2	10.8	3.42
17.8 keV	60.1	19	6
26.3 keV	140.5	44.4	14
Ratio1	69.1	21.8	6.9
Ratio2	144.6	45.7	14.5

It is observed from table 6.7 that RE decreases with the increase in ^{241}Am activity and it is lowest when ^{241}Am activity is estimated by CEs at 59.5 keV due to its high yield leading to higher counts.

The quantification of ^{241}Am activity in the wound using the present methodology is valid irrespective of the type of material in the wound site. For compounds of PABS or fragment categories, activity will remain in the wound site and no variation in activity is expected during the measurement time. For all the other categories, if activity does not vary during the period of measurement, then ^{241}Am activity can be estimated using the CEs provided.

6.7.2 Estimation of depth and embedded activity due to mixture of Pu isotopes and ^{241}Am

If wound contains activity due to Pu isotopes along with ^{241}Am, then by using Ratio2 (which is independent of the presence of Pu in the wound) the depth of contamination and by using CE at 59.5 keV for that depth, embedded Pu and ^{241}Am activity can be estimated. The

contribution of ^{241}Am in 17.8 keV region can be evaluated using CE at 17.8 keV from the calculated ^{241}Am activity. The remaining counts in 17.8 keV region will be due to Uranium L X-rays of Pu isotopes. CE of ^{241}Am at 17.8 keV can be used after applying the yield correction to estimate the activity of Pu isotopes. The error in the estimation of ^{241}Am will propagate [104] in the activity estimation of Pu, so it is important to estimate the depth and ^{241}Am activity precisely.

In case of contamination due to mixed activity of Pu and ^{241}Am, it is important to know the isotopic composition of Pu as the yield of its 17.2 keV U L X-rays will change accordingly. To estimate RE in Pu, 17.2 keV of ^{239}Pu with yield of 2.13 % [17] is assumed to be present in wound in different ratios of ^{241}Am. Table 6.8 gives the RE in pure ^{239}Pu activity estimation as well as when ^{239}Pu activity is estimated using ^{241}Am in case of mixed contamination for measurement period of 600 seconds for wound at 7 mm depth. For different ^{241}Am activities (10 and 100 Bq) and for different ^{239}Pu and ^{241}Am activity ratios (1, 5 and 10), counts due to ^{239}Pu are estimated. Total counts due to mixed ^{241}Am and ^{239}Pu activity, are obtained by summing ^{241}Am counts from Table 6.7 and pure Pu counts from Table 6.8. As ^{239}Pu is estimated by subtracting ^{241}Am counts from total counts due to ^{241}Am and ^{239}Pu, error in the ^{239}Pu estimation can be calculated by propagation of errors [26].

It is observed from Table 6.8 that RE in the estimation of ^{239}Pu activity in presence of ^{241}Am decreases with the increase in ^{241}Am activity and increase in ^{239}Pu to ^{241}Am ratio. This is due to increase in the number of counts with increase in ^{241}Am and ^{239}Pu activity. RE of about 80 % is observed for 100 Bq of ^{241}Am activity and for ^{239}Pu and ^{241}Am activity ratio of 1. As this Pu and Am activity ratio increases to 100, the error in ^{239}Pu estimation reduces to about 10 %. The error in estimation of ^{241}Am and the corresponding error in ^{239}Pu activity increases with increase in depth. At 17.8 keV, MDAs of ^{241}Am and ^{239}Pu are 6 Bq and 53 Bq for activities at 7

163

mm depth and 600 seconds of monitoring period using uncontaminated adult male background in standard geometry. For wound activities less than MDA, REs are above 100. The wound activities at this level cannot be quantifiable by external detectors. For accurately quantifiable results, RE should be less than 10 % [22].

Table 6.8 RE (%) in the estimation of pure ^{239}Pu and in ^{239}Pu estimated from ^{241}Am for monitoring period of 600 seconds of embedded mixed ^{241}Am and ^{239}Pu activity at 7 mm depth.

Ratio ^{239}Pu:^{241}Am activity	RE (%) in ^{239}Pu activity estimation for measurement time = 600 sec			
	Pure ^{239}Pu	^{239}Pu estimated from ^{241}Am	Pure ^{239}Pu	^{239}Pu estimated from ^{241}Am
	^{241}Am activity =10 Bq		^{241}Am activity =100 Bq	
1	56.5	244.0	17.9	77.3
5	25.3	53.8	8.0	17.0
10	17.9	29.7	5.7	9.4

6.8 Phoswich CEs using palm phantom and experimental measurements

For experimental measurements, ^{241}Am reference point source was kept in the palm phantom, which is a tissue equivalent 2 cm thick PMMA slab, with a 2 cm diameter and 4 mm depth well at its center. The ^{241}Am spectra were obtained for source to detector distance of 10 cm. The thickness of PMMA slabs over the source was varied from 1 mm to 30 mm to simulate activity embedded in a tissue at different depths and the integrated counts in the energy regions of 18 and 59.5 keV were determined. This data is then used to evaluate CEs in different energy regions and at various depths for a ^{241}Am point source.

Fig. 6.4 (a) gives estimated CEs (cpm kBq^{-1}) for ^{241}Am source as a function of thickness of the PMMA slabs for Phoswich detector. The ^{241}Am spectrum obtained using Phoswich detector

shows a composite peak at ~ 18 keV corresponding to Np L-X-rays of 13.9, 17.6, 21 keV due to its poor resolution. As a result, Fig.6.4 (a) shows CEs of Phoswich detector for 18 keV and 59.5 keV photons. The initial sharp fall in the CEs of Phoswich detector for 18 keV is due to the relatively much higher absorption of its low energy (13.9 keV) X-rays in the intervening PMMA slabs. Fig. 6.4 (b) depicts the ratio of the count rates in 18 and 59.5 keV energy regions for Phoswich detector as a function of depth.

(a)   (b)
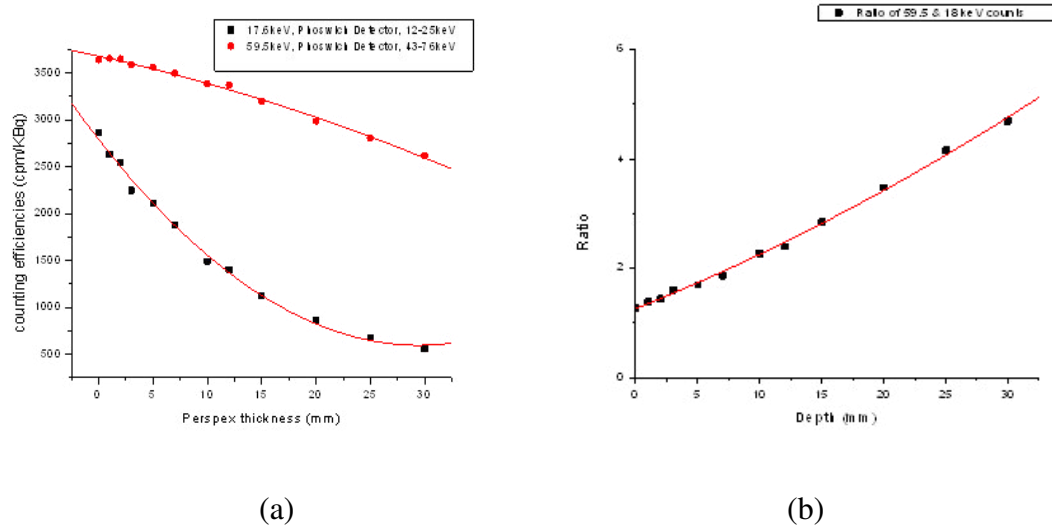
Figure 6.4 (a) CEs of Phoswich and (b) Ratios of count rates in different energy regions of ^{241}Am as a function of thickness of PMMA slabs.

For an actual case of 'Injection' intake of ^{241}Am through wound, monitoring should be carried out by positioning the wound at a 10 cm distance below the detector. The depth of the source can be determined by comparing the relevant ratios of count rates given in Fig. 6.4 (b) with the ratio of count rates obtained from measuring the wound under the detector. The CEs depicted in Fig. 6.4 (a) can then be used to assess the embedded activity in the wound of a subject for an evaluated depth. The Phoswich CEs can be used to assess contamination of pure

165

[241]Am. In case of mixed exposure case, it is required to assess the depth by using HPGe measurements, and then Phoswich data can be used to assess embedded activity.

6.9   Summary

There is a possibility of injury while handling actinides inside the glove boxes and this lead to the activity being embedded in the wound. In case of estimation of embedded activity in wounds located on hands or fingers of the workers, it is very important to estimate the depth accurately. In various laboratories, PMMA material is used as a tissue equivalent material in estimation of CEs for wound, but such an approximation is found to be valid only for wounds less than 1 cm deep. For wounds deeper than 1 cm, a material which is soft tissue equivalent at lower photon energies (< 100 keV) should be used. No change is observed in estimated CEs, when source size is modified. Therefore, Monte Carlo simulated CEs, Ratio1 and Ratio2 are provided at various depths inside the palm phantom due to a point source of [241]Am. The ratio of counts in 59.5 keV to 17.8 keV energy regions is defined as Ratio1 and the ratio of counts in 59.5 keV to 26.3 keV energy regions as Ratio2. In case of mixed contamination of Pu isotopes and [241]Am, Ratio2 should be used as Ratio1 will have contribution due to both Uranium L X-rays due to Pu and Neptunium L X-rays due to [241]Am. Ratio1 should be used in case of contamination due to pure [241]Am due to its lower contribution to error in the estimation of depth of activity. It is observed that RE in the estimation of [239]Pu activity in presence of [241]Am activity decreases with the increase in [241]Am activity and increase in [239]Pu to [241]Am activity ratio. The methodology developed in this work will help in the accurate estimation of depth and Pu\[241]Am activity localized in the wound.

CHAPTER 7

Modeling to predict the effect of DTPA on wound and lung activity

This chapter describes the effect of diethylenetriaminepentaacetic acid (DTPA) given intravenously for intake of actinides by wound and inhalation pathway. A methodology is given to predict enhanced urinary excretion rates by modification of Pu and Am biokinetic model.

7.1   Introduction: Chelation with DTPA

If a radiation worker is expected to receive significant internal dose then decorporation is carried out using medical countermeasures to reduce the dose. The method used for removal of internal contaminant depends upon the route of intake, chemical properties of material and its biokinetic behavior. In case of inhalation of insoluble compound of transuranics, which would give higher lung dose and CED of ~ 5 Sv within few weeks, lung lavage [105] is considered. In case of ingestion intake, gastric lavage and purgative are used to reduce the ingested activity [106]. In case of wound intakes, when large amount of insoluble activity is remaining at the wound site, excision is carried out to remove the wound activity [106]. In case of soluble compounds of transuranics such as Pu, Am and Cm which will be entered in the blood rapidly and will be deposited in tissues, mainly bone and liver, chelation is carried out using Ca-DTPA. The basic principle of decorporation therapy with chelating agents is the metal ion of Pu or Am is mobilized by the complexing agent DTPA and the formed complex does not follow the standard metabolic processes of the metal but that of the complexing agent [107].

Thus, inhalation or injection of DTPA formulations enhances the urinary excretion of Pu and Am compounds by forming stable Pu-DTPA or Am-DTPA complex, which is quickly eliminated into the urine for ~ hundred days [108; 109]. Thus, reduction of internal dose is possible

due to removal of internal contaminant. Typical dosage of ~ 0.5 - 1 g of DTPA diluted in 250 ml of 5 % dextrose in water is given intravenously over 60 to 90 minutes. In case of inhalation intakes, same amount of DTPA is given by nebulizer. Depending upon the amount of internal contaminant and treatment protocol, DTPA is administered by multiple daily treatments or single intravenous injection. Since Ca-DTPA can remove the essential metals such as iron, manganese and zinc from the body, the Zn-DTPA [106] is used due to its less toxicity, when multiple daily treatments are required to be given to the worker.

7.1   DTPA biokinetic model

7.1.1   DTPA biokinetic model by Stather et. al.

Biokinetic model of DTPA [110] given by Stather et al. based on retention data in human volunteers after intravenous injection of DTPA is described in the figure 7.1 (a). According to this model, DTPA is distributed in blood plasma and extracellular fluids (ECF). The rates of transfer of DTPA between the blood and ECF with a mean half-time of 2.5 min and subsequent return to blood with mean half-time of 6.3 min are found to be rapid. By 24 hour after injection, the cumulative urinary excretion was more than 99 % of the activity administered, but detectable amount of activity was continued to be excreted in the following week. The typical dosage of DTPA is 0.5 to 1 g and 0.5 g corresponds to ~ 1E-3 mol of DTPA. An intake of 1 kBq of ^{239}Pu corresponds to ~ 2E-9 mol. It is six orders of magnitude smaller than typical DTPA dosage. This explains higher urinary excretion of Pu for few days after treatment with Ca-DTPA of occupationally exposed persons, as there would be sufficient DTPA available in blood to chelate minute amounts of circulating Pu.
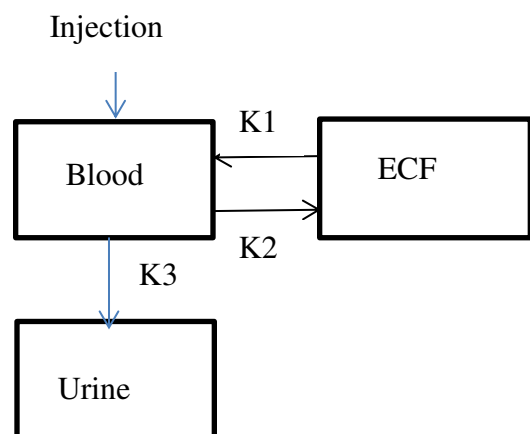
K1 = 403.2 d^{-1}, K2 = 158.4 d^{-1}, K3 = 53.28 d^{-1}
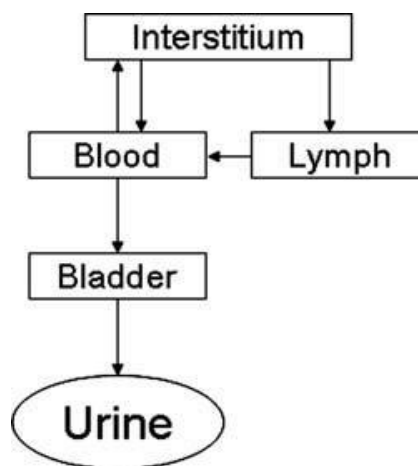
(a)   (b)

Figure 7.1 (a) Biokinetic model of DTPA as given by Stather et al. (b) Modified DTPA model

given by Breustedt et al.

7.1.2   DTPA biokinetic model by Breustedt et al.

In the modified DTPA model given by Breustedt et al. [111] extracellular fluid is divided

into interstitium and lymph and it is given in figure 7.1 (b). Injected DTPA is transferred to the

urinary bladder or to the interstitium. From the latter is goes back to blood either directly or

through the lymphatic circulation. The proposed model is able to describe all the available

injection DTPA data for blood retention and urinary excretion. The parameters of the modified

DTPA model are given in table 7.1.

7.2   The difficulties in estimating intake when DTPA is used for chelation

The modifications required to be made in the ICRP biokinetic model when DTPA is

administered is shown in figure 7.2. When DTPA is given, the Pu or Am present in the blood

will form complex with it, which will then follow the behavior of DTPA and will be excreted along with the Pu or Am excreted normally without the influence of DTPA.

Table 7.1 The parameters of the modified DTPA model by Breustedt et al.

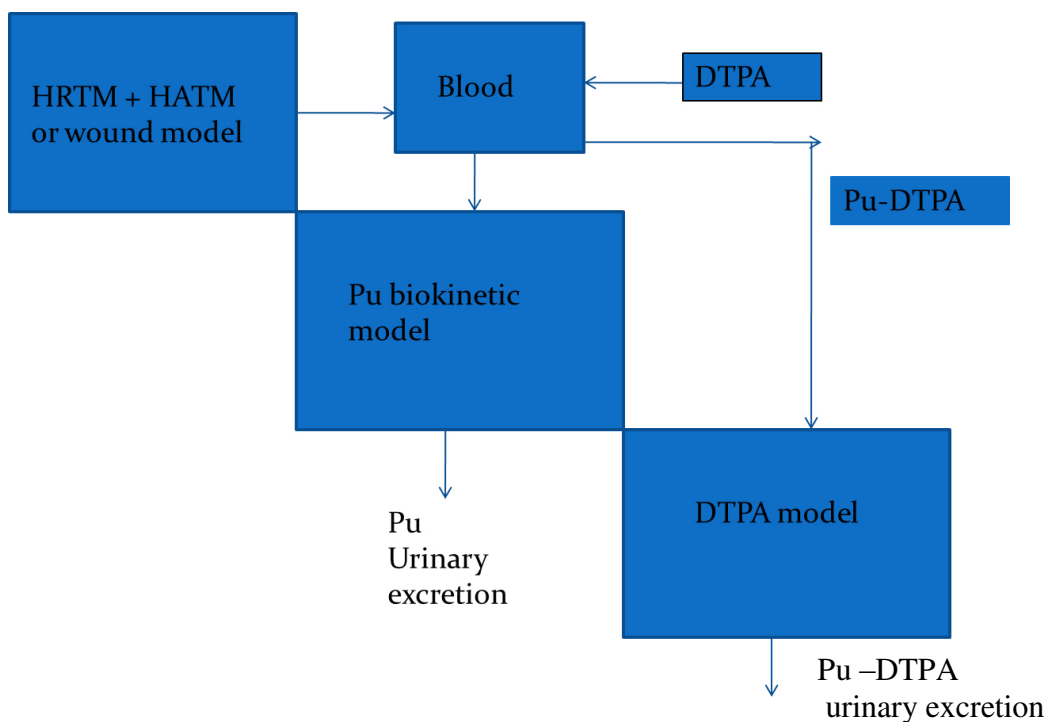| Transfer	transfer rate (d^{-1})
Blood to interstitium	145 ± 11
Interstitium to blood	64 ± 4
Interstitium to lymph	0.123 ± 0.012
Lymph to blood	0.405 ± 0.036
Blood to urinary bladder	45.7 ± 0.8

Figure 7.2 DTPA modelling for inhalation or wound intake.

As observed from figure 7.2, there will be an enhancement in urinary excretion of Pu or Am due to application of DTPA. From the urine excretion data reported in the literature, the

DTPA enhancement factor observed for internal contamination cases of Pu and Am, is in the range of 1 to 130 [112; 113]. The old data suggests the range of 60 to 100 by Jech et al. [108], 30 to 100 by Parker et al. [114], 1 to 130 by Shoefield et al. [95], around 80 by Hall et al. [109] and 25 to 100 by Piechowski et al. [93] for DTPA enhancement factor. There is also high intra-variability in DTPA enhancement factor [115].

Two methods are used to estimate the intake in case of DTPA administration. The first method is based on using urine excretion data 100 days after DTPA treatment. After ~ 100 days post DTPA treatment, the influence of DTPA is not present on urine excretion. As biokinetic models given by ICRP does not consider the effect of DTPA, urine data after 100 days of DTPA treatment can be used to predict intake and CED using ICRP models. However, this leads to the delay in intake and CED estimation. The second method is based on using default enhancement factor of ~ 50 [115] for Pu. This may lead to the over or underestimation of the dose as an enhancement factor for few wound cases is found to vary between 1 to 130 [115].

As the urine enhancement factor shows large variation, it would be advantageous to use modified biokinetic model for Pu or Am, which can be used to predict the intake. As Pu-DTPA or Am-DTPA complex will behave as DTPA, it is required that wound or HRTM model depending upon wound or inhalation intake, should be combined with biokinetic models of Pu or Am along with the DTPA model. Few researchers have tried developing this modified model. The success is limited, as the parameters evaluated are able to predict for one case considered in developing the model, but it cannot be used as a general model for other cases available in literature. Therefore, in this study, a general model available from literature [116] is used and the methodology is given to change the parameters in a systematic way so that it can evaluate the intake by fitting the predicted and measured urinary excretion data on individual case basis. This

will lead to the estimation of intake based on higher urinary excretion following DTPA administration using few data points of around 20 days, during DTPA treatments before delay of ~100 days.

7.3 Modification of Pu - biokinetic model for DTPA

A general model for Pu under the influence of DTPA, developed by Konzen et al. [116] is given in figure 7.3.
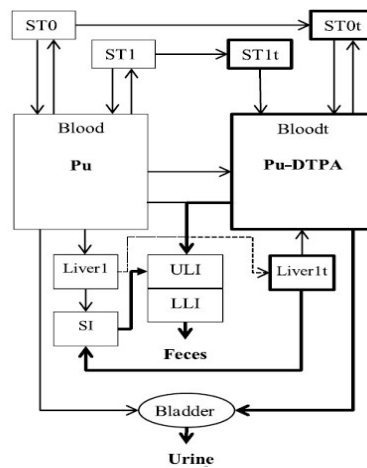
Figure 7.3 A general Pu- DTPA model given by Konzen et. al.

This is the modified version of the earlier model provided by Breustedt [111] et al. Earlier model was revised to include four transitional state compartments that describe the retention of Pu-DTPA complex using first order kinetics. The four transitional state compartments are ST0t for extracellular fluids, ST1t for intermediate soft tissues, bloodt for blood and liver1t for first liver compartment. The transfer rates between the transitional state and other ICRP biokinetic model compartments are given in table 7.2. For transitional state compartments, the rates are similar to the values given in table 7.1.

Table 7.2 Modified Pu-DTPA model given by Konzen et. al.

Compartment pathway	Transfer rate d^{-1}
ST0 to ST0t	3.65
ST1 to ST1t	1.925
Blood to Bloodt	1.378
ST0t to Bloodt	300
ST1t to Bloodt	0.12
Bloodt to ST0t	145
Bloodt to ULI	4
Bloodt to bladder	45.7
Liver to Liver1t	2.2
Liver1t to Bloodt	0.067
Liver1t to SI	0.067

7.4   Validation of the SAAM II results with the IMBA values

7.4.1   SAAM II software

In this study, for DTPA modeling SAAM II software [117] is used. It is simulation, analysis and modeling software used for solving biokinetic models. It creates systems of ordinary differential equations from the compartmental model structure.   It is a compartmental and numerical modeling program to assist in the development of models and use models to analyze data. It permits the simulation of complex experimental designs on the model and to obtain initial parameter estimates for the model from the data.

7.4.2 Validation of the SAAM II software for wound of avid category

Before using SAAM II software for DTPA modeling, it has been validated by solving the models for wound and inhalation intakes of 1 Bq each. Wound model for avid category of Pu is incorporated in the SAAM II, along with its biokinetic model and urine excretion rates are estimated and compared with urinary excretion rates obtained with Integrated Modules for Bioassay Analysis [118] (IMBA) program for intake of 1 Bq. IMBA uses latest biokinetic models and predicts the urine, fecal excretion rates and wound retention data. Figure 7.4 shows the urine excretion rates predicted by IMBA and SAAM II software for first twenty days. The values are within 1 % of each other.
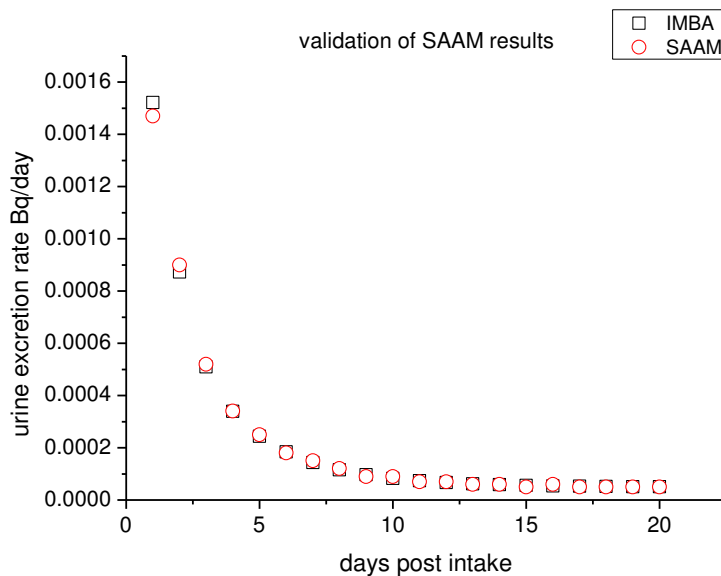
Figure 7.4 Comparing urinary excretion for intake by wound pathway of avid category.

7.4.3 Validation of the SAAM II software for lung retention

To validate the lung retention and urine excretion rates for inhalation intake of 1 Bq of ^{241}Am, HRTM along with the biokinetic model of Am is incorporated in SAAM II code. The

estimated lung retention and urine excretion values are found to be within 1 % of the IMBA values as observed from figures 7.5 and 7.6 respectively.
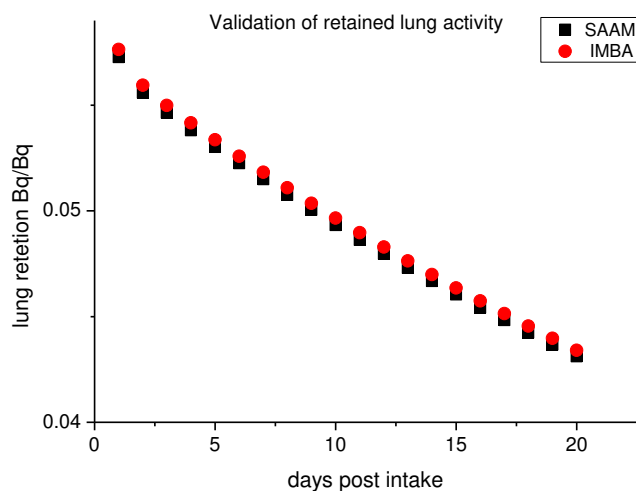
Figure 7.5 Comparing lung retention for intake by inhalation pathway type M compound
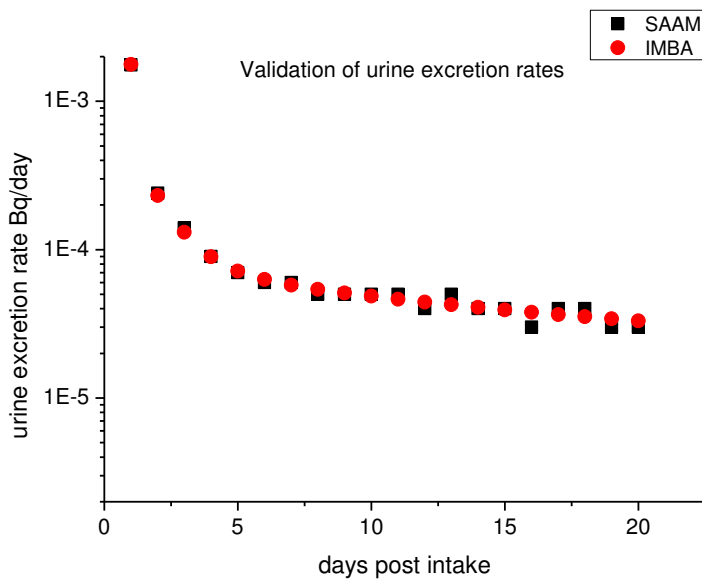
Figure 7.6 Comparing urinary excretion for intake by inhalation pathway type M compound.

7.5   Methodology for varying biokinetic parameters

The wound model of avid category along with biokinetic models of Pu and HRTM model for type M compound along with biokinetic models of Am are incorporated in SAAM II program. The pathways to the transitional states are given. In the model, transfer of activity will occur on these pathways only on two consecutive days when DTPA is administered. On other days, there is no transfer to the transitional compartments and the model will be solved as if there is no modification due to DTPA effect.

Intake is predicted by using default enhancement factor of 2 and for this intake, transfer rates to the transitional compartments are varied. The method used to fit the urine excretion measured data with the predicted data from model is to vary the parameters, given in table 7.2. The parameters are varied in the range obtained by dividing a parameter by 10 and multiplying a parameter by 10. In the selected range, the parameters are refined by reducing or increasing with 2, 4, 6, 8 and 10 respectively. Once the parameters are finalized so that the trend in the urine excretion rates is mimicked, further refining in the intake is carried out.   These refined parameters are used in the modified model for two days post administration of DTPA. Two days after administration of DTPA, transfer rates from ICRP biokinetic compartments to transient compartments are assumed to be zero. Finally, to verify the fitting of the data, Chi square, χ^2 and coefficient of auto correlation ρ, tests are used and probability of fitting is evaluated at 95 % confidence level.

7.5.1   Chi square test [119]

Considering measurements are log normally distributed, chi square is given by

$$\chi^2 = \sum_{i=1}^{N} \left[\frac{lnM_i - \ln P_i}{ln(SF_i)} \right]^2 \qquad\qquad \textbf{7.1}$$

Where M and P are measured and predicted excretion rates or wound activities and SF is a geometrical standard deviation of the ith data point. The estimated χ^2 is compared with the χ^2 tables for 95 % confidence level and N-1 degrees of freedom. If estimated χ^2 is smaller than the values given in χ^2 tables, the fit is accepted at 95 % confidence level.

The problem with the χ^2 test is it is biased with the assumed errors. χ^2 test is passed even though the scatter of the data around the fit is not random, therefore autocorrelation coefficient, ρ test is used along with χ^2 test.

7.5.2 Autocorrelation coefficient ρ test [119]

The autocorrelation coefficient, ρ, tests for non-randomness in a series of observations. ρ, for sequence of Ri residuals is calculated by

$$\rho = \frac{\sum_{i=1}^{N-1} R_i R_{i+1}}{\sum_{i=1}^{N} R_i^2} \qquad 7.2$$

Where Ri's are calculated using following equation

$$R_i = \frac{lnM_i - lnP_i}{\ln(SF)} \qquad 7.3$$

The numerator in equation 7.2 provides a measure of non-randomness and denominator is χ^2. Under totally random conditions one would expect ρ close to zero. However, as the sequence becomes less random, ρ approaches -1 or 1 and it indicates poor fitting of the data. When the number of data, N, in each artificial data set was greater than, or equal to, six, the null distribution of ρ could be approximated by a normal distribution. The mean and standard deviation of this distribution are a function of N and given by

$$\mu = -\frac{1}{N} \qquad 7.4$$

$$\sigma = \frac{N-2}{N\sqrt{N-1}} \qquad\qquad 7.5$$

At 95 % confidence level, the value of ρ is μ + 1.64σ. For N=20, ρ is 0.2886 at 95 % confidence level. To test for fitting of the data, estimated ρ from equation 7.2 is compared with ρ at 95 % confidence level. If estimated ρ is smaller, then the fit and the model used for generating data is accepted at 95 % confidence level.

7.6   Validation with literature cases

7.6.1   Intake of Pu- avid category by wound

The wound model for Pu of avid category intake along with the biokinetic model of Pu and additional transitional compartments incorporated in SAAM II are shown in figure 7.7.

In figure 7.7, the compartments 26 to 29 shows the biokinetic model of DTPA and it can be seen that transitional compartments 31 to 34 mimic the DTPA behavior.

The case chosen for predicting influence of DTPA on the wound of avid category of Pu, is taken from IDEAS database [120], case 45. The wound occurred on the right hand of the male worker in 1981 while working in the reprocessing plant. The composition of Pu in the wound is ^{238}Pu ~ 18.92 %, ^{239}Pu ~ 29.01 %, ^{240}Pu ~ 51.65 %, ^{242}Pu ~ 0.07 % and ^{241}Am ~ 0.35 % of the total alpha activity. The ratio in activity of ^{241}Pu/ ($^{238+239+240}$Pu) was 51.4. Urine excretion data was provided for 1 to 100 days. 1 g DTPA was given on 4th, 5th and 8th day and 0.5 g DTPA was given on 9th, 12th and 33rd day respectively. The urine excretion data used for modifying and solving the model is given in table 7.3
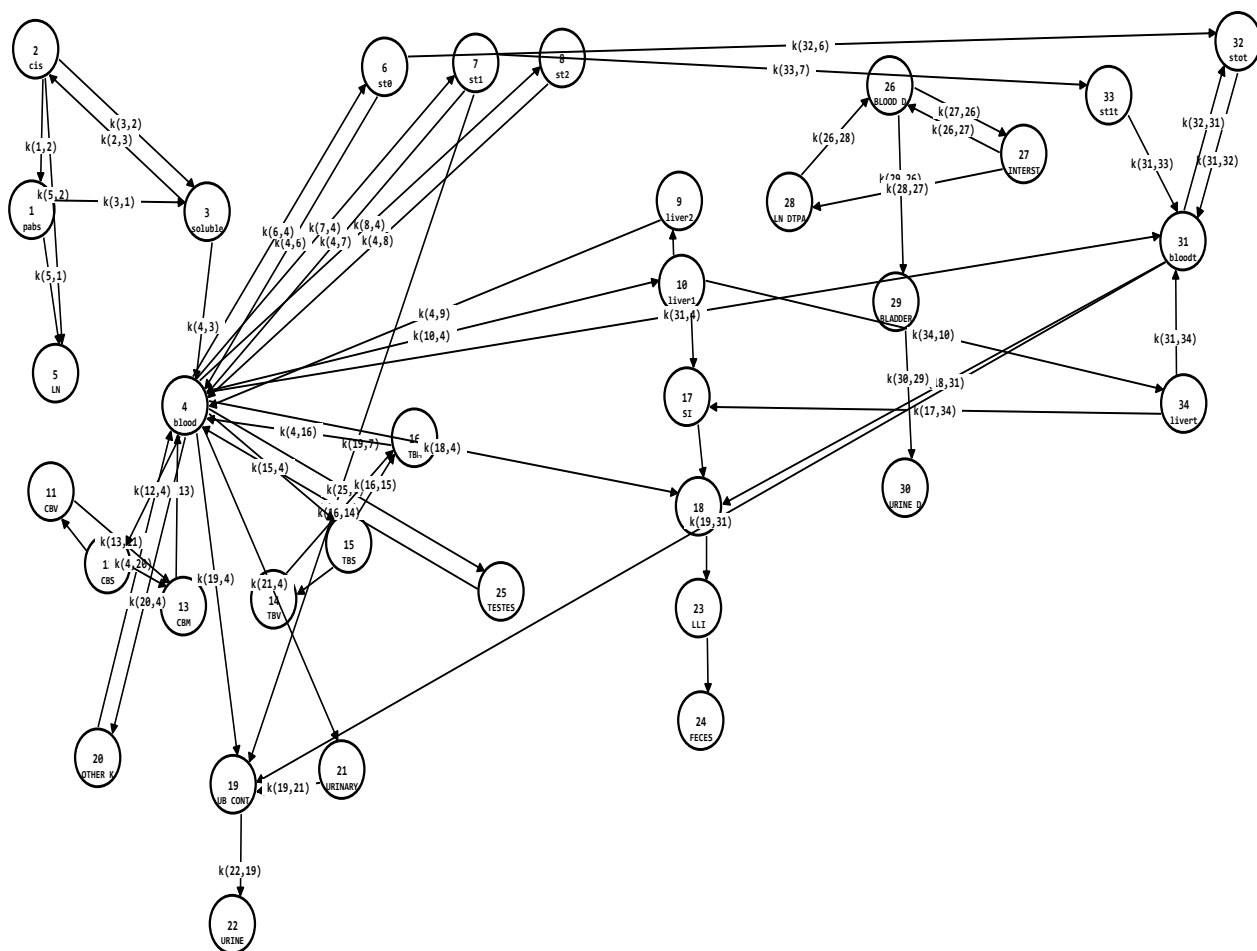
Figure 7.7 wound model for Pu avid category along with its biokinetic model and transitional compartments.

Table 7.3 Urine excretion data for IDEAS wound case 45

day	urine excretion rate	day	urine excretion rate	day	urine excretion rate	day	urine excretion rate
1	0.211	11	0.107	21	0.0259	35	0.0444
2	0.0888	12	0.0629	22	0.0185	37	0.0333
3	0.1665	13	0.252	23	0.0111	41	0.00259
4	0.0148	14	0.0629	24	0.0074	44	0.00444
5	3.389	15	0.0518	25	0.0185	48	0
6	0.585	16	0.0407	26	0.00925	50	0.01221
7	0.104	17	0.0407	28	0.00814	55	0
8	0.137	18	0.0222	30	0.00851	61	0
9	0.389	19	0.0407	33	0.01443	68	0
10	0.281	20	0.037	34	0.0888	75	0.00185

For the model depicted in figure 7.7, initial intake assumed was assumed 70.3 Bq using an enhancement factor of 2 to the first data point. The transfer rates varied for various transitional compartments as given in table 7.4. Finally, intake was varied to 50 Bq, which gives rise to good visible fitting of the predicted and measured urine excretion data as observed from figure 7.8.

Table 7.4 Modified transfer rates in d^{-1} for few compartments for final solution.

Path	Initial transfer rate d^{-1}	final transfer rate d^{-1}
Blood to bloodt	1.378	4.14
ST0t to bloodt	300	64
Bloodt to ST0t	145	72.5
Bloodt to ULI	4	6
Blood t to Bladder	45.7	7.62
Intake Bq	70.3	50
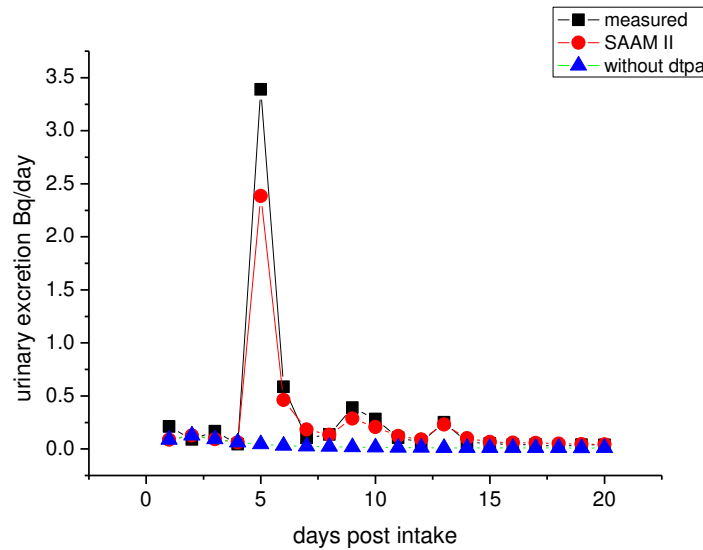
Figure 7.8 Comparison of the measured and predicted urine excretion rates for Pu wound case.

For DTPA given on 4th, 5th, 8th, 9th and 12th day, the predicted urinary excxretion follows the trend observed in the data. The χ^2 and ρ tests were carried out on the predicted and measured data for first 20 days. The χ^2 is calculated to be 20 using equation 7.1 and from tables at 95 % confidence level, the χ^2 is 31.41 for 20 degrees of freedom. Similarly, ρ is calculated to

be 0.0426 using residuals and from 20 data points, ρ is estimated at 95 % confidence level as

0.2886. Thus, the data set passes both χ^2 and ρ tests at 95 % confidence level.

7.6.2   Intake of type M compound of ^{241}Am by inhalation

The HRTM for Type M compound of ^{241}Am along with its biokinetic model and additional transitional compartments incorporated in SAAM II are shown in figure 7.9.

The case chosen for studying and modifying the model is given in IDEAS database [120] as case 32 and in IAEA TECDOC 1071 [121]. The person had internal contamination by inhalation pathway when dismantling the used ^{241}Am industrial source (~ 3.7 GBq) without taking precaution for preventing internal or external contamination. Urine excretion data was provided for 1 to 294 days in the database. 1 g DTPA was administered on 0th, 4th, 6th, 15th, 18th, 25th, 28th, 91st and 110th day respectively. The urine excretion data used for modifying and solving the model is given in table 7.5 for 1 to 111 days.

Default transfer rates for inhalation intake of type M compound of ^{241}Am and biokinetic model and transfer rates given in table 7.2 are used for solving the model. Initial intake assumed was 2.88 kBq using enhancement factor of 2, which was further refined to 2.07 kBq. With the intake of 2.07 kBq, the measured and predicted data set passes both χ^2 and ρ tests at 95 % confidence level. χ^2 is calculated to be 19 using measured and predicted data points of first 20 days. This is less than χ^2 of 31.41, for 20 degrees of freedom and thus passes the χ^2 test at 95 % confidence level. Excluding first data point, χ^2 is 11.39 and ρ is calculated to be 0.0829, that is less than the 95 % confidence value of 0.2886. The measured and predicted urine excretion rates are shown in figure 7.10.
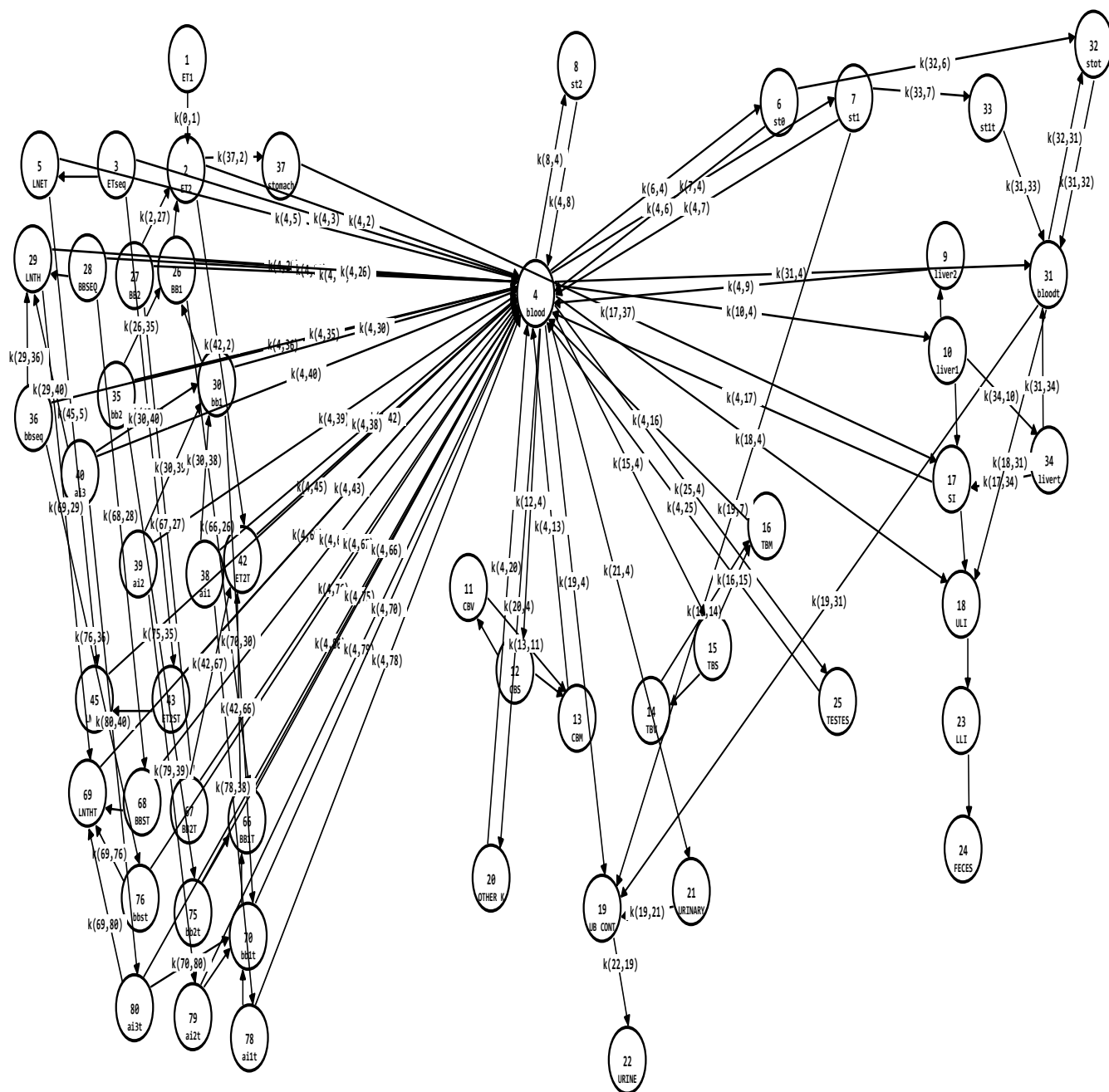
Figure 7.9 HRTM for type M compound of Am along with its biokinetic model and transitional compartments.

Table 7.5 Urine excretion data for IDEAS wound case 32

day	urine excretion rate	day	urine excretion rate	day	urine excretion rate	day	urine excretion rate	day	urine excretion rate
1	8.65	11	2.3	21	1.43	31	2.3	78	0.929
2	2.92	12	1.66	22	2.7	32	1.49	89	0.275
3	2.66	13	1.43	23	2.09	51	1.23	90	0.343
4	1.68	14	1.89	24	2.44	52	1.43	91	0.51
5	3.24	15	2.75	25	1.98	53	1.15	92	2.5
6	1.28	16	2.65	26	2.4	62	0.562	93	1.17
7	2.49	17	2.02	27	2.24	63	1.18	94	1.4
8	2.05	18	1.87	28	2.01	64	0.72	95	1.87
9	2.14	19	2.57	29	3.26	76	0.418	110	1.44
10	1.63	20	2.65	30	1.41	77	0.548	111	1.07
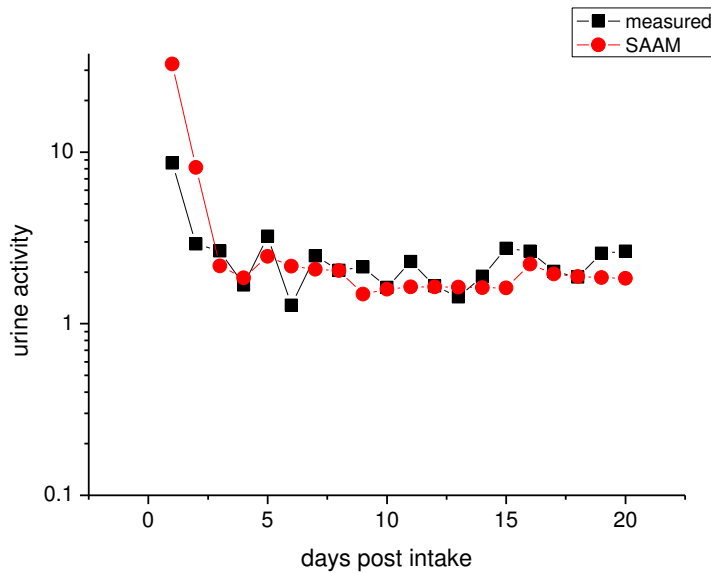
Figure 7.10 Comparison of the measured and predicted urine excretion rates for inhalation of ^{241}Am

7.7 Modeling DTPA effect to verify the dose reduction

Biokinetic models are modified for wound of avid category of Pu and inhalation of type M compound of ^{241}Am. The methodology developed can be used for other radionuclides as well as for intake by wound of any other categories and to verify the effect of DTPA on dose reduction.

7.7.1 Effect of DTPA on skeletal activity

For IDEAS case 45, effect of application of DTPA on skeletal activity is evaluated. The reduction in the skeletal activity is directly related to the reduction of CED. The skeletal activity in the presence and absence of DTPA is given in figure 7.11. Skeletal activity is a combination of cortical bone and trabecular bone activity. It can be seen from figure 7.11 that ~ 30 % reduction in the skeleton activity is expected due to administration of DTPA for this particular case.
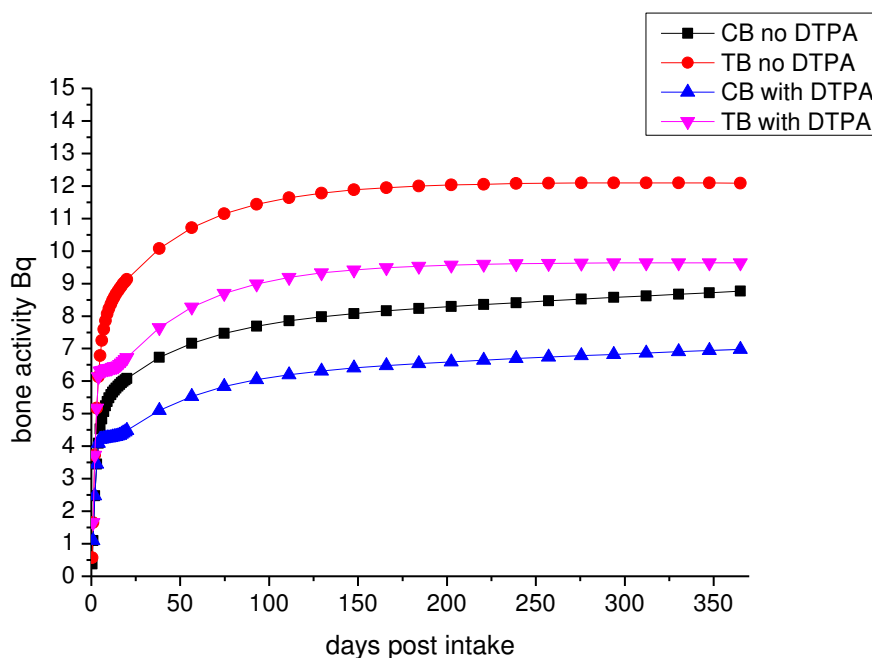
Figure 7.11 The skeletal activity in the presence and absence of DTPA.

7.7.2   Effect of application of Ca-DTPA on various days post intake

For intake of type M compounds of ^{241}Am by inhalation pathway, the effect of administration of DTPA on the day of incident, 1 or 2 days after incident and when DTPA is not given is studied.   The influence of DTPA is given in figure 7.12 when it is administered on various days post intake along with the excretion when DTPA is not administered.
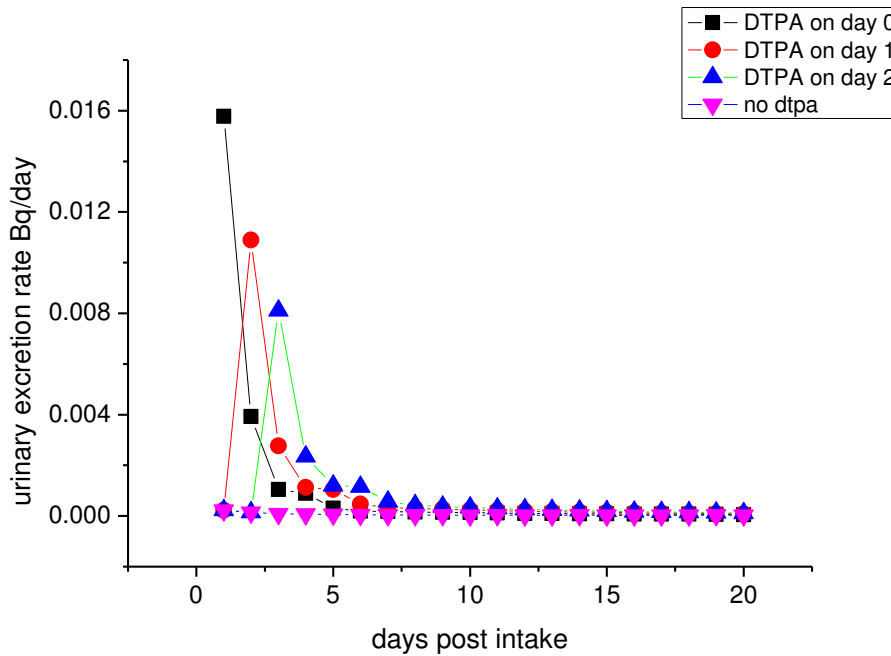
Figure 7.12 Influence of administration of DTPA on various days post intake and absence of DTPA

It can be seen from figure 7.12, that excretion is higher on the day DTPA is administered. Also highest excretion is observed when DTPA is administered on the day of incident. Thus, highest reduction of CED is possible, if DTPA is given as early as possible after the intake.

7.8   Summary

In this chapter, modeling of the effect of DTPA given intravenously for intake of actinides by wound and inhalation pathway is carried out. A methodology is given to predict enhanced urinary excretion rates by modification of Pu and Am biokinetic model for single or multiple DTPA intakes given by injection pathway in case of inhalation of type M compounds of ^{241}Am and avid category of ^{239}Pu wound intake. The methodology is validated using known cases of wound and inhalation intakes from literature.

CHAPTER 8

Summary and Conclusions

This chapter gives a summary of the work reported in the thesis and the main conclusions drawn. The scope of the future work is also included.

8.1 Summary of the work

8.1.1 Total combined uncertainty in lung activity assessment

In this thesis, various parameters that can influence lung activity assessments are identified. Uncertainties in the form of SFs are evaluated for important parameters such as MEQ-CWT, positional errors, normal background variation, non-uniform distribution of activity in lungs, counting statistics. Combined SFs due to all the components at different energies are evaluated and given in tables 8.1 and 8.2 for Phoswich and HPGe array respectively.

Table 8.1 SFs due to various parameters and combined SFs in lung measurements for Phoswich detector

Radio-nuclide	Energy keV	SFs due to					Combined SF
		MEQ-CWT	Positional errors	Normal Background variation	Non-uniform distribution	counting statistics	
Pu-239	18	1.25	1.12	1.12	1.78	1.5	2.13
Am-241	60	1.17	1.05	1.04	1.24	1.1	1.34
Th-234	63	1.17	1.05	1.03	1.34	1.1	1.42
Pb-212	74	1.2	1.05	1.03	1.24	1.1	1.35
Th-234	93	1.22	1.05	1.03	1.23	1.1	1.36
U-235	185	1.2	1.05	1.04	1.23	1.1	1.35
Pb-212	238	1.2	1.04	1.04	1.23	1.1	1.35

Table 8.2 SFs due to various parameters and combined SFs in lung measurements using HPGe array

Radio-nuclide	Energy keV	SFs due to					Combined SF
		MEQ-CWT	Positional errors	Normal Background variation	Non-uniform distribution	counting statistics	
Pu-239	18	1.25	1.14	1.46	1.56	1.5	2.13
Am-241	60	1.17	1.07	1.22	1.3	1.1	1.47
Th-234	63	1.17	1.07	1.24	1.29	1.1	1.47
Pb-212	74	1.2	1.06	1.24	1.28	1.1	1.48
Th-234	93	1.22	1.06	1.23	1.25	1.1	1.46
U-235	185	1.2	1.05	1.26	1.25	1.1	1.47
Pb-212	238	1.2	1.05	1.26	1.25	1.1	1.47

Highest SF of 2.13 is observed at 18 keV and as energy increases the combined SF decreases to 1.35 and 1.47 at 238 keV respectively, using Phoswich and HPGe array. The deviations in combined SFs obtained using HPGe array with respect to combined SFs obtained using Phoswich detector are found to be ~ 4 to 10 % higher for 60 to 238 keV photons.

The deviation in the total SFs obtained due to all the parameters studied in this thesis with the SFs predicted by experts is ~ 7 % (table 1.8) for energies less than 100 keV. For energies greater than 100 keV, the deviation in the total SFs obtained with respect to SFs predicted by experts is ~ 18 %. This is because though high energy photons are easier to detect and uncertainty due to counting statistics is expected to be low, the detection also depends upon the yield of the higher energy photons and amount of activity in the lungs. For 185 keV photons associated with ^{235}U, which is 0.72 % in Nat. U., the SF is found to be 1.3 at MDA level of activities of ^{235}U.

The studies are also carried out to evaluate the effect of variation of ^{239}Pu and ^{241}Am activity ratio in the lungs and contribution of source in other organs such as liver, skeleton and GI tract in lung measurements. It is found that for type S or type M categories of Pu and Am, ratio of ^{239}Pu and ^{241}Am activities in the lungs varies less than 5 % at the end of one year, the uncertainty in due to variation of Pu and Am activity ratio is given by a SF of 1.05. For other initial conditions when Pu and Am behaving differently, the change in the Pu and Am activity ratio is found to be ~ 5 or more.

Among the source in liver, skeleton and GI tract, liver contributes more in the right lung and thus it contribution can be evaluated by measuring right and left lung separately. As GI tract activity will be cleared fast, its contribution in the lung measurements will reduce with days post ingestion intake. The skeletal contribution can be evaluated from knee and skull measurements, by first estimating knee or skull activity, then predicting total skeletal activity. SF of 1.3 is recommended for estimation of skeletal activity for Pu and 1.1 for other radionuclides. This is because overestimation and underestimation of ~ 30 % could occur due to unknown distribution of skeletal activity in case of Pu. For other radionuclides, deviation of ~ ±10 % is observed in CEs obtained using skull and knee phantoms for uniform distribution of activity in TBBM and CB region with respect to the CEs obtained assuming ratio of 0.2 and 0.02 in TBBM and CB region.

8.1.2 Factors introducing uncertainty in ingestion intake

In the thesis, CEs of Phoswich and an array of HPGe detectors are estimated using voxel phantom considering the expected source distribution in GI tract as a function of time. The solution of HATM is used to estimate CEs for photon energies from 18 to 238 keV. Higher CEs are obtained on 0.5 day when source is in small intestine and colon regions. Thereafter, CEs

decrease with post intake days. It is found that to estimate ingested activity by direct measurements, CEs based on true activity distribution as per the solution of HATM should be used; otherwise, an error of ~ -16 to -75 % will occur in the assessed ingested activity. The contribution of lung activity on GI tract measurements is found to increase with increase in yield and activity of the radionuclide. Contribution of GI tract activity is found to be ~ 10 % in lung measurements on one day after ingestion intake and found to decrease with days post intake. The influence of liver activity on chest and abdomen measurements is found to be ~ 30 to 50 % and ~ 75 % respectively using both the detectors.

8.1.3   Factors introducing uncertainty in case of wound

Most of the wounds while working with actinides are found on the hands and fingers of the worker, which lead to the activity being embedded in the wound. In case of estimation of embedded activity in wounds, it is very important to estimate the depth accurately. In various laboratories, PMMA material is used as a tissue equivalent material in estimation of CEs for wound, but such an approximation is found to be valid only for wounds less than 1 cm deep. For wounds deeper than 1 cm, a material which is soft tissue equivalent at lower photon energies (< 100 keV) should be used. No change is observed in estimated CEs, when source size is modified. Therefore, Monte Carlo simulated CEs, Ratio1 and Ratio2 are provided at various depths inside the palm phantom due to a point source of ^{241}Am. The ratio of counts in 59.5 keV to 17.8 keV energy regions is defined as Ratio1 and the ratio of counts in 59.5 keV to 26.3 keV energy regions as Ratio2. In case of mixed contamination of Pu isotopes and ^{241}Am, Ratio2 should be used as Ratio1 will have contribution due to both Uranium L X-rays due to Pu and Neptunium L X-rays due to ^{241}Am. Ratio1 should be used in case of contamination due to pure ^{241}Am due to its lower contribution to error in the estimation of depth of activity. It is observed

that RE in the estimation of ^{239}Pu activity in presence of ^{241}Am activity decreases with the increase in ^{241}Am activity and increase in ^{239}Pu to ^{241}Am activity ratio. The methodology developed in this work will help in the accurate estimation of depth and Pu/ ^{241}Am activity localized in the wound.

8.1.4 Modeling the effect of administration of DTPA on urinary excretion for wound and inhalation cases

The biokinetic models given by ICRP do not consider the effect of DTPA on the urine excretion, which differs from excretion in the absence of the DTPA. A methodology is given to predict enhanced urinary excretion rates by modification of the biokinetic model. The modifications suggested by Konzen [116], Breustedt [111] et al. are used and few transitional compartments are added in the model representing DTPA biokinetics. This is because Pu-DTPA complex formed in the blood follows the DTPA behaviour. The variation in the urinary enhancement factor due to administration of DTPA is in range of 1 to 130 from the various internal contamination cases given in literature. Therefore, the transfer rates to the transitional compartments in the modified biokinetic model are varied around some assumed median values, in order to match the predicted and measured urinary excretion rates. The methodology is validated for two cases from literature: inhalation of ^{241}Am, type M compound and wound of avid category of ^{239}Pu. The fit of the measured and predicted urinary excretion rates is checked with chi-square and autocorrelation coefficient tests. The methodology developed in this investigation will be used to predict the enhanced urinary excretion rates, in case of intake by inhalation of type M compounds and different categories of wound contaminations, when single or multiple DTPA intakes are given by injection pathway. The methodology can also be used to predict the inhalation or wound intakes, using enhanced urine excretion data.

192

8.2   Conclusions: highlights of the work

- Uncertainties in various parameters influencing lung activity measurements of actinides are evaluated. Estimated values are compared with the available literature values.

- Uncertainties due to important parameters in abdomen and wound measurement of actinides are evaluated.

- Effect of DTPA on urinary excretion in case of intake by wound of avid category and inhalation pathway of type M compounds is studied. Methodology is provided to predict the intake using enhanced urine excretion data when DTPA is given by injection pathway.

The above developments constitute definite progress towards providing uncertainties in internal contamination of actinides. It is no longer necessary to make assumptions in assessing uncertainty in lung monitoring. Using experimental and theoretical studies, it is possible to estimate the uncertainties for all the parameters in the lung activity assessment. Similarly, the thesis makes a serious attempt to improve the ability of assessing the internal dose when DTPA is given for chelation of actinides by bridging the existing gap between the ICRP models that do not take into consideration DTPA effect and urine analysis data available for large number of internal contamination cases, through systematic theoretical analyses and modeling. The thesis combines experimental and theoretical acumen to address one of the outstanding issues in the area of internal dosimetry, ie. the quantification of uncertainties in in-vivo measurements of actinides. The output of this work will lead to accurate and realistic estimation of lung, GI tract and wound activity.

8.3   Future scope of the work

The methodology used here for quantification of uncertainties can be used in other areas such as monitoring of fission and activation products using direct methods by shadow shied whole body counter, thyroid monitoring etc. The methodology developed in the course of Ph. D. work can be applied to all the categories of wound and can predict the intake and committed effective dose. It is also possible to predict the biokinetic model based on the urinary, fecal excretion rates and various organ measurement data and to evaluate the intake for a radionuclide with unknown biokinetic behaviour.

BIBLIOGRAPHY

1. ICRP publication 78. Individual monitoring for internal exposure of workers. Pergamon, (1997). Vol. 27.

2. Radiation Protection for Nuclear Facilities. AERB, Mumbai (2005). AERB/NF/SM/O-2.

3. IAEA. Assessment of occupational exposure due to intakes of radionuclides. BARC, Mumbai. (2003). IAEA RCA Regional Training course.

4. In-Vivo Measurements of Low Energy Photon (LEP) Emitters. R.C.Sharma, T.Surendran, T. K. Haridasan and C.M. Sunta. Bull. Radiat. Prot. (1989) Vol. 12, pp. 41 - 56.

5. IAEA. Methods for Assessing Occupational Radiation Doses due to Intakes of Radionuclides. Vienna, Austria. (2004). STI/PUB/1190.

6. wikipedia. [Online] https://en.wikipedia.org/wiki/Actinide.

7. The Chemistry of the Actinide Elements. J.J. Katz, G. T. Seaborg and L. R. Morss. New York, Chapman and Hall (1986) Vol. 1. ISBN 0- 0412-10550-0.

8. http://www.world-nuclear.org/information-library/nuclear-fuel-cycle/nuclear-power-reactors/nuclear-power-reactors.aspx.

9. http://www.arpansa.gov.au/pubs/factsheets/SmokeDetectorsandHealth.pdf.

10. http://www.nndc.bnl.gov/nudat2/chartNuc.jsp.

11. Metabolism and Safety aspects of Plutonium: An Update. Pushparaja, A.M. Bhagwat and S.K. Mehta. Rad. Prot. Envir. (1998) Vol. 21, pp. 147-166.

12. Nuclear Reactor Engineering Reactor Design Basics. Samuel Glasstone and Alexander Sesonske. Delhi, Chapman and Hall (1994) Vol. 1.

13. IAEA-TECDOC-1587. Spent Fuel Reprocessing Options. (2008).

14. http://barc.gov.in. [Online] BARC. http://barc.gov.in/randd/nfdf.html.

15. Radiation Physics for Medical Physicist. E.B. Podgorsak. Springer (2006). ISSN 1618-7210.

16. https://www.remm.nlm.gov/ANL_ContaminantFactSheets_All_070418.pdf.

17. ICRP Publication 38. Radionuclide Transformations - Energy and Intensity of Emissions. Vienna : Pergamon Press. (1983). Annals of ICRP. 11-13..

18. ^{241}Am as a Metabolic Tracer for Inhaled Plutonium Nitrate in external Chest counting. N. Ishigure, T. Nakano and H. Enomoto. Radiat. Prot. Dosim. (2001) Vol. 97, pp. 271 - 273.

19. ICRU Report 69. Direct determination of Body content of Radionuclides. Kent, Nuclear Technology Publishing (2003).

20. NCRP report 156. National Council on Radiation Protection and Measurements. Development of a Biokinetic Model for Radionuclide-Contaminated Wounds and Procedures for their Assessment, Dosimetry and treatment. (2006).

21. Upgradation of Internal Dosimetry Facilities at BARC Trombay. Pendharkar K. A., Bhati S., Singh I.S., Sawant P. D., Satyabhama N., Nadar M. Y., Vijaygopal P., Patni H.K., Kalyane G.N., Prabhu S. P., Ghare V. P. and Garg S.P. BARC Newsletter.(2008) Vol. 296, pp. 9-23.

22. Limits for Qualitative Detection and Quantitative Determination. L.A. Curie Application to Radiochemistry. Analytical Chemistry. (1968) Vol. 40, pp. 586–593.

23. BIPM, IEC, IFCC,ILAC,ISO,IUPAC,IUPAP and OIML. Evaluation of measurement data - Guide to the expression of uncertainty in measurement. Geneva : JCGM, 2008. JCGM 100 (2008).

24. Radiation Detection and Measurement. G.F.Knoll. New Delhi, Wiley Publishing (2000).

25. FLUKA: a multi-particle transport code. A. Fasso`, A. Ferrari, J. Ranft and P. R. Sala.Geneva : INFN and CERN, 2005. CERN-2005-10, INFN/TC_05/11, SLAC-R-773.

26. The FLUKA code: description and benchmarking. G. Battistoni, S. Muraro, P.R. Sala, F. Cerutti, A. Ferrari, S. Roesler, A. Fasso`, and J. Ranft**.** Batavia, Illinois : AIP Conf. Proceedings. (2007) Vol. 896, pp. 31-49. http://dx.doi.org/10.1063/1.2720455.

27. Estimation of [241]Am Activity embedded in palm. M. Y. Nadar, H. K. Patni, D. K. Akar, L. Mishra, I. S. Singh, D. D. Rao and P. K. Sarkar. Radiat. Prot. Dosim. (2013) Vol. 154, pp. 148 -156.

28. FLAIR: A powerful but user friendly graphical interface for FLUKA. Vlachoudis, V. Saratoga Springs, American Nuclear Society. (2009) Proc. Int. Conf. on Mathematics, Computational Methods & Reactor Physics.

29. EG and G Ortec. Modular Pulse Processing Electronics and Semiconductor Radiation Detectors. Oak Ridge, Ortec, (1994).

30. A Sensitive Steel Room Whole Body Counter with three LOAX HPGe detectors for in vivo monitoring of personnel for actinides. I. S. Singh, Minal Y. Nadar, G. N. Kalyane, S. Bhati and K.A. Pendharkar. Mumbai, IARP. (2008).

31. IAEA-TECDOC 1334. Intercalibration of in vivo counting systems using an Asian Phantom. Vienna, IAEA (2003).

32. A Tissue Equivalent Torso Phantom for Intercalibration of In-vivo Transuranic Nuclide Counting Facilities. R.V. Griffith, P.N. Dean, A.L. Anderson and J.C. Fisher. Vienna, IAEA (1979). Advances in Radiation Protection Monitoring. pp. 493 - 504. Stockholm, Sweden; 26 - 30 Jun 1978. ISBN 92-0-020279-9.

33. Realistic Torsa Phantom for Calibration of In vivo Transuranic Nuclide Counting Facilities. Shirotani. J. Nucl. Sci. Tech. (1988) Vol. 25, pp. 875 - 883.

34. The Livermore Phantom as a Calibration Standard in the Assessment of Plutonium in Lungs. D. Newton, A.C. Wells, S. Mizushita, R.E. Toohey, J.Y. Aha, R. Jones, S.J.Jefferies, H.E. Palmer, G.A. Riekshts, A.L. Anderson and G.W. Campbell. Vienna : IAEA (1984). Assessment of Radioactive Contamination in Man. pp. 183-199. ISBN 92-0-020085-0.

35. Mathematical phantoms for use in reassessment of radiation doses to Japanese A- bomb survivors. M. Cristy. Oak Ridge National Laboratory (1985). ORNL/TM-9487.

36. ICRP Publication 110. Adult reference computational phantoms. Oxford, UK. Pergamon Press, 2009.

37. The construction of computer tomographic phantoms and their application in radiology and radiation protection. M. Zankl, R. Veit, G. Williams, K. Schneider, H. Fendel, N. Petoussi and G. Drexler. Radiat. Environ. Biophys. (1988) Vol. 27, pp. 153-164.

38. ICRP Publicaiton 119. Compendium of Dose Coefficients based on ICRP Publication 60. Great Britain, Elsevier (2012).

39. Radiation doses and risks from internal emitters. John Harrison and Philip Day. J. Radiol. Prot. (2008) Vol. 28, pp. 137-159.

40. Reliability of the ICRP's Systemic Biokinetic models. Leggett R. W., Bouville A., Eckerman K.F. Radiat. Prot. Dosim. (1998) Vols. 79, 1-4, pp. 335-342.

41. Toward improved Biokinetic models for Actinides: The United States Transuranium and Uranium Registries, A twenty-five year report. L. Kathren R. Radiat. Prot. Dosim. (1994) Vol. 53, 1-4, pp. 219- 227.

42. ICRP Publication 66. Human Respiratory Tract Model for Radiological Protection. Ann. ICRP 24, 1-3. Oxford, UK, Pergamon Press (1994). ISBN 0 08 041154 1.

43. ICRP Publication 30. Limits for Intakes of Radionuclides by Workers. Oxford, UK : Pergamon Press (1979). Ann. ICRP 2, 3-4.

44. ICRP publication 130. Occupational Intakes of Radionuclides: Part 1. SAGE (2015). Ann. ICRP 44 (2).

45. ICRP publication 100. Human alimentary tract model for radiological protection. Elsevier (2006).

46. ICRP. Age dependent doses to members of the public from Intake of Radionuclides, part 2: Ingestion Dose coefficients. Oxford, UK, Pergamon Press (1993). Annals of the ICRP. 23(3/4).

47. ICRP. Age dependent doses to members of the public from Intake of Radionuclides, part 3: Ingestion Dose coefficients. Pergamon Press, (1995a) Annals of the ICRP. 25 (1).

48. Dosimetric methodology of the ICRP. K. F. Eckerman. (1994) ORNL CONF-9406107-7

49. ICRP Publication 103. The 2007 recommendations of the International Commission on Radiological Protection. Pergomon Press (2007).

50. BIPM, IEC,ISO,OIML. Guide to the Expression of Uncertainty in Measurement. Geneva : ISO (1995). ISBN 92-67-10188-9.

51. NCRP report 164. Uncertainties in Internal Radiation Dose Assessment. (2009).

52. EU research project under 5th Framework. Project IDEAS Program. Guidance on internal dose assessments from monitoring data. (2003).

53. Design and implementation of monitoring programmes for internal exposure (project OMINEX). G.1.Etherington, G.N.Stradling, T. Rahola, B. LeGuen, C.Hurtgen, J.R. Jourdain, P. Bérard, Radiat. Prot. Dosim. (2003) Vols. 105 (1-4), pp. 641-644.

54. Measurements of the Human anterior Chest wall by ultrasound and estimates of chest wall thickness for use in determination of transuranic nuclides in the lung. T.J. Sumerling and S.P. Quant. Radiat. Prot. Dosim. (1982) Vol. 3 (4), 203 -210.

55. http://physics.nist.gov/PhysRefData/XrayMassCoef/tab4.html.

56. Monte Carlo: Basics. K.P.N. Murthy. Kalpakkam : Indian Society for Radiation Physics, (2000) ISRP - TD - 3.

57. Monte Carlo Primer – A practical approach to Radiation Transport. S. Dupree and S. Fraley. A New York : Kluwer Academic/Plenum Publishers (2001). ISBN 0-306-46748-8.

58. Exploring Monte Carlo Methods. William L. Dunn and J. Kenneth Shultis. Elsevier (2011). ISBN 0080930611.

59. Fundamentals of Monte Carlo particle transport. Forrest Brown. Los Almos National Laboratory (2005). LA-UR-05-4983.

60. A primer for the Monte Carlo Method . I.M.Sobol .Forida, USA, CRC Press (1994). ISBN 0-8493-8673-X.

61. Probability and Statistics. A. Papoulis. New Jersy, USA : Prentice Hall International Inc., (1990). ISBN 0-13-711730-2.

62. The 64-bit universal RNG. George Marsaglia and Wai Wan Tsang. Statistics & Probability Letters (2004) Vol. 66, pp. 183-187.

63. Monte Carlo Particle Transport methods: Neutron and Photon Calculations. Ivan Lux and Laszlo Koblinger. Floride, USA , CRC Press (1991). ISBN 0-8493-6074-9.

64. Monte Carlo Photon Transport Techniques. H. S. Kushwaha and P. Srinivasan. Applications of Monte Carlo methods in Nuclear sciences and Engineering. Sharda Bhati. Mumbai , Krystal Print Products (2009).

65. Mathematical Verification of a certain Monte Carlo Sampling Technique and Application of the technique to Radiation Transport Problems. W. A**.** Coleman. Nuclear Science and Engineering (1968) Vol. 32, pp. 76-81.

66. PENELOPE-2008: A Code System for Monte Carlo Simulatio of electron and photon transport. Francesc Salvat, José M. Fernández-Varea, Josep Sempau. Spain : NEA, OECD, (2008). ISBN 978-92-64-99066-1.

67. MCNP^{TM}–A General Monte Carlo N-Particle Transport code. Judith F. Briesmeister. Los Almos National Laboratory (2000). LA–13709–M.

68. An MCNP Primer. J.K. Shultis and R.E. Faw. Kansas State University (2008).

69. ICRP Publication 89. Basic anatomical and physiological data for use in Radiological Protection. Pergamon Press (2002).

70. Assessment of Uncertainties in the lung activity measurement of low energy photon emitters using Monte Carlo simulation of ICRP male thorax voxel phantom. M. Y. Nadar, D. K. Akar, M.S. Kulkarni, D. D. Rao and K. S. Pradeepkumar. Radiat. Prot. Dosim. (2015)Vol. 167, pp. 461-471.

71. Monte Carlo simulation of skull and knee voxel phantoms for the assessment of Skeletal burden of low energy photon Emiters. M. Y. Nadar, D. K. Akar, H. K. Patni, I. S. Singh, L. Mishra, D. D. Rao and K. S. Pradeepkumar. Radiat. Prot. Dosim. (2014) Vol. 162, pp. 469-477.

72. Methodology for the assessment of Ingested actinides from Monte Carlo simulation of voxel phantom. M. Y. Nadar, D. K. Akar, M.S. Kulkarni, D. D. Rao and K. S. Pradeepkumar. Radiat. Prot. Dosim. (2016). doi:10.1093/rpd/ncw015.

73. A microcomputer algorithm for solving a first order compartmental models involving recycling. A. Birchall and A.c. James. Health Phys. (1989) Vol. 56/6, pp. 857 -868.

74. The Scaling and Squaring Method for the Matrix exponential revisited. J. Nicholas Siam J. Higham, Matrix Anal. Appl.(2005) Vol. 26, No. 4. pp. 1179-1193.

75. Lognormal Distributions across the sciences: Keys and clues. E. Limpert, W. A. Stahel and M. Abbt. Bioscience (2001) Vol. 51, No. 5. pp. 341-352.

76. Ultrasonic measurements of chest wall thickness for the assessment of internal contamination due to actinides in Indian radiation workers. M. Y. Nadar, I. S. Singh, A. Chaubey, S. Kantharia and S. Bhati. Recent trends in Radiation Physics Research. Proceedings of NSRP-18. (2009) pp. 284-285.

77. IAEA-TECDOC-1005. Compilation of anatomical, physiological and metabolic characteristics for a reference Asian man. IAEA (1998). ISSN 1011-4289.

78. Examples of Mesh and NURBS Modelling for In Vivo Lung Counting Studies. Farah J., Broggio D. and Franck D. Radiat. Prot. Dosim. (2011) Vol. 144, No. 1 - 4, pp. 344-348.

79. Gaussian smearing of the detector spectrum obtained from Monte Carlo simulation in FLUKA. Minal Y. Nadar, D. D. Rao and K. S. Pradeepkumar. (2014). IARPNC-2014, Mumbai

80. Calculation and measurement of Calibration Factors for Bone Surface Seeking Low Energy Gamma Emitters and Determination of ^{241}Am Activity in a real case of Internal

Contamination. J.G. Hunt, I. Malatove and S. Foltanova. Radiat. Prot. Dosim. (1999) Vol. 82, No. 3, pp. 215-218.

81. Voxel Phantoms and Monte Carlo methods applied to in vivo Measurements for Simultaneous 241Am Contamination in four body regions. J.G. Hunt, B.M. Dantas, M.C. Lourenco and A.M. G. Azeredo. Radiat. Prot. Dosim. (2003) Vol. 105, No.1-4, pp. 549-552.

82. Monte Carlo Simulation of in vivo Measurement of the most suitable knee position for the optimal measurement of activity. M. Kalaf, R.R. Brey, J.T. Harris, D. Derryberry and G. Tabatadze. Health Phys. (2013) Vol. 104,No.4, pp. 405 - 412.

83. Assessing Skull Burdens of Actinides using a Mathematical Phantom: A Monte Carlo Approach. S. Bhati, R.C. sharma and V.V. Raj. Radiat. Prot. Dosim.(2003) Vol. 103, No. 3, pp. 247-254.

84. Design, Fabrication and Evaluation of a New Calibration Phantom for In vivo Measurement of Bone-Seeking Radionuclides. H.B. Spitz and J.C. Lodwick. Radiat. Prot. Dosim. (2000) Vol. 89, No.3-4, pp. 275-282.

85. The construction of computer tomographic phantoms and their application in radiology and radiation protection. M. Zankl, R.Veit, G. Williams, K. Schneider, H. Dendel, N. Petoussi and G. Drexler. Radiat. Environ. Biophys. (1988) Vol. 27, pp. 153-164.

86. Voxel-Based Models Representing the Male and Female ICRP Reference Adult – The Skeleton. M. Zankl, K.F. Eckerman and W.E. Bolch. Radiat. Prot. Dosim.(2007) Vol. 127, No. 1-4, pp. 174-186.

87. Measurement of the quantity 'activity' of radionuclides in simulated human organs: an international intercomparison. G. Kramer. http://kisoe.kins.re.kr/FileUp.

88. Toward improved Biokinetic models for Actinides: The United States Transuranium and Uranium Registries, A twenty-five year report. R.L. Kathren. Radiat. Prot. Dosim. (1994) Vol. 53, No. 1-4, pp. 219-227.

89. Reliability of the ICRP's Systemic Biokinetic models. R.W. Leggett, A. Bouville and K.F. Eckerman. Radiat. Prot. Dosim. (1998) Vol. 79, No.1-4, pp. 335-342.

90. ICRP. Guide for the practical application of the ICRP Human Respiratory Tract Model. Pergamon Press (2003).

91. Medical and Health Physics Management of a Plutonium Wound. E. H. Carbaugh, **W**. A. Decker and M.J. Swint. Radiat. Prot. Dosim. (1989) Vol. 26, No. 1/4, pp. 345-349.

92. Application of multi-compartment wound models to plutonium-contaminated wounds incurred by former workers at rocky flats. R.B. Falk, N.M. Daugherty, J.M. Aldrich, F.J. Furman and D.E. Hilmas. Health Phys. (2006) Vol. 91, No. 2, pp. 128-143.

93. Model and Practical Information Concerning the Radiotoxicological Assessment of a Wound Contaminated by Plutonium. J. Piechowski, D. Cavadore, J. Tourte, M. H. Cauqui, P. Raynaud, J. C. Harduin, P. Thomas and Y. Chaptinel. Radiat. Prot. Dosim. (1989) Vol. 26, No. 1/4, pp. 265-270.

94. New technique using Room Temperature diodes for the direct assessment of internal contamination by low energy gamma emitters. Jean-Louis Genicot and Jean-Pierre Alzetta. Appl. Radiat. Isot. (1997) Vol. 48,No. 3, pp. 349-358.

95. Assessment and Management of a Plutonium contaminated wound case. G. B. Schofield, H. Howells, F. Ward, J. C. Lynn and G. W. Dolphin. Health Phys.(1974) Vol. 26, No. 6, pp. 541-554.

96. Identification of [241]Am in the Axillary Lymph nodes with an Intrinsic Germanium Detector. S.G. Graham and S.J. Kirkham. Health Phys. (1983) Vol. 44, No.1, pp. 343-352.

97. The assessment of Plutonium and Americium in Contaminated Wounds with High Energy Resolution Semiconductor Detectors. Jean-Louis Genicot, F. Hardeman and S. Obestedt. Appl. Radiat. Isot. (1995) Vol. 46, No. 3, pp. 199-203.

98. Assessment of [241]Am embedded in tissue using Phoswich and an array of HPGe detectors. M. Y. Nadar, I. S. Singh and S. Bhati. Radiat. Prot. Environ. (2010) Vol. 33, No.4, pp. 213-0215.

99. Measurement of Plutonium in Contaminated Wound of Worker using an Array of HPGe Detector. I.S. Singh, M. Y. Nadar, L. Mishra and D. D. Rao. NUCAR, Visakhapatnam (2011).

100. Analytical and Monte Carlo assessment of activity and local dose after a wound contamination by Activation products. D. Broggio, B. Zhang and L. Carlan. Health Phys. (2009) Vol. 96, No. 2, pp. 155-163.

101. Calibration of a Am-241 wound-monitoring system using Monte Carlo techniques. D. P. Hickman, D. A. Kruchten and S.K. Fisher. Health Phys.(1994) Vol. 66., No.4, pp. 400-405.

102. Error Analysis for the in-vivo measurement of radionuclides in wounds: Monte Carlo study. Ahmed, A. S. M. Sabbir, K. Capello, T. Sabourin, G. H. Kramer. Health Phys.(2010) Vol. 99, No. 6, pp. 759-768.

103. IAEA. Update of X-ray and Gamma ray decay data standards for detector calibration and other applications. Vol.1 recommende Decay Data, High Energy Gamma ray Standards and Angular Correlation Coefficients. (2007).

104. Data Reduction and Error Analysis for the Physical sciences. P. R. Bevington. McGraw-Hill (1969).

105. Therapeutic whole lung lavage for inhaled plutonium oxide revisited. C. Morgan, D. Bingham, D. C. B. Holt, D. M. Jones and N. J. Lewis. J. Radiol. Prot. (2010) Vol. 30, pp. 735-746.

106. Radiological Protection. A. Kaul and D. Becker. Germany, Springer (2005) Vol. 4. ISSN 1619-4802.

107. http://www.fda.gov/downloads/Drugs/EmergencyPreparedness/BioterrorismandDrugPreparedness/UCM131638.pdf.

108. Interpretation of human urinary excretion of plutonium for cases treated with DTPA. J.J. Jech, B.V. Anderson and K.R. Heid. Health Phys.(1972) Vol. 22, pp. 787-792.

109. A mathematical model for estimation of plutonium in the human body from urine data influenced by DTPA therapy. R. M. Hall, G.A. Poda, R. R. Fleming and J. A. Smith. Health Phys. (1978) Vol. 34, pp. 419-431.

110. The retention of ^{14}C-DTPA in Human volunteers after inhalation or intravenous injection. J.W. Stather, H. Smith, M.R. Bailey, A. Birchall, R.A. Bulman and F.E.H. Crawley. Health Phys.(1983) Vol. 44, No. 1, pp. 45-52.

111. Biokinetic Modelling of DTPA decorporation therapy: the CONRAD approach. B. Breustedt, E. Blanchardon, P. Berard, P. Frisch, A. Giussani, M. A. Lopez, A. Luciani, D. Nosske, J. Piechowski, J. Schimmelpfeng and A. L. Serandour. Radiat. Prot. Dosim. (2009) Vol. 134, No. 1, pp. 38 -48.

112. An analysis of a puncture wound case with medical intervention. B. R. Bailey, K.F. Eckerman and L.W. Townsend. Radiat. Prot. Dosim. (2003) Vol. 105, pp. 509-512.

113. USTUR whole body case 0269: demonstrating effectiveness of I.V. Ca-DTPA for Pu. A.C. James, L.B. Sasser, D.B. Stuit, S.E. Glover and E.H. Carbaugh. Radiat. Prot. Dosim. (2007) Vol. 127, pp. 449-455.

114. Plutonium, industrial hygiene, health physics, and related aspects. Uranium-plutonium-transplutonic elements, handbook of experimental pharmacology. H. M. Parker. New York, Springer, 1973.

115. Influence of DTPA treatment on Internal dose estimates. E. Davesne, E. Blanchardon, D. Peleau, P. Correze, S. Bohand and D. Franck. Health Phys.(2016). Vol. 110,No. 6, pp. 551-557.

116. Development of the Plutonium-DTPA Biokinetic model. Kevin Konzen and Richard Brey. Health Phys.(2015) Vol. 108, No. 6, pp. 265-573.

117. SAAM II: Simulation, Analysis and modeling software for tracer and pharmacokinetic studies. P. Hugh R. Barrett, B. M. Bell, C. Cobelli, H. Golde, A. Schumitzky, P. Vicini and D. Foster. Metabolism. (1998) Vol. 47, No. 4, pp. 484-492.

118. The IMBA suite: Integrated modules for bioassay analysis. A. Birchall, N.S. Jarvis, N.S. Peace, A.E. Riddell and W. P. Battersby. Radiat. Prot. Dosim. (1998) Vol. 79, No. 1-4, pp. 107-110.

119. The Autocorrelation coefficient as a tool for assessing goodness of fit between bioassay predictions and measurement data. M. Puncher, A. Birchall and J. W. Marsh. Radia. Prot. Dosim. (2007) Vol. 127, No. 1-4, pp. 370-373.

120. IDEAS internal contamination database: a compilation of published internal contamination cases. A tool for the internal dosimetry community. C. Hurtgen. Radiat. Prot. Dosim. (2007) Vol. 125, pp. 520-522.

121. IAEA. Intercomparison and Biokinetic model validation of radionuclide intake assessment. Vienna : IAEA (1999). ISSN 1011-4289.